Integrin Linked Kinase is Critical for Hepatic Cellular Organization, Metabolism, and Glucoregulation

By

Elijah Trefts

Dissertation

Submitted to the Faculty of the

Graduate School of Vanderbilt University

In partial fulfillment of the requirements

for the degree of

DOCTOR OF PHILOSOPHY

In

Molecular Physiology & Biophysics

May 31st, 2019

Nashville, Tennessee

Approved:

John M. Stafford, M.D., Ph.D.

Alan D. Cherrington, Ph.D.

Ambra Pozzi, Ph.D.

Roy Zent, M.D., Ph.D.

ACKNOWLEDGEMENTS

I will remain eternally grateful for the individuals that have contributed their time and effort to my progress professionally and personally over the course of completing this degree. My time in the Wasserman laboratory has expanded my intellectual, technical, and professional skill sets on my path to becoming an independent scientist. Dr. David Wasserman has been perpetually generous with his time, experience, and scientific knowledge. For this generosity I will be forever grateful. His acumen in scientific research, publishing, networking, and telling terrible jokes will serve me throughout my scientific career as well as my personal life. Through David's mentorship I am set to become a world-class scientific researcher as well as a husband and friend to those around me. The work contained in this dissertation is not possible without a team of people committed to the ideals and goals of the Wasserman laboratory. In this regard I stand on the shoulders of giants, who have made my research possible every day for the past 5 years. I extend my gratitude to Deanna Bracy, Mickael Goelzer, Dr. Clinton Hasenour, Dr. Curtis Hughey, Freyja James, Dr. Li Kang, Dr. Louise Lantier, Dr. Ashley Williams, and Dr. Ian Williams. These individuals have helped with their knowledge, but also their time and seemingly inexhaustible effort. I would particularly like to thank Deanna Bracy who serves as a paragon for technical research support through her extensive commitment to the Wasserman laboratory including my time here. Dr. Curtis Hughey has provided extensive input and assistance in his vast knowledge of metabolism, but also navigating the professional landscape moving forward. Finally, Dr. Ian Williams has been a dear friend throughout our overlapping Ph.D. training in the Wasserman laboratory.

Drs. John Stafford, Alan Cherrington, Ambra Pozzi, and Roy Zent, have served as my Thesis Committee and were critical in the progress and conclusion of the work contained herein. Dr. Stafford has taught me to maintain a connection with the bigger picture and clinical impacts

of my research. Dr. Cherrington has enhanced my capacity for understanding processes within the scope of physiologic frameworks. Dr. Pozzi has helped me to better understand the role of integrins in physiology as well as how to marry fields of metabolism and integrin-cellular biology. Finally, Dr. Zent has taught me to maintain diligent critical thinking and to consider a broader range of scientific perspectives during the research process. Through the assembly of these mentors, their knowledge, their experience, and their time I am equipped to succeed throughout my research career. I would like to thank all the individuals in the Mouse Metabolic Phenotyping Center, Hormone Assay Core, Diabetes Center, Digital Histology Shared Resource, and Translational Pathology Shared Resource for their efforts and broad skillsets that fuel Vanderbilt's capacity for cutting edge research. I would especially like to thank Dr. Owen McGuiness for serving as a mentor and sounding board for all ideas relating to metabolism and physiology. Additionally, I thank Dr. Kelli Boyd for her expertise in veterinary pathology and extensive investment in this project.

As with progress in research, progress in life is not obtained in solitude. I have been the benefactor of supportive family members, friends, and fiancée, Katherine. These people have contributed to my drive and character throughout my life and in completing this milestone. Without them, I do not get here and I do not make it to the finish line. With completion of this chapter in my life I will maintain a commitment to these people and my career in biomedical research. I am eternally grateful for this time and the people who have made it possible.

TABLE OF CONTENTS

Page

LIST OF FIGURES

Figure **Page**

LIST OF TABLES

Chapter I

INTRODUCTION

Current data project obesity prevalence within the United States to reach ~42% by 2030 (73). As of 2008, the financial burden of obesity translated to $147 billion in extra healthcare expenditures, independent of comorbidities (74). Prolonged obesity is detrimental to many aspects of health (27) and the liver represents a keystone in development of obesity related pathologies. It is directly associated with aggregates of the metabolic syndrome (166) including dyslipidemia (239), hyperglycemia (293), insulin resistance (33, 57), and nonalcoholic fatty liver disease (NAFLD) (44). NAFLD is relatively new as an appreciated consequence of over-nutrition. NAFLD contributes to end stage liver disease (71), type 2 diabetes (T2D) (283), and cardiovascular disease (250). Estimates indicate 55 million adults in the United States have NAFLD with incidence predicted to increase parallel with rates of obesity (154). Additionally NAFLD is projected as the primary cause for liver transplants in the United states by 2030 (39). Despite the impacts of NAFLD on public health at the national and global levels there are currently no therapeutic options available for primary treatment of NAFLD (81). Given the immense effects on quality of patient lives and the current lack of therapeutic options, research efforts aimed at understanding pathologic mechanisms of NAFLD are imperative.

Hepatic insulin resistance (IR) is typically described as the loss of insulin's inhibitory effects on hepatic glucose output. This condition is highly correlated with both NAFLD and T2D (31, 57). Over last 15 years hepatic IR has also become increasingly associated with extracellular matrix (ECM) expansion (32). ECM deposition was formerly considered a sign of advanced disease progression in many liver pathologies including NAFLD. However, the fibrotic program is now thought to initiate early, parallel many progressive components of the disease, and play an active role in disease progression.

Hepatocytes are the primary site of insulin action and metabolic integration within the liver. Alterations in ECM during hepatic IR and NAFLD (9) has prompted research on the cadre of signals emanating from hepatocyte-ECM interactions that influence these pathologies. Studies have now demonstrated that integrins, the primary cell-ECM signaling receptors, have variegated effects on IR in different tissues during diet-induced obesity (DIO) (279). Integrin-linked kinase (ILK) is an intracellular signaling protein immediately downstream of integrin receptors that is requisite for development of hepatic IR during DIO (280). Hepatic IR and NAFLD are rooted in deficient hepatic glucoregulation and altered metabolism. Therefore, understanding ILK within the contexts of these processes serves to clarify the role of ILK, integrins, and ECM in these pathologies, but also in normal physiology.

Hypotheses, experiments, and resulting conclusions related to this work were formulated as the logical progression of historical interests within our research environment with modifications as new information became available. In this regard, the introduction acts as an orientation for the efforts and concepts that serve as the foundation of this body of work. Initially this section describes hepatic development as this establishes the liver as a center for metabolic function and maintenance of physiologic homeostasis. Next, control of hepatic metabolism through endocrine systems is introduced. This offers insight in to typical physiologic function as well as the aspects of this control that can go awry during pathology. Associations of ECM deposition with several pathologic states, including insulin resistance and NAFLD, are then discussed. In order to better approach hepatic ECM and its contributions to these pathologies the typical structure, contents, and organization of this compartment within the liver are briefly reviewed. Also considered are the means that cells interact with and interpret the ECM, emphasizing integrin receptors and their downstream signaling components. Amongst these components is integrin-linked kinase, whose actions serves as the primary molecular focus of this dissertation. Specifically the functions of this protein in cellular biology and how it impacts insulin resistance, hepatic metabolism as well as injury and regeneration.

The liver as a metabolic hub

The liver is a critical hub for numerous physiological processes. These include whole-body glucose homeostasis, blood volume regulation, immune system support, endocrine control of growth signaling pathways, lipid and cholesterol homeostasis, and the breakdown of xenobiotic compounds including many current drugs (4). Processing, partitioning, and metabolism of macronutrients provide energy for the aforementioned processes and are therefore among the liver's most critical functions (223, 255).

The liver's capacity to store glucose in the form of glycogen, with feeding, and assemble glucose via the gluconeogenic pathway, in response to fasting, are critical to whole body glucose homeostasis (99). The liver oxidizes lipids for provision of energy (177, 223) and maintenance of metabolite pools (200), while also packaging excess lipid for secretion to and storage in other tissues (107), such as the adipose. Finally, the liver is a major handler of protein and amino acid metabolism (28) as it is responsible for the majority of proteins secreted in the blood (whether based on mass or range of unique proteins), the processing of amino acids for carbon, and disposal of nitrogenous waste from protein degradation in the form of urea metabolism (2). This diverse array of metabolic integrations is determined through an intricate hierarchy of transcription factors and signaling processes that are initiated during development and reinforced throughout the life of the organism.

Initiation of liver development

As the function and organization of the liver are critical to so many processes it is important to understand how these aspects of the liver arise developmentally. Described here is the general organization of hepatic development that occurs in many animals including zebra fish, mice, rats, and humans. Duration and identity of signals involved in each of these developmental aspects may vary between species. The goal of this section is to give a general overview of hepatic

development in common model organisms and humans. For simplicity, specific proteins and transcription factors referenced have been derived from studies in mice and rats except where specifically noted.

The definitive endoderm, ectoderm, and mesoderm make up the three major cell layers established during embryonic gastrulation. Cells from the definitive endoderm proceed to form the epithelium of the respiratory and digestive tracts as well as associated organs such as liver and pancreas (88). The primary metabolic cell population of the liver, hepatocytes, and the bile duct lining epithelial cells, cholangiocytes, arise from the posterior foregut region within the definitive endoderm (258). Definitive endoderm specification and segregation require a complex array of extracellular growth factor signals in proper temporal organization. Some of the earliest signals for initiation of hepatic bud outgrowth from the posterior foregut endoderm include fibroblast growth factor (FGF) (61), and bone morphogenic proteins (BMPs) (172), which are provisioned from the overlying mesodermally-derived cardiac mesoderm and septum transversum. Other signals influencing this process include transforming growth factor β (TGF-β) (6), Wnt (55), and NOTCH. These signals are supported by expression and activity of transcription factors in the FoxA and GATA families within the endodermally-derived epithelium. Specific members of these families, notably FoxA1 and GATA4 (46), act as pioneer factors, interacting with their DNA binding motifs within compact chromatin to modify nucleosome localization. This alteration of chromatin conformation creates an environment of transcriptional competence for these and other downstream transcription factors. The sum of these epigenetic modifications results in a “footprint” of transcriptional access leading to establishment and maintenance of gene expression critical for differentiation and mature function (Figure 1.1).

Cell patterning and maturation during liver development

Cells of the hepatic bud give rise to bipotential progenitor cells known as hepatoblasts, which further differentiate into the liver parenchymal cells: hepatocytes and cholangiocytes (88, 91, 240). Importantly, prior to the formation of the bone marrow, the developing liver bud serves as the center of fetal hematopoiesis. Signals from hematopoietic cells, such as oncostatin M, can also govern hepatoblast proliferation (135) and E-cadherin-mediated cell junction formation (173) in hepatoblasts. While there are several other contributors to hepatoblast differentiation the gradient of TGF-β secreted from the portal vein mesenchyme is integral to cholangiocyte and hepatocyte differentiation (88). This contributes to the hepatoblast fates that are dependent on portal vein proximity. Mechanistically, higher TGF-β signaling in portal vein proximal hepatoblasts drives cholangiocyte fate by decreasing expression of CCAAT/Enhancer Binding Protein (C/EBP) α (291) and promoting expression of HNF6 (aka Oc1) and HNF1β (48). This transcription factor profile promotes cholangiocyte-specific gene transcription through HNF6 and HNF1β, while suppressing hepatocyte specific genes by decreasing C/EBPα levels. Hepatoblasts located further from the portal vein develop into hepatocytes, forming chords across the developing hepatic lobules. These cells receive lower levels of TGF-β, which leads to a higher level of C/EBPα. In turn C/EBPα inhibits the expression of TGF-β receptor II creating a positive feedback loop of TGF-β signal inhibition (48, 240). C/EBPα also regulates expression of HNF1α and HNF4α, which act as feed forward co-activators in a number of hepatocyte specific genes. Finalization of hepatocyte differentiation is linked to oncostatin M (135), glucocorticoids (68), hepatocyte growth factor (HGF) (234), Wnt/β-catenin (8, 55), and yes-associated protein signaling (YAP) (236).

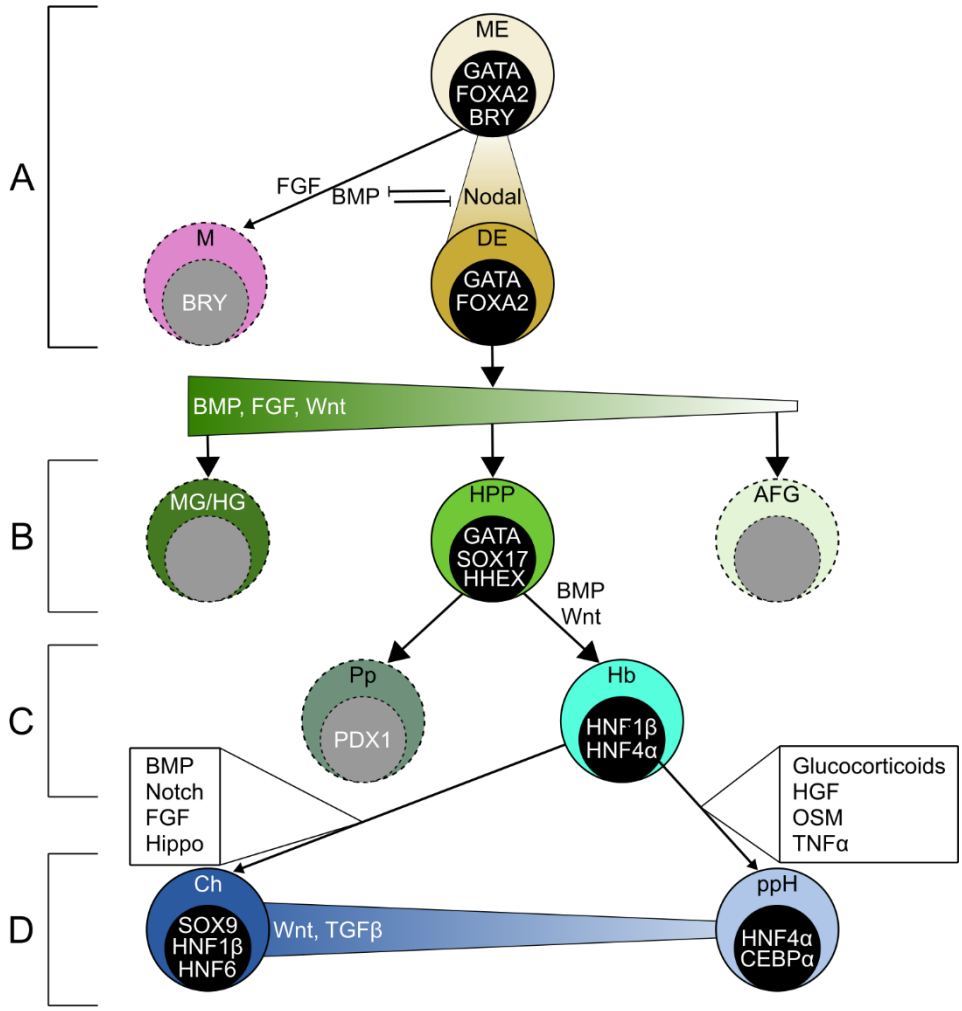

Adapted from Gordillo, Evans, & Gouon-Evans 2015

Figure 1.1- A model of hepatic epithelial cell development with supporting signals and transcription factors. A) Gastrulation and endoderm specification is driven by nodal signaling of the bipotential mesendoderm (ME). BMP inhibits nodal signaling and segregates brachyury (BRY) positive mesoderm from definitive endoderm (DE). **B)** DE cells expressing pioneering transcription factors FOXA2 and GATA4/6 (GATA) are driven by gradients of bone morphogenic proteins (BMPs), fibroblast growth factors (FGFs), and Wnt ligands through endoderm and gut tube patterning. DE cells will give rise to mid-gut/hind-gut (MG/HG) intestinal progenitors, anterior foregut (AFG) lung progenitors, and hepato-pancretic progenitors (HPP). **C)** Hepatoblast specification separates pancreatic progenitors (Pp) from hepatoblasts (Hb). Action of BMPs and Wnts drive the bipotential Hb population through expression of the biliary transcription factor hepatocyte nuclear factor 1β (HNF 1β) and the hepatocyte transcription factor HNF4α. **D)** Wnt ligands and transforming growth factor β (TGFβ) derived from the portal vein mesenchyme couple with BMP, Notch, FGF, and Hippo signals to drive cholangiocyte fate. These signals reinforce HNF1β while initiating activity of the definitive biliary transcription factors HNF6 and SRY-box 9 (SOX9). Hb cells distant from the portal vein mesenchyme are influenced by glucocorticoids, hepatocyte growth factor (HGF), Oncostatin M (OSM), and tumor necrosis factor α (TNFα) to finalize hepatocyte (H) differentiation.

Many of the transcriptional factors involved in the finalizing of hepatocyte development are critical to the establishment of hepatocyte glucoregulatory functions. C/EBPα cooperates with the insulin sensitive transcription factor Foxo1 in the establishment of gluconeogenic functions (235). Wnt/β-catenin signaling has also been implicated in establishment of differential metabolic functions based on hepatocyte localization within the liver known as metabolic zonation (98). In fact, a balance of stimulation and suppression of genes by HNF4α is influenced by the β-catenin activated transcription factor LEF1 to establish zonal specific expression of various enzymes (e.g. glutamine synthetase) (49). More recently a paradigm where glucagon and wnt/β-catenin signaling exist on opposing gradients across the liver sinusoid have been established. Glucagon signaling is stronger in the portal area and preserves a number of oxidative and gluconeogenic metabolic processes. Whereas, Wnt/β-catenin signaling drives expression of periportal metabolic genes such as glutamine synthetase (41). This is a complementary arrangement as glucagon is a major driver of amino acid utilization and nitrogen waste production within the liver while glutamine synthesis is a high affinity sink for nitrogenous waste that escapes the urea cycle (106). While these transcriptional programs are emphasized during development their importance in a number of mature physiologic processes are also becoming increasingly apparent. This is emphasized by the discovery that mutations in the classic hepatocyte developmental transcription factors, HNF4α and HNF1α, underlie genetic forms of diabetes known as maturity-onset diabetes of the young (MODY) (290). Furthermore, heterozygosity for MODY mutations in these transcription factors can influence glucose and insulin homeostasis, potentially contributing to increased risk of diabetes development (203).

Liver cellular anatomy and organization with respect to metabolism

Hepatic capacity for such a wide range of metabolic processes is rooted in its unique structure and organization as a result of the described developmental programming. Therefore,

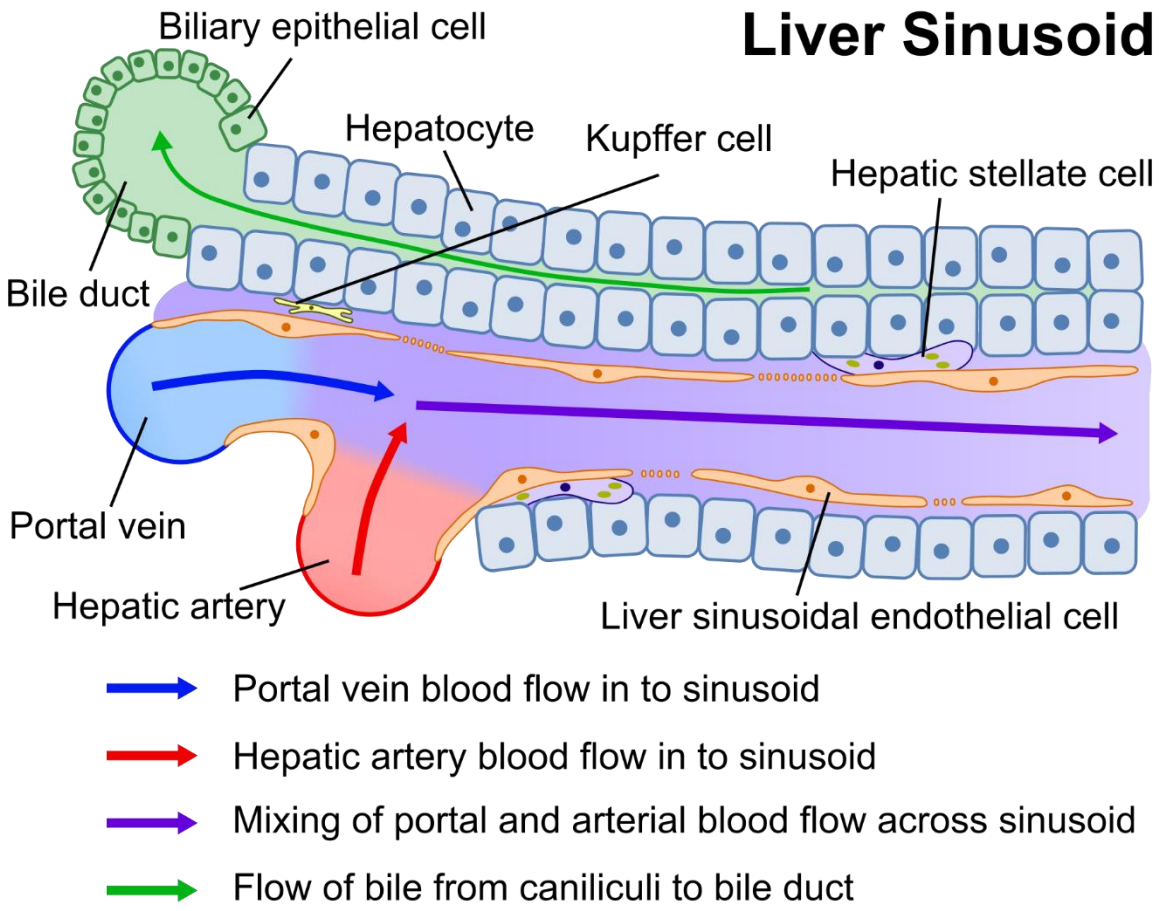

Figure 1.1- The organization and cellular populations of the liver sinusoid. A) A number of cell types exist within the sinusoid including hepatocytes, biliary epithelial cells (cholangiocytes), endothelial cells, Kupffer cells, and stellate cells. Blood flows through the sinusoid leading to a number of gradients along the length of this vessel. Liver endothelial cells do not form tight junctions, but instead have sieve plate networks between them. This allows for maximum exchange of macromolecules between the circulating blood and hepatocytes, which conduct a majority of the hepatic metabolic functions.

spatial components of hepatocellular anatomy and physiology serve as a critical foundation for understanding hepatic metabolism while informing critical points of pathologic progression.

The liver is composed of several cell types of different embryological origin including hepatocytes, biliary epithelial cells (cholangiocytes), stellate cells, Kupffer cells, and liver sinusoidal endothelial cells (Figure 1.2) (240). Each of these cell types possesses unique roles that cooperatively regulate hepatic function at multiple levels. Hepatocytes are the primary epithelial cell population of the liver. They make up the majority of the liver volume (21) and perform many of the functions, including metabolism, ascribed to the liver. Cholangiocytes are the second most abundant epithelial population of the liver and have a more traditional epithelial function as the cells lining the lumen of the bile ducts. Stellate cells represent a dynamic cell population that can exist in a quiescent or activated state (80). In the quiescent state stellate cells store Vitamin A in lipid droplets (230); however, other functions in this quiescent state remain unclear. Damage to the liver leads to activation of stellate cells (95). Upon activation stellate cells proliferate and progressively lose vitamin A stores. Stellate cells are also responsible for deposition and organization of ECM in the injured liver. This process contributes to fibrosis of the liver during various pathologies (139), which can progress to cirrhosis and contribute to end stage liver disease. Kupffer cells are the resident macrophage population of the liver. These cells recognize the many pathogenic stimuli introduced through the portal circulation and can attain pro- or anti-inflammatory roles in liver wound healing (209). Finally, liver sinusoidal endothelial cells are a specialized endothelial population with unique characteristics (59, 60). These cells form fenestrated sieve plates at the sinusoidal lumen (286). This structure creates pores ranging in size from 50-180 nm in humans or 50-280 nm in mice and rats (285). This organization is critical for exchange of metabolites, proteins, and particles within these size limits between plasma and the cell types of the liver, while maintaining certain barrier functions.

The cells of the liver are organized around the functional structural unit of the liver, the lobule or acinus (130). This consists of chords of hepatocytes organized in a typically hexagonal

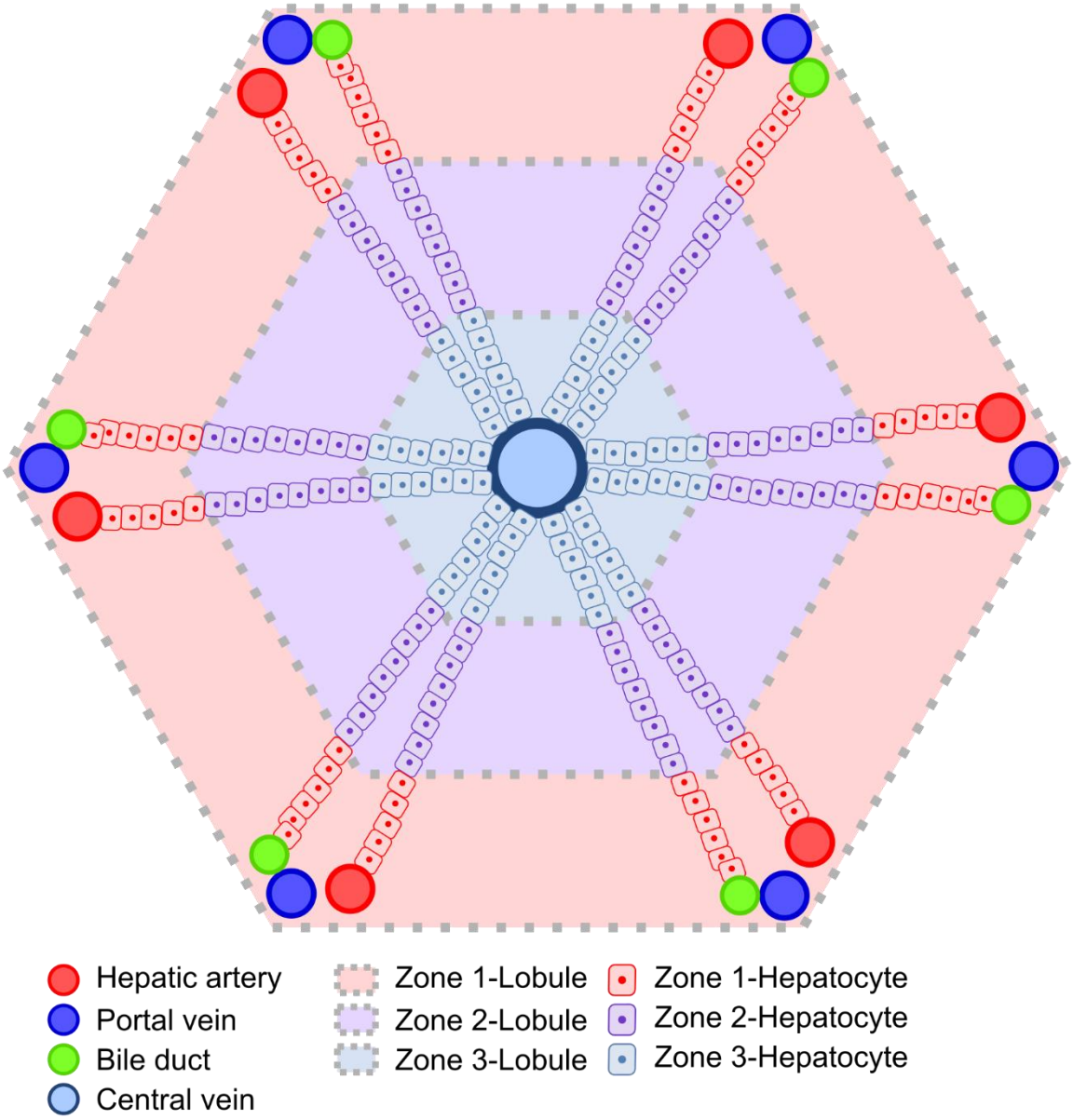

Figure 1.2- General structure and organization of a typical hepatic lobule. Appearing roughly hexagonal in shape the vertices represent the portal triad area. Each triad contains branches of the portal vein, hepatic artery, and bile duct. Oxygenated blood from the general arterial circulation enters the hepatic artery and mixes with nutrient rich blood from the portal circulation in the gut. Upon mixing this blood equilibrates and flows across the lobule through a sinusoidal network before draining in to branches of the central vein.

shape around the central vein (Figure 1.3). At the vertices of this hexagon are the portal triads consisting of closely grouped branches of the hepatic artery, portal vein, and bile ducts. Circulatory units within the hepatocyte chords differ from a typical capillary bed in that the endothelial cells of the liver do not form tight junctions (286). This creates a sinusoidal network that minimizes barriers between hepatocytes and the blood traversing the sinusoid (169, 285). Oxygen rich blood from the hepatic artery mixes with nutrient rich blood from the portal circulation in the sinusoid before flowing over the cells of the lobule and draining into the central vein (130, 255). This organization causes the blood composition exiting the lobule to have different characteristics than the blood entering the lobule (Figure 1.4). As blood progresses across the lobule, cells utilize oxygen, and process nutrients while generating metabolites and waste products. Blood becomes deoxygenated and metabolic byproducts are secreted from cells along the length of the sinusoid. This creates gradients of oxygen, nutrients, and waste presented to cells of the liver based on their lobular location. These and other gradients formed across the sinusoids of the lobule result in a partitioning of functions based on localization, such as increased oxidative metabolism in areas with higher blood oxygen content. This partitioning of functions has been termed metabolic zonation and typically classifies the lobule into one of three “zones” (84, 110, 130). Each zone possesses hepatocytes with differential metabolic gene expression and functionality. These metabolic zones are typically depicted as discrete regions, but hepatic zonation actually exists on a flexible spectrum (50). For example, hepatocytes from Zone 2 can assume the functional attributes of Zone 1 hepatocytes in the face of damage or loss of function (85). This may occur in response to various liver damaging pathologies such as viral hepatitis (189). Flexibility in functionality is a permeating theme relative to hepatocyte metabolism. This flexibility supports the variable metabolic requirements of normal physiologic shifts in nutrient intake and energy expenditure. This paradigm also ensures maintenance of metabolic homeostasis under the stresses of various pathophysiologic states that were likely encountered throughout evolution.

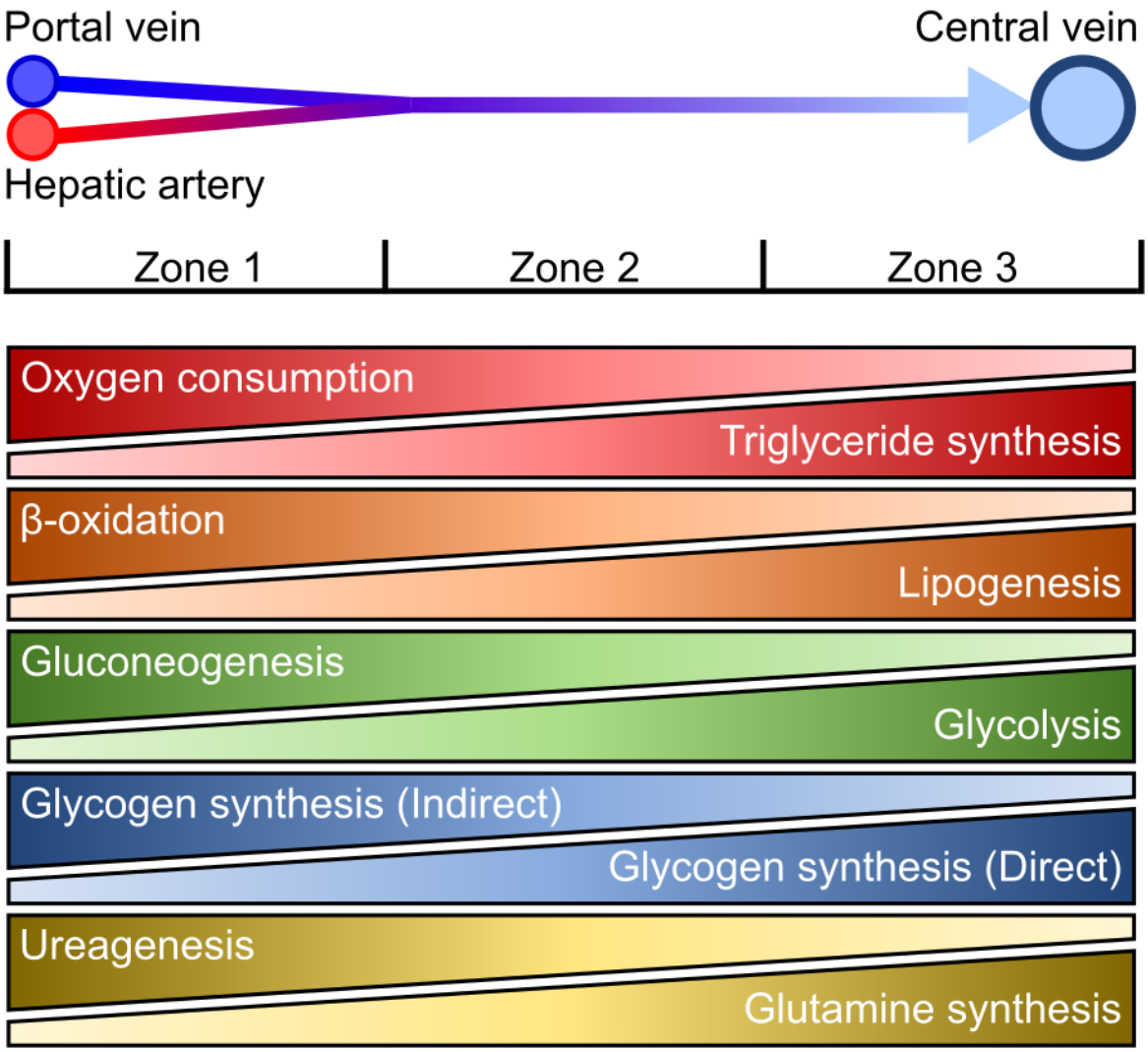

Figure 1.3- Hepatic lobular organization causes gradients in oxygen, hormones, nutrients, and waste products. This gradient formation and the consequential organization of relevant metabolic processes has been dubbed metabolic zonation. These zones are depicted as roughly equal, but can shift in size and location based on a number of factors (e.g. hepatocellular damage or altered blood flow). These gradients generally adopt opposing metabolic functionalities such as the gluconeogenic functions localizing to the periportal areas mirrored by more glycolytic processes in the perivenous areas.

Metabolism and glucoregulatory functions of the liver

Functional flexibility is embodied in the hepatic capacity to store, synthesize, metabolize, and release glucose as necessary for establishment and maintenance of circulating glucose levels (99, 128, 188, 255). Hepatic maintenance of circulating glucose homeostasis is supported by a highly regulated physiologic balancing act of nutrient and hormonal controls that vary with states of feeding and fasting. Spatial organization within the lobule integrates these controls with appropriate cellular behaviors creating a dynamic and highly regulated system of glucoregulatory functions.

During feeding water soluble nutrients enter the portal venous circulation from the intestine. Pancreatic interpretation of circulating glucose and nutrient results in increased secretion of insulin coupled with decreased secretion of glucagon. At the liver, the insulin to glucagon ratio is elevated driving net hepatic glucose uptake and storage (Figure 1.5) (188). This has been quantified by splanchnic balance studies in humans (72) and hepatic balance studies in dogs (1, 187). These studies are in general agreement that the liver is responsible for the disposal of 25-40% of an oral glucose load (1, 72, 187). Glucose may undergo glycolysis or may be stored as glycogen. Glycolysis serves to replenish depleted metabolites while restoring energetic content of the liver through oxidative and non-oxidative pathways (287). Glycogen stored in the liver serves as a source of glucose with relatively low energy requirements for release in to the circulation upon transitioning from the fed to postabsorptive state.

Processing of glucose at the liver does not occur in a vacuum and is supported by an intricate network of metabolism, which serves to appropriate metabolites and energy within the liver, but also throughout the body. Within this network amino acids may be utilized as anaplerotic substrates for the tricarboxylic acid (TCA) cycle (129), which can contribute to hepatic gluconeogenesis (257, 269, 270) or the synthesis of proteins. Ingested fats are assembled to form triglycerides from fatty acids and glycerol. These triglycerides are packaged on to chylomicrons,

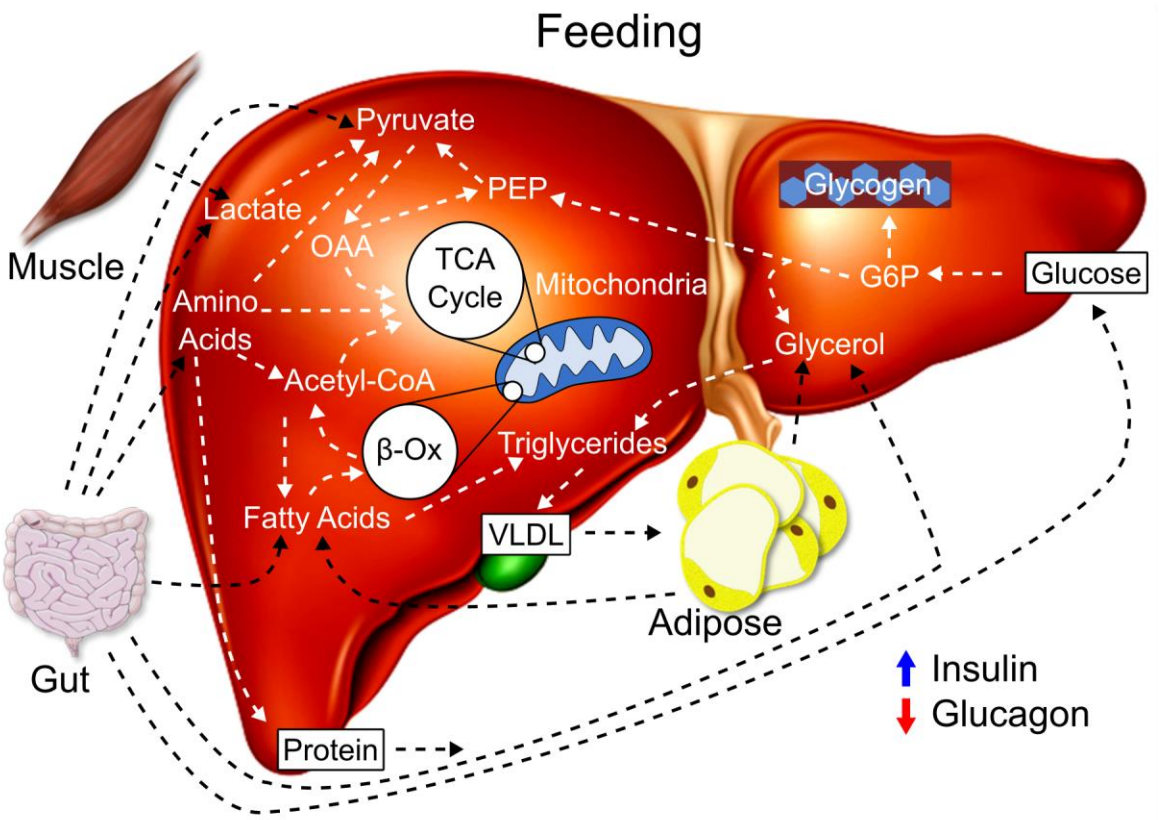

Figure 1.4- Hepatic hormonal drive and metabolic functions in the fed state. During feeding water soluble nutrients enter the portal venous circulation from the intestine. At the liver, the insulin to glucagon ratio is elevated leading to net hepatic glucose uptake. Glucose may undergo glycolysis, as a means of ATP production, or may be stored as glycogen. Amino acids may be oxidized for energy production or utilized as anaplerotic substrates for the TCA cycle. Once again these amino acids, as in the fasted state, may be used for synthesis of local or secreted proteins. Ingested fats are assembled to form triglycerides from fatty acids and glycerol. These triglycerides are packaged to on to chylomicrons, which then enter the lymphatic system. Chylomicrons drain from the lymphatics to the circulation and, upon reaching the liver, are unloaded of remaining fatty acids and glycerol. Fatty acids can be used for restoration of energy state, repletion of TCA cycle intermediates, or re-esterified to triglycerides. Triglycerides can be loaded on to very low density lipoproteins, which shuttle lipid to other tissues including muscle and adipose depots.

which then enter the lymphatic system. Chylomicrons are delivered from the lymphatics to the circulation through the thoracic duct. These particles are unloaded of remaining fatty acids and glycerol via lipoprotein lipase. Fatty acids can be used for restoration of energy state, repletion of TCA cycle intermediates, or re-esterified to triglycerides. Triglycerides can be loaded on to very low density lipoproteins, which shuttle lipid to other tissues including muscle and adipose depots.

As an organism transitions from an absorptive state to a post-absorptive/fasting state the ratio of insulin to glucagon decreases (Figure 1.6). This shifts the liver from glucose storage to net glucose output. Hepatic glucose output involves glycogen breakdown (glycogenolysis) and de novo synthesis of glucose molecules (gluconeogenesis). Contributions of glycogenolysis and gluconeogenesis to hepatic glucose output exist on a spectrum as the fasted state is extended. Whereas glycogenolysis is a major component of HGO early in the post-absorptive state the glycogen pool is finite and gradually depleted in the absence of nutrient intake. Gluconeogenesis replaces glycogenolysis as the primary contributor to HGO the more extended a fast becomes. While this process maintains circulating glucose levels for energetic provision throughout the body it requires sufficient carbon based substrates and energy to proceed.

Gluconeogenic substrates are provided in the form of amino acids (gut and muscle), lactate (muscle), pyruvate (muscle), and glycerol (adipose tissue). Fatty acids from adipose tissue lipolysis are also directed to several pathways, such as beta-oxidation and the TCA cycle. These processes support gluconeogenesis through production of ATP and reducing equivalents. Ketone bodies may also be produced from lipid oxidation acting as an additional energy shuttle between the liver and other organs. Amino acids can also enter the TCA cycle as anaplerotic substrates and be utilized for synthesis of proteins. Nitrogen released as a result of de-amination during amino acids metabolism is disposed of during ureagenesis. Urea is released from the liver where it is excreted by the kidneys. Glucose output is dynamic and responsive to the energy needs throughout the body (e.g. brain, skeletal muscle, and immune system).

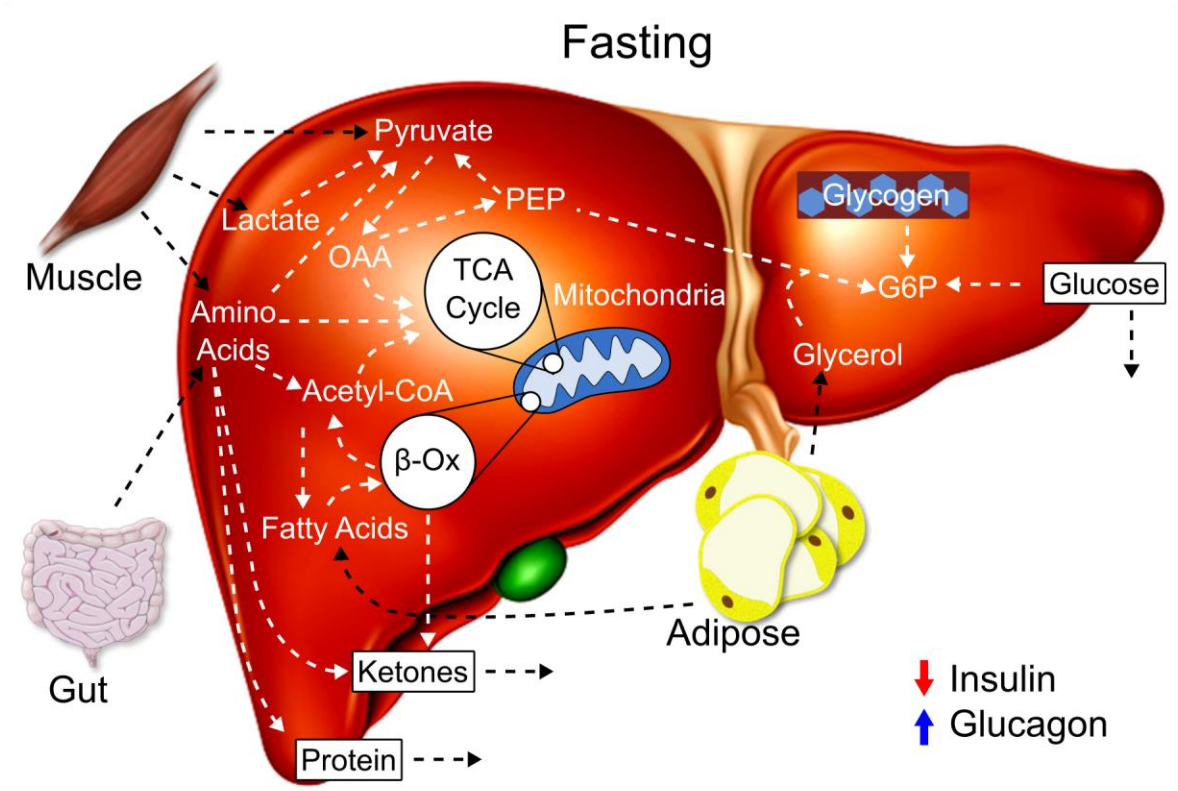

Figure 1.5- Hepatic hormonal drive and metabolic functions in the fasted state. During fasting the liver is a net glucose producer due to the low insulin to glucagon ratio. Glucose is derived from both glycogen and gluconeogenesis. Gluconeogenic substrates are provided in the form of amino acids (gut and muscle), lactate (muscle), pyruvate (muscle), and glycerol (adipose tissue). Fatty acids from adipose tissue lipolysis are also directed to several pathways, such as beta-oxidation and the TCA cycle. These processes support gluconeogenesis through production of ATP and reducing equivalents. Ketone bodies may be produced from lipid oxidation acting as an additional energy shuttle from liver to other organs. Amino acids can enter the TCA cycle as anaplerotic substrates or be utilized for protein synthesis. Nitrogen released amino acid deamination are disposed of during ureagenesis. Urea is released from the liver where it is excreted by the kidneys.

Hormonal control of hepatic glucoregulatory processes

In addition to metabolic support and contributions to the dynamic glucose handling properties of the liver there are a number of hormones that enable physiologic regulation of the liver's glucoregulatory programs. Among these hormonal inputs insulin and glucagon are the primary mediators of hepatic glucose handling and output. Both of these hormones are synthesized in the sub-organ endocrine compartments of the pancreas known as islets of Langerhans. Localization of these hormone-producing compartments in the pancreas is physiologically relevant as they are directly upstream of the hepatic portal vein circulatory input. Therefore, the liver is the first major site of action for these hormones.

Insulin signaling and control of hepatic glucomodulatory processes

Insulin secretion is primarily determined by circulating glucose. Immediately after consumption of a meal circulating glucose and nutrients drain from the gut to the portal circulation. Elevated glucose is interpreted by the insulin synthesizing β-cells of the pancreas resulting in a coordinated release of insulin in to the portal circulation. Elevated levels of insulin and glucose act on the hepatocytes of the liver to drive a host of metabolic processes that shift the liver to a state of net hepatic glucose uptake (Figure 1.1 & 1.3).

Insulin acts on the hepatocytes of the liver through the insulin receptor expressed on the cell membrane surface (79). The insulin receptor is a tetrameric protein consisting of two extracellular α subunits which are bound to two membrane spanning β subunits with receptor tyrosine kinase activity (118, 120, 242). Binding of insulin to its receptor commences a cascade of intracellular post-translational modifications and biochemical events, which mediate the diverse functional controls of insulin.

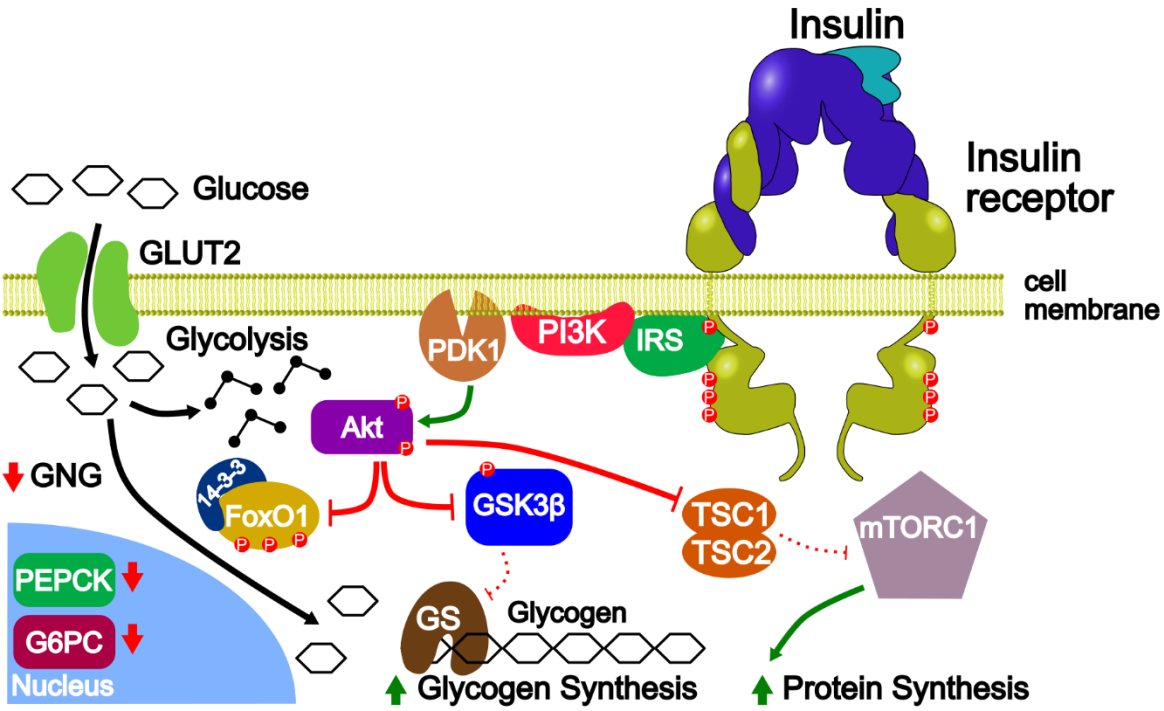

Figure 1.6- Insulin signaling and control of hepatic glucoregulatory processes. Depicted are the prominent signaling processes involved in the action of insulin within the hepatocyte. In general insulin acts to promote glycogen storage by releasing inhibitory tone upstream of glycogen synthase. Insulin inhibits gluconeogenic processes by sequestering FoxO1 in the cytosol, which limits its ability to transcribe gluconeogenic genes. Insulin also enhances mTORC1 signaling and activity resulting in enhanced protein synthesis. While enhanced protein synthesis is not directly linked to glucose homeostasis it constitutes a major sink for amino acid utilization, which will shift the flow of amino acids from gluconeogenic processes.

Following binding of a single insulin molecule to the extracellular α subunits the receptor undergoes conformational changes leading to intracellular β subunit trans-phosphorylation of tyrosine residues (141). Phosphorylated insulin receptor recruits intracellular signaling proteins with phosphotyrosine binding (PTB) or Src-homology 2 (SH2) domains (119). Among the immediate interaction partners of the insulin receptor the insulin receptor substrate (IRS) proteins 1 and 2 are attributed with the initiation of many metabolic and glucoregulatory aspects of insulin signaling in hepatocytes (97).

IRS1 and IRS2 propagate signals through recruitment of the lipid-modifying enzyme phosphoinositide 3-kinase (PI3K) (26). Recruitment and activation of PI3K results in rapid localized conversion of phosphatidylinositol 4,5-bisphosphate (PIP2) to generate phosphatidylinositol (3,4,5)-triphosphate (PIP3). PIP3 is a potent second messenger that binds and activates 3-phosphoinositide-dependent protein kinase 1 (PDK1). PDK1 is the primary input signal for a group of AGC kinases including protein kinase B (Akt), p70 ribosomal S6 kinase (S6K), serum- and glucocorticoid-induced protein kinase (SGK), and atypical isoforms of protein kinase C (PKC). While many of these proteins exert metabolic effects that can alter glucose handling in the liver Akt represents the primary direct driver of hepatocyte glucomodulatory behaviors.

Phosphorylation of Akt at Thr308 by PDK1 leads to a partial activation of Akt kinase activity. However, for complete activation of Akt a second phosphorylation at Ser473 by mammalian target of rapamycin complex 2 (mTORC2) must occur. Upon complete activation, Akt acts as a kinase for proteins in multiple signaling pathways. Akt phosphorylates tuberous sclerosis complex protein 2 (TSC-2) causing degradations of the TSC complex. This removes the inhibitory action of the TSC complex on mTORC1 resulting in a plethora of anabolic actions including protein synthesis. Akt also phosphorylates glycogen synthase kinase 3 beta (GSK3β). This phosphorylation event inhibits the activity of GSK3β that acts as an inhibitor of glycogen synthase (GS). Overall this results in decreased inhibitory phosphorylation of GS and promotion of glycogen

synthesis. Finally, the target of Akt phosphorylation which drives the inhibition of hepatic glucose output by insulin is the transcription factor Forkhead box O1 (FoxO1). FoxO1 is responsible for the transcription of phosphenolpyruvate carboxykinase (PEPCK) and the catalytic subunit of glucose-6 phosphatase (G6pc). Phosphorylation of FoxO1 by Akt results in its interaction with 14-3-3 proteins outside of the nucleus. This interaction sequesters FoxO1 in the cytoplasm resulting in decreased transcription of PEPCK and G6pc. As PEPCK and G6pc levels decrease gluconeogenesis is also usually decreased. While FoxO1-Akt signaling controls the pathway associated with classical hepatic insulin sensitivity elegant studies from Drs. Morris Birnbaum and Paul Titchenell at University of Pennsylvania have shed further light on the role of this pathway in insulin sensitivity. They have shown that loss of Akt signaling in the liver leads to an inability of insulin to inhibit hepatic glucose output indicating a potential role in insulin resistance. However, simultaneous knockout of Akt and Foxo1 from hepatocytes restores normal glucoregulatory function and insulin sensitivity. Therefore, there seem to be alternative or compensatory pathways supporting hepatic glucose output and insulin sensitivity.

Glucagon signaling repurposes carbon to guard against hypoglycemia

Glucagon is the antithetic force to insulin on hepatic glucoregulation and serves to maintain circulating glucose levels apropos of physiologic demand during fasting (43) and exercise (108). Glucagon secretion from the pancreas is mediated by a host of factors including nutrients, hormones, and nervous system control (213). Pancreatic α-cells sense decreasing insulin and glucose in the circulation as an organism transitions from the fed to the postabsorptive and fasting states or engages in energetically demanding behaviors, such as exercise. As with insulin, glucagon is secreted in to the portal vein circulation and acts directly upstream on the liver to stimulate glucose production. Stimulation of HGO exists on a spectrum of glycogenolysis and gluconeogenesis (42). Whereas glycogenolysis is the primary source of HGO early in the fasted state, gluconeogenesis gradually takes over as the primary source of HGO. Illustrative of the

critical feedback mechanisms between glucagon and insulin are the responses to glucagon in a typical fasted state. Exogenous introduction of glucagon in the fasted setting will elevate circulating glucose levels. However, in an organism with intact physiology this will stimulate release of insulin and its downstream glucose lowering effects, including the glucagon-stimulated actions at the liver. This feedback network creates difficulties in studying glucagon in the physiologic context of simple fasting and has limited the scientific pursuit towards an understanding of glucagon signaling and action, equivalent to that of insulin.

Despite the paucity of research on glucagon relative to insulin there have been critical studies conducted to elucidate the physiologic and molecular mechanisms of glucagon action (247). Glucagon action and signaling are initiated through the glucagon receptor (GcgR), a typical 7-trans-membrane spanning G-protein coupled receptor (10). GcgR is linked to the intracellular $G\alpha_s$ subunit. Stimulation of $G\alpha_s$ signaling propagates a classically defined pathway through activation of adenylate cyclase (219). Production of cyclic adenosine monophosphate (cAMP) by adenylate cyclase results in activation of the primary target of this pathway protein kinase A (PKA). PKA acts to modify a host of proteins involved in hepatic metabolism and glucose output including glycogen phosphorylase and fructose-2,6-bisphosphatase. These two enzymes catalyze two glucomodulatory functions of glucagon the stimulation of glycogenolysis, through modification of glycogen phosphorylase, and the inhibition of glycolysis, through modification of fructose-2,6-bisphosphatase. These functionalities of glucagon oppose those of insulin.

In addition to acute effects on glycogenolysis and glycolysis, glucagon stimulates the de novo synthesis of glucose by a sequence of reactions diametrically opposed to glycolysis. This process is known as gluconeogenesis and enables a repurposing of carbon metabolites and byproducts in to glucose molecules as a means to maintain circulating glucose for energetic provision to other tissues. Amino acids represent a primary source of carbons for gluconeogenesis. Glucagon facilitates amino acid contributions to gluconeogenesis by stimulating extraction (108, 270) via the A and N amino acid transport systems (36, 195), as well as utilization

within metabolic pathways (184). These amino acids are primarily derived from the gut (281) and the skeletal muscle (267). Lactate and glycerol represent the other primary metabolic precursors of gluconeogenesis utilized by the liver. Lactate is a glycolytic byproduct from skeletal muscle and other sources. Glycerol is the remaining backbone of triglycerides that have undergone lipolysis from various adipose depots. Glycerol serves as a significant contributor to gluconeogenesis which parallels rates of lipolysis (210).

Capacity to repurpose diverse carbon substrates for energetic exchange requires a centralized system of metabolic processes to maximize processing efficiency. While there are diverse metabolic pathways in action within the liver the TCA cycle is a central hub of carbon processing that serves to integrate metabolism and energy balance within the cell. The previously described gluconeogenic substrates are metabolized within the hepatocyte for entry in to the TCA cycle (i.e. anaplerosis). This enables the production of reducing equivalents through the TCA cycle, maintenance of TCA cycle intermediate metabolite levels, and finally the ability to provide PEP as a 3-carbon substrate for gluconeogenesis.

Metabolic, energetic, and mitochondrial considerations in gluconeogenesis

This de novo synthesis of glucose is energetically demanding. Energetic requirements of this process are met through provision of high energy phosphate bonds from nucleoside triphosphates, including ATP (19). TCA cycling from several metabolite sources including lactate, amino acids, and lipids maintains reducing equivalents in the form of NADH and $FADH_2$ (282). NADH and $FADH_2$ are requisite for oxidative phosphorylation (oxphos) (204). Oxphos is the set of biochemical processes coupled to chemiosmotic gradients enabling conversion of energy from various molecules to transferable phosphate bonds of ATP. Through processing of reducing equivalents, electrons are transferred to molecular oxygen and protons are exuded from the mitochondrial inner membrane. Exuding protons creates a pH gradient across the inner mitochondrial membrane. Potential energy from this gradient is harnessed by ATP synthase. This

complex enables the controlled flow of protons while harnessing proton movement to synthesize ATP from ADP and phosphate. Gluconeogenesis requires 6 high energy phosphate bonds, in the form of ATP and GTP, to synthesize each molecule of glucose (19). Therefore, appropriate TCA cycling and oxphos meet tandem requirements of provisioning energy and carbon for synthesizing glucose molecules.

Processing of metabolites through the TCA cycle and energetic intermediates through oxphos for support of gluconeogenesis occurs entirely within the mitochondria. Dynamic capabilities of this organelle determine cellular metabolic homeostasis and by doing so contribute to virtually every cellular process. Extensive integration of mitochondria across cell biology invokes a need for flexibility in function. Functional flexibility enables responsiveness to the variable demands placed on a cell. Mitochondria demonstrate this flexibility with regards to hepatic gluconeogenesis in several ways. In the acute setting mitochondria will alter processing of metabolites based on dynamic shifts in substrate availability (29, 149). These shifts in substrate availability will shift respiratory control of complex I and II (29) while also altering biophysical structure of mitochondrial membranes (149). Consistent increases in demand of energetic production by mitochondria, such as occurs during extensive exercise training, will lead to a shift in mitochondrial programming (25, 67, 96, 159, 214, 215, 257). This can be shown by indicators of increased mitochondrial content. Mitochondria from an exercise trained liver also have an increased capacity for complete oxidation of lipid based substrates (25, 159, 214, 215).

Mitochondria are often depicted as individual bacteria-like organelles. These organelles actually exist as a network with the capacity for dynamic integration or dissociation depending on the cellular requirements at a given time (111). Incorporation of mitochondrial organelles together as a means of increased networking has been termed fusion. These networks are hypothesized as a means to enhance oxidative extraction of ATP (225), but also as buffering system against mitochondrial damage (111). Mitochondrial fission can be invoked as a mechanism for removing damaged mitochondrial from a network (261), but is also required for distribution of daughter

mitochondria during cell division. Furthermore, mitophagy is a specific form of autophagy targeted at mitochondria that recycles organelle macromolecules for energy or synthetic functions (272). Loss of mitochdnrial membrane potential is a primary signal of organelle damage that stimulates interaction with mitophagy receptors, such as BNIP3, or stabilization of the mitophagy protein PINK1 at the outer mitochondrial membrane (272). These signals have distinct downstream pathways for promotion of mitophagy. One recently appreciated controller of mitochondrial dynamics is the integrin-actin cytoskeleton signaling system (22, 90, 143, 160). This system influences metabolic responses to integrin engagement or loss of ECM contact. In conjunction the actin cytoskeleton also mediates the physical organization and localization of mitochondrial networks. This is critical for minimization of diffusion limitations on metabolites and ATP delivery. Defects in these processes have now been linked to diseases including NAFLD (82) and insulin resistance (127). Therefore, consideration of metabolism and mitochondria can better inform our understanding of the plethora of diseases derived from overnutrition and obesity.

Pathologic dysregulation of hepatic metabolic functions

As highlighted previously the ability of the liver to maintain glucose homeostasis is a delicate balance between nutrient availability and hormone levels. Variability in food abundance and consumption throughout evolution underlies this intricately controlled network. Industrialization and contemporary lifestyle have altered variables in the equation of nutrient balance and given rise to disease states of overnutrition. Individuals in developed countries are exceedingly exposed to an increase in caloric density of food while engaging in significantly less physical activity in their daily routines. Imbalance in nutrient intake and expenditure has tipped the scales towards caloric excess. In the short term the body is well equipped to deal with this excess through storage of carbon substrates in to lipids in specialized adipose depots. However, as with all physiologic processes, there is an upper limit to the amount of storage that can occur before adverse effects become apparent. Consistent caloric excess of modern times has

manifested as an epidemic of obesity a condition with an array of pathologic associations and immense public health ramifications.

With the liver as a primary site of nutrient uptake, sensing, recycling and storage. It is hardly surprising that a disease state rooted in consistent overloading of these processes manifests as a pathologic sequelae. Perhaps the most recognized pathologic consequence of over nutrition is insulin resistance. Insulin resistance presents with differential effects in the tissues classically associated with insulin action (e.g. skeletal muscle, adipose tissue, and liver). Hepatic insulin resistance is most commonly associated with the loss of insulin's inhibitory effects on hepatic glucose output (57). Despite loss of typical insulin action on glucoregulatory processes, insulin maintains the capacity to stimulate lipogenesis (114, 237). This disconnect between gluco- and lipo- regulatory functions of insulin has been termed selective insulin resistance (30). This concept of selective insulin resistance has been recognized in other organs as early as 1991 (186), but has been popularized by Brown & Goldstein in relation to hepatic pathologies (30). Selective insulin resistance contributes to pathologic metabolism through two primary mechanisms: 1) altered kinetics of circulating glucose leading to increased hyperglycemic burden; 2) increased hepatic lipid synthesis, which compounds with overloading of adipose stores to cause inappropriate deposition of lipid within the liver. These pathologic shifts in metabolic homeostasis underlie the strong correlation of hepatic insulin resistance with both T2D and NAFLD (31, 57).

Insulin resistance and NAFLD have multisystem pathologic consequences and have been linked to a broad range of diseases including T2D, cardiovascular disease, chronic kidney disease, Alzheimer's disease, and cancer. This conglomeration of pathologies represent an immense burden on quality of life and economic outcomes around the world. Therefore, understanding mechanisms underlying metabolic pathologies of the liver and the associated network of pandemics are imperative. Efforts have aimed to understand the contributions of genetics, molecular signaling, metabolism, physiology, behavior, and socioeconomic factors to

these pathologies. This has resulted in an integrated view of hepatic glucoregulation in normal and pathophysiologic settings. Knowledge derived from this integrated view has resulted in therapeutic options for aspects glucose homeostasis and insulin resistance such as glucagon like peptide 1 (GLP-1) agonists (178), sodium glucose co-transporter 2 (SGLT2) (38) antagonists, and the ever effective metformin. Despite this renaissance in treatment of pathologic glucose homeostasis, no primary therapeutic option for NAFLD currently exists (245) and a trail of failed clinical trials have been left in the wake of this disease (126). To remedy this gap in therapeutic options research has broadened its scope in an attempt to solve the riddle of NAFLD with the hopes of improving therapeutic outcomes for this growing at-risk population. Over the past decade expansion of scientific considerations in NAFLD therapy has increased interest in the ECM and its related signals (139, 152, 196, 201, 278). This emphasis stems, in part, from observations linking ECM deposition and remodeling to states of metabolic dysregulation including insulin resistance (15, 109, 137, 243). Incorporating insights from metabolism and physiology with newfound understanding of the ECM and related cell signaling pathways serves as a means towards fruitful progress in therapeutic development for NAFLD.

Extracellular matrices of the liver in health and disease

Within all organs of the body are cells performing the specialized functions of the organ and a vast network of supporting extracellular components known as the extracellular matrix (ECM) (78, 252). ECMs present physical and biochemical cues to cells throughout the body (78, 252). Through these cues ECMs govern numerous aspects of cellular biology including survival, proliferation, migration, differentiation, and organization. Proteins with varying levels of glycosylation (e.g. collagens, fibronectins, laminins, and elastin) interact in differential combinations to form ECM compartments (24, 78, 252). Epithelia are one of the basic tissue classifications of the body and are typically in contact with a specialized ECM compartment known as a basement membrane (BM). BMs primarily consist of collagen IV, laminins, nidogens,

perlecan, and agrin (24, 208). These areas exist as highly organized ECM that, in addition to classical ECM signals, maintain significant barrier functions between epithelial cells and biological lumens (220).

As with many aspects of the liver, hepatic ECM is unique in its organization and composition compared to other epithelial organs (13, 169, 285, 286)**.** The primary epithelial population of the liver, hepatocytes, line sinusoids in the absence of a true BM (13, 169). In lieu of a true BM the space of Disse occupies perisinusoidal areas between hepatocytes and sinusoidal epithelial cells. Fibronectin (FN) represents the primary ECM component within the space of Disse (47, 171, 243). FN is a glycoprotein dimerized by sulfide bonds. It can be alternatively spliced at the transcriptional level to form a number of different FN isoforms (275), which contribute to the two pools of FN termed cellular (cFN) and plasma (pFN). The liver, is the primary site of pFN synthesis and export. This function of the liver is speculated to be the reason for the high FN content of the sinusoidal ECM.

In addition to FN, several types of collagens have been detected within the space of Disse. Collagens comprise the most abundant set of proteins in vertebrates (14, 182, 216). The collagen family is represented by 28 different proteins encoded by at least 45 unique genes. Each gene encodes a collagen alpha chain, which can partner homotrimerically or heterotrimerically with alpha chains of the same collagen type to form the standard triple helix structure of an individual collagen unit (14, 182, 216). This creates diversity at the level of collagen types, but also at the biochemical level creating differential alpha chain compositions. Collagen IV illustrates this concept as there are 6 different collagen IV alpha chain genes in mammals (Col4A1, Col4A2, Col4A3, Col4A4, Col4A5, Col4A6) (89). Differential expression of these alpha chains results in formation of distinct trimeric combinations (e.g. collagen IV α1α1α2, α3α4α5, and α5α5α6) (144). This allows for distinct biochemical characteristics of collagens within a unified structural framework. Collagen I is typically the second most abundant ECM protein within the space of Disse and presents as small bundles. Collagens III and VI can be detected as intermittent fibers,

while collagen IV only presents with occasional deposits. Other glycoproteins such as perlecan, tenascin, or laminin β2 may present sparsely or adjacent to the vascular areas (i.e. periportal or pericentral).

This organization of ECM within the space of Disse has direct links to physiologic functions of the liver (13) and represents a critical intersection of ECM and metabolism. Specifically, low ECM density and fenestrated endothelial cells allow for free exchange of macromolecules (e.g. glucose, amino acids, lipids, and various transport proteins) between the sinusoidal plasma and hepatocytes (286). Within this space, perisinusoidal ECM molecules are in direct contact with the basal surface of hepatocytes (259). Basal surfaces contain up to 70% of the hepatocyte membrane surface area (21) indicating potential for extensive cell-ECM interactions. These interactions enable two-way communication between sinusoidal cells and ECM within the space of Disse. Communication between these compartments is vital as the ECM of the liver is not a static construct. Rather, the ECM is modified and turns over as a result of stimuli including biomechanical forces, protein damage, or chemical toxicity (56, 139, 140). Despite a constitutively changing ECM compartment, the general contents and organization are maintained to support physiologic homeostasis of the organ.

Open exchange between hepatic circulation and hepatocytes is advantageous for rapid interaction, interpretation, and responses to a number of stimuli including nutritional and hormonal. However, the open barrier between sinusoidal blood and hepatocytes is not without caveats. In the absence of endothelial tight junctions and a true BM the liver risks exposure to toxic molecules and pathogens (179). Exposure to toxic compounds through ingestion was likely a common occurrence throughout evolution and remains an issue in current medical practice (45, 271). Elevated exposure to toxic compounds at the liver coupled with an immense functional repertoire required for health and viability likely pressured evolution of unique aspects of liver physiology. One likely result of these pressures is the hepatic capacity for processing and excreting exogenous toxins through a system of modifying enzymes (4). This limits the potential

for circulation of reactive and toxic compounds to other organs, such as the central nervous system. In conjunction with hepatic processing of toxic compounds, the liver also evolved an incredible capacity for regenerative responses.

Hepatic regenerative capacity is truly legendary with representation in the Greek mythologies of Prometheus and Tityus alike (254). Hepatic regeneration served as a tool of torture in these myths, but hepatic regeneration has garnered considerable interest as a means to better understand and treat diseases of the liver. Aggregate research on hepatic regeneration in a number of models has produced a general consensus on the time course and processes contributing to typical liver restoration (136, 179, 251). Priming is the initial phase of hepatic regeneration that prepare hepatocytes for entry to the cell cycle and ensures maintenance of hepatocyte function during regenerative demand(185). This early phase of liver regeneration is characterized by elevated ECM turnover and cytokine signaling. Elevated urokinase-type plasminogen activator (uPA) activity occurs within 5-10 minutes of partial hepatectomy (PHx) and causes appearance of plasminogen and fibrinogen breakdown products. These breakdown products can initiate activation of matrix metalloproteinase (MMP) cascades resulting in ECM remodeling. The cytokines Tumor Necrosis Factor α (TNFα) and interleukin 6 (IL6) are also elevated rapidly after PHx (147, 181). TNF-α and IL6 activate NF-κB and STAT3 transcription factors through interconnected mechanisms promoting G_0 to G_1 cell cycle transition. Completion of hepatocyte priming is denoted by initiation of DNA synthesis, which occurs 24h after PHx in mice and is delayed by approximately 12h in carbon tetrachloride (CCl_4) exposure models. This second stage is characterized by high anabolic activity leading to a wave of mitotic events across the hepatic lobule. The switch from priming to mitogenic events requires stimulation and recession of several growth factor pathways. HGF activates the c-Met receptor while epidermal growth factor (EGF) and TGF-α are primary mitogenic ligands for the EGF receptor (EGFR)(122, 192). Stimulation of these receptors produces pleiotropic signals including activation of the intracellular AKT and ERK. These signals promote replication while opposing apoptotic signals. Upon

complete restoration of hepatocyte mass organization of the liver remnant is reestablished until indistinguishable from normal livers.

One of the hallmarks of the hepatic damage response is a distinctly altered dynamic of ECM components within the parenchyma of the organ (170, 171). This is an altered expression of certain ECM components including cyclical deposition of FN and several types of collagen (148, 171). ECM of the liver is heavily modified by uPA and MMPs during regeneration (185). Cycles of degradation, deposition, and altered localization of ECM components occur throughout this process. After PHx this cycle can be observed for FN. FN undergoes decreases in protein content at 1-5min, 30-60min, and 6-12hours after PHx with restoration of protein levels between each interval (147). Restoration of FN content 12 hours after PHx also corresponds to an increased level of FN bound to hepatocyte membranes at this time point (211). This deposition typically persists up to 4 days post PHx and resolves as the organ restores cellular mass and function by 9-10 days after PHx. However, under conditions of severe or chronic hepatic insult ECM deposition and reorganization may become pathologic in nature leading to a fibrotic disease state (52, 139). This and returns to minimal levels Levels of the primary FN binding receptor, Integrin α5β1, at hepatocyte membranes follow a similar timeline to FN (211). This indicates increased binding activity of Integrin α5β1 binding of FN at the hepatocyte membrane from 12-96h post PHx, a period denoted by elevated DNA synthesis and proliferation. Given that increased FN binding to Integrin α5β1 coincides with times of elevated proliferation this signal may be relevant to the restoration of hepatocytes during regeneration.

As discussed earlier, fibrotic disease states have now been linked to pathologies rooted in overnutrition and obesity (152). This accumulation of excess ECM seems to occur predominantly in tissues that have a high metabolic activity and insulin action (278). Initially this metabolically-linked fibrosis was observed and studied in the adipose tissue (109, 246). However, fibrosis and altered ECM have now been documented in the insulin resistant liver (243) and skeletal muscle (137). Preceding gross changes in physical matrix of the liver, states of over-

nutrition upregulate transcriptional programs for ECM components, such as collagen alpha chain subunits and related proteins (224). Chronic exposure to overnutrition also causes metabolic stress at the cellular level through increased levels of toxic metabolites (53). Even simple exposure of hepatocytes to excess free fatty acids, a set of compounds that hepatocytes are equipped to handle in moderation, can cause apoptosis. This may be linked to production of reactive oxygen species (ROS) during periods of elevated TCA cycling (165, 202, 229). Eventually exposure to these metabolites and reactive molecules will exceed the cell's tolerance and succumb to apoptosis.

While a healthy liver would likely overcome a low-grade cell death, as occurs during NAFLD, a secondary consequence of over-nutrition in the liver is a relative inhibition of hepatocyte proliferation and regeneration capacity (54, 117, 222, 249). Induction of fatty liver through a number of over-nutrition paradigms generally hampers the liver's ability to respond to injury. This results in a delayed entry of hepatocytes in to the cell cycle and a dampened proliferative response during the synthetic phase of regeneration. Particularly relevant to hepatic disease progression during insulin resistance and NAFLD is the ability of hyperglycemia to limit hepatic regeneration after surgical resection (117). Under this paradigm, hyperglycemia may abrogate the requisite hypoglycemic signal for appropriate initiation and drive of hepatocyte proliferation.

ECM alteration and deposition are typical consequences of hepatic regeneration (148, 171). However, during NAFLD extensive propagation of chronic low-grade cell death couples with a general inhibition of hepatocyte proliferation causing organ damage in excess of hepatic regenerative capacity. This contributes to progression along the NAFLD spectrum towards a more advanced form of liver disease known as non-alcoholic steatohepatitis (NASH). Therefore, attempts to regenerate from constant loss of cell mass likely drive consistent ECM deposition during progression of NAFLD/NASH causing fibrotic phenotypes. Compounding this are the ongoing inflammatory responses, which evoke upregulated ECM transcriptional programs further driving expression, translation, and deposition of ECM proteins. Left unchecked this ECM

deposition will progressively distort the typical sinusoidal architecture towards that of a typical capillary (51, 232). This capillarization of the hepatic sinusoid is a hallmark of end stage liver diseases and cirrhosis.

Until recently, deposition of ECM during liver pathologies, including NAFLD, was seen as a disease endpoint with little possibility of resolution. This dogma was likely perpetuated by the methodologies available at the time. Classic histologic stains of fibrosis and liver damage would become apparent only during advanced disease states, but more subtle progressions in ECM alterations were likely overlooked. More recently advances in immunohistochemistry, multiplexed immunofluorescence imaging, and large-scale “omics” analyses have become regularly implemented in analyses of NAFLD and other liver pathologies. This has led to a shift in the general understanding of ECM and its contributions to hepatic disease. Rather than an endpoint of tissue damage, ECM is seen as an active participant in pathologic, but also regenerative processes (139, 148, 277). This acknowledgement of ECM as an active participant has expanded scientific interests in the ways that ECM elicits its effects on cells. As a results the various mechanisms and signaling components relating to cell-ECM interactions have become focal points in a number of research areas including metabolic disease (278), wound repair (244), and cancer (231).

Integrins facilitate two-way communication between ECM and intracellular space

Interactions of cells with their surrounding ECMs are mediated through multiple cell surface proteins including integrins, discoidin domain receptors, and several proteoglycans (78). Of these proteins, the family of integrin receptors represent the primary means for cell-ECM interactions (104). Integrins are cell surface receptors involved in cell-cell and cell-ECM interactions (124, 248). Integrin receptors bind to ECM components and span the cell membrane. Through this organization the ECM is coupled to cytosolic signaling events that regulate internal cellular physiology (35, 104, 284) and assembly of local ECM (125, 131, 156).

Integrin receptors consist of a heterodimeric α and β subunit pair (Figure 1.8). The integrin family in humans consists of 18 α and 8 β subunits, which form 24 identified heterodimeric pairs (Figure 1.9) (125). Integrins maintain specificity at several levels including variations in subunit pairing, ligand binding, and subunit expression (123). Integrin α subunits are more variable and provide the ligand binding specificity for the receptor. Integrin β subunits are less variable, but can pair with multiple α subunits to form several integrin receptors and interact with different matrix proteins. Integrin β subunits also possess a more extended intracellular tail domain. This enables an expanded set of interactions for the tail of β subunits with intracellular signaling components. Integrin facilitated connection of the ECM and intracellular environment serves as a two-way communication line. Integrins relay the composition, amount, and organization of the pericellular ECM to the intracellular environment. This flow of information is termed outside-in integrin signaling. Internally-derived cues can also influence conformational activation of integrins and influence forces applied by the cell to the ECM. This represents the second form of integrin signaling known as inside-out. Integrins physically interact with the matrix and span the cell membrane, but are inherently lacking in enzymatic activity. Therefore, integrins rely on intracellular proteins and biochemical processes to transduce their externally-derived information. Integrin β subunit intracellular tail interacts with cellular adhesion signaling proteins termed the “adhesome” (284). The adhesome consists of more than 200 proteins organized in distinct signaling nodes, which determine critical cellular processes including survival, proliferation, cell cytoskeletal engagement, and cell organization. Ligation of integrins to ECM results in a clustering

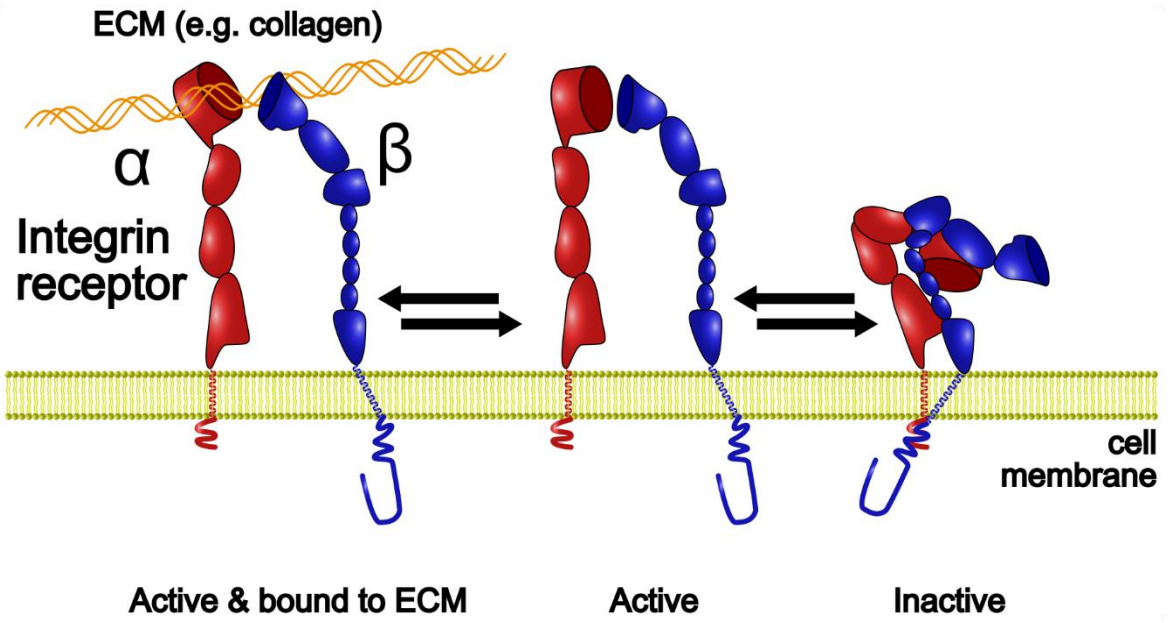

Figure 1.7- Depiction of an integrin receptor and its activations states within the cell membrane. Integrin receptors exist as heterodimers of α and β subunits at the cell membrane. These receptors are also in an equilibrium of states at the cell membrane. These states can be shifted by a variety of signals including exposure to ECM ligands or cytokine interactions. Upon exposure to an activating stimulus the receptor will extend, which enhances its capacity for interaction with ECM ligands in the pericellular environment. ECM-integrin interactions vary in their affinity and may constitute transient or stable interactions based quantity of matrix components, intracellular signaling state, or the mechanical properties of the matrix.

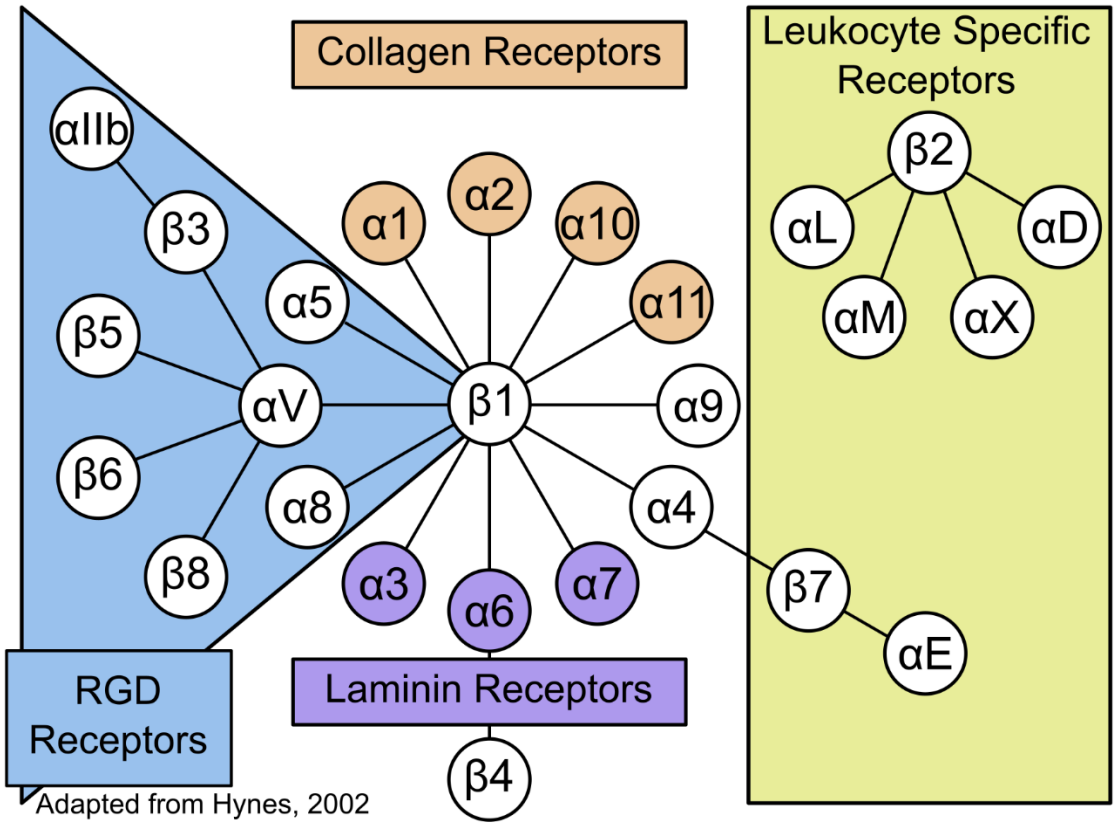

Figure 1.8- Integrin receptor heterodimer pairs and their ECM ligands. Integrin α and β subunits pair in a multitude of ways. Integrin α subunits determine specificity for of ECM ligands within a specific subgroup. Whereas the β subunit can determine the subgroup of the receptor as well as the types of intracellular signaling pathways that are engaged by the receptor.

of integrin receptors and assembly of focal adhesion complexes by adhesome proteins. Focal adhesion kinase (FAK), proto-oncogene tyrosine-protein kinase Src (Src), PI3K, and growth factor receptor-bound protein 2 (Grb2) are among the proteins recruited to focal adhesions. These proteins also perform critical roles in insulin signaling and action (18, 93, 115, 233). Influence of integrin signaling on these insulin signaling proteins is also contingent on integrin engagement with the ECM (92, 233). Given the link between integrin signaling and insulin action as well as alterations to ECM during insulin resistance studies are needed to better assess the role of integrin receptors in insulin resistant states *in vivo*.

Integrin receptors as modulators of *in vivo* insulin action

Whole body and tissue specific knockouts of integrin receptor subunits have revealed a variegated role of integrin receptors in insulin action. Knockout of the integrin β1 subunit from striated muscle of lean mice demonstrate a deficiency in insulin stimulated glucose uptake (295). This insulin resistant phenotype was associated with decreased Akt phosphorylation at Ser473. Engagement of integrin receptors containing the integrin β1 subunit have demonstrated effects on activation of the insulin receptor and IRS-1 (92). Loss of this signal reinforcement may limit complete activation of insulin signaling in the muscle compartment. Studies went on to assess the role of two collagen binding partners of the integrin β1 subunit, the integrin α1 (itgα1) and α2 (itgα2) subunits, in obesity-derived insulin resistance. Mice lacking either itgα1 (itgα1$^{-/-}$) or itgα2 (itgα2$^{-/-}$) subunits at the whole body level were shown to have no obvious metabolic phenotypes when fed a normal rodent chow (chow) diet (137, 279). However, itgα2$^{-/-}$mice demonstrated protection from skeletal muscle insulin resistance during obesity caused by a HF diet (137). This was linked to elevated phosphorylation of IRS-1 at Tyr612 and Akt at Ser473 in skeletal muscle of HF-fed itgα2$^{-/-}$ mice during insulin stimulation. Maintenance of insulin signaling in skeletal muscle of itgα2$^{-/-}$ mice during HF feeding occurred despite similar levels of collagens compared

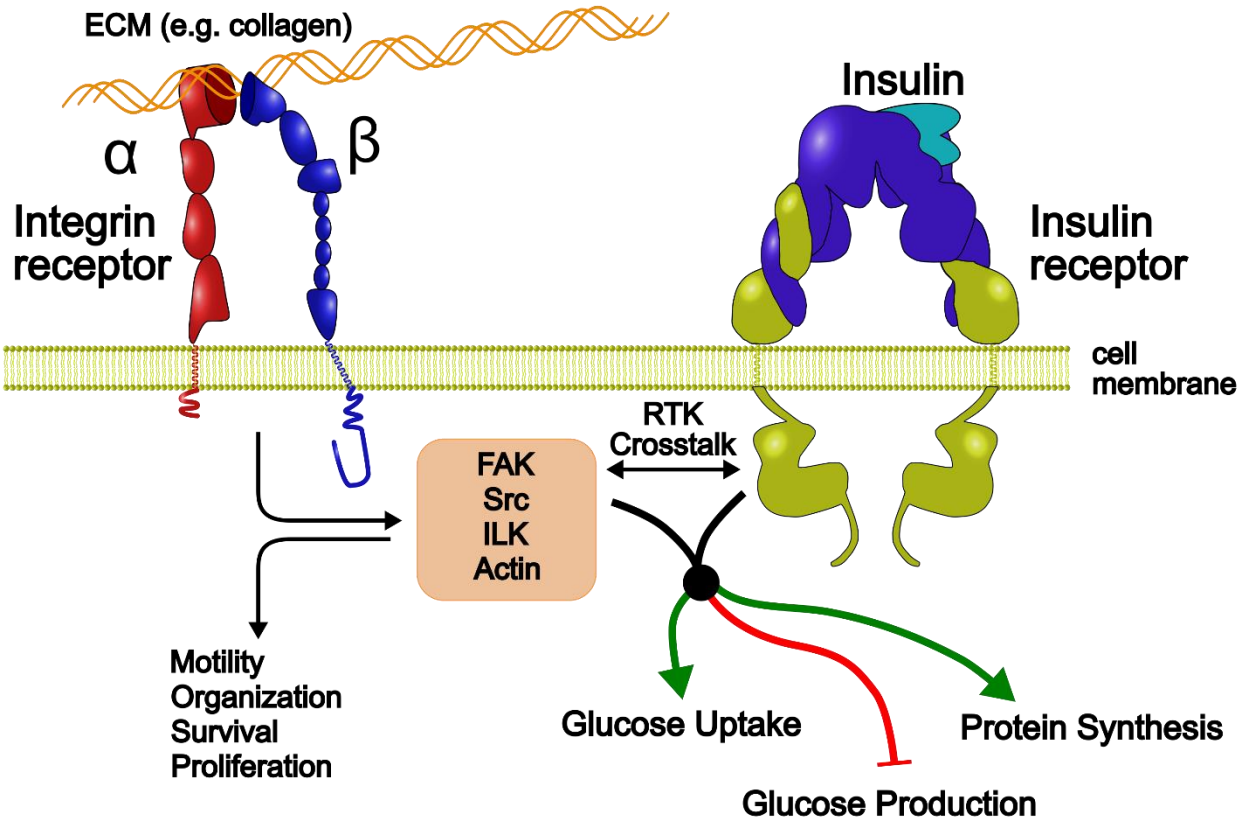

Figure 1.9- Simplified model of signaling crosstalk between insulin and integrin receptors to effect insulin action.

to itgα2$^{+/+}$ mice. This indicates a pathologic role for integrin α2β1 receptors in the promotion of skeletal muscle insulin resistance, perhaps through altered ECM signaling during obesity. In contrast to this finding itgα1$^{-/-}$ had no effect on muscle, but demonstrated a worsened hepatic insulin resistance during obesity (279). Hepatic insulin resistance of obese itgα1$^{-/-}$ mice was associated with decreased phosphorylation of IRS-1 at Tyr612 and Akt at Ser473. These results show a supportive role for integrin α1β1 receptors in hepatic insulin action during diet-induced obesity. Additionally, the opposing functions of two collagen binding integrins, α1β1 and α2β1, on insulin action indicate complex roles for these receptors in metabolic physiology. It is also important to re-iterate that alteration of these integrin receptors revealed no apparent metabolic phenotypes in the absence of obesity. It is likely that integrins play an enhanced role during the metabolic stress of obesity by mechanisms that are yet to be understood.

Mice lacking integrin α2 subunits demonstrated enhanced skeletal muscle insulin action during obesity. Whereas mice lacking integrin α1 subunits demonstrated hepatic insulin resistance during obesity with a somewhat paradoxical decrease in hepatic lipid deposition. Understanding mechanisms by which specific integrins impact insulin resistance and nutrient metabolism are clearly an important objective. Intracellular signaling components of the integrin adhesome were a logical starting point as they had been shown to modify aspects of insulin signaling and action in previous studies (18, 93, 115, 233). Interestingly, a central hub of integrin signaling, integrin-linked kinase (ILK), had been demonstrated to interact and affect signaling through PI3K, Akt, GSK3β, and mTORC1. This represented a clear overlap between ILK and insulin signaling. However, whether there was a requirement for ILK in insulin action had never been performed.

Within the adhesome, ILK is a central coordinator of integrin signaling (176). Protein scaffolding functions of ILK link the intracellular tails of β integrin subunits to cytoskeletal and cell signaling networks. ILK is able to engage signaling pathways as a result of its three structural domains. The kinase-like domain of ILK is at the C-terminus interacts with cytoplasmic tails of

integrin β1 and β3 subunits as well as the focal adhesion associated paxillins and parvins. The centrally located pleckstrin homology domain of ILK interacts with phosphoinositides and contributes to localization of ILK and its complexing partners. Finally the N-terminal contains 5 ankyrin repeats and this domain is responsible for interactions with particularly interesting new cysteine-histidine (PINCH) isoforms and several other signaling proteins. Isoforms of PINCH and parvin are often found in complex with ILK forming the ILK-PINCH-parvin or IPP complex. Complexing of these proteins is required for stabilization and incorporation of the complex in to focal adhesions (155, 176, 276). Beyond the classical IPP complex a number of proteins have been demonstrated to interact with ILK. Protein kinase B (Akt)(58) and glycogen synthase kinase 3-β (GSK3β)(260) are among ILK interacting proteins. These proteins mediate effects of ILK on proliferation and cell survival, but they also represent key points of insulin signaling in hepatocytes. These characteristics indicate the potential for ILK to coordinate integrin and insulin signaling crosstalk.

Integrin-linked kinase in hepatic injury, repair, and insulin resistance

With possible connections between ILK and hepatic insulin resistance it was necessary to assess the role of ILK in *in vivo* insulin action. ILK is a ubiquitously expressed protein and whole-body knockout of ILK results in pre-implantation embryonic lethality (226). In order to avoid this effect of ILK a mouse line with genetic insertion of loxp sites flanking the ILK1 gene was created ($ILK^{lox/lox}$). This model enables specific induction of genetic knockout in the presence of the cre-recombinase (cre). With the goal of assessing the role of ILK in obesity related pathologies of the liver, including insulin resistance, a hepatocyte-specific model of ILK-KO (hepILK-KO) was created (280). In order drive hepatocyte specific cre expression, and consequent hepILK-KO, mice expressing cre under control of the albumin promoter (alb-cre) were used (206). These mice were designed to assess hepatic insulin resistance and NAFLD progression in relation to obesity,

but other studies have used them to evaluate ILK in relation to hepatic development, injury, and regeneration.

The Michalopoulos group at University of Pittsburgh have studied aspects of the ECM and integrin signaling in relation to hepatic regeneration (86, 146, 147). This had prompted studies on the role of ILK in hepatic injury and regeneration (7, 17, 63, 65, 86, 87). Initial studies utilized an adenoviral vector to drive hepatocyte-specific cre expression and remove ILK from hepatocytes (87). While ILK-KO promoted hepatocyte apoptosis and hepatitis, these studies were complicated by mild apoptotic phenotypes with control adenovirus (87). To avoid this complication, a developmental model of hepatic ILK-KO was implemented, hereafter referred to as “liver ILK-KO” (86). Studies of liver ILK-KO mice demonstrate a consistently upregulated hepatic proliferative drive (7, 63, 86). Despite this no cancerous developments have been reported in liver ILK-KO mice. Inappropriate proliferative drive can lead to hepatomegaly and other complications (86). However, appropriately harnessed this proliferative drive enhances the regenerative capacity of the liver. The ability to harness this capacity of liver ILK-KO mice was demonstrated in several models of surgical and hepatotoxic damage (7, 17, 64, 65).

These studies utilized an alternative model for “hepatocyte” ILK-KO in mice. Specifically, cre expression was driven by an albumin promoter linked with an alfa-fetoprotein enhancer (alf-alb-cre). There are significant temporal differences in the alf-alb-cre and alb-cre systems. The alf-alb-cre becomes active early in development with expression of cre detectable by embryonic day 10.5 (E10.5) (142). This causes cre expression and genetic KO prior to differentiation of biliary epithelial cells from the bipotential hepatoblast progenitor population (~E13.5) (157, 238), which give rise to hepatocytes later in development. This system results in cre expression and consequent KO in hepatocytes derived from the developing hepatoblast population, as well as in biliary epithelial cells. Influence of this phenomenon on previous alf-alb-cre ILK-KO models is acknowledged as a potential contributor to observed phenotypes (86).

To avoid complications associated with the alf-alb-cre promoter assessment of hepatocyte ILK as a mediator of insulin resistance were performed in alb-cre driven hepILK-KO mice (280). For these studies control ($ILK^{lox/lox}$) and hepILK-KO mice were either maintained on a chow diet or fed a HF diet from 3 to 19 weeks of age. This diet length is known to induce hepatic steatosis and insulin resistance. As with $itg\alpha1^{-/-}$ and $itg\alpha2^{-/-}$ mice no phenotypes were observed in in hepILK-KO on a chow diet. However, HF-fed hepILK-KO mice were largely protected from hepatic insulin resistance (280). This maintenance of insulin sensitivity in the face of obesity was not attributable to alterations in insulin-stimulated phosphorylation of IRS-1, Akt, or FoxO1. Despite no altered activation of these signaling proteins HF-fed hepILK-KO livers had lower lipid content and increased expression of lipogenic genes. Parallel studies also demonstrated that ILK-KO from skeletal muscle resulted in a similar protection of the skeletal muscle compartment from insulin resistance during obesity (138). Together, these findings indicated ILK contributes to insulin resistance in a tissue-independent manner. With ILK-KO preventing insulin resistance and other pathologic complications of obesity in liver and skeletal muscle ILK has become a possible therapeutic target for treatment of these conditions.

Hypotheses

Pleiotropic metabolic benefits in tissue-specific ILK-KO models (138, 280) prompted interest in the mechanisms underlying these effects. In addition to the metabolic benefits of hepILK-KO we also understand there to be alternative functions of ILK in hepatic injury and repair (7, 17, 65, 86). Of particular note was a clear age-dependent effect of liver ILK-KO on hepatic histological organization, transcriptional profiles, and signaling (86). As these are definitive contributors to hepatic metabolism and pathologic progression, I hypothesized an age-dependent role for ILK in hepatic metabolism and glucoregulation. The results of Chapter III demonstrate that, indeed, hepatocyte ILK determines glucose homeostasis, resistance to obesity, and protection from steatosis in an age-dependent manner. These represent desirable therapeutic

endpoints in combatting these pathologies. However, the mechanisms driving these phenotypes in the absence of hepatocyte ILK are unknown. I hypothesized a diminished capacity for oxidative metabolism may improve glucoregulation in hepatocyte ILK-KO mice based on glucose tolerance and RNA-seq analyses. Chapter IV demonstrates a setting of reduced hepatic oxidative metabolism resulting in metabolic compensation and signaling pathway activation that modify hepatic glucoregulation in mice lacking hepatocyte ILK.

Chapter II

RESEARCH MATERIALS AND METHODS

Animal models

The Vanderbilt University Animal Care and Use Committee approved all procedures and animal protocols. Mice were maintained in a facility accredited by the Association for Assessment and Accreditation of Laboratory Animal Care. Mice were housed in a temperature- and humidity-controlled room on a 12:12 hour light/dark cycle. Male C57BL/6J mice with loxP sites flanking the ILK gene ($ILK^{lox/lox}$) (226) were kindly provided by Dr. Roy Zent. $ILK^{lox/lox}$ mice were crossed to transgenic mice heterozygous for expression of Cre recombinase under control of the albumin (Alb) promoter (Albcre, Tg(Alb-cre)21Mgn, The Jackson Laboratory, Bar Harbor, ME, USA) to generate $ILK^{lox/lox}$Alb*cre*$^{+/-}$ mice (referred to as hepILK-KO) and $ILK^{lox/lox}$ littermates (280). Alb-cre was utilized for hepatocyte-specific knockout due to temporal organization of cre expression and completion of hepatocyte specific knockout in this system (206).These mice were utilized for all experiments performed within the dissertation. Mice were removed from their mother's cage for weaning and separated by gender at 3 weeks of age. Upon weaning mice were provided free access to rodent chow (5.5% kcal from fat, PicoLab® Laboratory Rodent Diet 5L0D, Purina, Richmond, IN, USA) and water. For diet induced obesity studies in chapter I mice were switched to high fat diet (60% kcal from fat; F3282, BioServ, Flemington, NJ, USA) at 6 weeks of age. Mice were weighed and handled weekly to monitor body weight and minimize stress due to handling during studies. Studies were performed on mice at 6, 9, 12, 18, and 32 weeks of age in chapter I. Studies in chapter II and III were performed in mice at 6 weeks of age.

Surgical procedures

Catheter implantation procedures (11, 12) were performed on 5 week old mice in preparation of metabolic flux experiments using stable isotopes. Arterial catheters are made from polyethylene tubing (BPE-10, Instech Labs, Plymouth Meeting, PA, USA) attached to silicone tubing (0.3mm ID, 0.64mm OD, Dow Silicones, Midland, MI, USA). Jugular vein catheters are made from the same silicone tubing. These catheters were connected to an assembly (called a MASA™) consisting of stainless steel tubing (0.3mm ID, 0.41mm OD, 15mm, Dow Silicones) bent 90° and attached to polyethylene tubing (BPE-20, Instech Labs) and anchored with Silastic medical adhesive (Silicone Type A, Lakeside, AZ, USA). The catheters and the MASA™ were sterilized with ethylene oxide (). Mice were anesthetized using isoflurane (Piramal Critical Care, Bethlehem, PA, USA). After a surgical plane of anesthesia was achieved, the interscapular and neck areas were depilated and sterilized with betadine and 70% alcohol. Ketoprofen (Zoetis, Parsippany, NJ, USA) was administered subcutaneously at a dose of 5-10mg/kg. An incision was made midline, 5mm above the sternum. The left carotid artery was isolated and exposed after blunt dissection of connective tissues followed by ligation of the cephalic end with silk suture (6-0, Ethicon, Somerville, NJ, USA). The caudal end of the exposed artery was then loosely knotted with suture. The artery was clamped with micro-serrefines and cut below the ligated end with spring scissors. The catheter was inserted into a small incision on the artery, advanced 9mm, secured with silk suture (6-0, Ethicon), tested for patency, and temporarily plugged with wire (0.61mm OD, Ziggy's Wires and Tubes, Sparta, TN, USA). Another incision was made 5mm to the right of the midline. The right jugular vein was isolated and exposed after blunt dissection of connective tissues followed by ligation of the cephalic end with silk suture (6-0, Ethicon). The caudal end of the exposed vein was then loosely knotted with suture. The artery was clamped with micro-serrefines and cut below the ligated end with spring scissors. The catheter was inserted into a small incision on the vein, advanced 11mm, secured with silk suture (6-0, Ethicon), tested for patency, and temporarily plugged with wire (0.61mm OD, Ziggy's Wires and Tubes).

The mouse was turned to its stomach and a small incision was made between the scapulae. A 14-gauge needle (EXELINT, Los Angeles, CA, USA) was inserted through the ventral (stomach side) incisions and tunneled subcutaneously to the dorsal (back side) incision. Catheters were passed through the needle and exteriorized through the dorsal incision between the scapulae. Ventral incisions were sutured with nylon (7-0, Ethicon). The venous and arterial catheters was then clamped with micro-serrefine at the dorsal incision, cut 1cm above the clamp, and connected to the MASA™. The base of the MASA™ was then placed within the dorsal incision space and the incision was sutured with nylon (7-0, Ethicon). Catheters were filled with a 5mg/mL ampicillin (AuroMedics Pharma, Windsor, NJ, USA) and 200U heparin (Sagent Pharmaceuticals, Schaumburg, IL, USA) / ml saline (0.9%, Hospira, Lake Forest, IL, USA) solution. Following surgery, mice were housed individually in a warmed, cleaned cage for seven days prior to study.

In vivo experiments

Oral glucose tolerance tests

On the day of the study, mice were weighed and placed in bedded containers without food or water. Glucose solutions for oral gavaging were prepared by diluting 1.6mL of 50% glucose solution (Hospira) with 2.4 mL of tap water (Vanderbilt University, Nashville, TN, USA) to obtain a 20% glucose solution. After 5 hours of fasting, tails of mice were nicked and baseline samples (Time = -10 minutes) were taken for measurement of glucose (2uL) and future measurement of Insulin (20uL). Glucose was determined using Accu-chek Aviva glucometers (Roche Diabetes Care, Indianapolis, IN, USA) and Accu-chek Aviva Plus glucose test strips (Roche Diabetes Care). After the initial glucose sample a second pre-gavage glucose sample (Time = -5 minutes) was taken to establish effects of handling and sampling on the baseline glucose samples. An oral glucose gavage volume was equal to 10uL of glucose per mg of mouse body weight to achieve a 2g of glucose per kg of body weight dosing of glucose. For oral gavaging mice were scruffed,

restrained manually, and animal feeding needles (Cadence Science, Cranston, RI, USA) attached to syringes (1mL, luer slip, Becton-Dickinson, Franklin Lakes, NJ, USA) containing individual glucose doses were inserted in to the esophagus. Glucose doses were then introduced slowly (~100µL/s) while monitoring for indications of tracheal insertion such as bubbling from the nose. Samples of glucose concentrations were taken 9 more times over the next 120 minutes (Time = 5, 10, 15, 20, 30, 45, 60, 90, and 120 minutes). Plasma samples for insulin measurements were also taken 3 more times (Time = 10, 30, and 120 minutes) and all insulin samples were stored at -80°C prior to analysis. At the conclusion of the study mice are placed back in their previous housing and monitored for any adverse events.

Whole body indirect calorimetry and activity

Indirect calorimetry, activity, and associated behaviors were assessed in mice at 6 weeks of age in a Promethion Metabolic Analyzer (Sable Systems, North Las Vegas, NV, USA) at an ambient temperature (20-22°C). 1 week prior to study mice were acclimatized to individual housing. Cages contained Pure-O' Cel bedding (The Andersons Inc, Maumee, OH, USA) and were maintained in a temperature- and humidity-controlled room on a 12:12 hour light/dark cycle. Upon acclimatization, cages were transferred the the Promethion system. Mice had ad libitum access to chow diet and water throughout the study. Whole body VO2, VCO2, food intake, water intake, body weight, and cage behavior (XYZ beam breaks) were measured continuously in free-roaming mice over a 9 day period. Assessment of energy expenditure (EE) was calculated by the Weir formula (273) and is presented as kilocalories. Respiratory quotient (RQ; V_{CO2}/V_{O2}) is used as a surrogate for substrate utilization bounded by the theoretical limits of 0.7, 100% utilization of lipid for energy, and 1.0, 100% utilization of carbohydrate for energy. Analysis of covariance (ANCOVA) for EE was performed to assess interactions between lean body mass and genotypes in relation to EE (132–134). Energy intake (EI) was calculated using the equation {food intake (g) * energy content of rodent chow (cal/g)}.

Stable isotope infusions for metabolic flux analysis

On the day of the study, mice that had been catheterized 1 week prior were placed in bedded containers without food or water and fasted for 3h. After this initial fast mice were connected to a swivel sample-infusion apparatus (Figure 2.1). Upon connection to sampling and infusion lines an 80-µl arterial blood sample was drawn to determine the natural isotopic abundance of circulating glucose. Continuous infusates of [6,6-$^{2}H_{2}$]glucose and [$^{13}C_{3}$]propionate were prepared in 0.9%NaCl-4.5%$^{2}H_{2}O$ solution. Venous infusions were performed as previously described (105). After the baseline sample, a bolus of [$^{2}H_{2}$]water (99.9%, Cambridge Isotopes Laboratories, Tewksbury, MA, USA) with 0.9% NaCl was delivered over 25 minutes to enrich total body water to 4.5%. A [6,6-$^{2}H_{2}$]glucose (Cambridge Isotopes Laboratories) prime (440 µmol•kg^{-1}) was dissolved in the bolus. Following the prime a continuous infusion (4.4 µmol•kg^{-1}•min^{-1}) of [6,6-$^{2}H_{2}$]glucose was administered for the duration of the study. At time=120 min after the [$^{2}H_{2}$]water-0.9%NaCl bolus sodium [$^{13}C_{3}$]propionate (Cambridge Isotopes Laboratories) was delivered as a continuous infusion. Blood glucose was monitored (Roche) and donor erythrocytes were infused to maintain hematocrit throughout the study. At time=90 min after the onset of the [$^{13}C_{3}$]propionate infusion blood samples (100 µl each) were collected at 10 minute intervals over 30 minutes. Samples were centrifuged in EDTA-coated tubes for plasma isolation. The samples were stored at −80°C prior to glucose derivatization and GC-MS analysis. The duration between the [$^{2}H_{2}$]water-0.9%NaCl bolus/[6,6-$^{2}H_{2}$]glucose prime and steady-state isotopic sampling was 3.5 to 4 hours resulting in a fasting period of ~7 hours. Mice were then euthanized for liver extraction and analyses.

Hepatocyte isolation

Hepatocytes were isolated via a 2-step collagenase perfusion technique as previously described (76). Briefly, livers were perfused via the inferior vena cava with 50 ml of

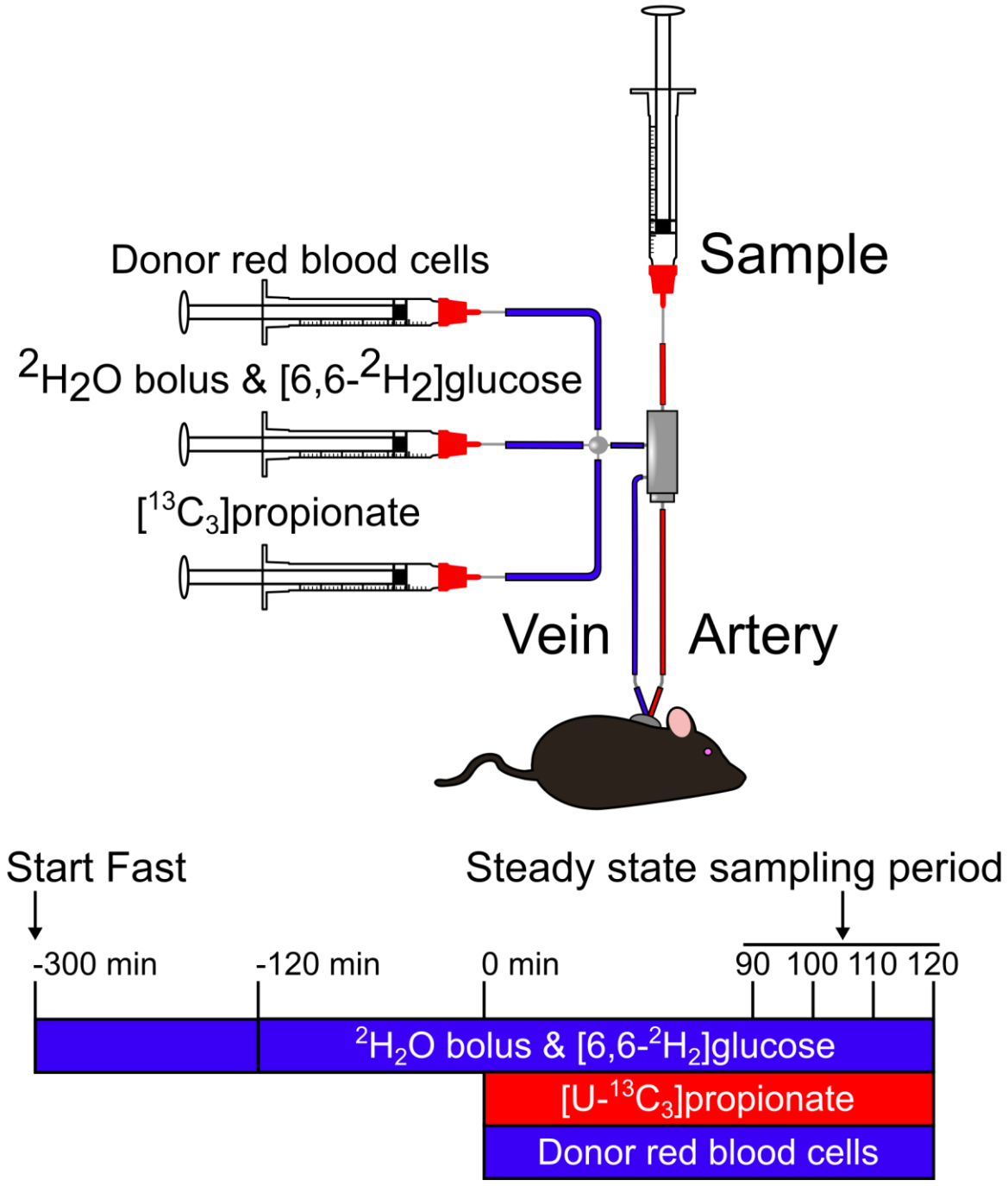

Figure 2.1- Depiction of the conscious catheterized mouse, experimental setup, and study design for metabolic flux analyses using stable isotopic tracers.

wash buffer (137 mM NaCl, 7 mM KCl, 0.7 mM $Na_2HPO_4 \bullet 12H_2O$, 10 mM Hepes, 50 mM EDTA) followed by 50 ml of digestion buffer (137 mM NaCl, 7 mM KCl, 0.7 mM $Na_2HPO_4 \bullet 12H_2O$, 10 mM Hepes, 0.75 mg/ml $CaCl_2$, and 0.4 mg/ml collagenase from *Clostridium histolyticum* (MilliporeSigma, Burlington, MA, USA)) at 5 ml/min and 37°C. Digested livers were carefully extracted from the peritoneal cavity and placed in a 35mM round cell culture dish (Becton-Dickinson) containing 3mL of 4°C DMEM (Gibco, Thermo Fisher Scientific, Waltham, MA, USA) on ice. The liver capsule was torn and removed from the cell suspension with fine forceps. Cells were screened with a 70 µm nylon cell strainer (Corning, Corning, NY, USA) in to a 50mL sterile tube (Corning) and centrifuged for 5 minutes at a speed of 50g to pellet hepatocytes. Cell supernatant containing media and enriched for non-parenchymal liver cells (Liver sinusoidal endothelial cells, Kupffer cells, stellate cells, and erythrocytes) was aspirated and remaining pelleted hepatocytes were resuspended in DMEM (Gibco) containing 1.125 g/L glucose and 584 mg/L L-glutamine for respirometry analyses. Cell counts and viability were obtained via trypan blue (Gibco) exclusion method. 3 separate 500µL aliquots of this suspension were then added to 1.5mL microcentrifuge tubes (VWR, Radnor, PA, USA) and centrifuged at a speed of 13000g to pellet cells for future molecular analyses.

Ex vivo experiments

Hepatocyte respirometry

To evaluate the functional oxidative metabolism of hepatocytes a method assessing the respiratory characteristics of O_2 consumption in intact hepatocytes was implemented (62, 204). This methodology was chosen so as to avoid the documented selection biases that are introduced by protocols in isolated mitochondria (113, 151) such as disruption of mitochondrial network interactions (227) and selection for specific populations of mitochondria (205). Hepatocyte O_2

consumption was evaluated using an Oxygraph-2k (O2K, Oroboros Instruments Corp.; Innsbruck, Austria) at 37°C. Prior to introduction of hepatocytes each chamber of the O2K instrument were filled with media (DMEM (Gibco) containing 1.125 g/L glucose and 584 mg/L L-glutamine) and equilibrated with atmospheric oxygen. Upon equilibration a volume of media no greater than 100µL containing 75,000 hepatocytes were injected in to each of the 2 O2K chambers. Routine respiration was measured in the suspension media alone. The ATP synthase inhibitor Oligomycin (2.5 mM, MilliporeSigma) was used to assess futile (LEAK) respiration, which is respiration that occurs without production of ATP. Maximal respiration by the electron transfer system (ETS) was determined via step-wise titrations (0.5 µM) of carbonyl cyanide-p-trifluoromethoxyphenylhydrazone (FCCP, MilliporeSigma).

Tissue processing and analyses

Liver histology and immunohistochemistry

Upon sacrifice a portion of mouse liver (4-16mm^3) was placed in a tissue fixation cassette (Thermo Fisher Scientific) and submerged in 10% zinc buffered formalin (Thermo Fisher Scientific). Liver histology, immunohistochemistry, and pathologic evaluation were performed with the assistance of the Vanderbilt Translational Shared Pathology Resource Core. Fixed tissues were paraffin embedded and sectioned at a thickness of 5 µm on to glass slides. Slides were placed on the Bond Max IHC stainer (Leica Biosystems, Buffalo Grove, IL, USA). Dehydration, clearing, and coverslipping were the only procudures not performed on the Bond Max. Slides were deparaffinized followed by heat induced antigen retrieval using Epitope Retrieval 2 solution (Leica Biosystems) for 20 minutes. Slides were then placed in a Protein Block (DAKO, Carpinteria, CA, USA) for 10 minutes. Liver sections were stained with hematoxylin and eosin (H&E) for assessment of gross liver histology as well as Masson's trichrome stain for evaluation of fibrosis. For immunohistochemistry, anti-cytokeratin 19 (Proteintech Group, Rosemont, IL, USA, Cat#

14965-1-AP, RRID:AB 2133324) coupled to 3,3′-Diaminobenzidine (DAB) staining, was used to assess biliary hyperplasia and anti-Ki67 (Cell Signaling Technology, Danvers, MA, Catalog #12202S RRID:AB_2620142) coupled to nuclear (DAB) staining, was used to assess proliferation. The Bond Refine Polymer detection system was used for visualization.

Immunoblotting

Proteins were obtained from lysates of Liver (15-25mg), gastrocnemius muscle (15-25mg), or isolated hepatocytes (pellet of ~4-5x10^6 cells). All were lysed in extraction buffer containing 50mM Tris, 1mM EDTA, 1mM EGTA, 10% glycerol, 1% Triton X-100 (pH 7.5), and a 1:100 dilutions of Halt™ protease and phosphatase single-use inhibitor cocktail (Thermo Fisher Scientific). Tissues were homogenized using 0.5 mm zirconium oxide beads (Next Advance, Troy, NY, USA) for liver or 0.9-2.0mm stainless steel beads (Next Advance) for gastrocnemius. Samples were homogenized for 5 minutes in a Bullet Blender (Next Advance). Samples were centrifuged at 13,000g for 15 minutes at 4°C and supernatant was extracted while avoiding upper lipid layer. Hepatocytes were vortexed in extraction buffer and frozen at -80°C for lysis. Upon thawing samples were centrifuged at 13,000g for 15 minutes at 4°C and supernatant was extracted while avoiding upper lipid layer.

Proteins levels from each of these sample types were quantified using Pierce™ BCA Protein Assay Kit (Thermo Fisher Scientific). Proteins were denatured and reduced at 70 °C, separated on a NuPAGE 4-12% Bis-Tris gel (Invitrogen, Carlsbad, CA, USA), and transferred to a PVDF membrane. Membranes were probed with the antibodies obtained from Cell Signaling Technology; (Danvers, MA) for ILK (Cat# 3856, RRID:AB_2233861), glycogen synthase kinase 3 β (GSK3β, Cat# 9315, RRID:AB_490890), GSK3β phosphorylated at ser^9 (Cat# 9323, RRID:AB_2115201), protein kinase B (Akt, Cat# 9271, RRID:AB_329825), Akt phosphorylated at ser^{473} (Cat# 9272, RRID:AB_329827), Glycogen synthase (GS) (Cat# 3893,

RRID:AB_2279563), GS phosphorylated at Ser^{641} (Cat# 3891, RRID:AB_2116390), 5' AMP-activated protein kinase (AMPK, Cat# 2532, RRID:AB_330331), AMPK phosphorylated at Thr^{172} (Cat# 2535, RRID:AB_331250), acetyl-CoA carboxylase (ACC, Cat# 3662, RRID:AB_2219400), ACC phosphorylated at Ser^{79} (Cat# 3661, RRID:AB_330337), sequestosome 1 (p62, Cat# 5114, RRID:AB_10624872), and BCL2/adenovirus E1B 19 kDa protein-interacting protein 3 (Bnip3, Cat# 3769, RRID:AB_2259284). Mitochondrial complexes were detected using the total OXPHOS rodent WB antibody cocktail (abcam, Cat# MS604-300). Membranes were exposed to a chemiluminescent horseradish peroxidase (HRP)-substrate (MilliporeSigma) after incubating with a HRP-conjugated secondary antibody or quantified on a Li-cor imaging system (Li-cor Biotechnology, Lincoln, NE, USA) after incubation with IRDye® 800CW secondary antibody (Li-cor). ImageJ software was used for densitometry measurements.

RNA isolation

RNA was extracted by homogenization in TRIzol® (Thermo Fisher Scientific) from livers or isolated hepatocytesof hepILK-KO or $ILK^{lox/lox}$ mice. For liver, 0.5 mL of TRIzol was added to 15-20 mg of liver in tubes containing 0.5 mm RNase-free zirconium oxide beads (Next Advance). Samples were homogenized for 5 minutes in a Bullet Blender (Next Advance). For hepatocytes, pelleted cells, (**Hepatocyte Isolation**) were resuspended in 0.4mL of TRIzol, vortexed, and frozen at -80°C. Homogenized liver or thawed, lysed hepatocytes were incubated for 5 minutes at room temperature. A volume equal to 10% of the homogenate volume of 1-Bromo-3-chloropropoane were added to homogenates and vortexed vigorously for 15 seconds. Samples were incubated for 1 minute at room temperature, vortexed vigorously for another 15 seconds, and centrifuged at 4° C and 12,000 g to separate phase layers. The upper phase was removed from the tube, combined with an equal volume of 70% ethanol, vortexed vigorously, and added directly to RNeasy columns (Qiagen, Hilden, GER). Columns for RNA sequencing included an on-column DNase (Qiagen).

RNA sequencing

For RNA sequencing studies total RNA quality was assessed using the 2100 Bioanalyzer (Agilent, Santa Clara, California). 200 ng of DNase-treated total RNA with an RNA integrity number greater than seven was used to generate polyA-enriched mRNA libraries using KAPA Stranded mRNA sample kits with indexed adaptors (Roche, Basel, Switzerland). Library quality was assessed using the 2100 Bioanalyzer (Agilent) and libraries were quantitated using KAPA Library Quantification Kits (Roche). Pooled libraries were subjected to 75 bp paired-end sequencing according to the manufacturer's protocol (HiSeq3000, Illumina; San Diego, California). Bcl2fastq2 Conversion Software (Illumina) was used to generate de-multiplexed Fastq files. Fastq data files were uploaded to Galaxy (3) and converted to fastqsanger files. Low quality reads were removed from fastqsanger files using trimmomatic v0.36.3 (23). Reads were aligned to the mm10 mouse reference genome with Hisat v1.1.2 (145). Counts of overlapping reads and gene exons from mm10 were determined using the counts function of HTseq v0.6.1p1 (5). Count expression levels were filtered and assessed for differential expression using edgeR v (218). Enrichment of gene ontology terms and KEGG pathways were determined for genes significantly increased or decreased in hepILK-KO livers compared to control livers using the limma v3.36.2 goana and kegga functions (217).

Quantitative polymerase chain reaction

For quantitative PCR (qPCR) analyses RNA was reverse transcribed using the iScript cDNA synthesis kit (Bio-Rad; Hercules, CA). qPCR was performed using TaqMan (Applied Biosystems; Foster City, CA) Universal PCR Master Mix as well as TaqMan probes for glucose-6-phosphatase catalytic subunit (G6pc, Cat# Mm00839363_m1), phosphoenolpyruvate carboxykinase (Pck1, Cat# Mm00440636), mitochondrial dynamin-like GTPase (Opa1,

Cat#Mm01349707_g1), mitofusin 2 (Mfn2, Cat# Mm00500120_m1), dynamin-1-like protein, (Dnm1l, Cat# Mm01342903_m1), and fibroblast growth factor 21 (Fgf21, Mm00840165_g1).

Hepatic adenine nucleotides

Rapid sacrifice-excision procedures were implemented to minimize degradation and shifts in the nucleotide pools. Mice were sacrificed via cervical dislocation and a portion of the liver was excised and freeze clamped within 30s. Livers were maintained at or below -80°C prior to homogenization.

For homogenization 50-70mg of rapidly excised liver were added to 1.5mL Safe-Lock microcentrifuge tubes (Eppendorf, Hamburg, GER) containing 0.5 mm zirconium oxide beads (Next Advance). Immediately prior to homogenization a 10x volume (10:1 volume:weight tissue) of 0.4M $HClO_4$ - 0.5mM EGTA was added to tube and samples were homogenized for 5 minutes in a Bullet Blender (Next Advance). After homogenization samples were placed in ice for 3 minutes and then centrifuged at 3200g, 4°C for 5 minutes. To neutralize homogenate in a new tube 400µL of supernatant was added to 136µL of 0.5MK_2CO_3, vortexed, and maintained on ice for 5 minutes. Samples were then centrifuged at 3200g, 4°C for 5 minutes. Supernatants were transferred to HPLC tubes and kept at -80°C prior to processing.

Supernatants were analyzed via HPLC on a Supelco Supelcosil LC18-T column (4.6 by 250mm, 5µm particle size) with a Waters 490 detector (254nm at 1.0 AUFS) and constant flow rate of 0.7mL·min-1. Adenine nucleotides (AMP, ADP, ATP) from samples and standards were spotted using a 12.5min mobile phase A (100nM KH_2PO_4, pH 6) and a 3.5min mobile phase B (90:10 100mM KH_2PO_4/Methanol), and 44min mobile phase A. Energy charge was calculated using the equation ([ATP] + (0.5*[ADP])) / [TAN].

Glycogen

Liver glycogen content was assessed using the method of Chan and Exton (37). Strips of 3mm chromatography paper (GE Healthcare Life Sciences, Marlborough, MA, USA) were cut to 2 inch lengths with 2 strips per sample, standard, and blank then labeled as A and B. ~40-60 mg of liver or gastrocnemius muscle were added to 1.5mL Safe-Lock microcentrifuge tubes (Eppendorf) containing 0.5 mm zirconium oxide beads (Next Advance) for liver or 0.9-2.0mm stainless steel beads (Next Advance) for gastrocnemius. Immediately prior to homogenization a 8x volume (8:1 volume:weight tissue) of 0.0.03N HCl was added to tubes and samples were homogenized for 5 minutes in a Bullet Blender (Next Advance). Samples were then incubated at 80°C for 15 minutes. Samples were removed from oven, vortexed briefly to ensure even mixing, and 200µL volume of homogenate was pipetted on to appropriately labeled chromatography strips. Standards of oyster glycogen (MilliporeSigma) were prepared in distilled water and similarly pipetted onto chromatography paper. Blanks consisted of 0.03N HCl were prepared similarly. All samples, standards, and blanks were allowed time to saturate paper strips (~10 minutes). Strips were then added to a glass beaker with a mesh screen sitting above a magnetic stir bar, to separate paper strips from moving bar. 70% ethanol was added to the beaker so as to completely submerge paper strips. The beaker was placed on a magnetic stirring apparatus and set to a medium stirring speed for 40 minutes. This wash step was repeated 2 more times. Upon completion of the third ethanol washing step the strips were briefly submerged and rinsed in acetone. Samples were then set to dry for at least 2 hours in a ventilated chemical hood.

After drying, strips were folded accordion style and placed in 13 mL polypropylene tubes (Sarstedt, Nümbrecht, GER) tubes. For 50 samples, 250mL of an amyloglucosidase solution consisting of 50mL of 0.2M sodium acetate (CH_3COONa, NaOAc), 10mg of amyloglucosidase from *Aspergillus niger* (MilliporeSigma), and 200mL of distilled water was prepared for glycogen digestion. 5 mL of the amyloglucosidase solution was added to tubes containing paper strips, so as to submerge the strips in solution, and incubated at room temperature for at least 16 hours.

Glucose concentrations were determined by enzymatic reaction in a 96 well plate. Glucose assay buffer was prepared fresh immediately prior to assay. Glucose assay buffer for 1x96 well plate contained 26mL of Tris-HCl at pH7.4, 0.542 mL of 500mM $MgCl_2$, 75.83mg of ATP, 54.17mg of NADP, and 0.135mL of Hexokinase (HK):Glucose-6-phosphate dehydrogenase (G6PDH) (2:1 activity) enzyme mixture (Roche Diagnostics, MilliporeSigma). Each sample, standard, and blank were added to a 96 well plate at a volume of 20µL in duplicate. For enzymatic determination of glucose 200µL of glucose assay buffer was added to each well. Represented below are the progressive enzymatic reactions that enable endpoint quantification of NADPH.

$$\text{Glucose} + \text{ATP} \xrightarrow{Hexokinase} \text{Glucose} - 6 - \text{phosphate} + \text{ADP}$$

$$\text{Glucose} - 6 - \text{phosphate} + \text{ADP} \xrightarrow{G6PDH} \text{phospho} - \text{D} - \text{gluconolactone} + \text{NADPH}$$

This reaction proceeded during a 15 minute room temperature incubation on a plate shaker at a speed of 125 RPM. After incubation, absorbance of each well was determined at a wavelength of 340nm to assess concentrations of NADPH. This allowed calculation of glucose content derived from tissue glycogen when compared to the NADPH content produced from glucose standard solutions included on each plate.

Hepatic triglycerides, diglycerides, phospholipids, and cholesterol

Tissue lipid content and speciation were obtained by the Vanderbilt Lipid Core. Lipids were extracted using the method of Folch et al. (75). The extracts were filtered, and lipids recovered in the chloroform phase. Individual lipid classes were separated by thin layer chromatography using Silica Gel 60 A plates developed in petroleum ether, ethyl ether, acetic acid (80:20:1) and visualized by rhodamine 6G. Diglycerides, triglycerides and cholesteryl esters were scraped from the plates and methylated using BF3/methanol as described by Morrison and Smith (191). Determination of total tissue cholesterol was adapted from Rudel et al. (221).

Hepatic hexokinase enzyme activities

Activity of liver hexokinases was assessed using a modified version of the method described by Tiedge et al. (253). 10-20mg of frozen liver from 18 hour fasted-6 hour refed mouse studies was added to 1.5mL Safe-Lock microcentrifuge tubes (Eppendorf) containing 0.5 mm zirconium oxide beads (Next Advance). Immediately prior to homogenization 200µL of 200mM Tris-HCl with 10mM $MgCl_2$ was added to tubes and samples were homogenized for 5 minutes in a Bullet Blender (Next Advance). Samples were then centrifuged at 13,000g for 15 minutes and a temperature of 4°C. Supernatants were then transferred to a new microcentrifuge tube. Protein levels from each sample were quantified using Pierce™ BCA Protein Assay Kit (Thermo Fisher Scientific). Samples were then diluted to a protein concentration of 1µg/µL in homogenization buffer and 20µL of sample were added to a 2 x 96 well plates in duplicate. Glucokinase (GK) and hexokinase (HK) assay buffers were prepared consisting of 200mM Tris-HCl at pH7.4, 10mM $MgCl_2$, 5.7mM ATP, 2.8mM NADP, 0.5U/mL G6PDH (Roche Diagnostics, MillipopreSigma), and either 100mM glucose (GK+HK assay buffer) or 1mM glucose (HK assay buffer). The below equation summarizes the enzymatic reactions to determine activities of GK and other HK through endpoint NADPH production.

Determination of GK and HK activities in liver:

$$100\text{mM Glucose} + \text{ATP} \xrightarrow{Tissue\ GK+HK} \text{Glucose} - 6 - \text{phosphate} + \text{ADP}$$

$$\text{Glucose} - 6 - \text{phosphate} + \text{NADP} \xrightarrow{G6PDH} \text{phospho} - \text{D} - \text{gluconolactone} + \text{NADPH}$$

Determination of HK activities in liver:

$$1\text{mM Glucose} + \text{ATP} \xrightarrow{Tissue\ HK} \text{Glucose} - 6 - \text{phosphate} + \text{ADP}$$

$$\text{Glucose} - 6 - \text{phosphate} + \text{NADP} \xrightarrow{G6PDH} \text{phospho} - \text{D} - \text{gluconolactone} + \text{NADPH}$$

For assessment of summed activity of liver GK and all other HKs, 200µL of GK+HK assay buffer was added to plate #1 containing samples. Immediately following addition of GK+HK assay buffer, absorbance of the plate at 340nm to determine resulting NADPH concentrations was monitored every minute for 30 minutes. For assessment liver HK activity, 200µL of HK assay buffer was added to plate #2 containing samples. Immediately following addition of HK assay buffer, absorbance of the plate at 340nm to determine resulting NADPH concentrations was monitored every minute for 30 minutes.

The principle of this assay takes advantage of the lower affinity of GK for glucose compared to other HKs. By using assay buffers with low concentrations of glucose, activity of HKs can be quantified separate from GK. While using a higher concentration of glucose in the assay buffer results in quantification of HK and GK activities simultaneously. By subtracting the results of low glucose concentration HK activity from the high glucose concentration GK+HK activity we are left with the remaining GK activity.

Blood or plasma processing and analyses

Blood glucose

Blood glucose was measured using an Accu-Chek® glucometer (Roche Diagnostics, Indianapolis, IN, USA).

Insulin

Plasma insulin was measured by radio-immunoassay (190). Samples and standards were incubated with an anti-rat/mouse insulin detection antibody for 3 days. After incubation, ^{125}I-insulin was added to the mixture. Secondary antibodies were used to precipitate antibody-bound insulin from samples. Samples were then centrifuged, supernatants decanted, and pellet radioactivity counts were determined using a Cobra II AutoGamma counter (Packard, IL). Counts in the pellet

were inversely proportional to insulin concentrations. A standard curve was constructed to calculate unknown insulin concentrations.

Glucagon

Plasma glucagon was assessed using a solid phase two-site enzyme-linked immuno-sorbent assay (ELISA) (Mercodia Inc, Winston Salem, NC, USA). 10µL of EDTA plasma and standards were added to 96 well plates with anti-glucagon antibodies (clone M5F9S) bound to microplate wells. 50µL of HRP-conjugated anti-glucagon antibody (clone E6A11K) is then added to each well containing samples and standards. Plates were covered, sealed, and incubated overnight at 4°C. Plates were then washed by adding 350µL of wash buffer and inverting plate in to sink with gentle tapping 6 times. For development, 200µL of 3,3',5,5'-tetramethyl-benzidine (TMB) substrate is added to wells and incubated at room temperature for 30 minutes. 50µL of 0.5M H_2SO_4 stop solution is then added to plate. Spectrophotometric absorbance of the plate is then read at 450nm and results are calculated through linear regression analysis of the standard curve.

FGF21

Plasma FGF21 was also quantified using an ELISA (abcam, Cambridge, MA, USA). 50µL of EDTA plasma and standards were added to 96 well plates with immobilization anti-tag antibodies bound to microplate wells. 50µL of antibody cocktail containing tag-conjugated anti-FGF21 antibody and HRP-conjugated anti-FGF21 antibody is then added to each well containing samples and standards. Plates were covered, sealed, and incubated 1 hour at room temperature on a plate shaker at 400 RPM. Plates were then washed by adding 350µL of wash buffer and inverting plate in to sink with gentle tapping 3 times. For development, 100µL of TMB substrate is added to wells and incubated for 15 minutes at room temperature on a plate shaker at 400 RPM in the dark. 100µL of 0.5M H_2SO_4 stop solution is then added to plate and incubated for 1 minute

at room temperature on a plate shaker at 400 RPM. Spectrophotometric absorbance of the plate is then read at 450nm and results are calculated through linear regression analysis of the standard curve.

Non-esterified fatty acids

Tubes for collection of plasma for non-esterified fatty acids (NEFAs) were prepared by adding 5µL of a 0.06mg of Tetrahydrolipstatin (THL)/ 1mL of ethanol and allowing to dry prior to plasma sample addition. For assessment of plasma NEFAs, 5µL of plasma collected at time=100 min during steady state period of MFA studies was added to THL tubes and placed at -80°C.

Plasma NEFAs were assayed using the HR series NEFA-HR (2) kit (FUJIFILM Wako Diagnostics U.S.A., Mountain View, CA, USA). Represented below are the progressive enzymatic reactions that enable endpoint spectrophotometric quantification of colorimetric product.

$$\mathrm{NEFA} + \mathrm{ATP} + \mathrm{CoA} - \mathrm{SH} \xrightarrow{Acyl-CoA\ Synthetase} \mathrm{Acyl} - \mathrm{CoA} + \mathrm{AMP} + \mathrm{Pyrophosphate}$$

$$\mathrm{Acyl} - \mathrm{CoA} + \mathrm{O_2} \xrightarrow{Acyl-CoA\ Oxidase} 2{,}3 - \mathrm{trans} - \mathrm{Enoyl} - \mathrm{CoA} + \mathrm{H_2O_2}$$

$$2\ \mathrm{H_2O_2} + \mathrm{MEHA} + 4 - \mathrm{aminoantipyrine} \xrightarrow{HRP} \mathrm{Blue\ purple\ pigment} + 3\ \mathrm{H_2O}$$

5µL of each plasma sample in THL tubes was diluted 1:1 in H_2O and added to a 96 well plate in duplicate. Oleic acid standards were also prepared according to manufacturer's instructions and loaded onto the 96 well plate in duplicate. 225µL of Reagent A was added to each well, mixed by shaking gently, and incubated at 37°C for 10min. 75µL Reagent B was added, mixed by shaking gently, and incubated at 37°C for 10min. Air bubbles were removed by light aspiration of air through a clean pipette tip. Endpoint blue-purple pigment was then quantified spectophotometrically at 550nm and NEFA concentrations were determined by linear regression analysis of the standard curve.

Lactate

Lactate levels in plasma from 5 hour fasted mice and liver of 18 hour fasted-6 hour refed mice were determined using an L-Lactate assay kit (abcam, Cat# ab65331). Represented below are the enzymatic reactions enabling quantification of lactate through spectrophotometric quantification of enpoint colorimetric product.

$$\text{Lactate} + \text{NAD}^+ \xrightarrow{Lactate\ Dehydrogenase} \text{Pyruvate} + \text{NADH} + \text{H}^+$$

$$\text{WST} - 1 + \text{NADH} \xrightarrow{Diaphorase} \text{WST} - 1\ \text{Formazan} + \text{NAD}^+$$

β-hydroxybutyrate

Plasma β-hydroxybutyrate (β-HB) levels in 5 hour fasted mice were quantified using a colorimetric assay kit (Cayman Chemical, Ann Arbor, MI, USA, Cat# 700190). Represented below are the progressive enzymatic reactions that enable endpoint spectrophotometric quantification of colorimetric product.

$$\beta - \text{HB} + \text{NAD}^+ \xrightarrow{\beta-HB\ Dehydrogenase} \text{Acetoacetate} + \text{NADH} + \text{H}^+$$

$$\text{WST} - 1 + \text{NADH} \xrightarrow{Diaphorase} \text{WST} - 1\ \text{Formazan} + \text{NAD}^+$$

Plasma was initially diluted 1:1 in assay buffer provided by the manufacturer. 50µL of the plasma mixture or standards were added to a 96 well plate. β-HB developer solution was assembled by combining enzyme (β-HB Dehydrogenase) with colorimetric detector (Water Soluble Tetrazolium Salt-1, WST-1). 50µL of β-HB developer solution was then added to each well. Platewas then wrapped in tin foil to minize effects of light on development and incubated at room temperature for 30 minutes. Endpoint WST-1 Formazan was then quantified spectophotometrically at 450nm and β-HB concentrations were determined by linear regression analysis of the standard curve.

Amino acids and related metabolites

Plasma amino acids were quantified in the Vanderbilt Hormone Assay and Analytical Services Core by ion exchange HPLC with lithium citrate buffer system and post column ninhydrin quantification (Biochrom US, Holliston, MA, USA).

$^{2}H/^{13}C$ metabolic flux analysis (MFA)

Glucose derivatizations, gas chromatography-mass spectrometry analysis, and MFA were completed using samples from 120 minutes prior to as well as 90, 100, and 110 minutes following the [$^{13}C_3$]propionate bolus as previously described (105, 121). Fragment ion ranges used for determining mass isotopomer distributions were aldonitrile, *m/z* 173–178, 259–264, 284–289, and 370–376; methyloxime, *m/z* 145–149; di-*O*-isopropylidene, *m/z* 301–311. Flux estimates in the network for each sample underwent 50 iterations beginning with random initial values to determine the best fit based. Goodness-of-fit was accepted according to a chi-square test ($p<0.05$). By taking multiple samples over time an isotopic steady state is confirmed over the interval of 90 to 120 min following the beginning of the [$^{13}C_3$]propionate infusion. Flux values for each mouse are an average of estimates at steady state (90, 100, and 110 minutes following the [$^{13}C_3$]propionate bolus) and were normalized to body weight. The fractional turnover of the glucose pool was defined as steady state glucose production [mg/(kg•min)]/(steady state average blood glucose [mg/ml]/200•[mL/kg]) and expressed as a percentage. In a steady state, glucose production is equivalent to glucose utilization.

Statistical analyses

Student's t-tests with Welch's correction were used to detect statistical differences ($p<0.05$) between 2 groups. 1-way ANOVA with Brown-Forsythe and Welch correction were used to detect statistical differences ($P<0.05$) between more than 2 groups. All data are reported as means ± SEM.

Chapter III

HEPTAOCYTE ILK KNOCKOUT MICE EXHIBIT IMPROVED GLUCOSE TOLERANCE ACCOMPANIED BY RESISTANCE TO HF-DIET INDUCED OBESITY AND HEPATIC STEATOSIS IN AN AGE-DEPENDENT MANNER

Aims

Hepatocyte integrin-linked kinase (ILK) has been demonstrated as a requirement for development of hepatic insulin resistance during diet-induced obesity. Other studies have demonstrated that hepatocyte ILK effects a number of outcomes related to histologic organization, transcriptional programming, cell proliferation, and hepatic regeneration. However, these effects may be age-dependent. Insulin resistance represents a dysfunctional regulation of glucose homeostasis and is affected by age and length of exposure to pathologic stimulus. Therefore, two aims were constructed for this chapter. The first aim was to determine whether hepatocyte ILK determines hepatic glucoregulatory functions and overall glucose homeostasis in an age-dependent manner consistent with studies of histology and regeneration. The second aim was to determine whether ILK effects the progressive dysfunction in glucoregulation and insulin resistance brought on by an obesogenic diet.

Introduction

Integrin-linked kinase (ILK) is necessary for normal liver development. Deletion of ILK from hepatic progenitor cells around embryonic day 10.5 (~E10.5), prior to hepatocyte differentiation (142), causes increased hepatocyte apoptosis, fibrosis, biliary hyperplasia, and mitosis at 6 weeks of age (86). However, by 30 weeks of age these biochemical and histological alterations were resolved, but a doubling of the liver to body weight ratio occurred. This was hypothesized to be a result of compensatory proliferation due to loss of contact inhibition. Even after morphologic

phenotypes are resolved, exposure of these mice to hepatic resection or toxicity results in an enhanced regenerative response (7, 17, 64, 66, 86).

More recently, studies have also shown that hepatocyte ILK contributes to hepatic insulin resistance during diet-induced obesity (280). This was shown in mice where ILK was deleted at E15.5, after initiation of hepatocyte differentiation (206). There is a clear age dependence for an array of hepatic outcomes as they relate to hepatic ILK knockout. However, studies assessing the role of ILK in development of hepatic insulin resistance only assessed an individual time point (~18-19 weeks) during the lifespan of the mice. As insulin resistance is driven by dysregulated glucose homeostatic processes, it was the goal of these studies to assess the role of ILK in metabolic and glucose homeostasis as they relate to age.

These studies demonstrate that hepatocyte-specific ILK knockout (hepILK-KO) in C57Bl6/J mice has an age-dependent effect on glucose homeostasis (256). Specifically, hepILK-KO mice have decreased blood glucose levels after a 5 hour fast and increased glucose tolerance at 6 weeks of age. This is accompanied by a significant decrease in fasting insulin and lower insulin responses during an oral glucose tolerance test. This effect on glucose homeostasis is accompanied by changes to hepatic histology and transcriptional programming. Over time glucose tolerance and histology gradually converge between hepILK-KO and $ILK^{lox/lox}$ mice on a chow diet. HF-fed hepILK-KO mice are initially resistant to hyperglycemia, obesity, and hepatic statosis copared to $ILK^{lox/lox}$ mice. However, hepILK-KO mice gradually match these traits compared to $ILK^{lox/lox}$ littermates. Additionally, hepatic transcriptional profiles of hepILK-KO mice appear to follow a similar paradigm with stark differences from $ILK^{lox/lox}$ at 6 weeks of age that mostly converge by 18 weeks of age, but have differences provoked if mice are fed a HF diet.

Experimental approach

To assess the aims set forth for Chapter III assessment of mice expressing normal hepatocyte ILK ($ILK^{lox/lox}$) or with a hepatocyte-specific removal of the ILK ($ILK^{lox/lox}$Alb*cre*$^{+/-}$;

HepILK-KO) was started at 6 weeks of age. Mice underwent basic metabolic characterization of weight and body composition. Fasting blood glucose levels and oral glucose tolerance tests coupled with plasma insulin quantification were used as metrics of glucose homeostasis. After initial 6 week assessments mice were either maintained on a chow diet or switched to a HF obesogenic diet. Basic metabolic characterizations and assessment of glucose homeostasis were repeated at 9, 12, 18, and 32 weeks of age in all groups. At 32 weeks of age, mice were sacrificed and tissues were taken for histologic analysis. In conjunction with these studies $ILK^{lox/lox}$ and hepILK-KO mice at 6 weeks (chow diet only) and 18 weeks of age (chow and HF diet) were sacrificed for assessment of hepatic histology and transcriptomic analysis.

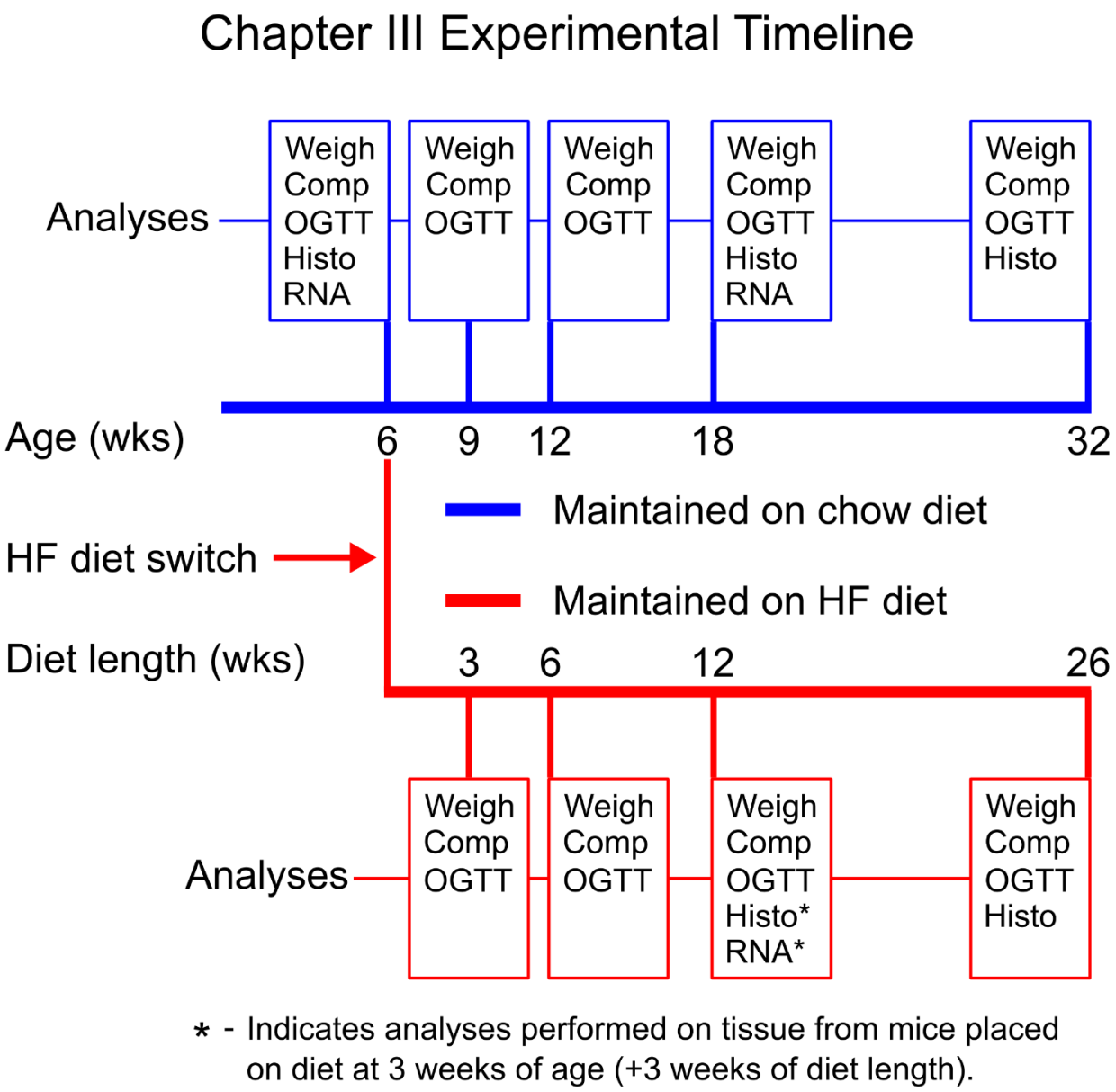

Figure 3.1- Overview of experimental timeline for age-dependent analyses of ILK$^{lox/lox}$ and hepILK-KO mice fed chow or switched to HF diets.

Results

Hepatocyte ILK is required for normal hepatic histology and glucose homeostasis in young mice.

Initial assessment of hepILK-KO mice at 6 weeks of age revealed a small, but significant decrease in body weight compared to $ILK^{lox/lox}$ mice (Table 3.1). While no difference in adipose mass as a percentage of total body mass were observed, there was a significant increase in lean mass percentage of hepILK-KO mice (Table 3.1). To assess fasting glucose homeostasis $ILK^{lox/lox}$ and hepILK-KO mice underwent a 5 hour fasting period for induction of a postabsorptive state. Initial blood samples were taken for measurement of blood glucose and plasma insulin. Blood glucose levels after a 5 hour fast were decreased by ~30% in hepILK-KO mice at 6 weeks of age (Table 3.1; Figure 3.2A). This effect was accompanied by lower fasting insulin (Table 3.1; Figure 3.2C). OGTTs revealed increased glucose tolerance in hepILK-KO mice at 6 weeks as the baseline-corrected area under the glucose curve (AUC) was decreased compared to $ILK^{lox/lox}$ mice (Fig 3.2B). Peak insulin responses during OGTT (T=10 minutes) also trended lower in hepILK-KO mice ($p=0.06$) before returning to comparable levels for the remainder of the GTT (Figure 3.2C).

Previous studies from the Michalopoulos group had demonstrated altered histologic and signaling characteristics in early life of an alternative hepatic ILK-KO model (86). As mentioned previously, this model may create off target knockout effects as the result early activation of cre expression. Our knockout model was designed to minimize developmental effects with later initiation and completion of cre recombinase driven knockout. As such, we felt it necessary to assess histology in early life as well. Histological evaluation of livers from hepILK-KO and $ILK^{lox/lox}$ were performed at 6 weeks of age. Livers from 6 week old $ILK^{lox/lox}$ and hepILK-KO mice stained with H&E (Figure 3.2D & E) were evaluated by a veterinary pathologist (Dr. Kelli L. Boyd). The presence of hepatocellular degeneration, inflammation, fibrosis, and biliary hyperplasia were

Table 3.1- Basic characterization of control ($ILK^{lox/lox}$) and hepILK-KO mice at 6 weeks of age after a 5 hour fast.

Gentoype	$ILK^{lox/lox}$	hepILK-KO
N	13-28	11-19
Weight (g)	21.0 ± 0.5	17.9 ± 0.6#
Fat mass (%)	4.8 ± 0.4	5.2 ± 0.9
Lean mass (%)	67.6 ± 0.4	70.8 ± 1.0*
Study age (wks)	6	6
Diet duration (wks)	-	-
FBG (mg/dL)	148 ± 4	103 ± 5#
FPI (ng/mL)	0.5 ± 0.05	0.3 ± 0.04**

Data are mean ± SEM. *p*-values are the result of Student's t-test with Welch's correction. *= $p<0.05$ chow-fed $ILK^{lox/lox}$ vs. chow-fed hepILK-KO; **= $p<0.01$ chow-fed $ILK^{lox/lox}$ vs. chow-fed hepILK-KO; # = $p<0.001$ chow-fed $ILK^{lox/lox}$ vs. chow-fed hepILK-KO. FBG and FPI are fasting blood glucose and fasting plasma insulin, respectively.

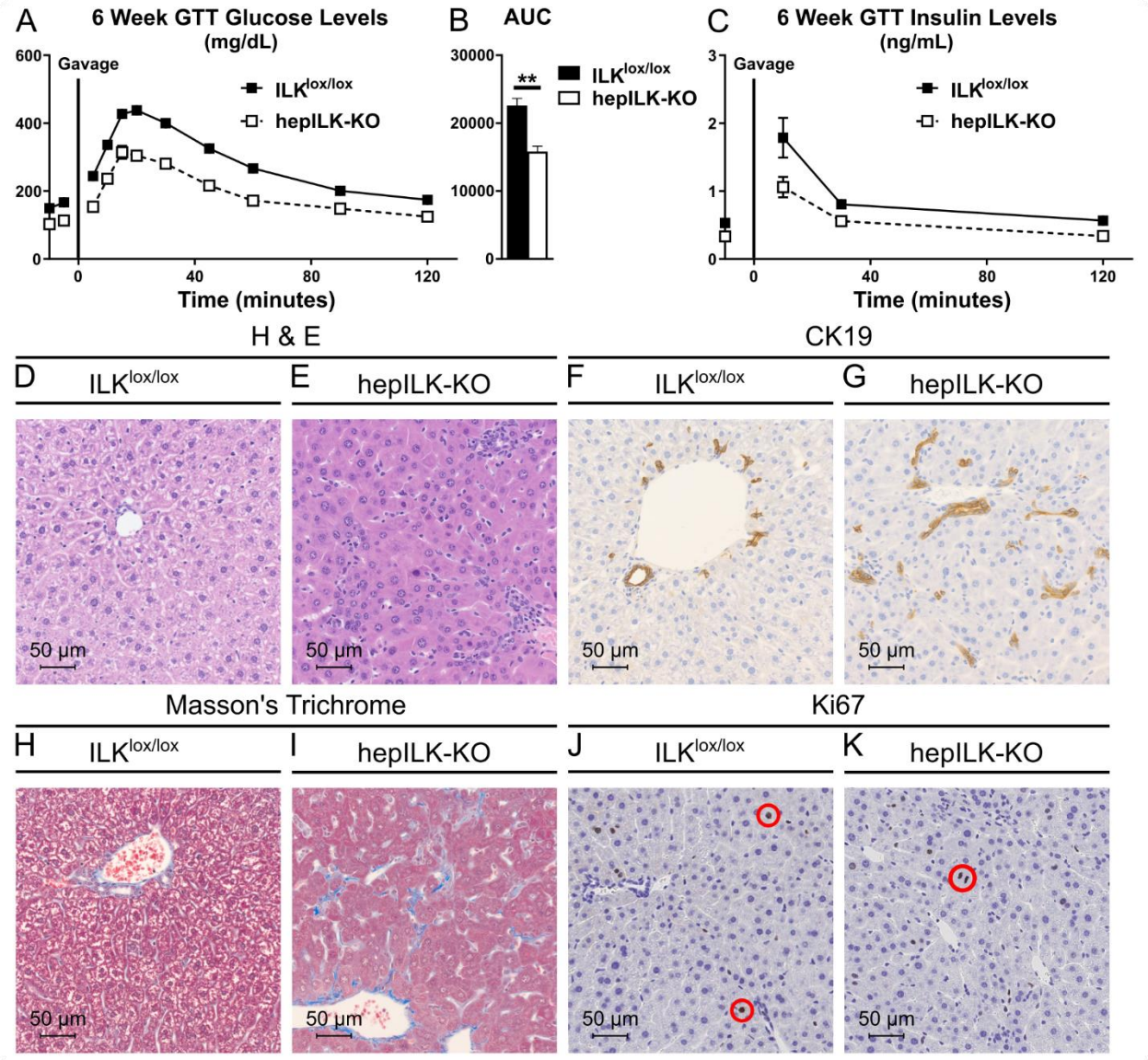

Figure 3.2- Hepatocyte ILK is required for establishment of normal glucose homeostasis and hepatic organization in 6 week old mice. A) Blood glucose levels of 6 week old ILK$^{lox/lox}$ (n=30) and hepILK- KO (n=20) mice during OGTTs. **B**) Baseline corrected area under the glucose curve (A) **C)** Insulin levels during OGTTs. **D)** Representative H&E stained liver micrographs at 40x magnification from 6 week old ILK$^{lox/lox}$ mice. **E)** Representative H&E stained liver micrographs at 40x magnification from 6 week old hepILK-KO mice. **F)** Representative CK19 IHC liver micrographs at 40x magnification from 6 week old ILK$^{lox/lox}$ mice. **G)** Representative CK19 IHC liver micrographs at 40x magnification from 6 week old hepILK-KO mice. **H)** Representative Masson's trichrome stained liver micrographs at 40x magnification from 6 week old ILK$^{lox/lox}$ mice. **I)** Representative Masson's trichrome stained liver micrographs at 40x magnification from 6 week old hepILK-KO mice. **J)** Representative Ki67 IHC liver micrographs at 40x magnification from 6 week old ILK$^{lox/lox}$ mice. **K)** Representative Ki67 IHC liver micrographs at 40x magnification from 6 week old hepILK-KO mice. Red circles denote nuclei stained positively for Ki67 in Fig 2E & F. **= p<0.01 chow-fed ILK$^{lox/lox}$ vs. chow-fed hepILK-KO

evident. Biliary hyperplasia was demonstrated with immunohistochemistry (IHC) for cytokeratin 19 (Figure 3.2F & G). Fibrosis was confirmed with Masson's trichrome staining (Figure 3.2H & I). At 6 weeks hepILK-KO mice lack any significant differences in hepatocyte proliferation index according to pathologist evaluation and IHC for nuclear Ki-67 (Figure 3.2J & K).

Observations at 6 weeks of age demonstrate a role for hepatocyte ILK in glucose homeostasis and hepatic organization. Continual basic characterization revealed a normalization in weight and body composition of chow-fed hepILK-KO mice at 9 weeks of age (Table 3.2). Interestingly, after 3 weeks of HF diet feeding hepILK-KO mice were resistant to obesogenic weight gain. HF feeding for 3 weeks only resulted in ~12% weight increase of hepILK-KO mice compared to a ~25% increase in control mice (Table 3.2). Despite normalizations in body weight and composition of chow-fed hepILK-KO mice OGTT AUCs remained significantly decreased at 9 weeks of age (Figure 3.3B) with a trend toward decreased fasting glucose levels as well (Table 3.2). Accompanying the resistance to weight gain in HF-fed hepILK-KO mice was a resistance to fasting hyperglycemia and hyperinsulinemia (Table 3.2). OGTT AUCs were not significantly different, but trended lower in the HF-fed hepILK-KO mice as well (Figure 3.3E; p=0.07).

12 week old chow-fed hepILK-KO mice have no differences in body weight or fat mass % (Table 3.3). These mice do possess a small but significant increase in lean mass as a percentage of body weight. OGTTs in chow-fed mice reveal no remaining differences in fasting glucose (Table 3.3) or glucose tolerance in hepILK-KO mice (Figure 3.3G-I). This represents a near complete normalization in body composition and glucose homeostasis in chow-fed hepILK-KO mice relative to $ILK^{lox/lox}$ counterparts. HF-fed hepILK-KO mice maintain a resistance to obesogenic weight gain at 12 weeks of age. Despite protection from obesity, hepILK-KO mice demonstrated an equivalent induction of hyperglycemia, hyperinsulinemia, and glucose intolerance by HF feeding. This represents an atypical pathologic progression in hepILK-KO mice as they are metabolically equivalent to obese $ILK^{lox/lox}$ mice, but resistant to obesogenic weight gain.

Table 3.2- Basic characterization of control ($ILK^{lox/lox}$) and hepILK-KO mice at 9 weeks of age after a 5 hour fast.

Diet	Chow	Chow	HF	HF
Gentoype	$ILK^{lox/lox}$	hepILK-KO	$ILK^{lox/lox}$	hepILK-KO
N	17	7	4-13	7-11
Weight (g)	24.7±0.5	23.4±0.6	30.0±0.6	26.3±0.7**
Fat mass (%)	4.7±0.3	5.1±0.5	13.2±0.2	10.0±0.8
Lean mass (%)	68.1±0.4	68.3±1.2	65.5±1.9	67.5±0.7
Study age (wks)	9	9	9	9
Diet duration (wks)	-	-	3	3
FBG (mg/dL)	137±5.0	113±7.3	181±10.6	145±7.3‡
FPI (ng/mL)	0.6±0.04	0.5±0.09	1.4±0.18	0.7±0.11‡

Table 3.3- Basic characterization of control ($ILK^{lox/lox}$) and hepILK-KO mice at 12 weeks of age after a 5 hour fast.

Diet	Chow	Chow	HF	HF
Gentoype	$ILK^{lox/lox}$	hepILK-KO	$ILK^{lox/lox}$	hepILK-KO
N	13-15	7-9	4-9	8-11
Weight (g)	27.2±0.7	25.6±0.6	36.3±0.9	31.8±1.1†
Fat mass (%)	6.0±0.5	5.4±0.5	21.8±2.0	17.9±2.2
Lean mass (%)	67.1±0.4	69.3±0.4*	58.3±1.6	61.2±1.4
Study age (wks)	12	12	12	12
Diet duration (wks)	-	-	6	6
FBG (mg/dL)	142±3.2	120±8.9	185±9.1	159±11.0
FPI (ng/mL)	0.6±0.06	0.5±0.06	2.5±0.33	2.1±0.45

Data are mean ± SEM. *p*-values are the result of 1-way ANOVA with Brown-Forsythe and Welch correction. *= $p<0.05$ chow-fed $ILK^{lox/lox}$ vs. chow-fed hepILK-KO; **= $p<0.01$ chow-fed $ILK^{lox/lox}$ vs. chow-fed hepILK-KO; # = $p<0.001$ chow-fed $ILK^{lox/lox}$ vs. chow-fed hepILK-KO; †= $p=0.05$ HF-fed $ILK^{lox/lox}$ vs. HF-fed hepILK-KO; ‡= $p<0.01$ HF-fed $ILK^{lox/lox}$ vs. HF-fed hepILK-KO; Ω=$p<0.001$ HF-fed $ILK^{lox/lox}$ vs. HF-fed hepILK-KO FBG and FPI are fasting blood glucose and fasting plasma insulin, respectively.

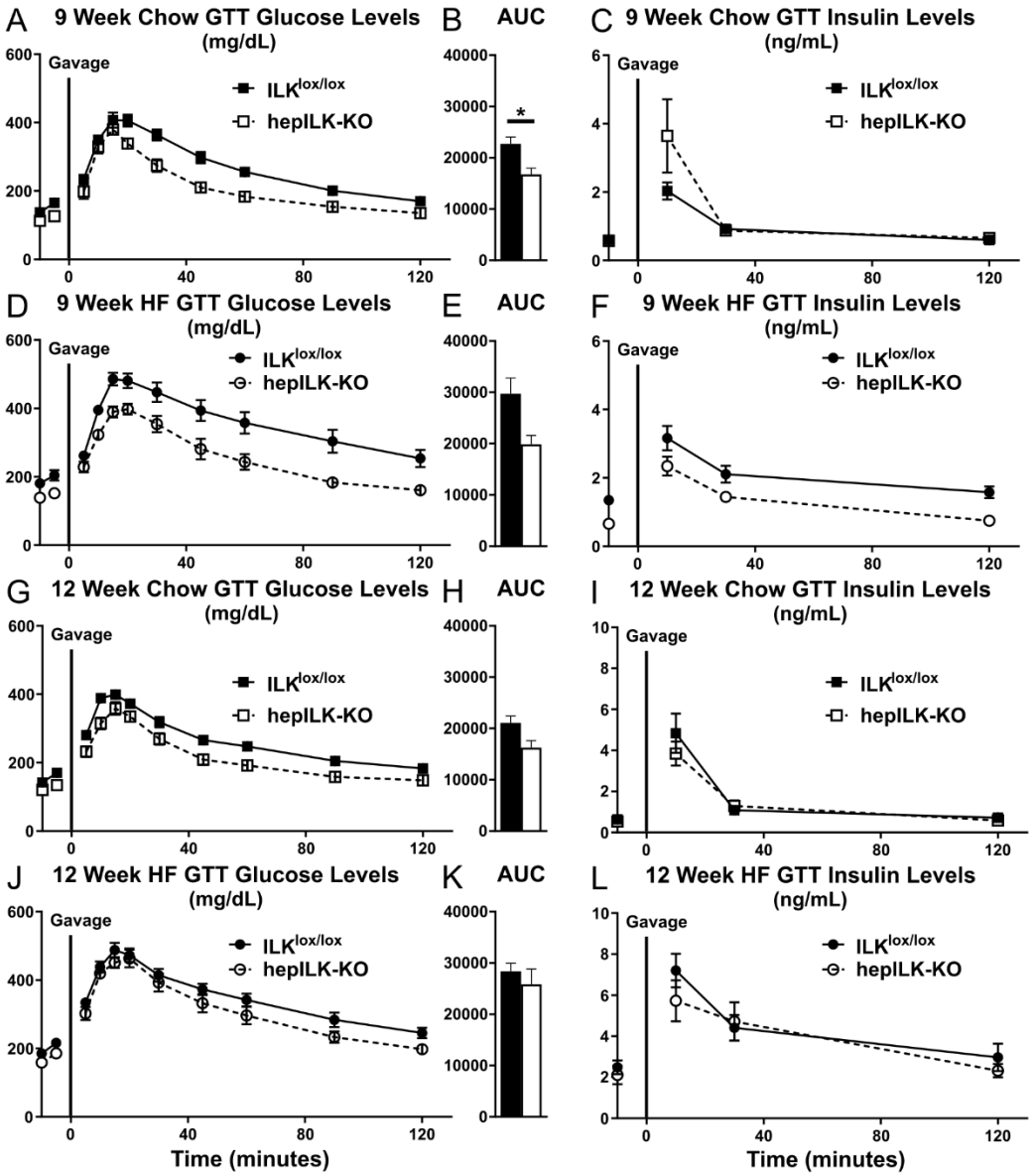

Figure 3.3- Glucose homeostasis normalizes over time in the absence of hepatocyte ILK. **A)** Blood glucose levels of 9 week old ILK$^{lox/lox}$ (n=17) and hepILK- KO (n=7) mice on chow diet during OGTTs. **B**) Baseline corrected area under the glucose curve (A) **C)** Insulin levels during OGTTs. **D)** Blood glucose levels of 9 week old ILK$^{lox/lox}$ (n=8) and hepILK- KO (n=10) mice on HF diet during OGTTs. **E**) Baseline corrected area under the glucose curve (A) **F)** Insulin levels during OGTTs. **G)** Blood glucose levels of 12 week old ILK$^{lox/lox}$ (n=15) and hepILK- KO (n=7) mice on chow diet during OGTTs. **H**) Baseline corrected area under the glucose curve (A) **I)** Insulin levels during OGTTs. **J)** Blood glucose levels of 12 week old ILK$^{lox/lox}$ (n=9) and hepILK-KO (n=11) mice on HF diet during OGTTs. **K**) Baseline corrected area under the glucose curve (A) **L)** Insulin levels during OGTTs. *=p<0.05 Chow ILK$^{lox/lox}$ vs. Chow hepILK-KO. *= p<0.05 chow-fed ILK$^{lox/lox}$ vs. chow-fed hepILK-KO.

Physical and glucoregulatory responses were again performed at 18 weeks of age. Physical evaluation of chow-fed $ILK^{lox/lox}$ and hepILK-KO mice revealed no significant differences to weight or body composition (Table 3.4). HF-fed mice were also lacking in significant weight or body composition differences. This was the first time HF-fed hepILK-KO mice did not demonstrate a resistance to weight gain relative to $ILK^{lox/lox}$ littermates. Therefore, between 12 weeks of age (6 weeks of HF feeding) and 18 weeks of age (12 weeks of HF feeding) hepILK-KO mice are no longer resistant to obesity induced by HF feeding. Evaluation of glucose homeostasis did not reveal significant differences in fasting glucose, fasting insulin, glucose tolerance, or insulin responses of hepILK-KO mice on chow or HF diet relative to $ILK^{lox/lox}$ littermates.

Despite loss of physical and metabolic differences between hepILK-KO and control mice within dietary groups at 18 weeks of age there has been a clear difference in the trajectory leading to this point of convergence. Therefore, a parallel histological follow up was performed. Histologic evaluations were performed on livers from 18 week old $ILK^{lox/lox}$ and hepILK-KO mice maintained on chow diet or switched to a HF diet at 3 weeks of age (+3 weeks of HF diet feeding; Figure 3.1). Veterinary pathologist revealed clear indices of biliary hyperplasia in 18 week old chow-fed hepILK-KO mice compared to $ILK^{lox/lox}$ littermates (Figure 3.4G & H). Interestingly limited inflammation and a distinct lack of fibrosis were demonstrated in 18 week old hepILK-KO livers. This indicated a complete recession of fibrosis and improved inflammatory status compared to 6 week old hepILK-KO mouse livers (3.1D-K). However, hepILK-KO livers did with hepatocyte hyperplastic phenotypes, which resulted in adenoma formation in ~40% of samples (Figure 3.4H blue circle). Livers from HF-fed $ILK^{lox/lox}$ mice presented with a typical pattern of steatosis. This is consistent with an early NAFLD phenotype, which would be expected in a setting of obesity, glucose intolerance, and insulin resistance. Opposing this observation was a near lack of steatosis in liver from HF-fed hepILK-KO mice (Figure 3.4J). This further emphasizes the differential responses of hepILK-KO mice to obesity. Despite a near complete coalescence of physical and metabolic phenotypes of hepILK-KO mice, they maintain a clear difference in hepatic

Table 3.4- Basic characterization of control ($ILK^{lox/lox}$) and hepILK-KO mice at 18 weeks of age after a 5 hour fast.

Diet	Chow	Chow	HF	HF
Gentoype	$ILK^{lox/lox}$	hepILK-KO	$ILK^{lox/lox}$	hepILK-KO
N	10-15	6-7	9	10
Weight (g)	30.4±0.7	30.1±0.8	49.0±1.3	44.3±1.4
Fat mass (%)	6.7±0.8	5.6±0.7	32.1±4.7	29.9±1.9
Lean mass (%)	66.0±0.7	67.6±1.0	50.4±1.7	52.7±1.6
Study age (wks)	18	18	18	18
Diet duration (wks)	-	-	12	12
FBG (mg/dL)	145±3.4	135±7.1	209±21.3	185±14.0
FPI (ng/mL)	0.6±0.06	0.7±0.14	10.9±1.4	7.4±0.1.4

Data are mean ± SEM. *p*-values are the result of 1-way ANOVA with Brown-Forsythe and Welch correction. *= $p<0.05$ chow-fed $ILK^{lox/lox}$ vs. chow-fed hepILK-KO; **= $p<0.01$ chow-fed $ILK^{lox/lox}$ vs. chow-fed hepILK-KO; # = $p<0.001$ chow-fed $ILK^{lox/lox}$ vs. chow-fed hepILK-KO; †= $p=0.05$ HF-fed $ILK^{lox/lox}$ vs. HF-fed hepILK-KO; ‡= $p<0.01$ HF-fed $ILK^{lox/lox}$ vs. HF-fed hepILK-KO; Ω=$p<0.001$ HF-fed $ILK^{lox/lox}$ vs. HF-fed hepILK-KO FBG and FPI are fasting blood glucose and fasting plasma insulin, respectively.

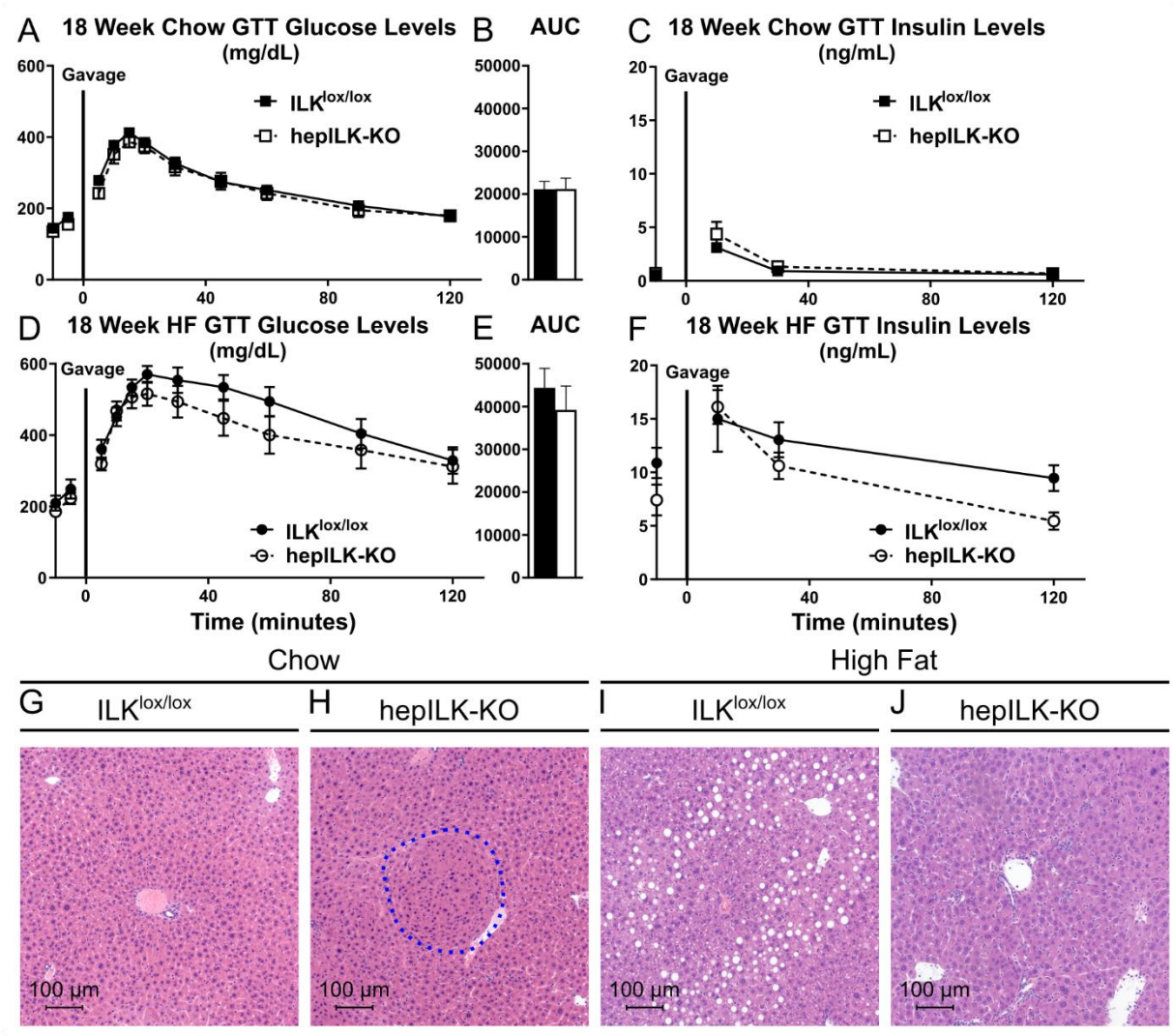

Figure 3.4- ILK contributes to steatosis formation during obesity independent of glucose tolerance. A) Blood glucose levels of 18 week old ILK$^{lox/lox}$ (n=15) and hepILK- KO (n=7) mice on chow diet during OGTTs. **B**) Baseline corrected area under the glucose curve (A) **C)** Insulin levels during OGTTs. **D)** Blood glucose levels of 18 week old ILK$^{lox/lox}$ (n=9) and hepILK- KO (n=10) mice on HF diet during OGTTs. **E**) Baseline corrected area under the glucose curve (A) **F)** Insulin levels during OGTTs. **G)** Representative H&E stained liver micrographs at 20x magnification from 18 week old chow-fed ILK$^{lox/lox}$ mice. **H)** Representative H&E stained liver micrographs at 20x magnification from 18 week old chow-fed hepILK-KO mice. Adenoma is designated by dashed blue border. **I)** Representative H&E stained liver micrographs at 20x magnification from 18 week old HF-fed ILK$^{lox/lox}$ mice. **J)** Representative H&E stained liver micrographs at 20x magnification from 18 week old HF-fed hepILK-KO mice.

histology related to lipid deposition. Overall, hepILK-KO mice appear to have a very distinct response to a relatively extended HF diet exposure.

At 32 weeks of age no significant differences in physical characteristics, fasting glucose, or fasting insulin were observed between hepILK-KO or $ILK^{lox/lox}$ mice regardless of diet (Table 3.5). As mice fed a HF diet for 26 weeks are quite obese and glucose intolerant it was necessary to alter the experimental design for OGTTs in these mice. Specifically, glucometers are not sensitive at glucose concentration >600 mg/dl. Pilot studies with the standard dose had used (2.0mg of glucose/ g body weight) exceed the range of the glucometer. Therefore, the glucose dosage was reduced by 75% (1.5mg of glucose/ g body weight) was used. hepILK-KO mice presented with a similar level of glucose tolerance to $ILK^{lox/lox}$ littermates on both diets (Figure 3.5). Possibly indicative of sustained insulin sensitivity was a trend toward a lower insulin peak response in HF-fed hepILK-KO mice compared to HF-fed $ILK^{lox/lox}$ controls (Figure 3.5F). This is consistent with previous findings from our lab indicating a protective effect of hepILK-KO against hepatic insulin resistance in obese mice (280).

Histologic evaluation of livers from 32 week old chow and HF-fed mice were performed as a comparison to analyses performed at 6 and 18 weeks of age. As had been observed at 6 and 18 weeks of age, livers from chow-fed hepILK-KO mice displayed prominent biliary hyperplasia, but were absent of any other characteristics (Figure 3.6A-F; 3.7A-H). This indicates a continued recession of fibrosis and a loss of inflammatory phenotypes previously observed at earlier ages, despite excessive ductular reactions. HF diet-induced steatosis was prominently displayed in $ILK^{lox/lox}$ liver in a relatively organized pattern within zones 1 and 2 of the hepatic lobule (Figure 3.6 G-I; 3.7O). Livers of HF-fed 32 week old hepILK-KO mice were remarkably steatotic with some differences in vacuole size and a prominent azonal organization of lipid depostition (Figure 3.6J-L; 3.7P). This represents a remarkable shift of hepatic phenotype of HF-fed hepILK-KO mice between 18 and 32 weeks of age. Thus, over the course of 14 weeks hepILK-KO mice have

Table 3.5- Basic characterization of control ($ILK^{lox/lox}$) and hepILK-KO mice at 32 weeks of age after a 5 hour fast.

Diet	Chow	Chow	HF	HF
Gentoype	$ILK^{lox/lox}$	hepILK-KO	$ILK^{lox/lox}$	hepILK-KO
N	16-18	4-9	9-12	7-9
Weight (g)	34.8±0.9	32.8±1.5	52.4±1.7	53.8±0.8
Fat mass (%)	11.5±1.3	7.7±2.0	33.3±1.0	33.2±0.4
Lean mass (%)	63.8±1.0	66.5±1.4	53.3±0.9	50.6±0.4
Study age (wks)	32	32	32	32
Diet duration (wks)	-	-	26	26
FBG (mg/dL)	134±4.2	124±8.3	148±10.1	179±14.3
FPI (ng/mL)	0.9±0.20	1.1±0.52	8.7±1.1	9.8±1.1

Data are mean ± SEM. *p*-values are the result of 1-way ANOVA with Brown-Forsythe and Welch correction. *= $p<0.05$ chow-fed $ILK^{lox/lox}$ vs. chow-fed hepILK-KO; **= $p<0.01$ chow-fed $ILK^{lox/lox}$ vs. chow-fed hepILK-KO; # = $p<0.001$ chow-fed $ILK^{lox/lox}$ vs. chow-fed hepILK-KO; †= $p=0.05$ HF-fed $ILK^{lox/lox}$ vs. HF-fed hepILK-KO; ‡= $p<0.01$ HF-fed $ILK^{lox/lox}$ vs. HF-fed hepILK-KO; Ω=$p<0.001$ HF-fed $ILK^{lox/lox}$ vs. HF-fed hepILK-KO FBG and FPI are fasting blood glucose and fasting plasma insulin, respectively.

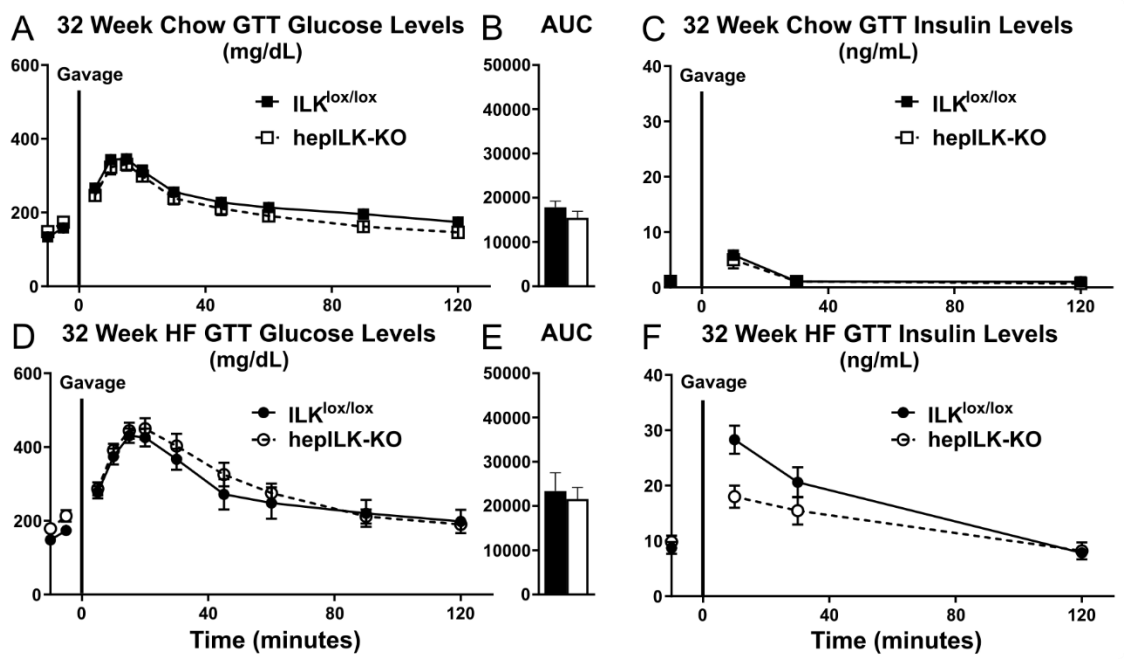

Figure 3.5- Hepatocyte ILK does not affect glucose tolerance after extended aging or exposure to obesity, but may limit insulin resistance. A) Blood glucose levels of 32 week old $ILK^{lox/lox}$ (n=18) and hepILK- KO (n=7) mice on chow diet during OGTTs. **B**) Baseline corrected area under the glucose curve (A) **C)** Insulin levels during OGTTs. **D)** Blood glucose levels of 32 week old $ILK^{lox/lox}$ (n=12) and hepILK- KO (n=9) mice on HF diet during OGTTs. **E**) Baseline corrected area under the glucose curve (A) **F)** Insulin levels during OGTTs.

"caught up" to ILK$^{lox/lox}$ littermates in terms of lipid deposition, but display a different pattern of steatotic progression.

Hepatocyte ILK determines the transcriptional program of the liver

Given the difference in glucose homeostasis of 6 and 18 week old hepILK-KO mice on chow or HF diet we hypothesized specific differences in hepatic transcriptional profiles relating to metabolic functions at these ages. To assess overall sample grouping, similarities, and dissimilarities a multi-dimensional scaling analysis was performed on the transcriptome data from all groups (Figure 3.8). This revealed a pattern consistent with our glucose tolerance and histology data. 6 week old hepILK-KO mice were quite distinct transcriptionally from their control littermates. While 18 week old chow-fed hepILK-KO mice were quite similar to their control counterparts if exposed to HF diet differences in transcriptional profiles became more evident. Quantification of differentially expressed genes from whole livers of 5 hour fasted, 6 week old ILK$^{lox/lox}$ and hepILK-KO mice revealed a large number (n=6437; 3258=up; 3159=down) of significantly different genes in hepILK-KO livers (Figure 3.9) representing broad alterations in transcriptional profiles.

To evaluate any thematic connections in this considerable difference in transcriptional milieu two types of analyses were performed. The first is a gene ontology (GO) analysis. This is a classification system whereby gene products are assigned a functional connotation based on their documented involvement in biological processes (BPs), molecular functions (MFs), or as cellular components (CCs). Additionally, specific gene ontologies describe broad aspects of cellular biology. Therefore this analysis can offer insight in to connections between a diverse set of individual transcripts. GO analysis of genes that were significantly different in 6 week old hepILK-KO livers offered results consistent with our initial hypothesis regarding transcriptional programming of metabolic processes (Table 3.6). Specifically, Aspects of mitochondria and oxidative metabolic processes were highly downregulated in hepILK-KO livers. In line with our genetic manipulation of the ECM-integrin signaling system were significant increases in GOs

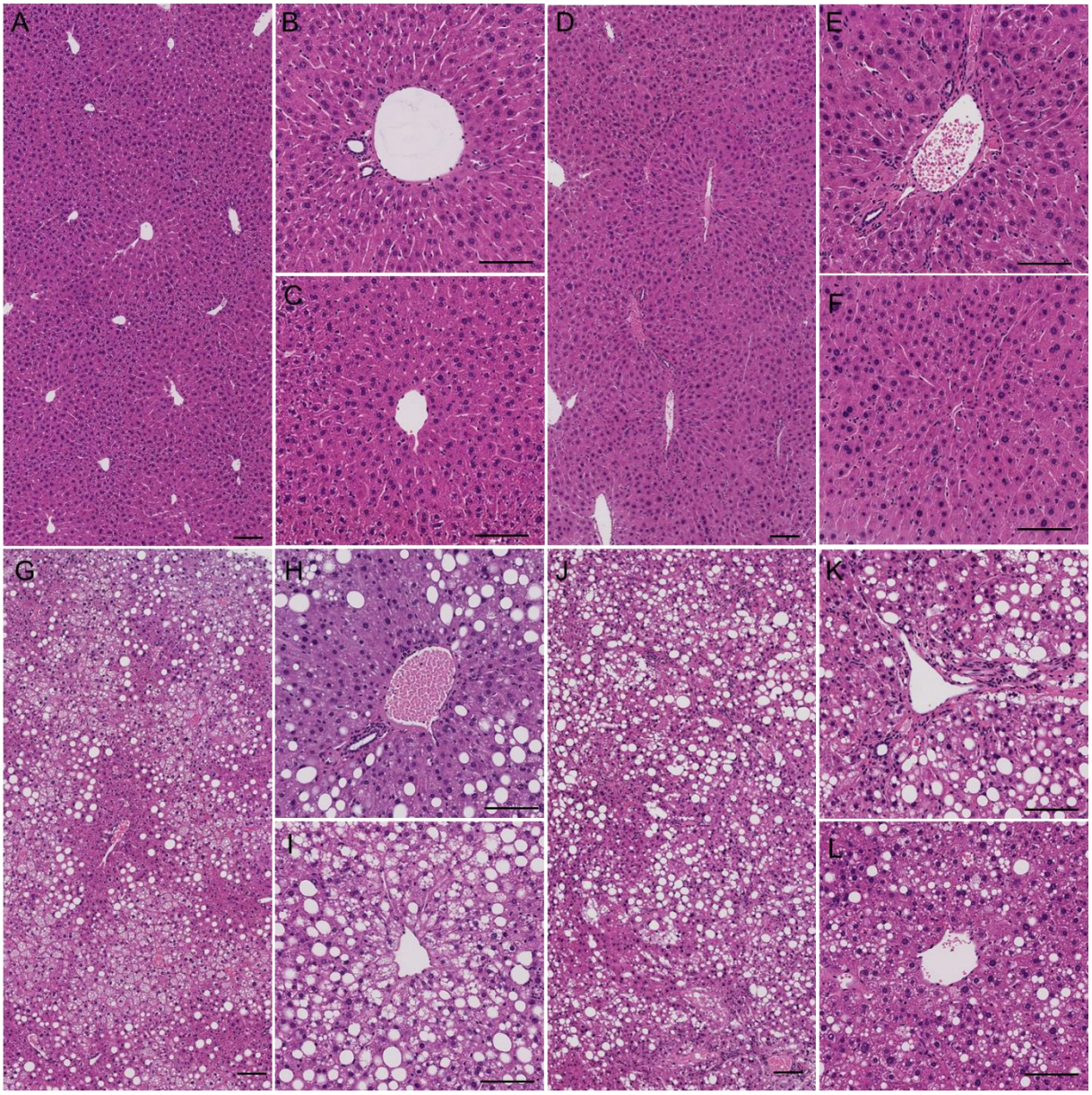

Figure 3.6- ILK determines zonation and organization of steatosis during extended HF diet feeding. A-C) Representative H&E stained liver micrographs at 10x (A) and 20x (B & C) magnification from 32 week old chow-fed $ILK^{lox/lox}$ mice. **D-F)** Representative H&E stained liver micrographs at 10x (D) and 20x (E & F) magnification from 32 week old chow-fed hepILK-KO mice. **G-I)** Representative H&E stained liver micrographs at 10x (G) and 20x (H & I) magnification from 32 week old HF-fed $ILK^{lox/lox}$ mice. **J-L)** Representative H&E stained liver micrographs at 10x (J) and 20x (K & L) magnification from 32 week old HF-fed hepILK-KO mice. Scale bar = 100 µm.

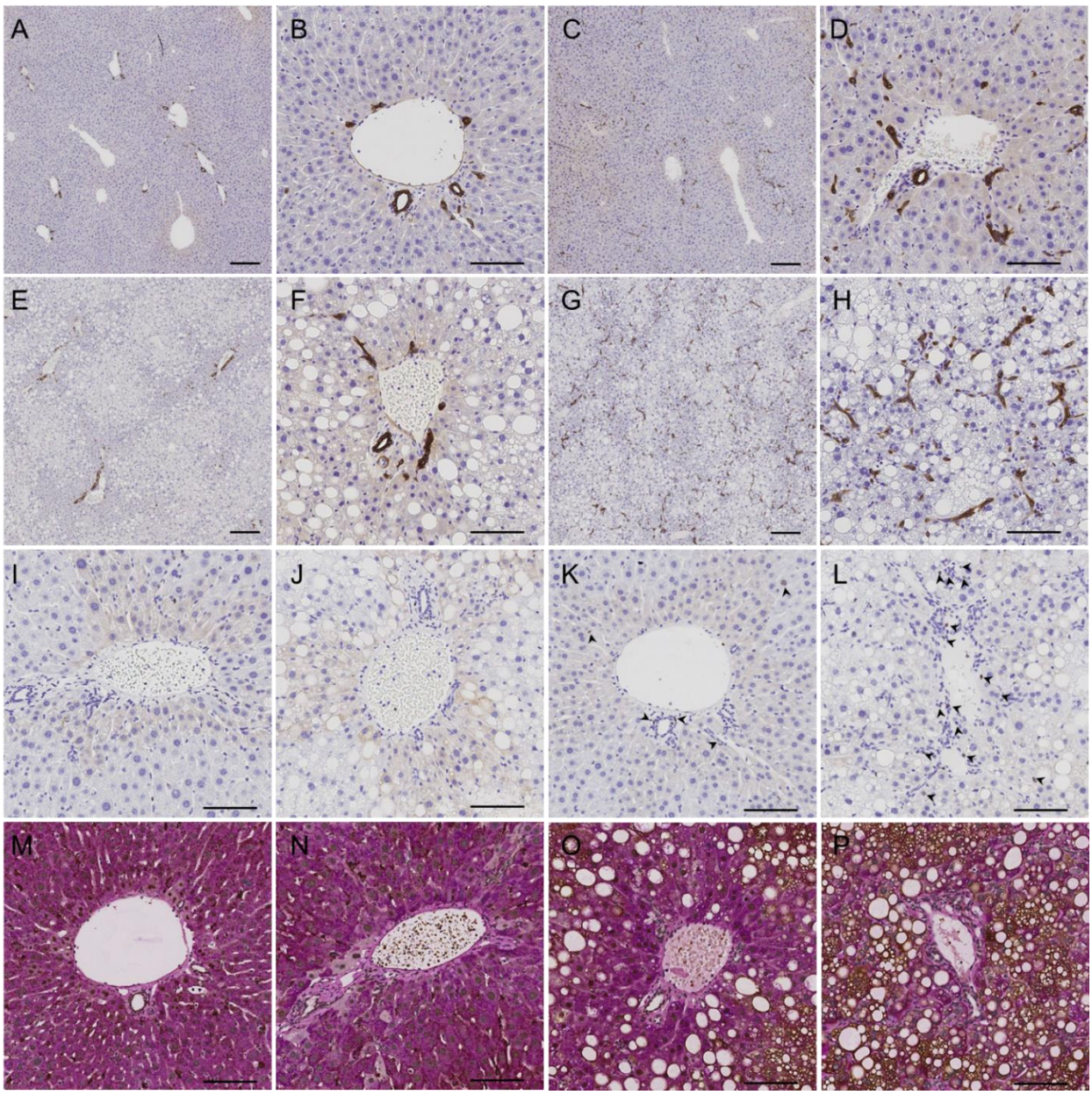

Figure 3.7- Biliary hyperplasia persists and steatosis is confirmed as azonal lipid deposition in the absence of hepatocyte ILK. A-H) Representative CK19 IHC liver micrographs at 10x (A,C,E,G) and 20x (B,D,F,H)magnification from 32 week old $ILK^{lox/lox}$ (A,B,E,F) or hepILK-KO (C,D,G,H) mice maintained on a chow (A-D) or HF (E-H) diet. **I-L)** Representative Ki67 IHC liver micrographs at 20x magnification from 32 week old $ILK^{lox/lox}$ (I,J) or hepILK-KO (K,L) mice maintained on a chow (I,K) or HF (J,L) diet. **M-P)** Representative adipophilin IHC with periodic acid Schiff co-stained liver micrographs at 20x magnification from 32 week old $ILK^{lox/lox}$ (M,O) or hepILK-KO (N,P) mice maintained on a chow (M,N) or HF (O,P) diet. Scale bar = 100 µm.

relating to cellular organization and interactions with the ECM. Kyoto encyclopedia or genes and genomes (KEGG) also curates a database of pathways representative of cellular processes and interactions in relation to health and disease. These pathways are somewhat more conceptually oriented. KEGG pathway analysis demonstrated upregulation of pathways related to integrin interactions and cell adhesion molecules, which is consistent with GO analyses (Table 3.7). Further support for the metabolic underpinnings of altered glucose homoeostasis in hepILK-KO mice at this age were significant downregulation of metabolic pathways including oxidative phosphorylation.

Consistent with the immense convergence of physical and metabolic characteristic of hepILK-KO mice with $ILK^{lox/lox}$ littermates between 6 and 18 weeks of age transcriptional profiles are largely similar in 18 week old chow-fed animals (Figure 3.9). RNA-sequencing of livers from 5 hour fasted, 18 week old $ILK^{lox/lox}$ and hepILK-KO mice showed far fewer differentially expressed genes (n=665; 263=up; 402=down) and the magnitude of differential expression was considerably less (Figure 3.9). With considerably fewer differences in transcriptional profiles the magnitude of overrepresentation in GO terms were considerably decreased (*p*-values of 3E-12 or greater vs. *p*-values of 3E-150 or greater in 6 week chow-fed GO analyses) (Tables 3.6 & 3.8). Despite decreased magnitude of transcriptional differences enrichment of GO terms remained fairly consistent compared with 6 week chow-fed mice. Upregulated GO terms encompassed aspects of the extracllular space and cellular interactions with this space. While downregulated GO terms were primarily indicative of metabolic shifts aspects of proteasomal function and proteins metabolism were more obvious in these mice. Only 10 KEGG pathways were detected as significant (*p*-value <0.001; 2 increased and 8 decreased) in the 18 week old chow-fed hepILK-KO mice. The focal adhesion pathway was one of the only increased pathways, which is likely due to feedback mechanism whereby cells are attempting to restore focal adhesion stability and function in the absence of ILK. The glucagon signaling KEGG pathway was significantly decreased in hepILK-KO livers from this comparison. We did not observe any differecens in

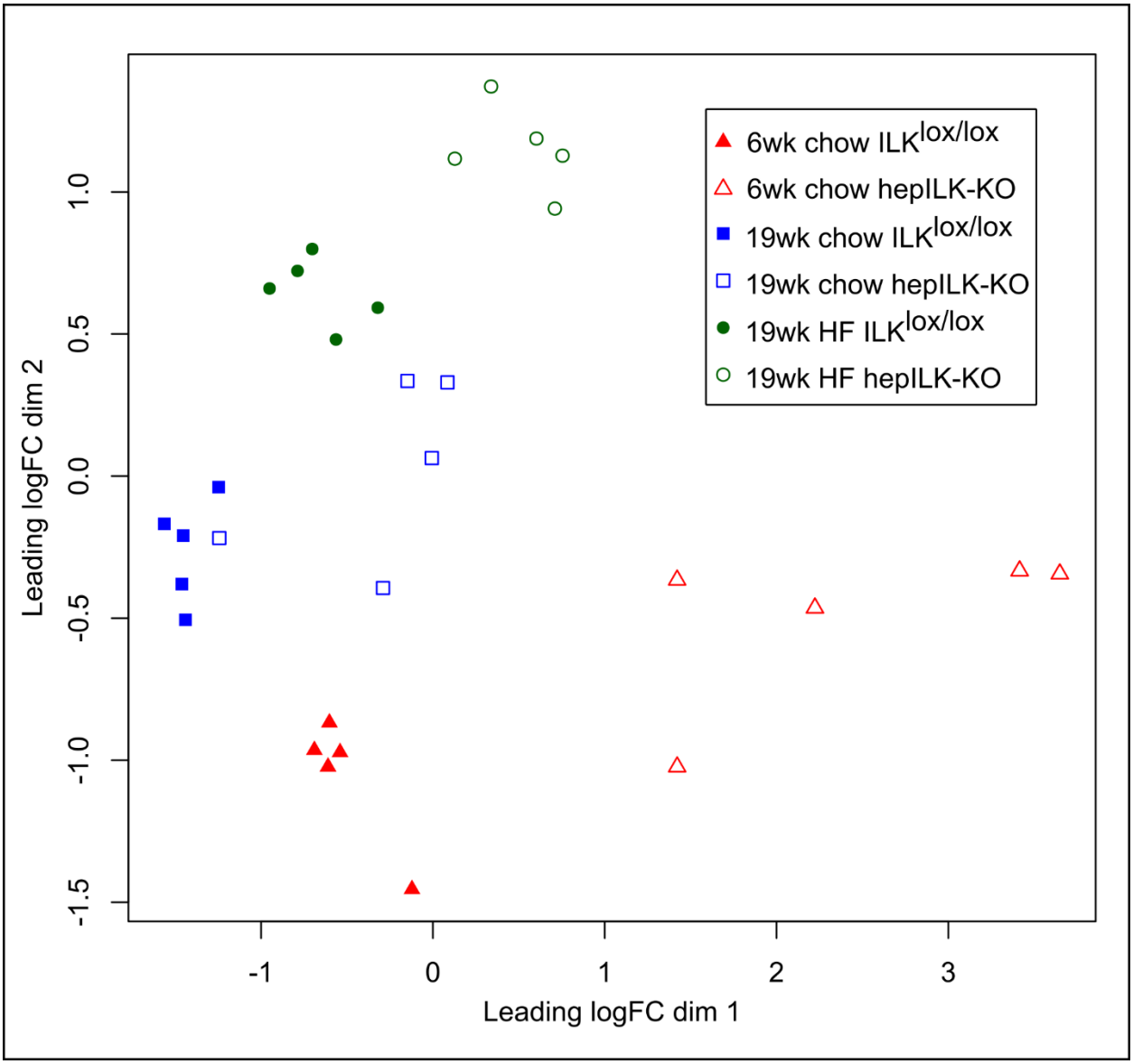

Figure 3.8- RNA seq results produce consistent grouping during multi-dimensional scaling (MDS) analysis. This chart spatially represents the similarity and dissimilarity relationships between the samples analyzed for RNA seq.

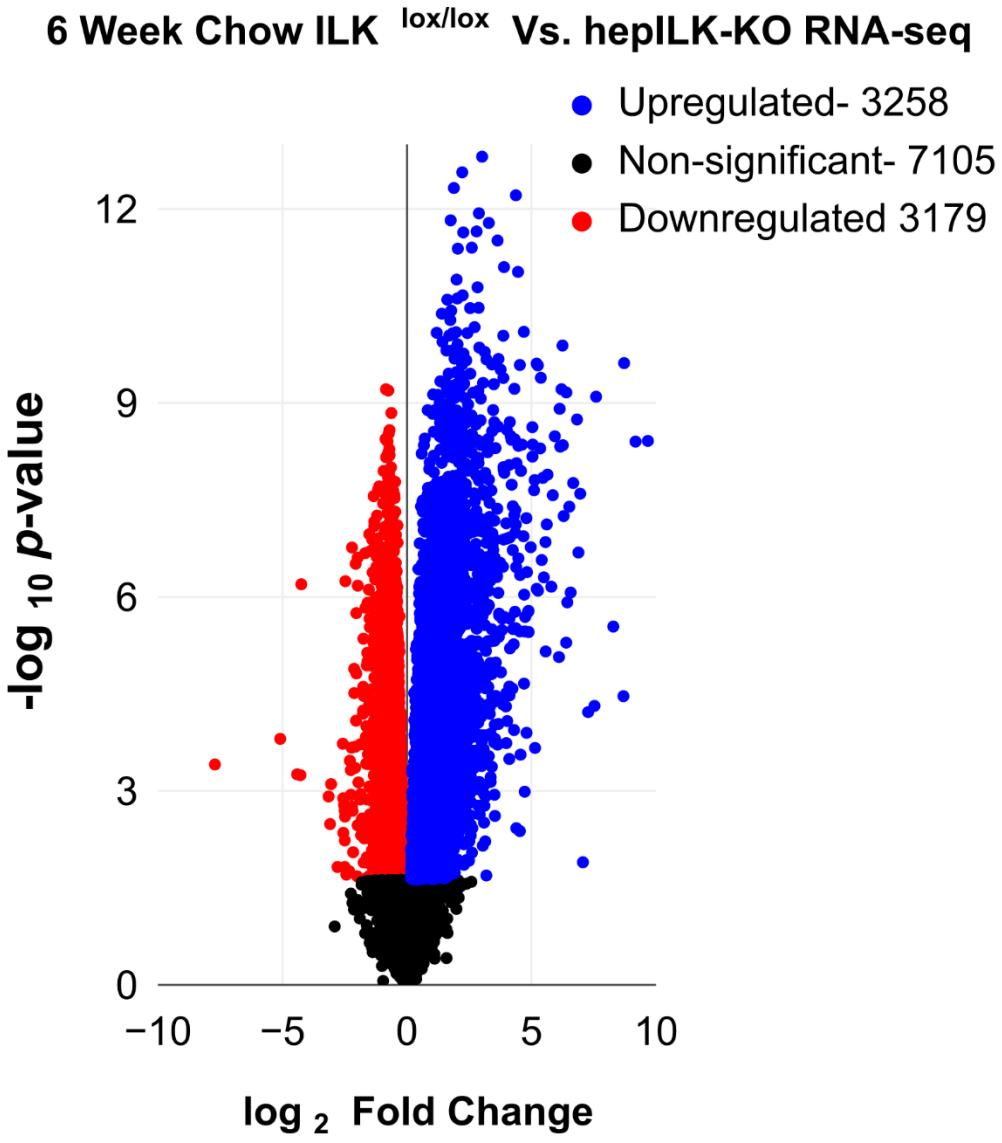

Figure 3.9- Volcano plot of quantified transcripts via RNA-seq analysis of liver from 6 week old chow-fed ILK$^{lox/lox}$ and hepILK-KO mice. Genes that were non-significantly altered between the two groups are indicated in black circles. Genes that were significantly increased ("upregulated") in hepILK-KO mice compared to controls are indicated in blue circles. Genes that were significantly decreased ("downregulated") in hepILK-KO mice compared to controls are indicated in red circles. The number of genes present in each category are indicated next to the distinguished category within the legend.

Table 3.6- Significantly increased and decreased GO terms in 6 week old chow-fed hepILK-KO mice.

Acc. Number	Term	Ont	p.Up
GO:0071944	cell periphery	CC	5.55E-104
GO:0005886	plasma membrane	CC	2.61E-96
GO:0023052	signaling	BP	2.92E-77
GO:0007165	signal transduction	BP	1.70E-72
GO:0007154	cell communication	BP	1.72E-72
GO:0050896	response to stimulus	BP	3.22E-71
GO:0007155	cell adhesion	BP	2.04E-65
GO:0022610	biological adhesion	BP	7.52E-65
GO:0044459	plasma membrane part	CC	2.86E-64
GO:0051716	cellular response to stimulus	BP	7.44E-59
GO:0048583	regulation of response to stimulus	BP	1.58E-56
GO:0032501	multicellular organismal process	BP	1.50E-54
GO:0002376	immune system process	BP	1.94E-54
GO:0006928	movement of cell or subcellular component	BP	1.08E-53
GO:0051239	regulation of multicellular organismal process	BP	3.99E-53
Acc. Number	**Term**	**Ont**	**p.Down**
GO:0005739	mitochondrion	CC	2.40E-150
GO:0044429	mitochondrial part	CC	6.05E-125
GO:0098798	mitochondrial protein complex	CC	7.52E-103
GO:0005743	mitochondrial inner membrane	CC	1.01E-96
GO:0019866	organelle inner membrane	CC	1.08E-86
GO:0031966	mitochondrial membrane	CC	3.93E-86
GO:0005740	mitochondrial envelope	CC	2.76E-85
GO:0044455	mitochondrial membrane part	CC	1.24E-69
GO:0055114	oxidation-reduction process	BP	3.12E-67
GO:0005759	mitochondrial matrix	CC	1.31E-58
GO:0044281	small molecule metabolic process	BP	1.34E-58
GO:0098800	inner mitochondrial membrane protein complex	CC	2.49E-57
GO:0031967	organelle envelope	CC	1.39E-54
GO:0031975	envelope	CC	1.39E-54
GO:0016491	oxidoreductase activity	MF	2.43E-48

The top 15 significantly altered GO terms with overrepresentation of increased (Top half) and decreased genes (Bottom half) in chow-fed 6 week old, 5 hour fasted hepILK-KO livers. Acc. Number = gene ontology accession number. Term= GO term. BP= Biological process. CC= Cellular component. MF= Molecular function. Ont= general gene ontology. p.Up= *p*-value for overrepresentation of increased genes in GO term. p.Down= *p*-value for overrepresentation of decreased genes in GO term.

Table 3.7- Significantly increased and decreased KEGG pathways in 6 week old chow-fed hepILK-KO mice.

Acc. Number	Pathway	P.Up
path:mmu04514	Cell adhesion molecules (CAMs)	5.80E-16
path:mmu04512	ECM-receptor interaction	7.54E-15
path:mmu04060	Cytokine-cytokine receptor interaction	7.54E-15
path:mmu04510	Focal adhesion	6.13E-14
path:mmu04810	Regulation of actin cytoskeleton	4.45E-13
path:mmu04640	Hematopoietic cell lineage	6.33E-11
path:mmu05140	Leishmaniasis	1.87E-10
path:mmu05414	Dilated cardiomyopathy (DCM)	2.85E-10
path:mmu04145	Phagosome	2.93E-10
path:mmu04360	Axon guidance	4.85E-10
path:mmu05410	Hypertrophic cardiomyopathy (HCM)	5.10E-10
path:mmu05323	Rheumatoid arthritis	7.59E-10
path:mmu05412	Arrhythmogenic right ventricular cardiomyopathy	1.54E-09
path:mmu04062	Chemokine signaling pathway	4.03E-09
Acc. Number	**Pathway**	**P.Down**
path:mmu01100	Metabolic pathways	1.79E-49
path:mmu00190	Oxidative phosphorylation	1.21E-35
path:mmu05012	Parkinson disease	1.29E-34
path:mmu04714	Thermogenesis	8.31E-28
path:mmu04932	Non-alcoholic fatty liver disease (NAFLD)	4.84E-23
path:mmu05010	Alzheimer disease	6.60E-23
path:mmu05016	Huntington disease	6.97E-20
path:mmu04146	Peroxisome	7.48E-20
path:mmu00280	Valine, leucine and isoleucine degradation	1.44E-18
path:mmu03050	Proteasome	1.25E-11
path:mmu00140	Steroid hormone biosynthesis	3.74E-11
path:mmu01200	Carbon metabolism	8.63E-11
path:mmu03010	Ribosome	3.51E-10
path:mmu04723	Retrograde endocannabinoid signaling	6.94E-10
path:mmu00630	Glyoxylate and dicarboxylate metabolism	1.81E-09

The top 15 significantly altered KEGG pathways with overrepresentation of increased (Top half) and decreased genes (Bottom half) in chow-fed 6 week old, 5 hour fasted hepILK-KO livers. Acc. Number = KEGG pathways accession number. p.Up= *p*-value for overrepresentation of increased genes in KEGG pathway. p.Down= *p*-value for overrepresentation of decreased genes in KEGG pathway.

glucose tolerance for hepIL-KO mice at this age on a chow diet and previous studies indicated no differences in insulin sensitivity of chow-fed mice at this age. However, as hyper-functionality of the glucagon pathways is known to contribute to aspects of hyperglycemia, insulin resistance, and T2D (264) development while hepILK-KO mice at this age are protected from hepatic insulin resistance. A relatively blunted capacity for glucagon action may contribute to a protection from hepatic insulin resistance in these mice.

18 week old $ILK^{lox/lox}$ and hepILK-KO mice fed a HF diet present with considerable amounts of obesity and glucose intolerance compared to chow-fed groups, but were not significantly different from each other (Figure 3.3). Despite these similarities HF-fed hepILK-KO mice at this age were relatively protected from hepatic steatosis. In line with differential hepatic phenotypes in hepILK-KO mice on a HF diet RNA-seq revealed considerably different transcriptional profiles of hepILK-KO mice compared to $ILK^{lox/lox}$ mice on a HF diet (Figure 3.10). While hepatic transcriptional profiles of 18 week old hepILK-KO and $ILK^{lox/lox}$ mice fed a HF diet were not as starkly different as 6 week old mice they were considerably more differential gene expression (n=1554; 804=up; 750=down) than chow-fed comparisons. GO analysis maintained the trend of upregulated enrichment of extracellular matrix and adhesion related terms (Table 3.10). Also present were a number of ribosomal components and processes indicating possible shifts in protein synthesis. Downregulated terms were primarily related to energy metabolism, but autophagy and organelle organization were also present. KEGG pathway analysis confirmed altered pathways relating to energy metabolism to be downregulated and aspects of cellular adhesion to be upregulated. Interestingly the pathway for PI3K-Akt signaling was also upregulated (Table 3.11). As these mice are known to have maintained hepatic insulin sensitivity on a HF diet (280) it is possible that maintained or elevated function of this pathway relative to HF-fed $ILK^{lox/lox}$ counterparts may contribute to this protection.

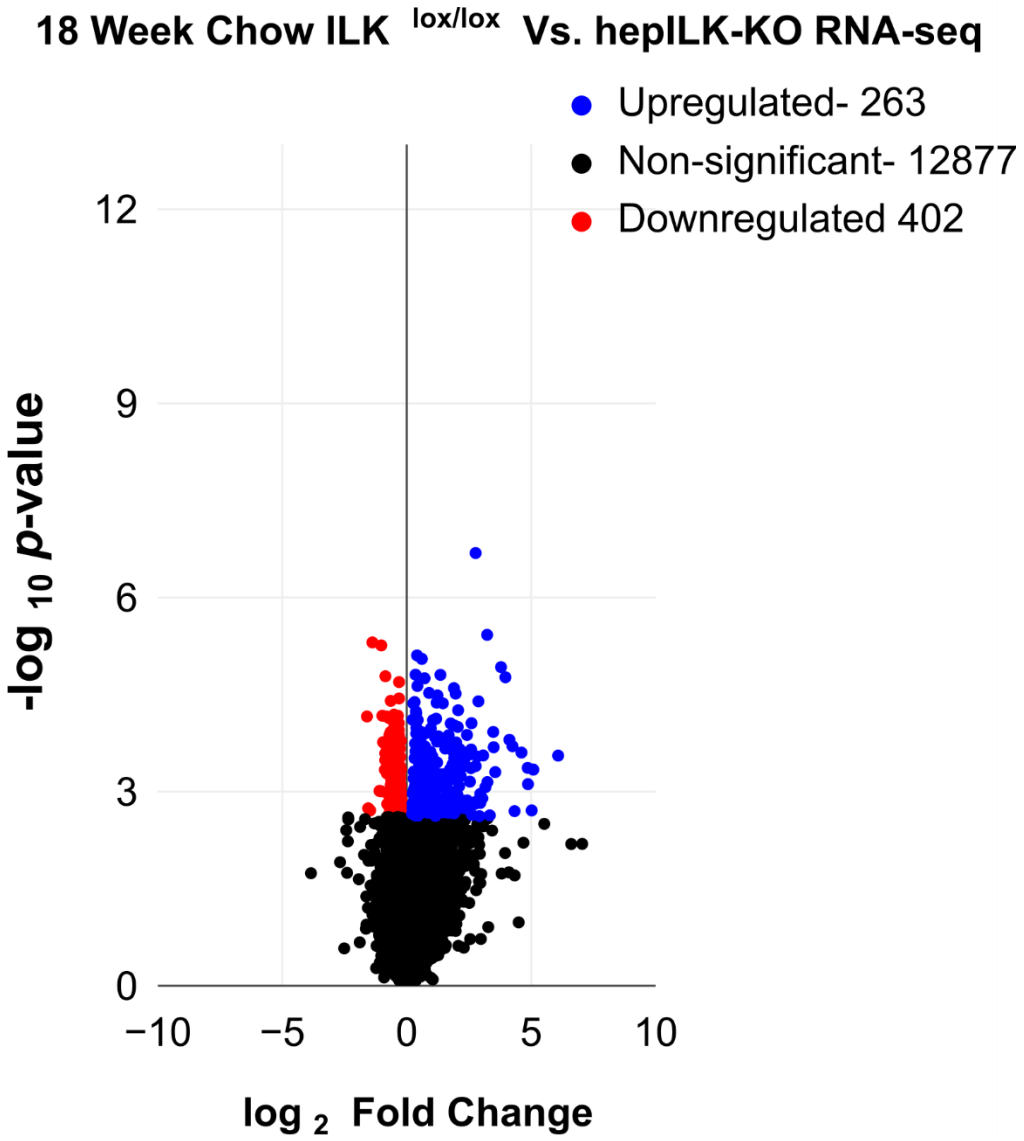

Figure 3.10- Volcano plot of quantified transcripts via RNA-seq analysis of liver from 18 week old chow-fed ILK$^{lox/lox}$ and hepILK-KO mice. Genes that were non-significantly altered between the two groups are indicated in black circles. Genes that were significantly increased ("upregulated") in hepILK-KO mice compared to controls are indicated in blue circles. Genes that were significantly decreased ("downregulated") in hepILK-KO mice compared to controls are indicated in red circles. The number of genes present in each category are indicated next to the distinguished category within the legend.

Table 3.8 - Significantly increased and decreased GO terms in 18 week old chow-fed hepILK-KO mice.

Acc. Number	Term	Ont	P.Up
GO:0005576	extracellular region	CC	5.23E-07
GO:0030018	Z disc	CC	2.28E-06
GO:0005615	extracellular space	CC	2.29E-06
GO:0043292	contractile fiber	CC	3.13E-06
GO:0009986	cell surface	CC	3.24E-06
GO:0031674	I band	CC	4.56E-06
GO:0009966	regulation of signal transduction	BP	4.98E-06
GO:0044421	extracellular region part	CC	5.57E-06
GO:0051049	regulation of transport	BP	5.89E-06
GO:0030016	myofibril	CC	6.76E-06
GO:0032879	regulation of localization	BP	7.69E-06
GO:0023052	signaling	BP	9.21E-06
GO:0005886	plasma membrane	CC	1.00E-05
GO:0030017	sarcomere	CC	1.13E-05
GO:0010959	regulation of metal ion transport	BP	1.27E-05
Acc. Number	**Term**	**Ont**	**P.Down**
GO:0043170	macromolecule metabolic process	BP	2.55E-12
GO:0005634	nucleus	CC	6.85E-12
GO:0006464	cellular protein modification process	BP	1.20E-11
GO:0036211	protein modification process	BP	1.20E-11
GO:0044260	cellular macromolecule metabolic process	BP	2.56E-11
GO:0043412	macromolecule modification	BP	5.84E-11
GO:0044267	cellular protein metabolic process	BP	2.28E-10
GO:0140096	catalytic activity, acting on a protein	MF	4.02E-10
GO:0004842	ubiquitin-protein transferase activity	MF	8.89E-10
GO:0005654	nucleoplasm	CC	1.07E-09
GO:0070647	protein modification by small protein conjugation	BP	1.70E-09
GO:0019787	ubiquitin-like protein transferase activity	MF	3.10E-09
GO:0016567	protein ubiquitination	BP	5.84E-09
GO:0019538	protein metabolic process	BP	2.20E-08
GO:0090304	nucleic acid metabolic process	BP	2.33E-08

The top 15 significantly altered GO terms with overrepresentation of increased (Top half) and decreased genes (Bottom half) in chow-fed 18 week old, 5 hour fasted hepILK-KO livers. Acc. Number = gene ontology accession number. Term= GO term. BP= Biological process. CC= Cellular component. MF= Molecular function. Ont= general gene ontology. p.Up= *p*-value for overrepresentation of increased genes in GO term. p.Down= *p*-value for overrepresentation of decreased genes in GO term.

Table 3.9- Significantly increased and decreased KEGG pathways in 18 week old chow-fed hepILK-KO mice.

Acc. Number	Pathway	P.Up
path:mmu04510	Focal adhesion	0.00015
path:mmu04974	Protein digestion and absorption	0.00049
Acc. Number	**Pathway**	**P.Down**
path:mmu04120	Ubiquitin mediated proteolysis	1.21E-08
path:mmu05166	Human T-cell leukemia virus 1 infection	0.0004
path:mmu04720	Long-term potentiation	0.00057
path:mmu04010	MAPK signaling pathway	0.0007
path:mmu04922	Glucagon signaling pathway	0.00085
path:mmu04662	B cell receptor signaling pathway	0.00089
path:mmu01522	Endocrine resistance	0.00093
path:mmu05161	Hepatitis B	0.00096

Significantly altered (*p*-value <0.001) KEGG pathways with overrepresentation of increased (Top) and decreased genes (Bottom) in chow-fed 18 week old, 5 hour fasted hepILK-KO livers. Acc. Number = KEGG pathways accession number. p.Up= *p*-value for overrepresentation of increased genes in KEGG pathway. p.Down= *p*-value for overrepresentation of decreased genes in KEGG pathway.

Discussion

ILK is a central hub of integrin signaling associated with cellular motility, organization, and adhesion to the ECM (212). Recently ECM and downstream integrin signaling systems have been associated with metabolically driven pathologies including insulin resistance, NAFLD, and T2D (152, 278). Previous studies demonstrated a role for ILK in the progression of hepatic insulin resistance during diet induced obesity (280). ILK is also a critical mediator of hepatic organization, injury response, transcription, and signaling (7, 17, 63, 65, 86). However, these functions of ILK are highly influenced by age (86). Studies linking ILK to hepatic insulin resistance focused on an individual time point. Metabolic stress and insulin resistance that are promoted by the obesogenic model are inherently dependent on age and length of diet exposure (77, 175). As ILK function is known to affect hepatic outcomes in an age-dependent manner it was necessary to assess the role of age in contributions of hepatocyte ILK to metabolic homeostasis and obesity related pathologic progression.

These studies demonstrate a clear effect of hepILK-KO on metabolism and glucose homeostasis early in life. These effects are age-dependent, but lead to differences in metabolic and pathologic trajectories throughout the life of the mouse. At 6 weeks of age hepILK-KO mice demonstrated a significant decrease in blood glucose and plasma insulin after a 5 hour fast. Lower insulin levels are indicative of an intact physiologic feedback response to decreased circulating glucose. Oral glucose tolerance was significantly increased even when accounting for decreased fasting glucose concentrations. Postabsorptive circulating glucose is primarily maintained through hepatic glucose production to meet glucose utilization requirements throughout the body (266). Given the hepatocyte-specific nature of our knockout a difference in hepatic capacity for glucose provision from glycogen or gluconeogenesis is hypothesized to underlie decreased circulating glucose. Increased glucose utilization may also drive decreased fasting glucose and increased glucose tolerance. While this is a hepatocyte-specific knockout the liver is known to communicate

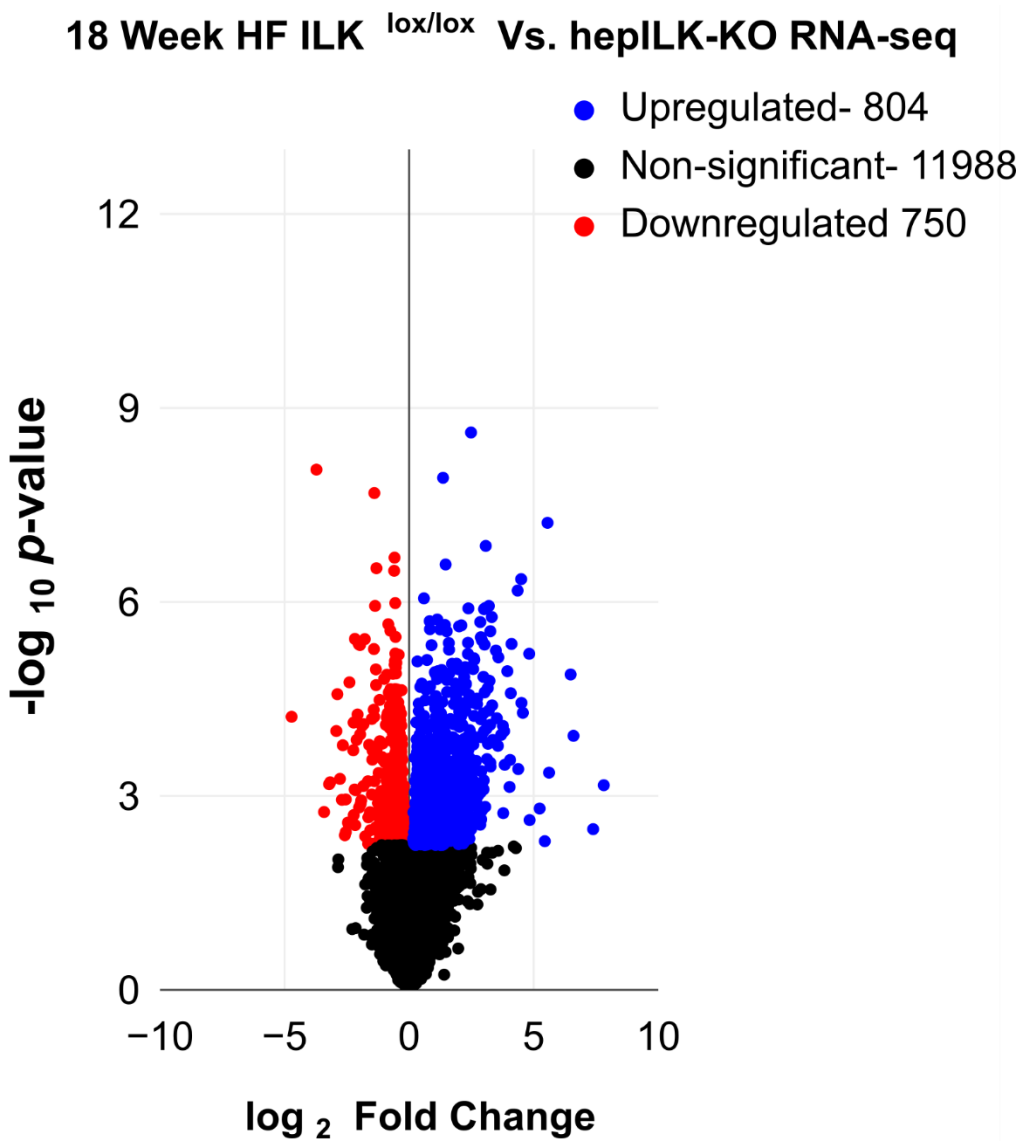

Figure 3.11- Volcano plot of quantified transcripts via RNA-seq analysis of liver from 18 week old HF-fed ILK$^{lox/lox}$ and hepILK-KO mice. Genes that were non-significantly altered between the two groups are indicated in black circles. Genes that were significantly increased ("upregulated") in hepILK-KO mice compared to controls are indicated in blue circles. Genes that were significantly decreased ("downregulated") in hepILK-KO mice compared to controls are indicated in red circles. The number of genes present in each category are indicated next to the distinguished category within the legend.

Table 3.10- Significantly increased and decreased GO terms in 18 week old HF-fed hepILK-KO mice.

Acc. Number	Term	Ont	P.Up
GO:0022626	cytosolic ribosome	CC	1.12E-31
GO:0005198	structural molecule activity	MF	1.26E-26
GO:0007155	cell adhesion	BP	4.97E-24
GO:0044421	extracellular region part	CC	6.25E-24
GO:0022610	biological adhesion	BP	1.28E-23
GO:0022625	cytosolic large ribosomal subunit	CC	7.75E-23
GO:0031012	extracellular matrix	CC	5.12E-22
GO:0005576	extracellular region	CC	5.62E-22
GO:0003735	structural constituent of ribosome	MF	7.20E-22
GO:0071944	cell periphery	CC	7.63E-20
GO:0005615	extracellular space	CC	2.90E-19
GO:0044391	ribosomal subunit	CC	4.18E-19
GO:0005886	plasma membrane	CC	1.43E-18
GO:0005840	ribosome	CC	3.08E-17
GO:0007154	cell communication	BP	1.38E-16
Acc. Number	**Term**	**Ont**	**P.Down**
GO:0012505	endomembrane system	CC	5.53E-08
GO:0044248	cellular catabolic process	BP	4.46E-06
GO:0003824	catalytic activity	MF	7.85E-06
GO:1901565	organonitrogen compound catabolic process	BP	8.86E-06
GO:0009056	catabolic process	BP	1.42E-05
GO:0007034	vacuolar transport	BP	3.26E-05
GO:0044444	cytoplasmic part	CC	4.22E-05
GO:0030242	autophagy of peroxisome	BP	4.49E-05
GO:0045053	protein retention in Golgi apparatus	BP	4.49E-05
GO:0055114	oxidation-reduction process	BP	4.67E-05
GO:0005794	Golgi apparatus	CC	5.00E-05
GO:0015980	energy derivation by oxidation of organic compounds	BP	5.01E-05
GO:0006112	energy reserve metabolic process	BP	6.65E-05
GO:0017016	Ras GTPase binding	MF	7.24E-05
GO:0051020	GTPase binding	MF	7.88E-05

The top 15 significantly altered GO terms with overrepresentation of increased (Top half) and decreased genes (Bottom half) in HF-fed 18 week old, 5 hour fasted hepILK-KO livers. Acc. Number = gene ontology accession number. Term= GO term. BP= Biological process. CC= Cellular component. MF= Molecular function. Ont= general gene ontology. p.Up= *p*-value for overrepresentation of increased genes in GO term. p.Down= *p*-value for overrepresentation of decreased genes in GO term.

Table 3.11- Significantly increased and decreased KEGG pathways in 18 week old HF-fed hepILK-KO mice.

Acc. Number	Pathway	P.Up
path:mmu03010	Ribosome	4.23E-27
path:mmu04512	ECM-receptor interaction	1.49E-08
path:mmu04510	Focal adhesion	3.43E-08
path:mmu04974	Protein digestion and absorption	7.80E-06
path:mmu05414	Dilated cardiomyopathy (DCM)	8.37E-06
path:mmu05410	Hypertrophic cardiomyopathy (HCM)	1.86E-05
path:mmu04514	Cell adhesion molecules (CAMs)	2.11E-05
path:mmu04360	Axon guidance	4.59E-05
path:mmu04810	Regulation of actin cytoskeleton	0.00012
path:mmu04151	PI3K-Akt signaling pathway	0.00018
path:mmu04640	Hematopoietic cell lineage	0.00022
path:mmu05412	Arrhythmogenic right ventricular cardiomyopathy	0.00044
path:mmu05332	Graft-versus-host disease	0.00069
path:mmu04672	Intestinal immune network for IgA production	0.0008
Acc. Number	**Pathway**	**P.Down**
path:mmu00340	Histidine metabolism	0.00057
path:mmu00640	Propanoate metabolism	0.00084
path:mmu04120	Ubiquitin mediated proteolysis	0.001

Significantly altered (*p*-value <0.001) KEGG pathways with overrepresentation of increased (Top) and decreased genes (Bottom) in HF-fed 18 week old, 5 hour fasted hepILK-KO livers. Acc. Number = KEGG pathways accession number. p.Up= *p*-value for overrepresentation of increased genes in KEGG pathway. p.Down= *p*-value for overrepresentation of decreased genes in KEGG pathway.

with peripheral organs and the central nervous system through several mechanisms (42, 183, 207). Secretion of the hepatokine FGF21 has been linked to increased energy expenditure (198) and carbohydrate utilization (288). Understanding factors affecting hepatic glucoregulation in hepILK-KO mice at 6 weeks of age will define the role of ILK in overall hepatic metabolism, but also in progression of insulin resistance. Therefore, this topic is explored in depth in the following chapter. Histologic evaluation of hepILK-KO livers at 6 weeks of age revealed fibrosis and biliary hyperplasia, but a lack of hepatocyte proliferation. Fibrosis and biliary hyperplasia were consistent with another hepatic ILK-KO model, but the lack of hepatocyte proliferation diverged from previous studies. We attribute this to differences in model design and characteristics discussed later in this section.

Maintaining hepILK-KO mice on a chow diet through 9 and 12 weeks of age revealed a gradual resolution of differences in fasting glucose, insulin, and glucose tolerance of hepILK-KO mice relative to $ILK^{lox/lox}$ littermates. However, maintaining these mice on a HF diet revealed an initial resistance to obesity induced hyperglycemia at 9 weeks and a resistance to weight gain during HF feeding through 12 weeks in hepILK-KO mice. The resistance to obesity was interesting as chow-fed hepILK-KO animals had completely resolved weight differenes from $ILK^{lox/lox}$ mice on a chow diet by 9 weeks of age. Several possibilities may underlie this obesity resistance in hepILK-KO mice. Obesity is the result of excess nutrient intake relative to energy expenditure. Therefore, obesity resistance may indicate a significant increase in energy expenditure of hepILK-KO mice and limited accumulation of adipose mass. Conversely a decrease in relative energy intake of hepILK-KO mice may also drive a resistance to obesity. Decreased drive for food intake would certainly limit the accumulation of excess adiposity in hepILK-KO mice. Alternatively an alteration in absorption of calories from food may also underlie a resistance to obesity progression. Assessment of energy balance and food intake in hepILK-KO mice would clarify the underlying contributors to initial obesity resistance in these mice.

Continuing analyses of chow and HF-fed mice to 18 weeks of age resulted in complete loss of any physical or metabolic differences assessed in hepILK-KO and $ILK^{lox/lox}$ mice. Despite convergence of these characeristics evaluation of hepatic histologic sections of hepILK-KO mice maintained on a chow or HF diet revealed novel phenotypes. Livers of chow-fed mice maintained their characteristic biliary hyperplasia, but were devoid of fibrosis. Additionally, hepILK-KO chow livers presented with hepatocyte hyperplasia with occasional adenoma formation (~40% of samples). Excessive proliferation has been documented in other models of epithelial cell ILK knockout from liver and other organs (7, 86, 241). This effect is hypothesized as a loss in contact inhibition signals in the absence of ILK likely due to diminished capacity for extracellular interaction sensing. Hepatocyte contact inhibition, in particular has been linked to the ability of cells to fully differentiate and express enzymes of glucose and lipid metabolism (162). Therefore, loss of contact inhibition may have direct impacts on hepatocyte metabolic function leading to a shift in hepatic glucoregulatory capacity.

Typically, the proliferation of liver epithelial cells in the sinusoidal and/or ductular compartments is indicative of an injured state (16, 146, 150). Hepatic injury is often accompanied by deposition of ECM and can progress to a pathologic level in fibrosis (139, 171). The alleviation of fibrosis in the presence of biliary and hepatocyte hyperplasia is somewhat paradoxical, but may indicate a characteristic of livers lacking hepatocyte ILK. Loss of ILK may result in an artificial decrease in pericellular ECM sensing by hepatocytes. Healthy livers have a limited ECM compartment that interacts with the extensive sinusoidal surface area of hepatocytes (21, 158). Therefore, receiving limited ECM signal input in absence of ILK may limit injury responses in hepatocytes that are known to further promote tissue damage and fibrosis.

In assessing livers of HF-fed hepILK-KO mice a distinct lack of steatosis was observed when compared to $ILK^{lox/lox}$ mice. This lack of steatosis occurs in the absence of any differences in obesity or glucose homeostasis. Additionally hepatocyte proliferation and adenoma formation were absent in all except one HF-fed hepILK-KO liver. While chow-fed livers of hepILK-KO mice

are hyperproliferative this is corrected in the presence of HF feeding. There is precedent for overnutrition to limit hepatocyte proliferation, but these states were often linked to hepatic lipid content and steatosis (54, 116, 153, 249). Perhaps relevant to our hepILK-KO model however is the known effect of hyper or euglycemia on limiting hepatic regenerative responses (117). While this is not a model of regeneration per se hyperglycemia may act independently within the liver to limit proliferative drive resulting in a beneficial effect for a model with hepatocyte hyperplasia and adenoma.

Progressing the mice to 32 weeks of age reinforces the metabolic and physiologic convergence of hepILK-KO mice with $ILK^{lox/lox}$ littermates regardless of diet. Histologically, hepILK-KO mice continue to present with biliary hyperplasia on a chow diet. Opposing the lack of steatosis at 18 weeks of age in HF-fed hepILK-KO mice, 32 week old (26 weeks of HF feeding) hepILK-KO mice present with an equivalent or greater amount of steatosis compared to $ILK^{lox/lox}$ mice. This represents a complete loss of steatotic protection between 18 and 32 weeks of age. In addition to the novel steatosis in hepILK-KO mice the lipid deposition patterning is deposited throughout the liver with no zonal preferences. $ILK^{lox/lox}$ mice maintain a zonal organization of lipid deposition with limited steatosis in hepatic zone 1. This is a typical phenotype in NAFLD as the zone 1 hepatocytes are exposed to higher oxygen content and engaging oxidative metabolism at higher rates. Lack of this zonation in hepIL-KO mice may represent a shift in metabolic zonation or a compromise to oxidative metabolism in hepatocytes of hepILK-KO mice.

In order to assess underlying drivers of the age-dependent effects of hepILK-KO on metabolism and steatosis we conducted a seris of RNA-seq analyses. Full transcriptional profiles were generated from livers of $ILK^{lox/lox}$ and hepILK-KO mice (6 week chow-fed, 18 week chow-fed, and 18 week HF-fed). Comparison of transcriptional profiles of 6 week old hepILK-KO mice with $ILK^{lox/lox}$ mice revealed profound differences. Most informative were GO and KEGG analyses revealing potential metabolic drivers of different hepatic glucoregulatory capacity. Pathways relating to mitochondrial function and oxidative metabolism were consistently downregulated in

hepILK-KO livers. In the field of obesity and NAFLD impaired mitochondrial function is often associated with glucose intolerance and insulin resistance. However, oxidative metabolism is also a prerequisitie of normal hepatic gluconeogeneic processes through provision of high energy phosphate bonds. Additionally, the TCA cycle is housed within the mitochondria and prvisions the necessary carbon for gluconeogenesis. Therefore, compromised mitochondrial structure or function may underlie decreased fasting glucose and enhanced glucose tolerance in 6 week old hepILK-KO mice.

RNA-seq analysis of livers from 18 week old $ILK^{lox/lox}$ and hepILK-KO mice on chow or HF diets revealed a general convergence of transcriptional profiles, which is conisitent with other characeristics described in these mice. For 1 week old chow-fed mice the numbers of differentially expressed genes was reduced by ~90%. This resulted in a limited enrichment of GO terms and KEGG pathways. Terms and pathways that were significant were consistent with themes extablished in 6 week old hepILK-KO mice, but to a lesser degree. Increased pathways related to cellular adhesion and ECM interactions. Decreased pathways generally related to oxidative metabolism. Of particular interest was a significant decrease in the enrichment of genes relating to glucagon signaling. Impariment in glucagon signaling would certainly contribute to deficient hepatic glucose output and/or oxidative metabolism. While HF-fed hepILK-KO mice at 18 weeks presented with more differentially expressed genes thatn their chow-fed counterparts the themes and pathways were largely similar.

Throughout analyses of hepILK-KO mice created using the alb-cre system similarities, but also critical differences were observed compared to liver ILK-KO mice created using the alf-alb-cre system of the Michalopoulos group. As in the alf-alb-cre model we observe a persistence of biliary hyperplasia in the alb-cre ILK-KO livers and a relative normalization of the transcriptional profiles by 18 weeks of age. It is notable that several phenotypes seen in alf-alb-cre ILK KO mice were not recapitulated in the alb-cre ILK-KO model including no changes in hepatocyte proliferation at 6 weeks of age and no change in liver to body weight ratio in mice aged to match

studies in the alf-alb-cre ILK-KO (0.045±0.001 in controls vs. 0.044±0.002 in alb-cre ILK-KOs). These differences are likely attributable to differences in promoter activation timing during development. The alf-alb-cre becomes active early in development with expression of cre detectable by embryonic day 10.5 (E10.5) (142). This causes cre expression and genetic KO prior to differentiation of biliary epithelial cells from the bipotential hepatoblast progenitor population (~E13.5) (157, 238), which give rise to hepatocytes later in development. This system results in cre expression and consequent KO in hepatocytes derived from the developing hepatoblast population, as well as in biliary epithelial cells. Influence of this phenomenon on previous alf-alb-cre ILK-KO models is acknowledged as a potential contributor to observed phenotypes (86). The alb-cre differs from alf-alb-cre as it does not express cre and delete ILK until differentiation of the albumin expressing hepatocyte population is complete (206, 274). Cre expression occurring after differentiation of hepatocytes from hepatoblasts combined with dynamic perinatal and postnatal changes to the hepatocyte population result in later onset and completion of hepatocyte-specific KO (between 3 and 6 weeks of age) (206). Benefits of this delayed KO are 1) an ability to mitigate *in utero* and developmental consequences of earlier gene KO and 2) a truly hepatocyte-specific cre expression profile. These benefits are a powerful conceptual distinction from previous studies using the alf-alb-cre lox system to delete ILK.

In summation, we have shown that hepatocyte ILK is required for establishment of normal glucose homeostasis in mice. Hepatocyte specific removal of ILK results in hyperglycemia

Chapter IV

HEPATOCYTE ILK IS REQUIRED FOR NORMAL HEPATIC OXIDATIVE METABOLISM AND SUPPORT OF GLUCOREGULATORY FUNCTIONS

Aims

Results form Chapter III demonstrated a functional contribution of hepatocyte ILK to glucose homeostasis, transcriptional profiles relating to metabolism, and the progressive sequelae of diet induced obesity in mice. In the absence of hepatocyte ILK the most profound effects are observed in 6 week old mice. Specifically, hepILK-KO mice have decreased circulating glucose, increased glucose tolerance, and a profound downregulation in transcriptional programming of mitochondria and oxidative metabolism. The goal of this chapter was to determine the metabolic and signaling mechanisms that underlie altered glucose homeostasis of 6 week old hepILK-KO mice. The hope is that discerning these mechanisms will progress our understanding of ILK as it pertains to metabolic pathologies such as insulin resistance and NAFLD.

Introduction

Studies from Chapter III aimed to unify the understanding of ILK in hepatic insulin resistance with previous studies implicating an age-dependent role for hepatic ILK in liver injury and regeneration. Results from this work demonstrated metabolically protective phenotypes in hepILK-KO mice including increased glucose tolerance, resistance to obesogenic weight gain, and limitation in hepatic steatosis. Among these metabolic alterations the changes to glucose tolerance and fasting glucose levels in hepILK-KO mice were among the most profound. These represent desirable endpoints for the treatment of dysregulation of hepatic glucose metabolism in multiple pathologic settings. Therefore, understanding the role of hepatocyte ILK in glucose

homeostasis of 6 week old mice is the focus of this Chapter. Assessment of hepatic transcriptional profiles of hepILK-KO mice at this age revealed decreased transcriptional signatures for mitochondria and oxidative metabolism. As such, it was hypothesized that ILK is required for establishment of functional hepatic oxidative metabolism, which reinforces hepatic glucoregulatory functions *in vivo*.

To test this hypothesis, 6 week old hepILK-KO mice were used in studies of oxidative function and glucoregulatory processes contributing to altered glucose homeostasis. Through this work we demonstrate a clear oxidative deficiency in hepILK-KO hepatocytes despite elevated indicators of mitochondrial content. This apparent incongruence is reconciled by markers of deficient autophagy or mitophagy. 6 week old hepILK-KO mice are able to maintain elevated steady state hepatic glucose output and whole body glucose utilization despite decreased circulating glucose. Decreased net glycogen synthetic capacity and hepatic energy charge drive an energetically inefficient paradigm of elevated hepatic glucose utilization in the face of deficient oxidative metabolism (256). We hypothesize that oxidative deficiency contributes to this energetic inefficiency and underlies protection from hepatic insulin resistance during obesity. Deficiencies in oxidative metabolism can create beneficial outcomes relating to insulin resistance and glycemic control during obesity. While this may appear counterintuitive decreased mitochondrial function is the very mechanism by which metformin, the most commonly used drug for insulin resistance, acts.

Experimental Approach

Studies in chapter IV were conducted using the control ($ILK^{lox/lox}$) and hepatocyte specific ILK knockout (hepILK-KO) mice described in chapter III. Chapter III established a profound alteration to glucose homeostasis and transcriptional programming of mitochondrial metabolism in hepILK-KO mice. Experiments in chapter IV were designed to assess the functional consequences of decreased mitochondrial transcription. Furthermore, these studies evaluated

contributions of hepatic glucoregulatory processes to altered glucose homeostasis and the metabolic underpinnings of these shifts.

Results

Hepatocyte ILK is necessary for hepatocyte oxidative metabolism

Hepatic compensation from 6 to 18 weeks was so effective that differences in fibrosis, glucoregulation, and the transcriptional profile, were diminished by 18 weeks of age. Thus, we focused on metabolic mechanisms underlying altered regulation of circulating glucose in hepILK-KO mice at 6 week of age. First, we assessed whether decreased expression of genes involved in mitochondrial structure and oxidative processes was linked to functional capacity at the cellular level. O_2 consumption in isolated primary hepatocytes without treatment (Routine), treated with oligomycin (Leak), or FCCP (ETS) was lower in hepILK-KO hepatocytes than in $ILK^{lox/lox}$ hepatocytes (Figure 4.1A). In hepILK-KO hepatocytes the ratio of O_2 consumption during oligomycin treatment to O_2 consumption in cells without treatment was higher. This reflects a greater fraction of O_2 consumption uncoupled from ATP production (Figure 4.1B). With apparent deficiencies in mitochondrial function of hepILK-KO hepatocytes, protein content of mitochondrial oxidative phosphorylation complexes and voltage-dependent anion channel (VDAC) were assessed as indicators of mitochondrial content and function. Interestingly, mitochondrial complexes were either unchanged (complexes II, III, and V) or increased (complex I and IV) (Figure 4.2A & B). VDAC protein was also significantly increased (~two-fold) in hepILK-KO cells (Figure 4.2A & B), indicating that hepILK-KO hepatocytes possess no deficiencies in the number mitochondria despite decreased functionality.

Mitochondrial function can be affected by differential management of the mitochondrial network. Mitochondrial fission and fusion markers were assessed to evaluate these processes.

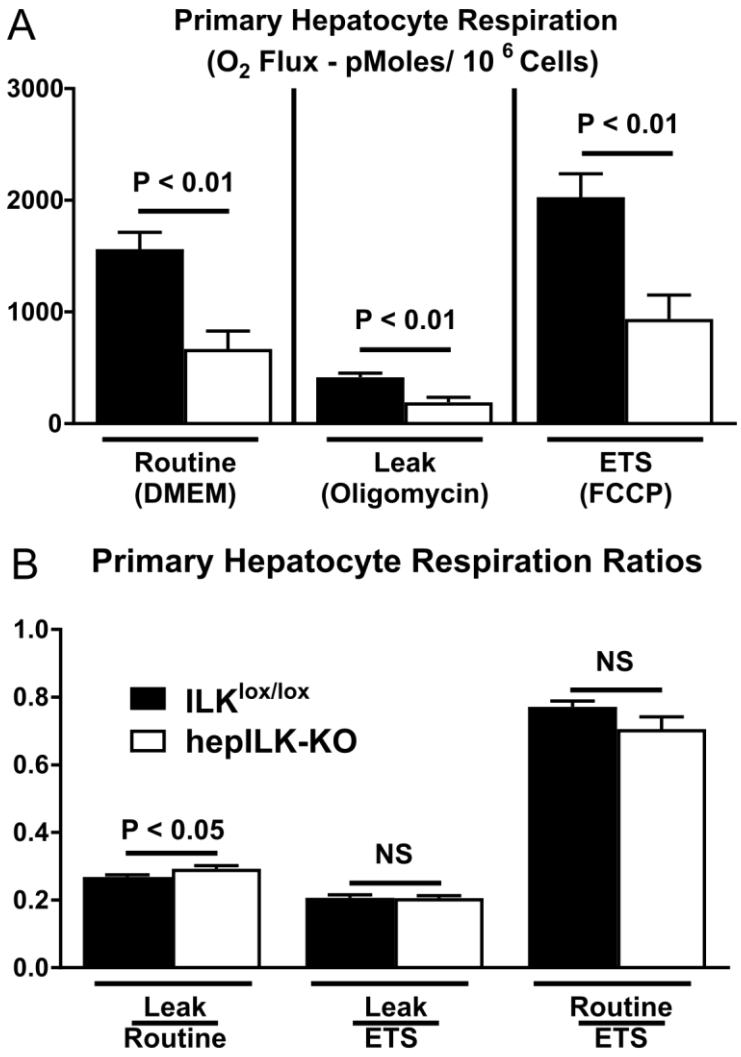

Figure 4.1- Oxygen consumption is significantly reduced in hepatocytes isolated from ILK-KO mice. A) Respiration of hepatocytes isolated from $ILK^{lox/lox}$ (n=6) or hepILK-KO (n=7) in basal media (Routine), in the presence of oligomycin (Leak), and in the presence of FCCP (ETS). **B)** Ratios of respiration rates in the three conditions represented in **(A)**. Data are mean +/- SEM.

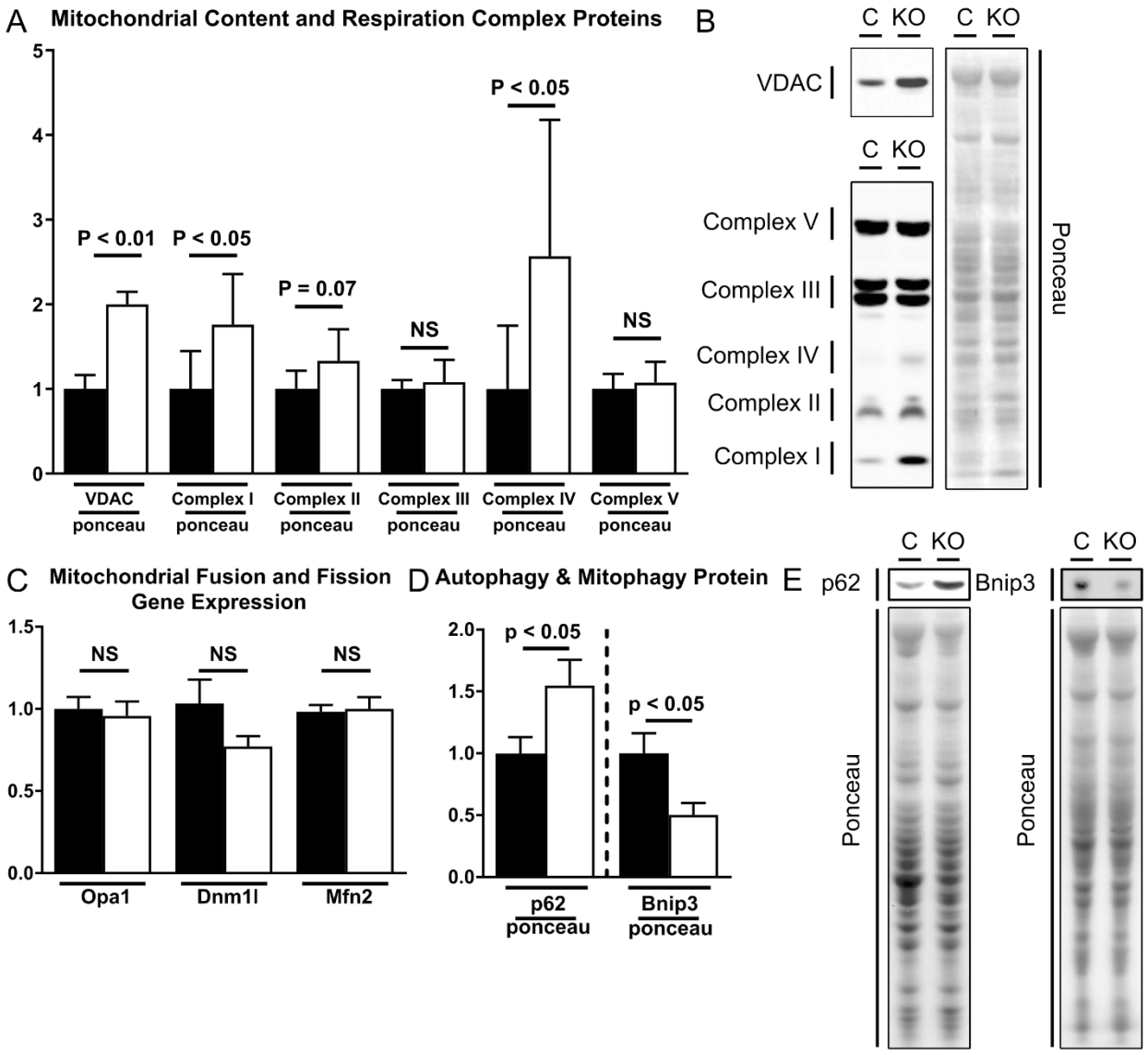

Figure 4.2- Increased mitochondrial content coupled with deficient autophagy and mitophagy contributes to decreased hepatocyte oxygen consumption of hepILK-KO mice. **A)** Quantification of VDAC and mitochondrial complex protein levels relative to Ponceau total protein stain from samples used in **(Figure 4.1A)**. **B)** Representative images of VDAC, mitochondrial complexes, and Ponceau total protein stain in **(A) C)** Gene expression of optic atrophy 1 (opa1), dynamin 1 like protein (dnm1l), and mitofusin 2 (mfn2) in samples used in **(Figure 4.1A)**. GAPDH was used as a control gene. **D)** Quantification of p62 and Bnip3 protein relative to Ponceau total protein stain in livers of $ILK^{lox/lox}$ (n=8) and hepILK-KO (n=7), which underwent MFA analysis. **E)** Representative western blots of p62 and Bnip3 protein as well as Ponceau staining quantified in **(D)**. Data are mean +/- SEM.

Transcript of the fission gene, dynamin 1-like (Dnm1l), and the fusion genes, optic atrophy 1/mitochondrial dynamin-like GTPase (Opa1) and mitofusin 2 (Mfn2) were not different between hepILK-KO and $ILK^{lox/lox}$ mice (Figure 4.2C). Protein content of autophagy (p62) and mitophagy (Bnip3) markers demonstrated an increase in p62 and a decrease in Bnip3 content in these livers (Figure 4.2D & E). These p62 and Bnip3 levels reflect decreases in autophagy and mitophagy, which can decrease mitochondrial function (163, 262).

Overall, these data reflect poorly functioning hepatocyte mitochondria in hepILK-KO livers. This impaired hepatic mitochondrial function is related to an altered transcriptional program and impaired autophagy/mitophagy.

Loss of hepatocyte ILK reduces whole-body EE and increases carbohydrate oxidation

Deficient mitochondrial function in the liver has the capacity to alter whole body metabolism. Substrate utilization at the whole body level was assessed using indirect calorimetry. EE (Figure 4.3A) was decreased in hepILK-KO mice at 6 weeks of age during both the light and dark phases (Figure 4.3B). EE remained significantly lower in hepILK-KO after accounting for differences in lean mass by ANCOVA (24hr $P<0.05$; Light Cycle $P<0.001$; Dark Cycle $P<0.01$). Therefore, EE in hepILK-KO mice was not due to lower lean mass and was driven by a genotype effect. Consistent with decreased EE, hepILK-KO mice consume less food and have lower EI overall (Figure 4.3C). EI matched controls during the light cycle and remained significantly decreased during the dark cycle (Figure 4.3D). This reflects more active feeding behavior during the light cycle as quantified by number and length of meals (Figure 4.3E & F). Overall, hepILK-KO maintain a positive energy balance (EB; the difference between EI and EE), which is no different from control animals (Figure 4.3G). While the RQ during the dark cycle was no different between $ILK^{lox/lox}$ and hepILK-KO mice, light cycle RQ was significantly elevated in hepILK-KO mice indicating increased utilization of carbohydrates as fuel (Figure 4.3H). The decrease in energy expenditure is related to a decrease in activity of hepILK-KO mice (Figure 4.3I & J). FGF21, which

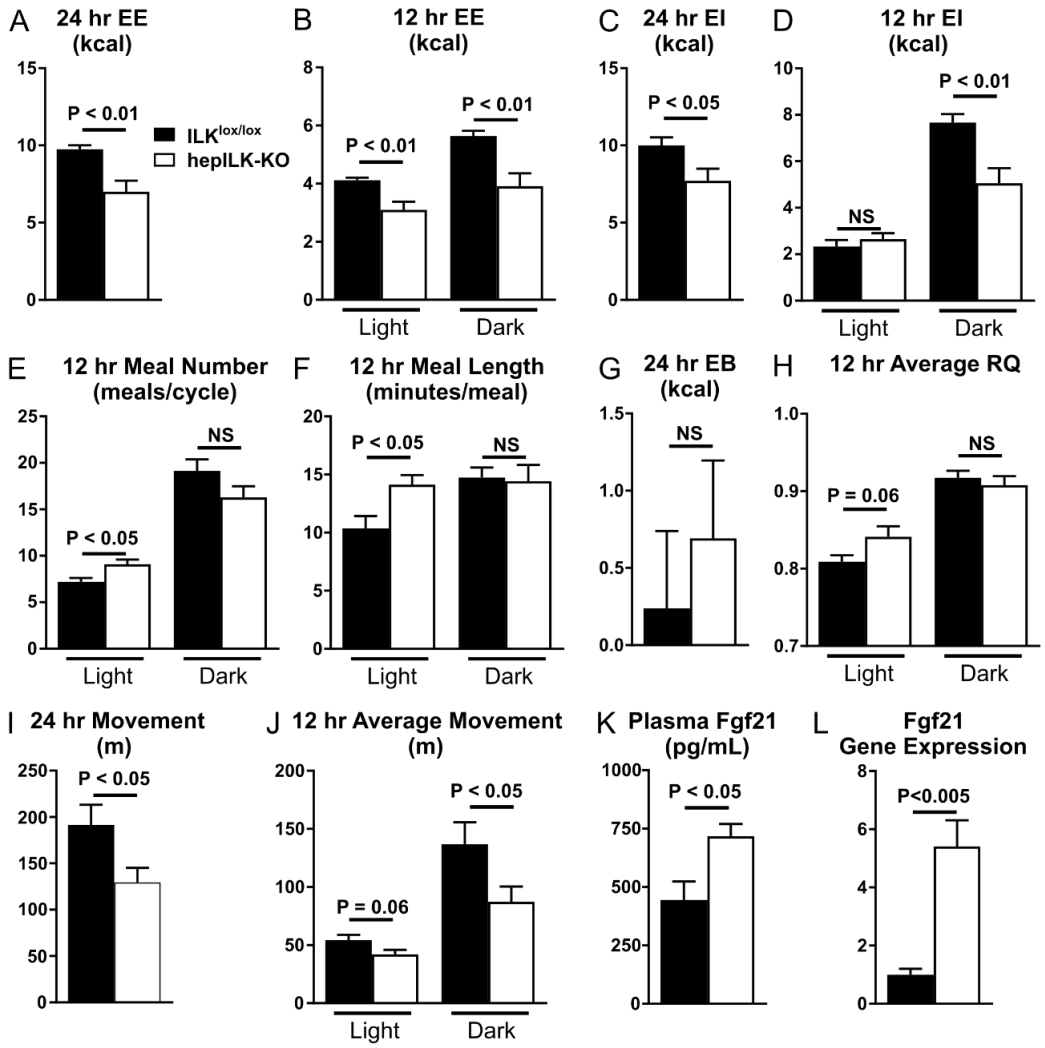

Figure 4.3- Energy expenditure is decreased and feeding behavior is altered in hepILK-KO mice. A) Average 24 hour energy expenditure (EE) of $ILK^{lox/lox}$ (n=8) and hepILK-KO (n=7) mice measured over a 7 day period. **B)** EE during 12 hour light and dark phase, $ILK^{lox/lox}$ (n=8) and hepILK-KO (n=7). **C)** 24 hour energy intake (EI) of $ILK^{lox/lox}$ (n=8) and hepILK-KO (n=7) mice. **D)** EI during 12 hour light and dark phase, $ILK^{lox/lox}$ (n=8) and hepILK-KO (n=7). **E)** 24 hour energy balance (EB = EI-EE) in ($ILK^{lox/lox}$ (n=8) and hepILK-KO (n=7) mice. **F)** Average number of meals per day during the light and dark phase, $ILK^{lox/lox}$ (n=8) and hepILK-KO (n=7). 24 hour energy intake (EI) of $ILK^{lox/lox}$ (n=8) and hepILK-KO (n=7) mice. **G)** Average time of each meal period during the light and dark phase, $ILK^{lox/lox}$ (n=8) and hepILK-KO (n=7). **H)** Average respiratory quotient during 12 hour light and dark phase, $ILK^{lox/lox}$ (n=8) and hepILK-KO (n=7). **I)** Average 24 hour movement of $ILK^{lox/lox}$ (n=8) and hepILK-KO (n=7) mice measured over a 7 day period. **J)** Movement during 12 hour light and dark phase, $ILK^{lox/lox}$ (n=8) and hepILK-KO (n=7). **K)** Concentration of FGF21 in plasma from $ILK^{lox/lox}$ (n=5) and hepILK-KO mice (n=7) after a 5 hour fast. **L)** Gene expression of FGF21 from livers of $ILK^{lox/lox}$ (n=6) and hepILK-KO (n=7) mice after a 5 hour fast. GAPDH was used as the control gene. Data are mean +/- SEM.

is secreted by the liver and is known to promote glucose utilization, was measured to gain insight into the possible mechanism by which hepILK-KO increased carbohydrate oxidation. Hepatic FGF21 transcript levels were increased (~5 fold) and plasma FGF21 was increased (~twofold) in 6 week-old hepILK-KO mice (Figure 4.3K & L). The increase in circulating FGF21 could explain the preference for utilization of carbohydrates in hepILK-KO mice as FGF21 stimulates carbohydrate utilization on extrahepatic tissues.

Hepatocyte ILK is necessary for hepatic glucoregulation, glycogen storage, and energy status

Given increased preference for carbohydrates, deficient hepatic mitochondrial function, and altered glucose homeostasis of hepILK-KO mice at 6 weeks of age, endogenous glucose production (EGP) and metabolic processes contributing to EGP were quantified using stable isotopes (Figure 4.4A). Based on reduced blood glucose after a 5 hour fast and impaired mitochondrial function we hypothesized that EGP would be decreased. Arterial glucose was decreased in the hepILK-KO mice consistent with previous fasting glucose data (Figure 4.4B). However, a paradoxical increase in EGP due to accelerated gluconeogenic pathway flux was observed (Figure 4.4C). As blood glucose was in a steady state, glucose utilization was increased equivalently. Increased glucose utilization from a reduced circulating glucose pool requires a marked increase in fractional glucose turnover (Figure 4.4D). No difference in glycogenolytic rates between genotypes were evident (Figure 4.4C). Increases in flux rates associated with the tricarboxylic acid cycle (TCA) did not reach significance (Figure 4.4E). Increases in gluconeogenic fluxes were not coupled to changes in the expression of gluconeogenic genes, Pck1 and G6pc (Figure 4.4F).

The absence of an increase in hepatic glycogenolysis occurred despite increased plasma glucagon ($p=0.0501$) (Figure 4.5A). As glucagon is known to affect amino acid uptake and metabolism to stimulate hepatic glucose output plasma amino acid profiles were assessed in

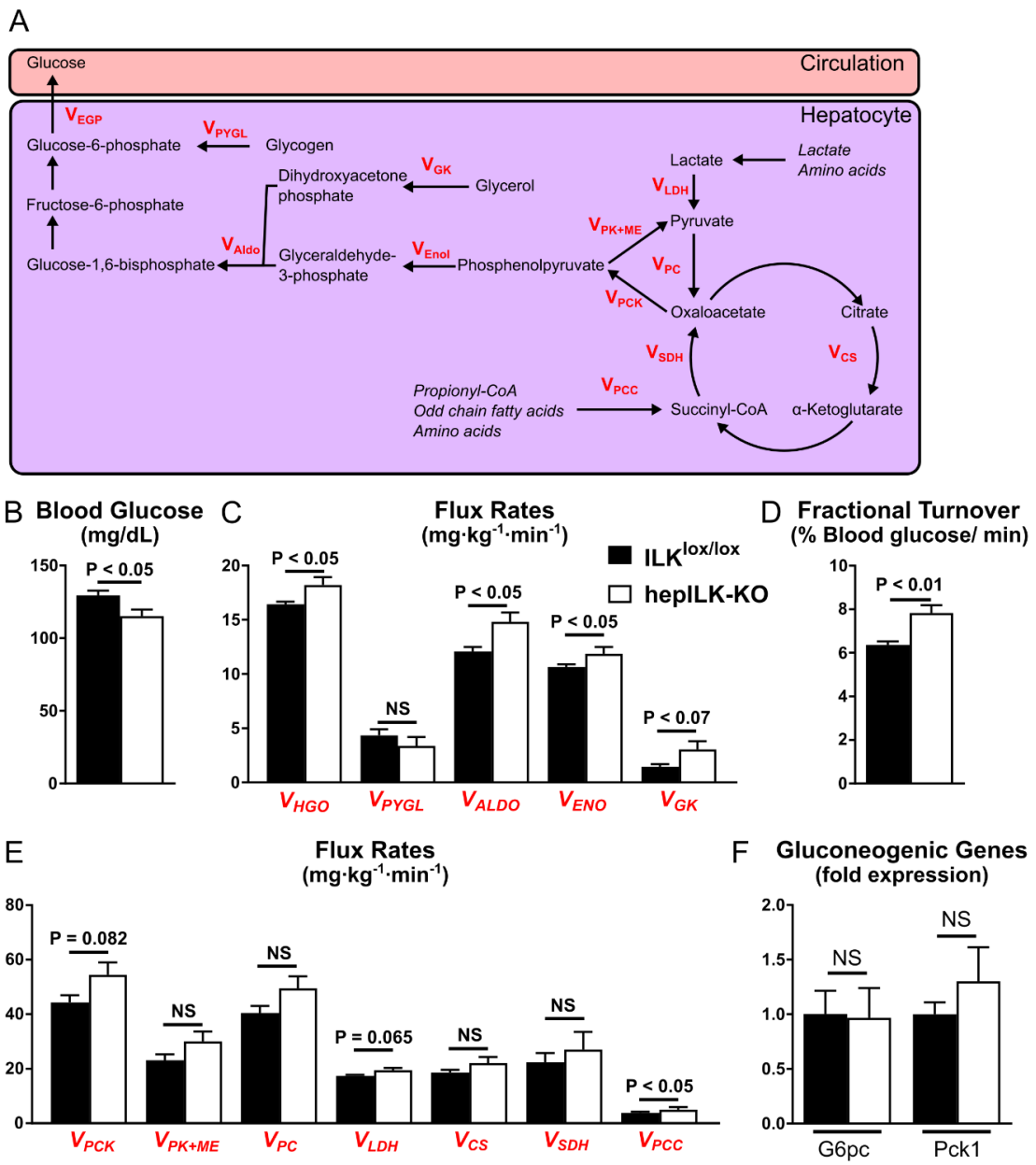

Figure 4.4- Hepatic glucose output is elevated due to increased gluconeogenesis in hepILK-KO mice. A) Graphical model of metabolic fluxes contributing to hepatic glucose output obtained from metabolic flux analysis (MFA). **B**) Average blood glucose concentration during steady state of MFA for $ILK^{lox/lox}$ (n=8) and hepILK-KO (n=7) mice. **C**) Rates of fluxes contributing to hepatic glucose production in $ILK^{lox/lox}$ (n=8) and hepILK-KO (n=7) mice modeled by MFA. **D**) Fractional turnover of the circulating glucose pool determined by dividing V_{EGP} by the blood glucose concentration at each time-point during MFA in $ILK^{lox/lox}$ (n=8) and hepILK-KO (n=7) mice. **E**) Rates of fluxes contributing to hepatic glucose production as well as the TCA cycling in $ILK^{lox/lox}$ (n=8) and hepILK-KO (n=7) mice modeled by MFA. **F**) Gene expression of gluconeogenic genes (glucose-6-phosphatase catalytic subunit- G6PC and phosphoenolpyruvate carboxykinase 1-PEPCK) from livers of $ILK^{lox/lox}$ (n=8) and hepILK-KO (n=7) mice after undergoing MFA. GAPDH was used as the control gene. Data are mean +/- SEM.

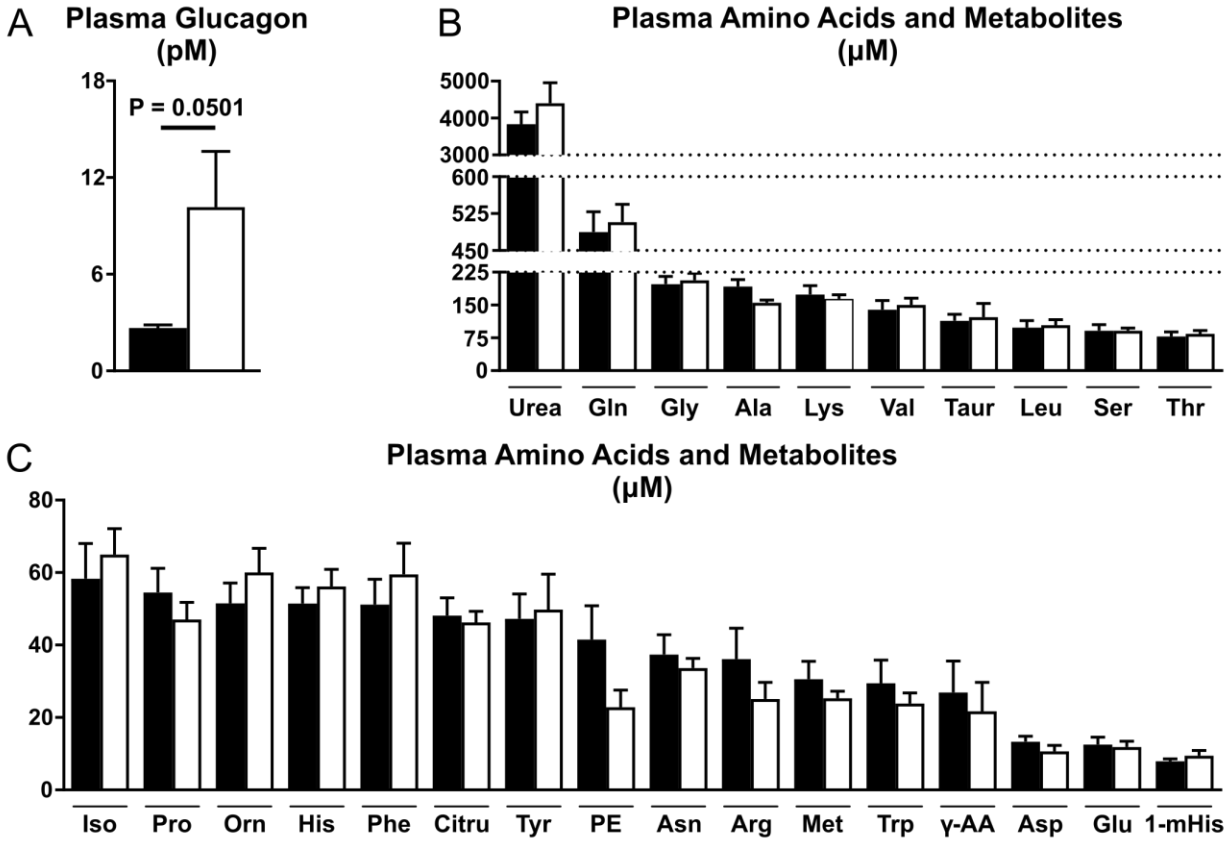

Figure 4.5- Glucagon is elevated in hepILK-KO mice, but circulating amino acids remain unchanged. A) Plasma glucagon concentrations in $ILK^{lox/lox}$ (n=7) and hepILK-KO (n=9) mice during metabolic flux analysis experiments. **B)** Concentration of higher level plasma amino acids and related metabolites in plasma samples taken at t=120 during MFA studies of 6 week old $ILK^{lox/lox}$ (n=8) and hepILK-KO (n=7) mice. **C)** Concentration of lower level plasma amino acids and related metabolites in plasma samples taken at t=120 during MFA studies of 6 week old $ILK^{lox/lox}$ (n=8) and hepILK-KO (n=7) mice. All amino acids are depicted with standard three letter abbreviations. The remaining metabolites are abbreviated as follows (Taur = Taurine; Orn = Ornithine; Citru = Citrulline; PE = Phosphoethanolamine; γ-AA = γ-Aminobutyric Acid; 1-mHis = 1-methyl-Histidine) Data are mean +/- SEM. * = $P<0.05$.

hepILK-KO mice. No significant changes in circulating amino acids or related metbaolites, such as urea, were observed in hepILK-KO mice (Figure 4.5B & C). The paradox of increased glucagon an elevated hepatic glucose output without aan increase in glycogenolysis led us to evaluate glycogen metabolism in hepILK-KO mice. Glycogen content in 5 hour fasted hepILK-KO mice was decreased to the point of near depletion (Figure 4.6A). Phosphorylation of glycogen synthase kinase 3β (GSK3β) was unchanged (Figure 4.6B). No changes in plasma lactate (Figure 4.6C) or β-hydroxybutyrate (Figure 4.6D) were observed despite lower hepatic glycogen. To determine the effectiveness by which hepILK-KO mice stored glycogen, fasting-refeeding studies were conducted. After 18 hours of fasting, blood glucose was reduced in $ILK^{lox/lox}$ mice to levels in hepILK-KO mice (Figure 4.6E). After 6 hours of refeeding, blood glucose rose similarly in both groups (Figure 4.6E). Hepatic lactate content (Figure 4.6F), as well as glucokinase and hexokinase activities (Figure 4.6G) were no different between hepILK-KO and $ILK^{lox/lox}$ livers after refeeding. However, net hepatic glycogen storage was ~50% lower in refed hepILK-KO mice (Figure 4.7A).To examine whether there was a deficit in the insulin-stimulated glycogen synthesis signaling cascade, levels of total and phosphorylated proteins (Akt, GSK3β, and GS) were assessed. Phosphorylation of Akt (ser^{473}) was similar in $ILK^{lox/lox}$ and hepILK-KO mice (Figure 4.7B & C). Additionally, the inhibitory Akt-dependent phosphorylation of GSK3β (ser^{9}) was similar in the two genotypes (Fig 9J & K). The ratio of GS phosphorylated at ser^{641} to total GS was decreased in hepILK-KO mice (Figure 4.7B & C). This GS phosphorylation site is GSK3β-dependent site and is inhibitory for GS activity. The decrease in phosphorylation of GS (ser^{641}) would thereby favor glycogen synthesis. The altered ratio of phosphorylated to total GS was primarily due to a ~fourfold increase in total GS protein in hepILK-KO livers (Figure 4.7B & C). A signal associated with low hepatic glycogen storage may feedback to upregulate GS protein expression.

As skeletal muscle can account for a significant portion of glucose disposal, we assessed the glycogen content and related signaling in gastrocnemius muscle in hepILK-KO and $ILK^{lox/lox}$

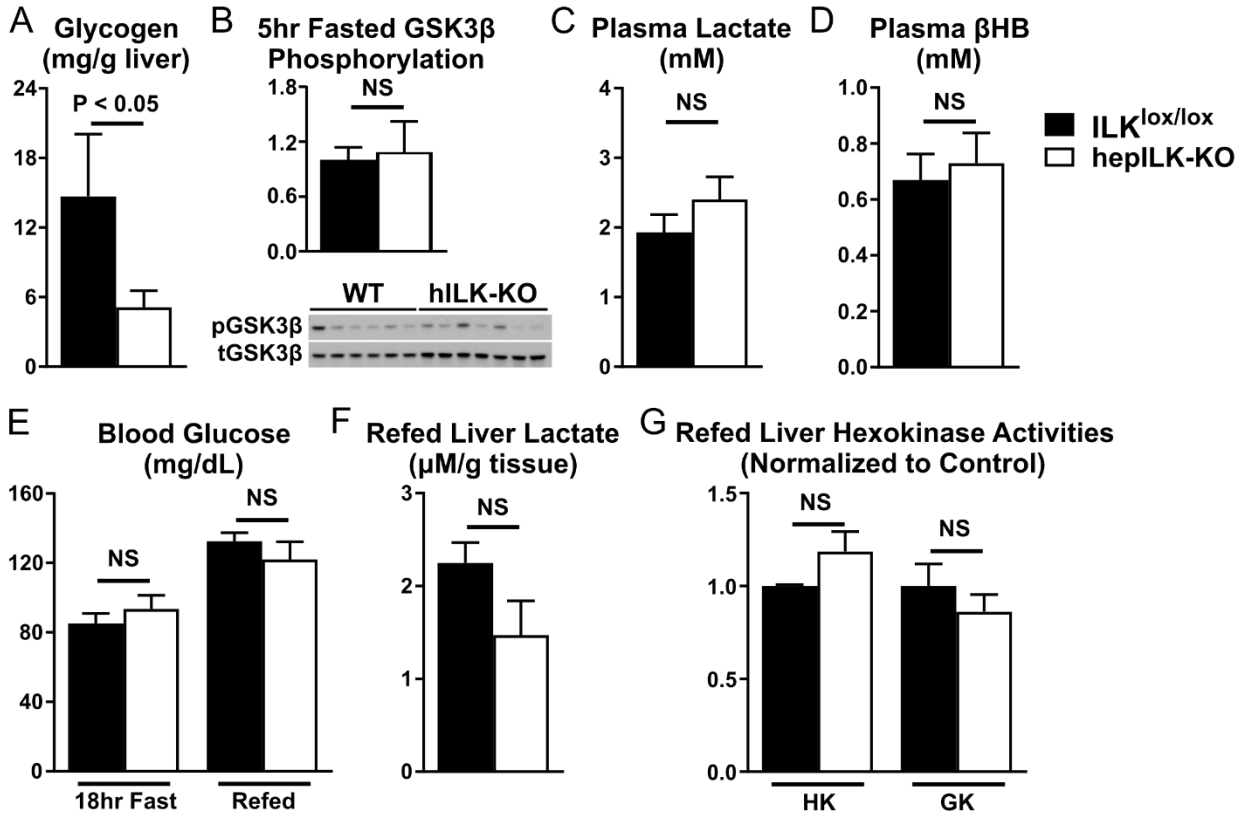

Figure 4.6- Hepatic glycogen is decreased in hepILK-KO mice. A) Hepatic glycogen content of $ILK^{lox/lox}$ (n=6) and hepILK-KO (n=6) mice after a 5 hour fast. **B)** Quantification of the ratio of GSK3β phosphorylated at ser^{9} to total GSK3β protein in livers of $ILK^{lox/lox}$ (n=6) and hepILK-KO (n=7) mice after a 5 hour fast. **C)** Plasma lactate concentration of $ILK^{lox/lox}$ (n=5) and hepILK-KO (n=5) mice after a 5 hour fast. **D)** Plasma β-hydroxybutyrate concentration of $ILK^{lox/lox}$ (n=5) and hepILK-KO (n=5) mice after a 5 hour fast. **E)** Blood glucose concentration of $ILK^{lox/lox}$ (n=4) and hepILK-KO (n=4) mice after an 18 hour fast and after 6 hours of ad libitum food access following the 18 hour fast. **F)** Liver lactate content of $ILK^{lox/lox}$ (n=4) and hepILK-KO (n=4) mice following the 6 hour refeed period. **G)** Enzymatic activities of glucokinase (GK) and all other hexokinases (HK) in livers of $ILK^{lox/lox}$ (n=4) and hepILK-KO (n=4) mice following the 6 hour refeed period.

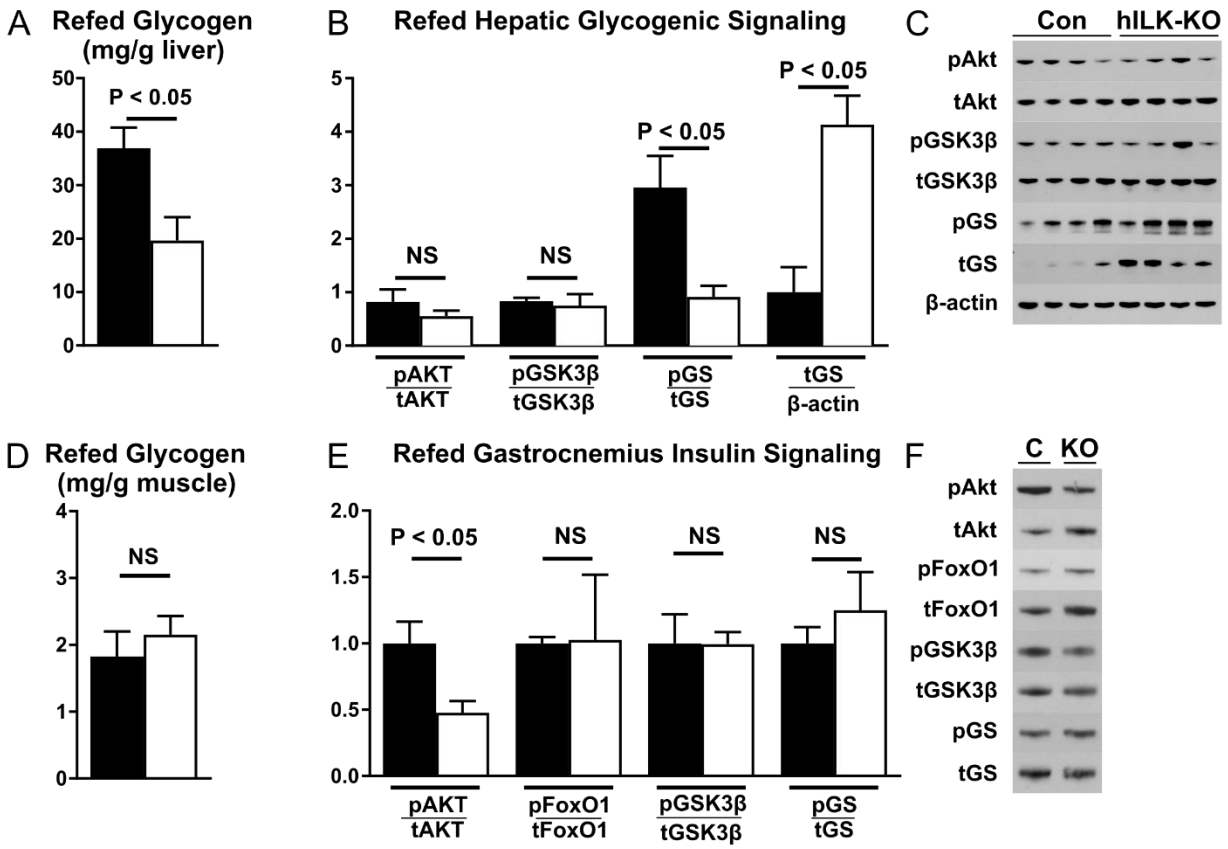

Figure 4.7 Net glycogen synthesis is decreased despite increased glycogenic signaling tone of hepILK-KO livers. **A)** Hepatic glycogen content of $ILK^{lox/lox}$ (n=4) and hepILK-KO (n=4) mice following the 6 hour refeed period. **B)** Quantification of densitometric ratios for designated phosphorylated and total proteins **(Panel C)**. Ratio of total GS protein to β-actin is also shown. **C)** Images of blots for Akt phosphorylated at ser^{473}, total Akt, GSK3β phosphorylated at ser^{9}, total GSK3β, Glycogen Synthase (GS) phosphorylated at Ser^{641}, total GS, and β-actin in livers from $ILK^{lox/lox}$ (n=4) and hepILK-KO (n=4) mice following the 6 hour refeed period. **D)** Gastrocnemius muscle glycogen content of $ILK^{lox/lox}$ (n=4) and hepILK-KO (n=4) mice following the 6 hour refeed period. **E)** Quantification of densitometric ratios for designated phosphorylated and total proteins **(Panel F)**. **F)** Representative images of blots for Akt phosphorylated at ser^{473}, total Akt, FoxO1 phosphorylated at ser^{256}, total FoxO1, GSK3β phosphorylated at ser^{9}, total GSK3β, Glycogen Synthase (GS) phosphorylated at Ser^{641}, and total GS in livers from $ILK^{lox/lox}$ (n=3) and hepILK-KO (n=4) mice following the 6 hour refeed period. Data are mean +/- SEM.

mice following refeeding. No differences were observed in glycogen content (Figure 4.7D) or phosphorylation of FoxO1, GSK3β, and GS in muscle (Figure 4.7E & F). However, a significant decrease in muscle Akt phosphorylation was observed in these mice (Figure 4.7E & F). Based on results from OGTTs, this may be a result of a reduced insulin response to feeding. Overall the hepatic signaling profile favors glycogen synthesis, even though net glycogen accumulation is reduced compared to $ILK^{lox/lox}$ mice. The net accumulation of glycogen could be attenuated due to simultaneous liver glycogen breakdown. In support of this possibility, the fractional glycogen turnover (the ratio of glycogenolysis to liver glycogen) was increased in hepILK-KO mice.

Hepatocyte ILK is necessary for energy status

Deficient oxidative function coupled with gluconeogenesis decreased energetic content of the adenine nucleotide pool. In line with this, ATP content was significantly reduced in livers of hepILK-KO mice with a concurrent increase in ADP and AMP (Figure 4.8A). Total adenine nucleotides were the same in both hepILK-KO and $ILK^{lox/lox}$ mice (Figure 4.8A). Increased AMP/ATP and decreased energy charge were observed in the liver of hepILK-KO mice (Figure 4.8B). Upon refeeding AMP and ATP in hepILK-KO mouse livers returned to concentrations in $ILK^{lox/lox}$ mice; while ADP was elevated (Figure 4.8C). Energy charge of refed hepILK-KO livers was restored to levels in $ILK^{lox/lox}$ mice (Figure 4.8D). Decreased energy charge in hepILK-KO mice caused a fourfold increase in AMPK phosphorylation after a 5 hour fast (Figure 4.8E & F). Phosphorylation of the downstream AMPK target protein, acetyl-CoA carboxylase (ACC), was also increased (Figure 4.8E & F) confirming that AMPK phosphorylation leads to functional activation. Changes in energy status and inhibitory phosphorylation of the lipogenic enzyme ACC prompted the quantification of hepatic and circulating lipids of hepILK-KO mice (Figure 4.9). No significant differences in hepatic cholesterol (Figure 4.9E), diglycerides (Figure 4.9C & D), or circulating NEFAs (Figure 4.9 F) were observed. Minor species of saturated triglycerides were

significantly decreased in hepILK-KO livers (Figure 4.9B), but was not accompanied by changes to total liver triglycerides (Figure 4.9A).

Discussion

Liver ILK signaling has been proposed as a therapeutic target for several disease states including insulin resistance (100, 102, 161, 280) yet there is little known about the physiology or metabolism of ILK signaling. These experiments, coupled with results from the previous chapter, demonstrate that hepatocyte ILK is required for glucose homeostasis through transcriptional and metabolic programming of the liver. Gene ontology analysis of RNA-seq data showed that liver-specific deletion of ILK caused an upregulation of genes involved in classic integrin functions such as ECM-receptor interactions, focal adhesion, and actin cytoskeleton regulation. On the other hand, these analyses revealed decreased expression of genes encoding proteins involved in mitochondrial structure and function. Differential transcriptional profiles in hepILK-KO mice were resolved by 18 weeks of age. ILK deletion resulted in functional defects characterized by reduced fasting blood glucose, plasma insulin, and more rapid disposal of an oral glucose load at 6 weeks of age. As with differential gene expression at 6 weeks, differences in the glucoregulatory variables were also resolved by 18 weeks. The liver was, for the most part, histologically, transcriptionally, and metabolically reconstituted over time. The results of these studies and the temporal organization of hepatocyte-specific knockout in the alb-cre system directed us to focus on metabolic regulation in 6 week old mice.

Consistent with the genetic reprogamming in 6 week old mice, hepatocyte mitochondrial O_2 consumption and whole body EE were diminished. Mitochondrial function was decreased even though protein content indicative of mitchondrial content were either unchanged (mitochondrial complexes II, III, and V) or increased (mitochondrial complexes I, IV, and VDAC) in hepatocytes

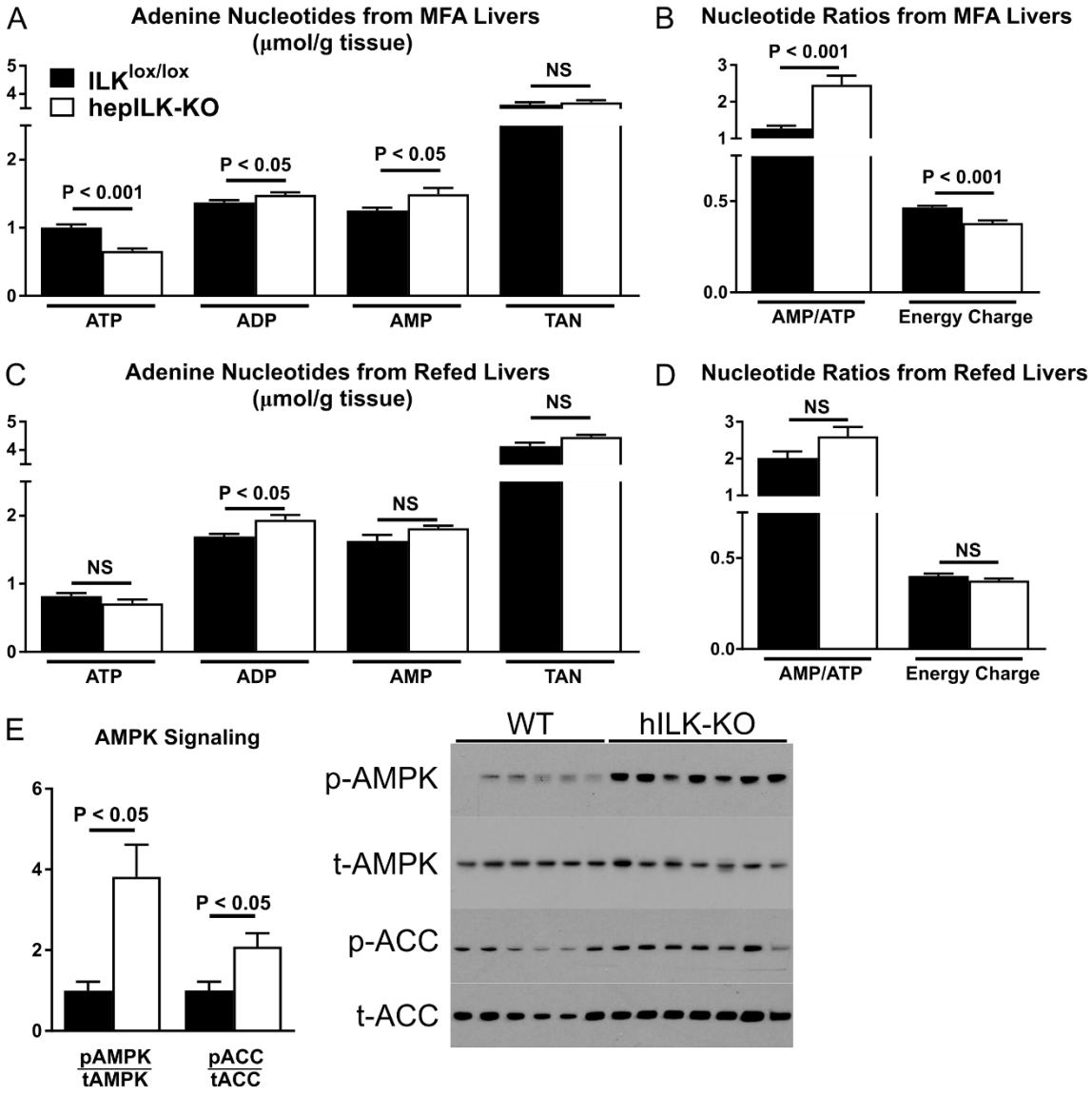

Figure 4.8- Hepatic energy charged is decreased and AMPK signaling is activated in hepILK-KO livers. A) Adenine nucleotide levels (ATP, ADP, and AMP) in livers from $ILK^{lox/lox}$ (n=8) and hepILK-KO (n=9) mice, which underwent MFA. **B)** Total adenine nucleotide (TAN) levels (sum of ATP, ADP, and AMP levels) in livers from $ILK^{lox/lox}$ (n=8) and hepILK-KO (n=9) mice, which underwent MFA. Ratio of AMP to ATP and calculated energy charge from the same liver samples. **C)** Adenine nucleotide levels (ATP, ADP, and AMP) in livers from $ILK^{lox/lox}$ (n=4) and hepILK-KO (n=4) mice, which underwent 18 hour fast and 6 hour refeed. **D)** Total adenine nucleotide (TAN) levels (sum of ATP, ADP, and AMP levels) in livers from $ILK^{lox/lox}$ (n=4) and hepILK-KO (n=4) mice, which underwent 18 hour fast and 6 hour refeed. Ratio of AMP to ATP and calculated energy charge from the same liver samples. **E)** Quantification of AMPK phosphorylated at Thr^{172} and ACC phosphorylated at Ser^{79} relative to their respective total proteins from livers of 5 hour fasted $ILK^{lox/lox}$ (n=6) and hepILK-KO (n=7). Data are mean +/- SEM.

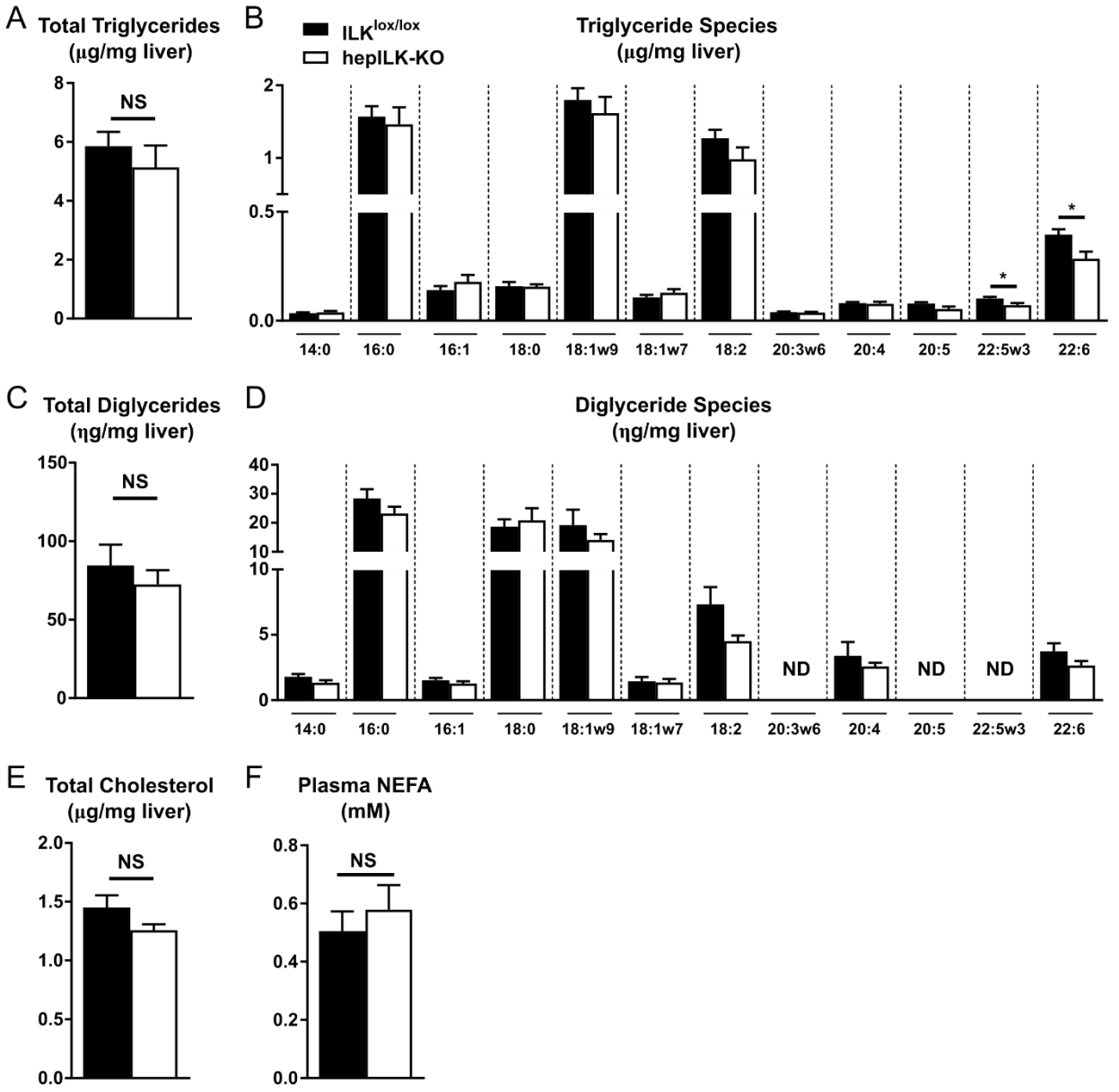

Figure 4.9- Hepatic and circulating lipid profiles are not changed in hepILK-KO mice. A) Total triglyceride content of livers from 5 hour fasted, 6 week old ILK$^{lox/lox}$ (n=7) and hepILK-KO (n=8) mice. **B)** Quantification of triglycerides side chain species from **(A)**. **C)** Total diglyceride content of livers from 5 hour fasted, 6 week old ILK$^{lox/lox}$ (n=7) and hepILK-KO (n=8) mice. **D)** Quantification of diglyceride side chain species from **(D)**. **E)** Total cholesterol content of livers from 5 hour fasted, 6 week old ILK$^{lox/lox}$ (n=7) and hepILK-KO (n=8) mice. **F)** Concentration of non-esterified fatty acids in plasma samples taken at t=100 during MFA studies of 6 week old ILK$^{lox/lox}$ (n=8) and hepILK-KO (n=7) mice.

of hepILK-KO mice. Moreover, hepatic TCA cycle fluxes were not different in the hepILK-KO livers. Results indicate a buildup of poorly functioning mitochondria that contributes to decreased respiration. Deficits in autophagy and mitophagy were reflected by increased p62 and decreased Bnip3 protein in hepILK-KO livers. Impairments in autophagy and mitophagy can contribute to mitochondrial dysfunction as it could underlie ineffective “pruning” of the mitochondrial network (164, 263).

Impaired mitochondrial function resulted in decreased energy charge. The increased AMP and decreased ATP, as observed in these studies, stimulate glycolysis by allosteric mechanisms and underlie a striking fourfold increase in AMPK activation. This signal alters the fate of glucose by inhibiting glycogen synthase (34) and activating glycolytic flux (167, 168). In this regard, the impaired capacity to store liver glycogen shown in the present study suggests glucose is directed to glycolysis. AMPK activation also stimulates pathways for substrate oxidation to counter the decreased energy state of the cell (83). However, in the presence of impaired mitochondrial function even a fourfold increase in AMPK was unable to fully compensate for impaired mitochondrial function in hepILK-KO livers. While AMPK activation stimulates lipid oxidation, comprehensive analyses revealed no reduction in circulating free fatty acids, total liver triglycerides, diglycerides, or cholesterol.

Glucose fluxes and the hepatic metabolic pathways contributing to it were assessed using $^{2}H/^{13}C$ metabolic flux analysis in conscious 5 hour fasted mice. Despite ILK deletion from the primary glucose producing organ, the reduced blood glucose in hepILK-KO mice was not due to an impairment in EGP but rather an increase in the removal of glucose, as measured by absolute and fractional glucose turnover rate. This finding was consistent with the greater glucose tolerance and elevated the light cycle RQ in hepILK-KO mice. Although blood glucose was reduced, overt hypoglycemia was prevented by accelerated gluconeogenic flux rates upstream of the pyruvate cycle (e.g. through enolase) in hepILK-KO mice. A reduction in glycogen stores

and a decreased capacity to store glycogen is consistent with impaired mitochondrial function and a greater reliance on glycolysis. The liver is simultaneously a glucose consuming and glucose producing organ even in the fasted state (268). We speculate that the liver may be the site of both increased glucose utilization and production. Analysis of skeletal muscle insulin signaling show that it is not increased making it an unlikely site for the added glucose disposal. Glucagon was elevated (p=0.0501) and insulin decreased in hepILK-KO mice in response to the reduced blood glucose. Increased glucagon to insulin ratio in hepILK-KO mice can potently stimulate gluconeogenesis even in the presence of a reduced hepatic energy state (266).

FGF21 hepatic gene expression and circulating levels were elevated in hepILK-KO mice. FGF21 increases EE (207, 228). However, the effects of FGF21 on EE were offset in the hepILK-KO mice by decreased physical activity. Energy balance in hepILK-KO mice was in steady state as EE and EI were equal at 6 weeks. The elevated FGF21 in the light phase is consistent with the relative preference for carbohydrate as a fuel as described above. This is consistent with increased glucose turnover and the actions of FGF21. Feeding behavior was also altered in hepILK-KO mice. Increased number of meals and length of meals during the light cycle were increased in hepILK-KO mice. The increase in light cycle feeding is consistent with the elevated circulating FGF21 in this phase (199).

Although blood glucose is reduced in hepILK-KO mice after a 5 hour fast, blood glucose was equal in $ILK^{lox/lox}$ and hepILK-KO mice after an 18 hour fast and rose equally during subsequent refeeding. Despite equal glucose loads, net hepatic glycogen storage was reduced by 50% in hepILK-KO mice. Impaired net glycogen storage occurred in the despite comparable glucokinase activities, metabolite levels, and a signaling profile that favors glycogen synthesis. Remarkably, GS protein was elevated nearly fourfold in hepILK-KO livers. Net hepatic glycogen storage is the difference between the rate of glucosyl unit incorporation into glycogen and the rate of glycogenolysis. Reduced net hepatic glycogen storage in the presence of a signaling

environment conducive to glycogen synthesis, suggests increased glycogen breakdown. Using MFA we show that glycogenolysis is equal in $ILK^{lox/lox}$ and hepILK-KO mice despite the fact that glycogen stores are reduced by ~70% in hepILK-KO mice, indicating the fractional glycogen turnover (e.g. glycogenolysis per glycogen mass) is increased in hepILK-KO mice. This supports the concept that impaired net liver glycogen storage is a result of concurrent glycogen synthesis and breakdown.

Fibrosis at 6 wks of age results from hepILK-KO regardless of the hepatic/hepatocyte cre system (86, 87). Effects of hepatic damage, fibrosis, and cirrhosis to altered glucose homeostasis have been well characterized (174, 194, 197). However, these conditions are typically associated with impaired glucose tolerance, hyperinsulinemia, and impaired insulin sensitivity. Results of our studies in 6 week old hepILK-KO mice reveal improved glucose tolerance and decreased insulin in addition to previously documented protection from insulin resistance during over-nutrition in mature mice (280). In the absence of acute signals from the fibrotic environment, hepatocyte oxidative mitochondrial function is still impaired. The liver is also a central hub for amino acid and urea metabolism. Distinct changes in circulating amino acids and related metabolites have been linked to fibrogenic severity (69, 112). Plasma profiles of amino acids and these other key metabolites were equivalent in hepILK-KO mice. The ability to sustain gluconeogenesis at an accelerated rate also indicates that liver damage is not severe. It may be that hepILK-KO limits the hepatocyte interpretive capacity of the fibrotic environment by limiting aspects of integrin sensing and signaling related to the extracellular matrix. While speculative, it may explain certain metabolic protections observed in hepILK-KO mice.

Previous studies have implicated inhibition of ILK signaling in treatment of a number of conditions, including insulin resistance (280), cancer (101, 102, 176, 292), and fibrosis (20, 294). This study defines the requirement for ILK in fundamental metabolic processes of the liver. The proposed role of ILK and the effects of hepatic-specific ILK KO is summarized in Figure 12. In the

present studies we show that although ILK deletion accelerates recovery of the liver from stress, ILK deletion compromises hepatic metabolism in healthy, young mice. Specifically, 6 week old hepILK-KO mice exhibit differential gene expression and functional changes in hepatic metabolism that lead to increased glucose removal, impaired net glycogen storage, impaired mitochondrial function, and increased gluconeogenesis.

In conclusion, our study establishes a role for ILK in maintaining liver metabolism and glucoregulatory functions. These effects likely contribute to the role of ILK in mediating insulin resistance during diet induced obesity. Furthermore, these findings inform our understanding of pathologic conditions affiliated with altered ECM and metabolism including non-alcoholic fatty liver disease. As such, it is important to consider the physiological and metabolic effects of ILK when targeting the inhibition of integrin-mediated signaling pathways and potentially invoking this metabolic influence for therapeutic potential in the future.

Working model of ILK in liver metabolism and glucoregulation

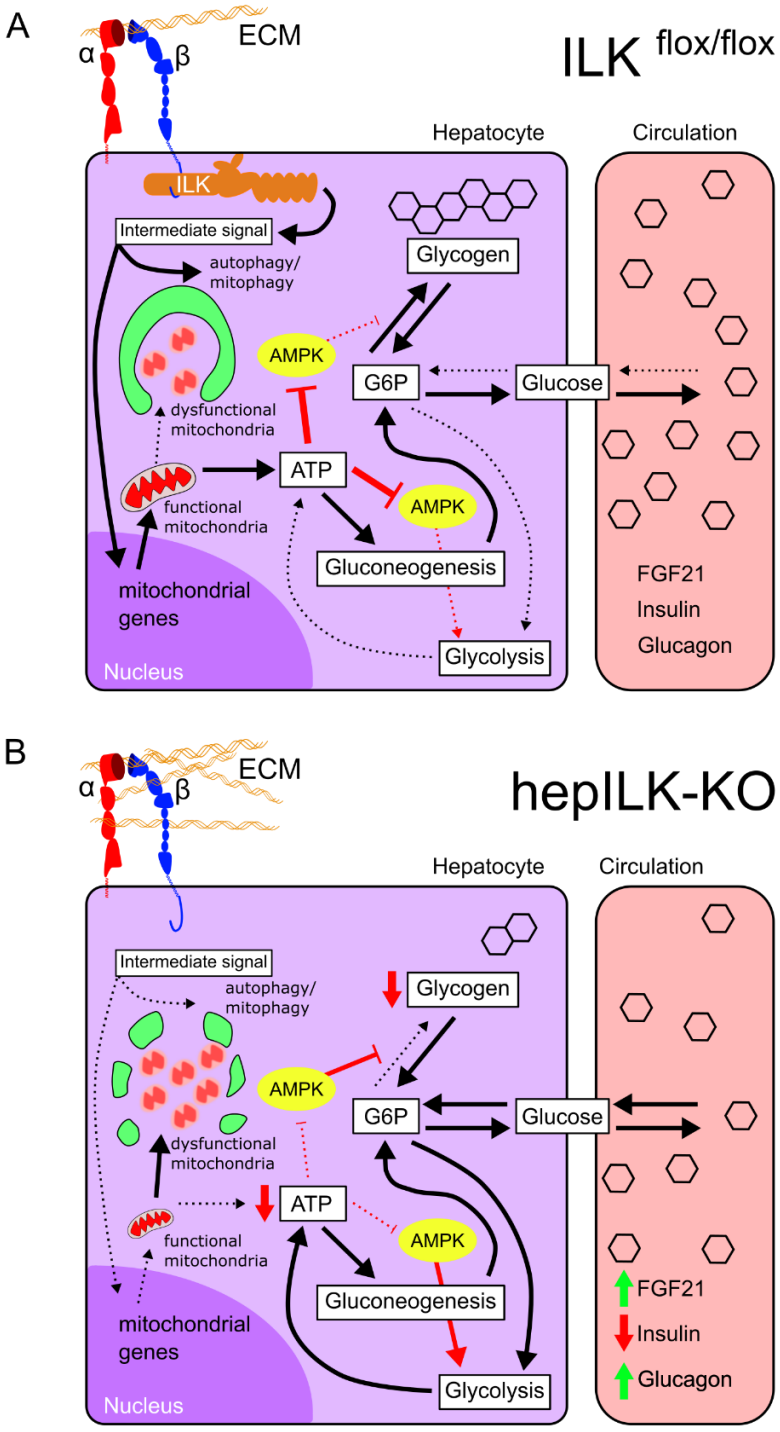

Figure 4.7- Summary figure for the role of ILK in hepatocyte metabolism and glucoregulation. A) Proposed model of ECM-integrin-ILK signaling and contributions to hepatic metabolism and glucoregulatory functions. **B)** Model of altered hepatocyte metabolism and glucoregulatory functions upon disruption of integrin signaling via hepILK-KO.

Chapter V

SUMMARY AND FUTURE DIRECTIONS

The data presented herein establish ILK as a critical mediator of hepatic metabolic responses in an age and diet-dependent manner. The convergence of ILK-mediated effects on glucose homeostasis, development of obesity, and indices of NAFLD with control mice in an age dependent manner are novel results. Extensive transcriptomic analyses provide insights on the mechanisms of ILK action. Additionally, these studies are the first to determine the hepatic influence of ILK on oxidative metabolism and energy charge within the liver. Chapter III demonstrates a role for ILK in maintaining glucose homeostasis in 6 week old mice while contributing to hyperglycemia, obesity progression, and steatotic development in older, HF-fed mice. Chapter III also defines transcriptional themes in mice lacking hepatocyte ILK independent of age and diet. Specifically, pathways related to cell adhesion are upregulated while pathways relating to mitochondria and oxidative metabolism are downregulated in livers of hepILK-KO mice. Chapter IV expands on these results to determine metabolic mechanisms contributing to altered glucose homeostasis in hepILK-KO mice. This dissertation creates a novel paradigm whereby ILK determines the quality of hepatocyte mitochondria and efficiency of oxidative metabolism to affect aspects of liver glucose regulation. These studies show how novel pathways controlled by ILK may have implications for hepatic diseases, such as NAFLD and insulin resistance, but also for other diseases with metabolic and fibrotic comorbidities.

Hepatic developmental programming determines the immense functional capacity of this organ. This programming has been utilized to develop research tools for in depth understanding of the liver. In this regard, multiple model systems have been implemented for the hepatocyte specific genetic modification of mice. One such model, the alf-alb-cre, was previously utilized in the knockout of ILK from hepatocyte, but may also have off target developmental and biliary cell

consequences. By utilizing the alb-cre system to perform a truly hepatocyte specific knockout of ILK these studies are the first to perform analyses parallel to an alternate developmental model cre-recombinase driven knockout. Differential characteristics seen in the alb-cre model system included lack of hepatocyte proliferation and hepatomegaly, which differ from the alf-alb-cre model used previously (7, 86). However, our studies recapitulated a number of histologic effects of the alf-alb-cre model, such as fibrosis and biliary hyperplasia. These phenotypes are important to consider when assessing aspects of metabolism, but may be even more relevant to the study of hepatic injury and regeneration.

Assessment of the age-dependent metabolic phenotypes of hepILK-KO mice demonstrated decreased fasting glucose levels and enhanced glucose tolerance of 6 week old hepILK-KO mice. We show a convergence of these metabolic characteristics with control mice by 12 weeks of age. These studies are some of a limited number that assess age-dependence of phenotypes relating to an *in utero* knockout system. Transient effects of genetic knockouts may be more common than is currently appreciated. It could even contribute to a failure to reproduce data in genetic mouse models. The liver may be particularly resilient against specific genetic knockout models as it has high regenerative and compensatory capacity (179–181, 251). This is the first time our lab has systematically looked at a phenotype over time other than by simple body weight measurement. We feel that perhaps this should be done with more regularity. We hope that this work will lead to the recognition that age is an important consideration for the study of physiology in KO mice.

Studies assessing hepILK-KO mice over the course of HF feeding were conducted in parallel with standard chow feeding. These experiments served to strengthen the understanding of age-dependent roles of ILK in metabolism while reinforcing the role of hepatocyte ILK during obesity from previously published work (280). Results show initial resistance to hyperglycemia, weight gain, and hepatic steatosis brought on by HF feeding relative to $ILK^{lox/lox}$ mice. At 32 weeks of age, hepILK-KO mice converge metabolically and physically with their control littermates.

Interestingly, at this time point hepILK-KO mice seem to transition to a state of less glucose tolerance and increased hepatic steatosis. This indicates a “flip” from metabolic protection of hepILK-KO early in obesity to metabolic compromise after the compounded metabolic stress of extended obesity. It is likely that a longer obesogenic paradigm would result in more sever glucose intolerance and NAFLD-like phenotypes in hepILK-KO mice.

Mice with a hepILK-KO on a chow diet demonstrated hepatocyte hyperplasia and adenoma formation in certain cases. This correlates with the role of ILK in cellular contact inhibition programming demonstrated in other organ systems (241). Interestingly, HF diet leads to loss of these phenotypes in hepILK-KO mice. In multiple studies, protein-protein interactions between ILK and *de novo* lipogenesis enzymes including acetyl-coA carboxylase and fatty acid synthase have been demonstrated (70, 265). Links have also been made between the inhibition of lipogenesis and development of cancer in liver (94, 193). ILK may play a role in maintaining hepatic lipogenesis, which coordinates metabolic and proliferative balances within the liver. Upon hepILK-KO this balance is disturbed leading enhanced proliferation in the basal state, but also in response to injury (7, 17). Augmentation of hepatic lipid balance in hepILK-KO mice by HF feeding diminishes hepatocyte proliferative drive in the hepILK-KO setting. Parsing out the mechanistic links between ILK, *de novo* lipogenesis, and hepatocyte proliferation represents a potential therapeutic avenue in addressing the spectrum of pathologies linked with NAFLD including steatosis and hepatocellular carcinoma.

This work utilized the unbiased approach of RNA-seq analysis to discover a link between hepatocyte ILK and the transcriptional programming of the liver relating to oxidative metabolism. These studies denoted stark transcriptional downregulation of oxidative metabolism and mitochondria in hepILK-KO mice at 6 weeks of age. *In silico* analysis of promoter sequence enrichment of significantly downregulated genes iin hepILK-KO livers (data not shown) demonstrated significant representation of sequence targeted by the transcription factor NRF1. Loss of this transcription factor from mouse liver results in hepatic neoplasia and development of

NAFLD phenotypes (289). NRF1 is also critical to maintained redox status and hepatocyte survival in developing mice (40). These phenotypes directly correlate with those observed in our hepILK-KO models. Therefore, it is possible that metabolic and cellular turnover phenotypes related to ILK expression are linked to the NRF1 transcription factor and its activity. In the future it will be essential to evaluate the role of NRF1 and other transcription factors responsible for such drastic transcriptomic alterations in hepILK-KO mice. The magnitude of transcriptomic changes decline with age of hepILK-KO mice. Livers from hepILK-KO mice at 18 weeks of age only have ~10% of the differentially expressed genes as 6 week old mice. However, 18 week old HF-fed hepILK-KO mice, which are resistant to steatosis, present with more pronounced differences in transcriptional profiles, ~2.5-fold increase, compared with analyses of chow-fed mice. While raw numbers of differentially expressed genes were variable based on age and diet several valuable connections were made possible with these studies.

RNA-seq, glucose homeostasis, weight gain on a HF diet, and histologic characteristics of hepILK-KO mice follow a consistent age-dependent paradigm. Specifically, hepILK-KO mice present with initially pronounced phenotypes, which gradually subside over time. This is not particularly surprising as the liver has a renowned ability to regenerate cellular mass and functional capacity in the face of deficiency (179, 251). However, application of provocative stimuli in the form of HF diet (280), surgical resection (7), or hepatotoxic challenge (17, 63, 65) reveals a clear difference in responses of mature mice lacking hepatic ILK. Therefore, it is critical to consider set and setting when dealing with various knockout models. Secondly, oxidative metabolism pathways were consistently downregulated in RNA-seq results from livers of hepILK-KO mice regardless of age or dietary intervention. We also know these mice are resistant to a number of metabolic pathologies relating to overnutrition. These results prompted the assessment of functional outcomes relating to mitochondria and oxidative metabolism to integrate ILK function with metabolic pathologies including insulin resistance and NAFLD.

Quantifying oxidative metabolism of isolated hepatocytes revealed the first documentation of functional deficits of hepatocyte oxidative metabolism in the absence of ILK. This demonstrated a clear connection between transcriptional program and functional capacity of these mice. Despite decreased transcription and function relating to mitochondria, several indicators of mitochondrial content were maintained or increased in hepatocytes of hepILK-KO mice. In conjunction with content, mitochondrial connectivity is a critical component of oxidative metabolism (22, 111). Processes mediating this connectivity are intimately linked to the actin cytoskeleton and are influenced directly by focal adhesion signaling from integrins (90, 143, 160). Given connections between focal adhesion dynamics and mitochondrial network processing we assessed aspects of mitochondrial fusion, fission, and autophagy. These experiments were the first indication that mitophagy may be deficient in the absence of ILK. This would support our findings related to deficient oxidative metabolism in the presence of excess mitochondrial content. Poorly damaged mitochondria that are not undergoing appropriate degradation can compromise mitochondrial networks and overall function. Going forward it is critical to assess the signaling mechanisms linking ILK to altered mitochondrial networking. Mitochondrial networking processes require dynamic physical organization and manipulation within the cell. As a result the actin cytoskeleton is intimately linked with appropriate function of fission, fusion, autophagy, and mitophagy. ILK is linked to cytoskeletal dynamics through its interactions with PINCH and other downstream proteins. Therefore going forward the ILK-PINCH signaling network will serve as a mechanistic target in assessing the role of ILK in mitochondrial dynamics.

We have shown decreased 5 hour fasted glucose levels, increased glucose tolerance, and deficient oxidative metabolism in 6 week old hepILK-KO mice. Therefore, hepatic glucose output and related metabolic fluxes were quantified to assess the hypothesis of deficient hepatic glucose output in hepILK-KO mice. Counter to this hypothesis was the discovery that hepatic glucose output was significantly upregulated in the postabsorptive state of hepILK-KO mice. This elevation in glucose output was derived from gluconeogenesis. This was in line with a trend

towards increased TCA cycling. By definition, increased hepatic glucose output must correspond to an equal increase in glucose utilization. This increased utilization of glucose occurs despite decreased circulating glucose levels, indicating increased fractional turnover of the glucose pool in hepILK-KO mice. Mice with hepILK-KO do possess the appropriately functioning endocrine control systems as they have elevated insulin during GTTs and also increase glucagon in response to reduced fasting glucose relative to $ILK^{lox/lox}$ counterparts. Glycogenolysis increases were absent despite increased glucagon in hepILK-KO mice. This represented a potential control point for altered glucose homeostasis.

Fasting/refeeding studies revealed deficient net hepatic glycogen synthesis in hepILK-KO mice. This decreased hepatic glycogen storage contributed to altered glucose homeostasis in hepILK-KO mice. This deficiency occurred despite cell signaling indicative of elevated hepatic glycogen synthesis. This may be an adaptive mechanism, whereby hepILK-KO livers scavenge blood glucose for glycogen synthesis during feeding. Perhaps contributing to an inability to store glycogen are decreased hepatic energy charge and AMPK activation in hepILK-KO livers. AMPK activation can directly inhibit glycogen storage (34). This energetic deficiency and the consequent signaling are likely a result of decreased oxidative metabolism. Inefficient processing of oxidative substrates would limit the ability to maintain hepatic energy during postabsorption and extended fasting. AMPK activation also stimulates the utilization of glucose through glycolysis (167, 168). Limited glycogen storage coupled to accelerated glycolysis would extract more circulating glucose and cause an increased glucagon to insulin ratio. This would then increase gluconeogenesis. Gluconeogenesis being an energetically demanding process would further compound energetic stress within the organ. This energetic inefficiency would be observed as a detrimental effect in healthy mice. However, energetic inefficiency may act beneficially in a model of overnutrition. This creates a sink for excess carbon intake limiting accumulation of lipid in the form of obesity or steatosis.

Overall these studies show a metabolic role for ILK in mice *in vivo*. Enhancing the direct clinical relevance of ILK in the liver, a set of studies by Dr. C. Robb Flynn at Vanderbilt has indicated a link between transitioning of steatosis to NASH with the activation of ILK signaling pathways in human liver (unpublished data). Therefore, continuing to elucidate the underlying connections of hepatic ILK with normal and pathophysiologic processes could have implications for preventing disease progression of NAFLD in humans. Consequently, this body of work further implicates the ECM-integrin-metabolism axis as contributors to and a therapeutic target. As such, we continue to move forward with models of altered hepatic integrin signaling as a means to better understand these connections.

Future directions for integrins in hepatic metabolism and insulin resistance

There are a number of possible future directions for the study of integrins in hepatic metabolism and insulin resistance. One critical research avenue we are pursuing is determining the definitive upstream integrin receptor input for ILK mediated effects on liver metabolism. Specifically, we have implemented a hepatocyte specific Integrin β1 (hepItgβ1-KO) knockout mouse to assess the role of this protein in glucose homeostasis.

Integrin β1 (Itgβ1) is a ubiquitously expressed integrin receptor subunit that directly binds to and is an upstream signal input for ILK (103, 155). We have begun assessing whether the effects of hepILK-KO on glucose homeostasis are due to an inability to transduce upstream integrin-ECM signaling. To do this a genetic hepatocyte knockout model of Itgβ1 is currently being studied. Similar to hepILK-KO mice, mice lacking hepatocyte Itgβ1 (hepItgβ1-KO) demonstrated lower body weights compared to Itgβ1$^{lox/lox}$ littermates. However, this difference did not reach statistical significance (Figure 5A). As was the case with hepILK-KO mice, hepItgβ1-KO did not affect % lean and % fat masses (Figure 5B & C). Fasting blood glucose was decreased in hepItgβ1-KO mice and the glucose tolerance was increased (Fig 5D & E) similarly to hepILK-KO mice (Figure 5E & Figure 3.1A). Fasting plasma insulin in hepItgβ1-KO mice was reduced

compared to Itgβ1$^{lox/lox}$ littermates. This decrease was similar to the decrease in fasting plasma insulin in hepILK-KO mice. (Figure 5F & Table 3.1). Overall the effects of hepItgβ1-KO on fasting glucose, fasting insulin, and glucose tolerance are nearly identical to the phenotype of hepILK-KO mice. Findings in the hepItgβ1-KO show that the results seen in the hepILK-KO mice on hepatic metabolism and glucose homeostasis is a result of disruption of ECM signals transmitted through the Itgβ1 subunit of integrin receptors. These studies will continue in order to further understand the role of integrins in normal and pathologic hepatic metabolism.

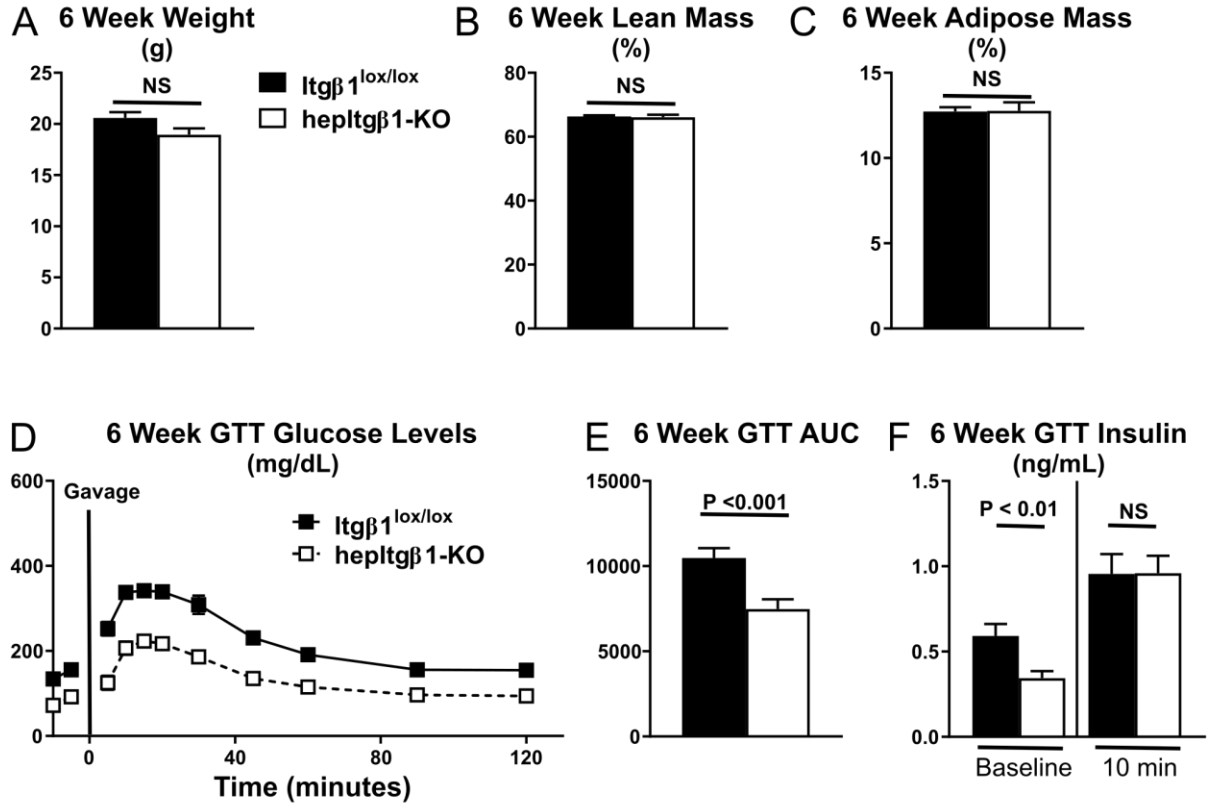

Figure 5.1- Hepatocyte Itgβ1 operates upstream of ILK to mediate glucose homeostasis. A) Body weight of Itgβ1lox/lox (n=17) and hepItgβ1-KO (n=14) mice at 6 weeks of age. B) Lean mass body composition of Itgβ1lox/lox (n=17) and hepItgβ1-KO (n=14) mice at 6 weeks of age. C) Adipose mass body composition of Itgβ1lox/lox (n=17) and hepItgβ1-KO (n=14) mice at 6 weeks of age. D) Blood glucose levels of 6 week old Itgβ1lox/lox (n=17) and hepItgβ1-KO (n=14) mice during oral glucose tolerance tests. E) Baseline corrected area under the glucose curves of 6 week old Itgβ1lox/lox (n=17) and hepItgβ1-KO (n=14) mice during oral glucose tolerance tests. F) Plasma insulin concentrations of 6 week old Itgβ1lox/lox (Baseline; n=17, 10 min; n=17) and hepItgβ1-KO (Baseline; n=11, 10 min; n=13) mice during oral glucose tolerance tests. Data are mean +/- SEM.

REFERENCES

1. **Abumrad NN**, **Cherrington AD**, **Williams PE**, **Lacy WW**, **Rabin D**. Absorption and disposition of a glucose load in the conscious dog. *Am J Physiol Metab* 242: E398–E406, 1982.

2. **Adeva MM**, **Souto G**, **Blanco N**, **Donapetry C**. Ammonium metabolism in humans. *Metabolism* 61: 1495–1511, 2012.

3. **Afgan E**, **Baker D**, **van den Beek M**, **Bouvier D**, **Chilton J**, **Clements D**, **Coraor N**, **Guerler A**, **Hillman-jackson J**, **Hiltemann S**, **Jalili V**, **Rasche H**, **Soranzo N**, **Goecks J**, **Taylor J**, **Nekrutenko A**, **Blankenberg D**. The Galaxy platform for accessible , reproducible and collaborative biomedical analyses : 2018 update. *Nucleic Acids Res* 46: 537–544, 2018.

4. **Almazroo OA**, **Miah MK**, **Venkataramanan R**. Drug metabolism in the liver. *Clin Liver Dis* 21: 1–20, 2017.

5. **Anders S**, **Pyl PT**, **Huber W**. HTSeq — a Python framework to work with high-throughput sequencing data. *Bioinformatics* 31: 166–169, 2015.

6. **Antoniou A**, **Raynaud P**, **Cordi S**, **Zong Y**, **Tronche F**, **Stanger BZ**, **Jacquemin P**, **Pierreux CE**, **Clotman F**, **Lemaigre FP**. Intrahepatic bile ducts develop according to a new mode of tubulogenesis regulated by the transcription factor SOX9. *Gastroenterology* 136: 2325–2333, 2009.

7. **Apte U**, **Gkretsi V**, **Bowen WC**, **Mars WM**, **Luo JH**, **Donthamsetty S**, **Orr A**, **Monga SPS**, **Wu C**, **Michalopoulos GK**. Enhanced liver regeneration following changes induced by hepatocyte-specific genetic ablation of integrin-linked kinase. *Hepatology* 50: 844–851, 2009.

8. **Apte U**, **Zeng G**, **Thompson MD**, **Muller P**, **Micsenyi A**, **Cieply B**, **Kaestner KH**, **Monga SPS**. beta-Catenin is critical for early postnatal liver growth. *Am J Physiol Gastrointest liver Physiol* 292: G1578-85, 2007.

9. **Arthur I**. Hepatocyte-matrix interactions [Online]. *Gut* 35: 729–732, 1994. papers3://publication/uuid/6D45AF17-6348-41E2-848B-A238688F9181.

10. **Authier F**, **Desbuquois B**. Glucagon receptors. *Cell Mol Life Sci* 65: 1880–1899, 2008.

11. **Ayala JE**, **Bracy DP**, **Malabanan C**, **James FD**, **Ansari T**, **Fueger PT**, **McGuinness OP**, **Wasserman DH**. Hyperinsulinemic-euglycemic clamps in conscious, unrestrained mice. *J Vis Exp* : 1–8, 2011.

12. **Ayala JE**, **Bracy DP**, **McGuinness OP**, **Wasserman DH**. Considerations in the design of hyperinsulinemic-euglycemic clamps in the conscious mouse. [Online]. *Diabetes* 55: 390–7, 2006. http://www.ncbi.nlm.nih.gov/pubmed/16443772.

13. **Bedossa P**, **Paradis V**. Liver extracellular matrix in health and disease. *J Pathol* 200: 504–515, 2003.

14. **Bella J**. Collagen structure: new tricks from a very old dog. *Biochem J* 473: 1001–1025, 2016.

15. **Berria R**, **Richardson DK**, **Finlayson J**, **Belfort R**, **Kashyap S**, **Wang L**, **Mandarino LJ**, **De Filippis EA**, **Pratipanawatr T**. Increased collagen content in insulin-resistant skeletal muscle. *Am J Physiol Metab* 290: E560–E565, 2005.

16. **Bezerra J a**, **Currier a R**, **Melin-Aldana H**, **Sabla G**, **Bugge TH**, **Kombrinck KW**, **Degen JL**. Plasminogen activators direct reorganization of the liver lobule after acute injury. *Am J Pathol* 158: 921–929, 2001.

17. **Bhushan B**, **Edwards G**, **Desai A**, **Michalopoulos GK**, **Apte U**. Liver-specific deletion of integrin-linked kinase in mice attenuates hepatotoxicity and improves liver regeneration after acetaminophen overdose. *Gene Expr* 17: 35–45, 2016.

18. **Bisht B**, **Srinivasan K**, **Dey CS**. In vivo inhibition of focal adhesion kinase causes insulin resistance. *J Physiol* 586: 3825–37, 2008.

19. **Blackman D**. The economics of gluconeogenesis. *Biochem Educ* 10: 141, 1982.

20. **Blattner SM**, **Kretzler M**. Integrin-linked kinase in renal disease: Connecting cell-matrix interaction to the cytoskeleton. *Curr Opin Nephrol Hypertens* 14: 404–410, 2005.

21. **Blouin A**, **Bolender RP**, **Weibel ER**. Distribution of Organelles and Membranes Between Hepatocytes and Nonhepatocytes in the Rat Liver Parenchyma- A Stereological Study. *J Cell Biol* 72: 441–455, 1977.

22. **Boldogh IR**, **Pon L a**. Mitochondria on the move. *Trends Cell Biol* 17: 502–10, 2007.

23. **Bolger AM**, **Lohse M**, **Usadel B**. Trimmomatic : a flexible trimmer for Illumina sequence data. *Bioinformatics* 30: 2114–2120, 2014.

24. **Bonnans C**, **Chou J**, **Werb Z**. Remodelling the extracellular matrix in development and disease. *Nat Rev Mol Cell Biol* 15: 786–801, 2014.

25. **Borengasser SJ**, **Rector RS**, **Uptergrove GM**, **Morris EM**, **Perfield JW**, **Booth FW**, **Fritsche KL**, **Ibdah J a.**, **Thyfault JP**. Exercise and omega-3 polyunsaturated fatty acid supplementation for the treatment of hepatic steatosis in hyperphagic OLETF rats. *J Nutr Metab* 2012, 2012.

26. **Boucher J**, **Kleinridders A**, **Kahn CR**. Insulin receptor signaling in normal and insulin-resistant states. *Cold Spring Harb Perspect Biol* 6: 1–23, 2014.

27. **Bray GA**, **Bellanger T**. Epidemiology, trends, and morbidities of obesity and the metabolic syndrome. *Endocrine* 29: 109–17, 2006.

28. **Brosnan JT**. Interorgan amino acid transport and its regulation. *J Nutr* 133: 2068S–2072S, 2003.

29. **Brown JCL**, **Staples JF**. Mitochondrial metabolism during fasting-induced daily torpor in mice. *Biochim Biophys Acta - Bioenerg* 1797: 476–486, 2010.

30. **Brown MS**, **Goldstein JL**. Selective versus Total Insulin Resistance: A Pathogenic Paradox. *Cell Metab* 7: 95–96, 2008.

31. **Browning JD**, **Horton JD**. Molecular mediators of hepatic steatosis and liver injury. *J Clin Invest* 114: 147–152, 2004.

32. **Brunt EM**. Pathology of nonalcoholic fatty liver disease. *Nat Rev Gastroenterol Hepatol* 7: 195–203, 2010.

33. **Bugianesi E**, **Mccullough AJ**, **Marchesini G**. Insulin resistance : A metabolic pathway to chronic liver disease. *Hepatology* 42: 987–1000, 2005.

34. **Bultot L**, **Guigas B**, **Von Wilamowitz-Moellendorff A**, **Maisin L**, **Vertommen D**, **Hussain N**, **Beullens M**, **Guinovart JJ**, **Foretz M**, **Viollet B**, **Sakamoto K**, **Hue L**, **Rider MH**. AMP-activated protein kinase phosphorylates and inactivates liver glycogen synthase. *Biochem J* 443: 193–203, 2012.

35. **Campbell ID**, **Humphries MJ**. Integrin structure, activation, and interactions. *Cold Spring Harb Perspect Biol* 3, 2011.

36. **Cariappa R**, **Kilberg MS**. Plasma membrane domain localization and transcytosis of the glucagon-induced hepatic system A carrier. *Am J Physiol Metab* 263: E1021–E1028, 1992.

37. **Chan TM**, **Exton JH**. A rapid method for the determination of glycogen content and radioactivity in small quantities of tissue or isolated hepatocytes. *Anal Biochem* 71: 96–105, 1976.

38. **Chao EC**, **Henry RR**. SGLT2 inhibition-A novel strategy for diabetes treatment. *Nat Rev Drug Discov* 9: 551–559, 2010.

39. **Charlton MR**, **Burns JM**, **Pedersen RA**, **Watt KD**, **Heimbach JK**, **Dierkhising RA**. Frequency and outcomes of liver transplantation for nonalcoholic steatohepatitis in the United States. *Gastroenterology* 141: 1249–1253, 2011.

40. **Chen L**, **Kwong M**, **Lu R**, **Ginzinger D**, **Lee C**, **Leung L**, **Chan JY**. Nrf1 is critical for redox balance and survival of liver cells during development. *Mol Cell Biol* 23: 4673–4686, 2003.

41. **Cheng X**, **Kim SY**, **Okamoto H**, **Xin Y**, **Yancopoulos GD**, **Murphy AJ**, **Gromada J**. Glucagon contributes to liver zonation. *Proc Natl Acad Sci* 115: E4111–E4119, 2018.

42. **Cherrington AD**. Control of glucose production in vivo by insulin and glucagon. In: *Supplement 21: Handbook of physiology, the endocrine system, the endocrine pancreas and regulation of metabolism.* 2001, p. 759–785.

43. **Cherrington AD**, **Liljenquist JE**, **Shulman GI**, **Williams PE**, **Lacy WW**. Importance of hypoglycemia-induced glucose production during isolated glucagon deficiency. *Am J Physiol - Endocrinol Metab* 236: E263–E271, 1979.

44. **Chiang DJ**, **Pritchard MT**, **Nagy LE**. Obesity , diabetes mellitus , and liver fibrosis. *Am J Physiol Gastrointest Liver Physiol* 300: 697–702, 2011.

45. **Church RJ**, **Kullak-Ublick GA**, **Aubrecht J**, **Bonkovsky HL**, **Chalasani N**, **Fontana RJ**, **Goepfert JC**, **Hackman F**, **King NMP**, **Kirby S**, **Kirby P**, **Marcinak J**, **Ormarsdottir S**, **Schomaker SJ**, **Schuppe-Koistinen I**, **Wolenski F**, **Arber N**, **Merz M**, **Sauer JM**, **Andrade RJ**, **van Bömmel F**, **Poynard T**, **Watkins PB**. Candidate biomarkers for the diagnosis and prognosis of drug-induced liver injury: An international collaborative effort. *Hepatology* 69: 760–773, 2019.

46. **Cirillo LA**, **Lin FR**, **Cuesta I**, **Friedman D**, **Jarnik M**, **Zaret KS**. Opening of compacted chromatin by early developmental transcription factors HNF3 (FoxA) and GATA-4. 9: 279–

289, 2002.

47. **Clement B**, **Rissel M**, **Peyrol S**, **Mazurier Y**, **Grimaud J-A**, **Guillouzo A**. A procedure for light and electron microscopic intracellular immunolocalization of collagen and fibronectin in rat liver. *J Histochem Cytochem* 33: 407–414, 1985.

48. **Clotman F**, **Jacquemin P**, **Plumb-Rudewiez N**, **Pierreux CE**, **Van Der Smissen P**, **Dietz HC**, **Courtoy PJ**, **Rousseau GG**, **Lemaigre FP**. Control of liver cell fate decision by a gradient of TGFβ signaling modulated by Onecut transcription factors. *Genes Dev* 19: 1849–1854, 2005.

49. **Colletti M**, **Cicchini C**, **Conigliaro A**, **Santangelo L**, **Alonzi T**, **Pasquini E**, **Tripodi M**, **Amicone L**. Convergence of wnt signaling on the hNF4α-driven transcription in controlling liver zonation. *Gastroenterology* 137: 660–672, 2009.

50. **Comar JF**, **Suzuki-Kemmelmeier F**, **Nascimento ÉA**, **Bracht A**. Flexibility of the hepatic zonation of carbon and nitrogen fluxes linked to lactate and pyruvate transformations in the presence of ammonia. *Am J Physiol Liver Physiol* 293: G838–G849, 2007.

51. **Couvelard A**, **Scoazec J-Y**, **Feldmann G**. Expression of cell-cell and cell-matrix adhesion proteins by sinusoidal endothelial cells in the normal and cirrhotic human liver. [Online]. *Am J Pathol* 143: 738–52, 1993. http://www.pubmedcentral.nih.gov/articlerender.fcgi?artid=1887198&tool=pmcentrez&rendertype=abstract.

52. **Cox TR**, **Erler JT**. Remodeling and homeostasis of the extracellular matrix: implications for fibrotic diseases and cancer. *Dis Model Mech* 4: 165–78, 2011.

53. **Cusi K**. Role of obesity and lipotoxicity in the development of nonalcoholic steatohepatitis: Pathophysiology and clinical implications. *Gastroenterology* 142: 711–725, 2012.

54. **DeAngelis RA**, **Markiewski MM**, **Taub R**, **Lambris JD**. A high-fat diet impairs liver regeneration in C57BL/6 mice through overexpression of the NF-κB inhibitor, IκBα. *Hepatology* 42: 1148–1157, 2005.

55. **Decaens T**, **Godard C**, **De Reyniès A**, **Rickman DS**, **Tronche F**, **Couty JP**, **Perret C**, **Colnot S**. Stabilization of β-catenin affects mouse embryonic liver growth and hepatoblast fate. *Hepatology* 47: 247–258, 2008.

56. **Decaris ML**, **Emson CL**, **Li K**, **Gatmaitan M**, **Luo F**, **Cattin J**, **Nakamura C**, **Holmes WE**, **Angel TE**, **Peters MG**, **Turner SM**, **Hellerstein MK**. Turnover rates of hepatic collagen and circulating collagen-associated proteins in humans with chronic liver disease. *PLoS One* 10: 1–13, 2015.

57. **DeFronzo RA**, **Simonson D**, **Ferrannini E**. Hepatic and peripheral insulin resistance: A common feature of type 2 (non-insulin-dependent) and type 1 (insulin-dependent) diabetes mellitus. *Diabetelogia* 23: 313–319, 1982.

58. **Delcommenne M**, **Tan C**, **Gray V**, **Rue L**, **Woodgett J**, **Dedhar S**. Phosphoinositide-3-OH kinase-dependent regulation of glycogen synthase kinase 3 and protein kinase B/AKT by the integrin-linked kinase. *Proc Natl Acad Sci U S A* 95: 11211–11216, 1998.

59. **DeLeve L**. Liver sinusoidal endothelial cells and liver regeneration. *J Cinical Investig* 123:

1861–1866, 2013.

60. **Deleve LD**. Liver Sinusoidal Endothelial Cells In Hepatic Fibrosis. *Hepatology*. .

61. **Deutsch G**, **Jung J**, **Zheng M**, **Lóra J**, **Zaret KS**. A bipotential precursor population for pancreas and liver within the embryonic endoderm. [Online]. *Development* 128: 871–81, 2001. http://www.ncbi.nlm.nih.gov/pubmed/11222142.

62. **Djafarzadeh S**, **Jakob SM**. High-resolution Respirometry to Assess Mitochondrial Function in Permeabilized and Intact Cells. *J Vis Exp* : 1–11, 2017.

63. **Donthamsetty S**, **Bhave VS**, **Kliment CS**, **Bowen WC**, **Mars WM**, **Bell AW**, **Stewart RE**, **Orr A**, **Wu C**, **Michalopoulos GK**. Excessive Hepatomegaly of Mice with Hepatocyte-Targeted Elimination of Integrin Linked Kinase Following Treatment by TCPOBOP. *Hepatology* 53: 587–595, 2011.

64. **Donthamsetty S**, **Bowen W**, **Mars W**, **Bhave V**, **Luo JH**, **Wu C**, **Hurd J**, **Orr A**, **Bell A**, **Michalopoulos G**. Liver-specific ablation of integrin-linked kinase in mice results in enhanced and prolonged cell proliferation and hepatomegaly after phenobarbital administration. *Toxicol Sci* 113: 358–366, 2009.

65. **Donthamsetty S**, **Mars WM**, **Orr A**, **Wu C**, **Michalopoulos GK**. Protection against Fas-induced fulminant hepatic failure in liver specific integrin linked kinase knockout mice. *Comp Hepatol* 10: 11, 2011.

66. **Donthamsetty S**, **Mars WM**, **Orr A**, **Wu C**, **Michalopoulos GK**. Protection against Fas-induced fulminant hepatic failure in liver specific integrin linked kinase knockout mice. *Comp Hepatol* 10: 11, 2011.

67. **E L**, **Lu J**, **Burns JM**, **Swerdlow RH**. Effect of exercise on mouse liver and brain bioenergetic infrastructures. *Exp Physiol* 98: 207–19, 2013.

68. **Eisen HJ**, **Goldfine ID**, **Glinsmann WH**. Regulation of Hepatic Glycogen Synthesis During Fetal Development: Roles of Hydrocortisone, Insulin, and Insulin Receptors. *Proc Natl Acad Sci* 70: 3454–3457, 2006.

69. **Enomoto H**, **Sakai Y**, **Aizawa N**, **Iwata Y**, **Tanaka H**, **Ikeda N**, **Hasegawa K**, **Yoh K**, **Ishii A**, **Takashima T**, **Iwata K**, **Saito M**, **Imanishi H**, **Iijima H**, **Nishiguchi S**. Association of amino acid imbalance with the severity of liver fibrosis and esophageal varices. *Ann Hepatol* 12: 471–478, 2013.

70. **Ewing RM**, **Chu P**, **Elisma F**, **Li H**, **Taylor P**, **Climie S**, **McBroom-Cerajewski L**, **Robinson MD**, **O'Connor L**, **Li M**, **Taylor R**, **Dharsee M**, **Ho Y**, **Heilbut A**, **Moore L**, **Zhang S**, **Ornatsky O**, **Bukhman Y V**, **Ethier M**, **Sheng Y**, **Vasilescu J**, **Abu-Farha M**, **Lambert JP**, **Duewel HS**, **Stewart II**, **Kuehl B**, **Hogue K**, **Colwill K**, **Gladwish K**, **Muskat B**, **Kinach R**, **Adams S-L**, **Moran MF**, **Morin GB**, **Topaloglou T**, **Figeys D**. Large-scale mapping of human protein-protein interactions by mass spectrometry. *Mol Syst Biol* 3: 1–17, 2007.

71. **Fassio E**, **Alvarez E**, **Dominguez N**, **Landeira G**, **Longo C**. Natural history of nonalcoholic steatohepatitis: A Longitudinal Study of Repeat Liver Biopsies. *Hepatology* 40: 820–826, 2004.

72. **Ferrannini E**, **Bjorkman O**, **Geichard Jr. GA**, **Pilo A**, **Olsson M**, **Wahren J**, **DeFronzo RA**. The disposal of an oral glucose load in healthy subjects. *Diabetes* 34: 580–588, 1985.

73. **Finkelstein EA**, **Khavjou OA**, **Thompson H**, **Trogdon JG**, **Pan L**, **Sherry B**, **Dietz W**. Obesity and severe obesity forecasts through 2030. *Am J Prev Med* 42: 563–570, 2012.

74. **Finkelstein EA**, **Trogdon JG**, **Cohen JW**, **Dietz W**. Annual medical spending attributable to obesity: Payer-and service-specific estimates. *Health Aff* 28: 822–831, 2009.

75. **Folch J**, **Lees M**, **Sloane Stanley GH**. A simple method for the isolation and purification of total lipides from animal tissues. *J Biol Chem* 226: 497–509, 1957.

76. **Foretz M**, **Hébrard S**, **Leclerc J**, **Zarrinpashneh E**, **Soty M**, **Mithieux G**, **Sakamoto K**, **Andreelli F**, **Viollet B**. Metformin inhibits hepatic gluconeogenesis in mice independently of the LKB1 / AMPK pathway via a decrease in hepatic energy state. *J Clin Invest* 120: 2355–2369, 2010.

77. **Franceschi C**. Healthy ageing in 2016: Obesity in geroscience-is cellular senescence the culprit? *Nat Rev Endocrinol* 13: 76–78, 2017.

78. **Frantz C**, **Stewart KM**, **Weaver VM**. The extracellular matrix at a glance. *J Cell Sci* 123: 4195–4200, 2010.

79. **Freychet P**, **Roth J**, **Neville Jr. DM**. Insulin receptors in the liver: Specific binding of [125I]insulin to the plasma membrane and its relation to insulin bioactivity. *Proc Natl Acad Sci* 68: 1833–1837, 1971.

80. **Friedman SL**. Hepatic Stellate Cells : Protean , Multifunctional , and Enigmatic Cells of the Liver. *Physiol Rev* 88: 125–172, 2008.

81. **Friedman SL**, **Neuschwander-Tetri BA**, **Rinella M**, **Sanyal AJ**. Mechanisms of NAFLD development and therapeutic strategies. *Nat Med* 24: 1–15, 2018.

82. **Galloway C a**, **Lee H**, **Brookes PS**, **Yoon Y**. Decreasing mitochondrial fission alleviates hepatic steatosis in a murine model of nonalcoholic fatty liver disease. *Am J Physiol Gastrointest Liver Physiol* , 2014.

83. **Garcia D**, **Shaw RJ**. AMPK: Mechanisms of cellular energy sensing and restoration of metabolic balance. *Mol Cell* 66: 789–800, 2017.

84. **Gebhardt R**, **Matz-Soja M**. Liver zonation: Novel aspects of its regulation and its impact on homeostasis. *World J Gastroenterol* 20: 8491–8504, 2014.

85. **Ghafoory S**, **Breitkopf-Heinlein K**, **Li Q**, **Scholl C**, **Dooley S**, **Wölfl S**. Zonation of Nitrogen and Glucose Metabolism Gene Expression upon Acute Liver Damage in Mouse. *PLoS One* 8: 1–11, 2013.

86. **Gkretsi V**, **Apte U**, **Mars WM**, **Bowen WC**, **Luo JH**, **Yang Y**, **Yu YP**, **Orr A**, **St.-Arnaud R**, **Dedhar S**, **Kaestner KH**, **Wu C**, **Michalopoulos GK**. Liver-specific ablation of integrin-linked kinase in mice results in abnormal histology, enhanced cell proliferation, and hepatomegaly. *Hepatology* 48: 1932–1941, 2008.

87. **Gkretsi V**, **Mars WM**, **Bowen WC**, **Barua L**, **Yang Y**, **Guo L**, **St-Arnaud R**, **Dedhar S**, **Wu C**, **Michalopoulos GK**. Loss of integrin linked kinase from mouse hepatocytes in vitro and

in vivo results in apoptosis and hepatitis. *Hepatology* 45: 1025–1034, 2007.

88. **Gordillo M**, **Evans T**, **Gouon-Evans V**. Orchestrating liver development. *Development* 142: 2094–2108, 2015.

89. **Gordon MK**, **Hahn RA**. Collagens. *Cell Tissue Res* 339: 247–257, 2010.

90. **Grose R**, **Dinsdale D**, **Shaked-Rabi M**, **Salomoni P**, **Campanella M**, **McEvoy A**, **Sanzone S**, **Brandner S**, **Galavotti S**, **Bartesaghi S**, **Jones C**, **Faccenda D**, **Condorelli F**. The autophagy-associated factors DRAM1 and p62 regulate cell migration and invasion in glioblastoma stem cells. *Oncogene* 32: 699–712, 2012.

91. **Gruppuso PA**, **Sanders JA**. Regulation of Liver Development: Implications for Liver Biology across the Lifespan. *J Mol Endocrinol* 56: 115–125, 2016.

92. **Guilherme A**, **Torres K**, **Czech MP**. Cross-talk between insulin receptor and integrin alpha5 beta1 signaling pathways. [Online]. *J Biol Chem* 273: 22899–903, 1998. http://www.ncbi.nlm.nih.gov/pubmed/9722509.

93. **Gupta A**, **Dey CS**. PTEN and SHIP2 regulates PI3K/Akt pathway through focal adhesion kinase☆. *Mol Cell Endocrinol* 309: 55–62, 2009.

94. **Guri Y**, **Colombi M**, **Dazert E**, **Hindupur SK**, **Roszik J**, **Moes S**, **Jenoe P**, **Heim MH**, **Riezman I**, **Riezman H**, **Hall MN**. mTORC2 Promotes Tumorigenesis via Lipid Synthesis. *Cancer Cell* 32: 807–823, 2017.

95. **Guyot C**, **Lepreux S**, **Combe C**, **Doudnikoff E**, **Bioulac-Sage P**, **Balabaud C**, **Desmoulière A**. Hepatic fibrosis and cirrhosis: the (myo)fibroblastic cell subpopulations involved. *Int J Biochem Cell Biol* 38: 135–51, 2006.

96. **Haase TN**, **Ringholm S**, **Leick L**, **Bienso RS**, **Kiilerich K**, **Johansen S**, **Nielsen MM**, **Wojtaszewski JF**, **Hidalgo J**, **Pedersen P a.**, **Pilegaard H**. Role of PGC-1 in exercise and fasting-induced adaptations in mouse liver. *AJP Regul Integr Comp Physiol* 301: R1501–R1509, 2011.

97. **Haeusler RA**, **McGraw TE**, **Accili D**. Metabolic Signalling: Biochemical and cellular properties of insulin receptor signalling. *Nat Rev Mol Cell Biol* 19: 31–44, 2018.

98. **Hailfinger S**, **Jaworski M**, **Braeuning A**, **Buchmann A**, **Schwarz M**. Zonal gene expression in murine liver: Lessons from tumors. *Hepatology* 43: 407–414, 2006.

99. **Han H-S**, **Kang G**, **Kim JS**, **Choi BH**, **Koo S-H**. Regulation of glucose metabolism from a liver-centric perspective. *Exp Mol Med* 48: e218-228, 2016.

100. **Han KS**, **Li N**, **Raven PA**, **Fazli L**, **Ettinger S**, **Hong SJ**, **Gleave ME**, **So AI**. Targeting integrin-linked kinase suppresses invasion and metastasis through downregulation of epithelial-to-mesenchymal transition in renal cell carcinoma. *Mol Cancer Ther* 14: 1024–1034, 2015.

101. **Han KS**, **Li N**, **Raven PA**, **Fazli L**, **Ettinger S**, **Hong SJ**, **Gleave ME**, **So AI**. Targeting integrin-linked kinase suppresses invasion and metastasis through downregulation of epithelial-to-mesenchymal transition in renal cell carcinoma. *Mol Cancer Ther* 14: 1024–1034, 2015.

102. **Hannigan G**, **Troussard AA**, **Dedhar S**. Integrin-linked kinase: A cancer therapeutic target unique among its ILK. *Nat Rev Cancer* 5: 51–63, 2005.

103. **Hannigan GE**, **Leung-Hagesteijn C**, **Fitz-Gibbon L**, **Coppolino MG**, **Radeva G**, **Filmus J**, **Bell JC**, **Dedhar S**. Regulation of cell adhesion and anchorage-dependent growth by a new beta 1-integrin-linked protein kinase. *Nature* 379: 91–96, 1996.

104. **Harburger DS**, **Calderwood D a.** Integrin signalling at a glance. *J Cell Sci* 122: 1472–1472, 2009.

105. **Hasenour CM**, **Wall ML**, **Ridley DE**, **Hughey CC**, **James FD**, **Wasserman DH**, **Young JD**. Mass spectrometry-based microassay of ^{2}H and ^{13}C plasma glucose labeling to quantify liver metabolic fluxes in vivo. *Am J Physiol - Endocrinol Metab* 309: E191–E203, 2015.

106. **Haüssinger D**. Nitrogen metabolism in liver: structural and functional organization and physiological relevance. *Biochem J* 267: 281–290, 1990.

107. **Hellerstein MK**, **Christiansen M**, **Kaempfer S**, **Kletke C**, **Wu K**, **Reid JS**, **Mulligan K**, **Hellerstein NS**, **Shackleton CH**. Measurement of de novo hepatic lipogenesis in humans using stable isotopes. *J Clin Invest* 87: 1841–52, 1991.

108. **Hendrick GK**, **Wasserman DH**, **Frizzell RT**, **Williams PE**, **Lacy DB**, **Jaspan JB**, **Cherrington AD**. Importance of basal glucagon in maintaining hepatic glucose production during a prolonged fast in conscious dogs. *Am J Physiol Metab* 263: E541–E549, 1992.

109. **Henegar C**, **Tordjman J**, **Achard V**, **Lacasa D**, **Cremer I**, **Guerre-Millo M**, **Poitou C**, **Basdevant A**, **Stich V**, **Viguerie N**, **Langin D**, **Bedossa P**, **Zucker J-D**, **Clement K**. Adipose tissue transcriptomic signature highlights the pathological relevance of extracellular matrix in human obesity. *Genome Biol* 9: R14, 2008.

110. **Hijmans BS**, **Grefhorst A**, **Oosterveer MH**, **Groen AK**. Zonation of glucose and fatty acid metabolism in the liver: Mechanism and metabolic consequences. *Biochimie* 96: 121–129, 2014.

111. **Hoitzing H**, **Johnston IG**, **Jones NS**. What is the function of mitochondrial networks? A theoretical assessment of hypotheses and proposal for future research. *BioEssays* 37: 687–700, 2015.

112. **Holecek M**. Ammonia and amino acid profiles in liver cirrhosis: Effects of variables leading to hepatic encephalopathy. *Nutrition* 31: 14–20, 2015.

113. **Horan MP**, **Pichaud N**, **Ballard JWO**. Review: Quantifying mitochondrial dysfunction in complex diseases of aging. *Journals Gerontol - Ser A* 67: 1022–1035, 2012.

114. **Horton JD**, **Goldstein JL**, **Brown MS**. SREBPs: activators of the complete program of cholesterol and fatty acid synthesis in the liver. *J Clin Invest* 109: 1125–1131, 2002.

115. **Huang D**, **Cheung AT**, **Thomas Parsons J**, **Bryer-Ash M**. Focal adhesion kinase (FAK) regulates insulin-stimulated glycogen synthesis in hepatocytes. *J Biol Chem* 277: 18151–18160, 2002.

116. **Huang J**, **Rudnick D a.** Elucidating the metabolic regulation of liver regeneration. *Am J Pathol* 184: 309–321, 2014.

117. **Huang J**, **Schriefer AE**, **Cliften PF**, **Dietzen D**, **Kulkarni S**, **Sing S**, **Monga SPS**, **Rudnick DA**. Postponing the hypoglycemic response to partial hepatectomy delays mouse liver regeneration. *Am J Pathol* 186: 587–599, 2016.

118. **Hubbard SR**. Crystal structure of the activated insulin receptor tyrosine kinase in complex with peptide substrate and ATP analog [Online]. *EMBO J* 16: 5573–5581, 1997. papers://c33b182f-cf88-47e8-a9c5-ad67b5626483/Paper/p1886.

119. **Hubbard SR**. The insulin receptor: Both a prototypical and atypical receptor tyrosine kinase. *Cold Spring Harb Perspect Biol* 5: 1–12, 2013.

120. **Hubbard SR**, **Wei L**, **Ellis L**, **Hendrickson WA**. Crystal structure of the tyrosine kinase domain of the human insulin receptor. *Nature* 372: 746–754, 1994.

121. **Hughey CC**, **James FD**, **Bracy DP**, **Patrick Donahue E**, **Young JD**, **Viollet B**, **Foretz M**, **Wasserman DH**. Loss of hepatic AMP-activated protein kinase impedes the rate of glycogenolysis but not gluconeogenic fluxes in exercising mice. *J Biol Chem* 292: 20125–20140, 2017.

122. **Huh C-G**, **Factor VM**, **Sánchez A**, **Uchida K**, **Conner E a**, **Thorgeirsson SS**. Hepatocyte growth factor/c-met signaling pathway is required for efficient liver regeneration and repair. *Proc Natl Acad Sci U S A* 101: 4477–4482, 2004.

123. **Humphries JD**, **Byron A**, **Humphries MJ**. Integrin ligands at a glance. *J Cell Sci* 119: 3901–3903, 2006.

124. **Hynes RO**. Integrins: a family of cell surface receptors. [Online]. *Cell* 48: 549–54, 1987. http://www.ncbi.nlm.nih.gov/pubmed/3028640.

125. **Hynes RO**. Integrins : Bidirectional , allosteric signaling machines in their roles as major adhesion receptors. *Cell* 110: 673–687, 2002.

126. **Issa D**, **Patel V**, **Sanyal AJ**. Future therapy for non-alcoholic fatty liver disease. *Liver Int* 38: 56–63, 2018.

127. **Jacobi D**, **Liu S**, **Burkewitz K**, **Kory N**, **Knudsen NH**, **Alexander RK**, **Unluturk U**, **Li X**, **Kong X**, **Hyde A**, **Gangl MR**, **Mair WB**, **Lee C**. Hepatic Bmal1 regulates rhythmic mitochondrial dynamics and promotes metabolic fitness. *Cell Metab* 22: 709–720, 2016.

128. **Jones JG**. Hepatic glucose and lipid metabolism. *Diabetologia* 59: 1098–1103, 2016.

129. **Jungas RL**, **Halperin ML**, **Brosnan JT**. Quantitative analysis of amino acid oxidation and related gluconeogenesis in humans. *Physiol Rev* 72: 419–448, 1992.

130. **Jungermann K**, **Kietzmann T**. Zonation of parenchymal and nonparenchymal metabolism in liver. *Annu Rev Nutr* 16: 179–203, 1996.

131. **Kadler KE**, **Hill A**, **Canty-Laird EG**. Collagen fibrillogenesis: fibronectin, integrins, and minor collagens as organizers and nucleators. *Curr Opin Cell Biol* 20: 495–501, 2008.

132. **Kaiyala KJ**. Mathematical model for the contribution of individual organs to non-zero y-intercepts in single and multi-compartment linear models of whole-body energy expenditure. *PLoS One* 9: 19–21, 2014.

133. **Kaiyala KJ**, **Morton GJ**, **Leroux BG**, **Ogimoto K**, **Wisse B**, **Schwartz MW**. Identification of body fat mass as a major determinant of metabolic rate in mice. *Diabetes* 59: 1657–1666, 2010.

134. **Kaiyala KJ**, **Schwartz MW**. Toward a more complete (and less controversial) understanding of energy expenditure and its role in obesity pathogenesis. *Diabetes* 60: 17–23, 2011.

135. **Kamiya A**, **Kinoshita T**, **Ito Y**, **Matsui T**, **Morikawa Y**, **Senba E**, **Nakashima K**, **Taga T**, **Yoshida K**, **Kishimoto T**, **Miyajima A**. Fetal liver development requires a paracrine action of oncostatin M through the gp130 signal transducer. *EMBO J* 18: 2127–2136, 1999.

136. **Kandilis AN**, **Koskinas J**, **Tiniakos DG**, **Nikiteas N**, **Perrea DN**. Liver regeneration: Focus on cell types and topographic differences. *Eur Surg Res* 44: 1–12, 2010.

137. **Kang L**, **Ayala JE**, **Lee-Young RS**, **Zhang Z**, **James FD**, **Neufer PD**, **Pozzi A**, **Zutter MM**, **Wasserman DH**. Diet-induced muscle insulin resistance is associated with extracellular matrix remodeling and interaction with integrin alpha2beta1 in mice. *Diabetes* 60: 416–26, 2011.

138. **Kang L**, **Mokshagundam S**, **Reuter B**, **Lark DS**, **Sneddon CC**, **Hennayake C**, **Williams AS**, **Bracy DP**, **James FD**, **Pozzi A**, **Zent R**, **Wasserman DH**. Integrin-linked kinase in muscle is necessary for the development of insulin resistance in diet-induced obese mice. *Diabetes* 65: 1590–1600, 2016.

139. **Karsdal M a.**, **Manon-Jensen T**, **Genovese F**, **Kristensen JH**, **Nielsen MJ**, **Sand JMB**, **Hansen N-UB**, **Bay-Jensen A-C**, **Bager CL**, **Krag A**, **Blanchard A**, **Krarup H**, **Leeming DJ**, **Schuppan D**. Novel insights into the function and dynamics of extracellular matrix in liver fibrosis. *Am J Physiol - Gastrointest Liver Physiol* 308: G807–G829, 2015.

140. **Karsdal MA**, **Genovese F**, **Madsen EA**, **Manon-Jensen T**, **Schuppan D**. Collagen and tissue turnover as a function of age: Implications for fibrosis. *J Hepatol* 64: 103–109, 2016.

141. **Kasuga M**, **Zick Y**, **Blithe DL**, **Crettaz M**, **Kahn CR**. Insulin stimulates tyrosine phosphorylation of the insulin receptor in a cell-free system. *Nature* 298: 667–669, 1982.

142. **Kellendonk C**, **Opherk C**, **Anlag K**, **Schütz G**, **Tronche F**. Hepatocyte-specific expression of Cre recombinase. *Genesis* 26: 151–153, 2000.

143. **Kenific CM**, **Stehbens SJ**, **Goldsmith J**, **Leidal AM**, **Faure N**, **Ye J**, **Wittmann T**, **Debnath J**. NBR 1 enables autophagy-dependent focal adhesion turnover. *J Cell Biol* 212: 577–590, 2016.

144. **Khoshnoodi J**, **Pedchenko V**, **Hudson BG**. Mammalian collagen IV. *Microsc Res Tech* 71: 357–370, 2008.

145. **Kim D**, **Langmead B**, **Salzberg SL**. HISAT : a fast spliced aligner with low memory requirements. *Nat Methods* 12: 357–360, 2015.

146. **Kim TH**, **Bowen WC**, **Stolz DB**, **Runge D**, **Mars WM**, **Michalopoulos GK**. Differential expression and distribution of focal adhesion and cell adhesion molecules in rat hepatocyte differentiation. *Exp Cell Res* 244: 93–104, 1998.

147. **Kim TH**, **Mars WM**, **Stolz DB**, **Petersen BE**, **Michalopoulos GK**. Extracellular matrix

remodeling at the early stages of liver regeneration in the rat. *Hepatology* 26: 896–904, 1997.

148. **Klaas M**, **Kangur T**, **Viil J**, **Mäemets-Allas K**, **Minajeva A**, **Vadi K**, **Antsov M**, **Lapidus N**, **Järvekülg M**, **Jaks V**. The alterations in the extracellular matrix composition guide the repair of damaged liver tissue. *Sci Rep* 6: 1–12, 2016.

149. **Klug GA**, **Krause J**, **Knoll G**, **Brdiczka D**. Alterations in liver miochondrial function as a result of fasting and exhaustive exercise. *Biochim Biophys Acta - Bioenerg* 764: 272–282, 1984.

150. **Köhn-Gaone J**, **Gogoi-Tiwari J**, **Ramm GA**, **Olynyk JK**, **Tirnitz-Parker JEE**. The role of liver progenitor cells during liver regeneration, fibrogenesis and carcinogenesis. *Am J Physiol - Gastrointest Liver Physiol* : ajpgi.00215.2015, 2015.

151. **Kuznetsov A V.**, **Veksler V**, **Gellerich FN**, **Saks V**, **Margreiter R**, **Kunz WS**. Analysis of mitochondrial function in situ in permeabilized muscle fibers, tissues and cells. *Nat Protoc* 3: 965–976, 2008.

152. **Lark DS**, **Wasserman DH**. Meta-fibrosis links positive energy balance and mitochondrial metabolism to insulin resistance. *F1000Research* 6: 1–10, 2017.

153. **Laudadio I**, **Manfroid I**, **Achouri Y**, **Schmidt D**, **Wilson MD**, **Cordi S**, **Thorrez L**, **Knoops L**, **Jacquemin P**, **Schuit F**, **Pierreux CE**, **Odom DT**, **Peers B**, **Lemaigre FP**. A feedback loop between the liver-enriched transcription factor network and miR-122 controls hepatocyte differentiation. *Gastroenterology* 142: 119–129, 2012.

154. **Lazo M**, **Hernaez R**, **Eberhardt MS**, **Bonekamp S**, **Kamel I**, **Guallar E**, **Koteish A**, **Brancati FL**, **Clark JM**. Prevalence of nonalcoholic fatty liver disease in the United States: the Third National Health and Nutrition Examination Survey, 1988-1994. *Am J Epidemiol* 178: 38–45, 2013.

155. **Legate KR**, **Montañez E**, **Kudlacek O**, **Fässler R**. ILK, PINCH and parvin: the tIPP of integrin signalling. *Nat Rev Mol Cell Biol* 7: 20–31, 2006.

156. **Leiss M**, **Beckmann K**, **Girós A**, **Costell M**, **Fässler R**. The role of integrin binding sites in fibronectin matrix assembly in vivo. *Curr Opin Cell Biol* 20: 502–7, 2008.

157. **Lemaigre FP**. Development of the biliary tract. *Mech Dev* 120: 81–87, 2003.

158. **Lin X-Z**, **Horng MH**, **Sun Y-N**, **Shiesh S-C**, **Chow N-H**, **Guo X-Z**. Computer morphometry for quantitative measurement of liver fibrosis: Comparison with Knodell's score, colorimetry and conventional description reports. *J Gastroenterol Hepatol* 13: 75–80, 1998.

159. **Linden MA**, **Fletcher JA**, **Morris EM**, **Meers GM**, **Kearney ML**, **Crissey JM**, **Laughlin MH**, **Booth FW**, **Sowers JR**, **Ibdah JA**, **Thyfault JP**, **Rector RS**. Combining metformin and aerobic exercise training in the treatment of type 2 diabetes and NAFLD in OLETF rats. *Am J Physiol Endocrinol Metab* 306: E300-10, 2014.

160. **Lock R**, **Kenific CM**, **Leidal AM**, **Salas E**, **Debnath J**. Autophagy-dependent production of secreted factors facilitates oncogenic RAS-Driven invasion. *Cancer Discov* 4: 466–479, 2014.

161. **Lu H**, **Fedak PWM**, **Dai X**, **Du C**, **Zhou YQ**, **Henkelman M**, **Mongroo PS**, **Lau A**, **Yamabi**

H, **Hinek A**, **Husain M**, **Hannigan G**, **Coles JG**. Integrin-linked kinase expression is elevated in human cardiac hypertrophy and induces hypertrophy in transgenic mice. *Circulation* 114: 2271–2279, 2006.

162. **Mancone C**, **Conti B**, **Amicone L**, **Bordoni V**, **Cicchini C**, **Calvo L**, **Perdomo AB**, **Fimia GM**, **Tripodi M**, **Alonzi T**. Proteomic analysis reveals a major role for contact inhibition in the terminal differentiation of hepatocytes. *J Hepatol* 52: 234–243, 2010.

163. **Mansouri A**, **Gattolliat C-H**, **Asselah T**. Mitochondrial dysfunction and signaling in chronic liver diseases. *Gastroenterology* 155: 629–647, 2018.

164. **Mansouri A**, **Gattolliat C-H**, **Asselah T**. Mitochondrial dysfunction and signaling in chronic liver diseases. *Gastroenterology* 155: 629–647, 2018.

165. **Mantena SK**, **Vaughn DP**, **Andringa KK**, **Eccleston HB**, **King AL**, **Abrams G a**, **Doeller JE**, **Kraus DW**, **Darley-Usmar VM**, **Bailey SM**. High fat diet induces dysregulation of hepatic oxygen gradients and mitochondrial function in vivo. *Biochem J* 417: 183–93, 2009.

166. **Marchesini G**, **Brizi M**, **Bianchi G**, **Tomassetti S**, **Bugianesi E**, **Lenzi M**, **Mccullough AJ**, **Natale S**, **Forlani G**, **Melchionda N**. Nonalcoholic Fatty Liver Disease- A Feature of Metabolic Syndrome. *Diabetes* 50: 1844–50, 2001.

167. **Marsin AS**, **Bertrand L**, **Rider MH**, **Deprez J**, **Beauloye C**, **Vincent MF**, **Van den Berghe G**, **Carling D**, **Hue L**. Phosphorylation and activation of heart PFK-2 by AMPK has a role in the stimulation of glycolysis during ischaemia. *Curr Biol* 10: 1247–1255, 2000.

168. **Marsin AS**, **Bouzin C**, **Bertrand L**, **Hue L**. The stimulation of glycolysis by hypoxia in activated monocytes is mediated by AMP-activated protein kinase and inducible 6-phosphofructo-2-kinase. *J Biol Chem* 277: 30778–30783, 2002.

169. **Martinez-Hernandez A**, **Amenta PS**. The hepatic extracellular matrix I. Components and distribution in normal liver. *Virchows Arch A Pathol Anat Histopathol* 423: 1–11, 1993.

170. **Martinez-Hernandez A**, **Amenta PS**. The hepatic extracellular matrix II. Ontogenesis, regeneration and cirrhosis. *Virchows Arch A Pathol Anat Histopathol* 423: 77–84, 1993.

171. **Martinez-Hernandez A**, **Amenta PS**. The extracellular matrix in hepatic regeneration. *FASEB J* 9: 1401–1410, 1995.

172. **Mastrodonato M**, **Calamita G**, **Rossi R**, **Mentino D**, **Bonfrate L**, **Portincasa P**, **Ferri D**, **Liquori GE**. Altered distribution of caveolin-1 in early liver steatosis. *Eur J Clin Invest* 41: 642–651, 2011.

173. **Matsui T**, **Kinoshita T**, **Morikawa Y**, **Tohya K**, **Katsuki M**, **Ito Y**, **Kamiya A**, **Miyajima A**. K-Ras mediates cytokine-induced formation of E-cadherin-based adherens junctions during liver development [Online]. *EMBO J* 21: 1021–1030, 2002. papers3://publication/uuid/A80F6D89-D0ED-4860-8230-007792A17500.

174. **Mavrogiannaki A**, **Karamanos B**, **Manesis EK**, **Papatheodoridis G V.**, **Koskinas J**, **Archimandritis AJ**. Prevalence of glucose intolerance in patients with chronic hepatitis B or C: A prospective case-control study. *J Viral Hepat* 16: 430–436, 2009.

175. **McCrindle BW**. Cardiovascular consequences of childhood obesity. *Can J Cardiol* 31: 124–130, 2015.

176. **McDonald PC**, **Fielding AB**, **Dedhar S**. Integrin-linked kinase - essential roles in physiology and cancer biology. *J Cell Sci* 121: 3121–3132, 2008.

177. **McGarry JD**, **Foster DW**. Regulation of hepatic fatty acid oxidation and ketone body production. *Annu Rev Biochem* 49: 395–420, 1980.

178. **Meier JJ**. GLP-1 receptor agonists for individualized treatment of type 2 diabetes mellitus. *Nat Rev Endocrinol* 8: 728–742, 2012.

179. **Michalopoulos GK**. Liver Regeneration. *J Cell Physiol* 213: 286–300, 2007.

180. **Michalopoulos GK**. Liver regeneration after partial hepatectomy: critical analysis of mechanistic dilemmas. *Am J Pathol* 176: 2–13, 2010.

181. **Michalopoulos GK**, **DeFrances MC**. Liver regeneration. *Science (80-)* 276: 60–66, 1997.

182. **Mienaltowski MJ**, **Birk DE**. Structure, Physiology, and Biochemistry of Collagens. In: *Progress in heritable soft connective tissue diseases*, edited by Halper J. Dordrecht: Springer, 2014, p. 5–29.

183. **Miller RA**, **Chu Q**, **Le Lay J**, **Scherer PE**, **Ahima RS**, **Kaestner KH**, **Foretz M**, **Viollet B**, **Birnbaum MJ**. Adiponectin suppresses gluconeogenic gene expression in mouse hepatocytes independent of LKB1-AMPK signaling. *J Clin Invest* 121: 2518–2528, 2011.

184. **Miller RA**, **Shi Y**, **Lu W**, **Pirman DA**, **Jatkar A**, **Blatnik M**, **Wu H**, **Cardenas C**, **Wan M**, **Foskett JK**, **Park JO**, **Zhang Y**, **Holland WL**, **Rabinowitz JD**, **Birnbaum MJ**. Targeting hepatic glutaminase activity to ameliorate hyperglycemia. *Nat Med* 24: 518–524, 2018.

185. **Mohammed FF**, **Khokha R**. Thinking outside the cell: Proteases regulate hepatocyte division. *Trends Cell Biol* 15: 555–563, 2005.

186. **Moller DE**, **Flier JS**. Insulin resistance - Mechanisms, syndromes, and implications. *N Engl J Med* 325: 938–948, 1991.

187. **Moore MC**, **Cherrington AD**, **Cline G**, **Pagliassotti MJ**, **Jones EM**, **Neal DW**, **Badet C**, **Shulman GI**. Sources of carbon for hepatic glycogen synthesis in the conscious dog. *J Clin Invest* 88: 578–587, 1991.

188. **Moore MC**, **Coate KC**, **Winnick JJ**, **An Z**, **Cherrington AD**. Regulation of hepatic glucose uptake and storage in vivo. *Adv Nutr* 3: 286–294, 2012.

189. **Moreau M**, **Rivière B**, **Vegna S**, **Aoun M**, **Gard C**, **Ramos J**, **Assenat E**, **Hibner U**. Hepatitis C viral proteins perturb metabolic liver zonation. *J Hepatol* 62: 278–285, 2015.

190. **Morgan CR**, **Lazarow A**. Immunoassay of pancreatic and plasma insulin following alloxan injection of rats. *Diabetes* 14: 669–671, 1965.

191. **Morrison WR**, **Smith LM**. Preparation of fatty acid methyl esters and dimethylacetals from lipids with boron fluoride--methanol. *J Lipid Res* 5: 600–608, 1964.

192. **Natarajan A**, **Wagner B**, **Sibilia M**. The EGF receptor is required for efficient liver regeneration. *Proc Natl Acad Sci U S A* 104: 17081–17086, 2007.

193. **Nelson ME**, **Lahiri S**, **Chow JDY**, **Byrne FL**, **Hargett SR**, **Breen DS**, **Olzomer EM**, **Wu**

LE, **Cooney GJ**, **Turner N**, **James DE**, **Slack-Davis JK**, **Lackner C**, **Caldwell SH**, **Hoehn KL**. Inhibition of hepatic lipogenesis enhances liver tumorigenesis by increasing antioxidant defence and promoting cell survival. *Nat Commun* 8: 1–11, 2017.

194. **Nishida T**. Diagnosis and Clinical Implications of Diabetes in Liver Cirrhosis: A Focus on the Oral Glucose Tolerance Test. *J Endocr Soc* 1: 886–896, 2017.

195. **Nissim I**, **Brosnan ME**, **Yudkoff M**, **Nissim I**, **Brosnan JT**. Studies of hepatic glutamine metabolism in the perfused rat liver with 15 N-labeled glutamine. *J Biol Chem* 274: 28958–28965, 1999.

196. **Novo E**, **Parola M**. Redox mechanisms in hepatic chronic wound healing and fibrogenesis. *Fibrogenesis Tissue Repair* 1: 5, 2008.

197. **Ochi T**, **Kawaguchi T**, **Nakahara T**, **Ono M**, **Noguchi S**, **Koshiyama Y**, **Munekage K**, **Murakami E**, **Hiramatsu A**, **Ogasawara M**, **Hirose A**, **Mizuta H**, **Masuda K**, **Okamoto N**, **Suganuma N**, **Chayama K**, **Yamaguchi M**, **Torimura T**, **Saibara T**. Differences in characteristics of glucose intolerance between patients with NAFLD and chronic hepatitis C as determined by CGMS. *Sci Rep* 7: 1–9, 2017.

198. **Owen BM**, **Ding X**, **Morgan DA**, **Coate KC**, **Bookout AL**, **Rahmouni K**, **Kliewer SA**, **Mangelsdorf DJ**. FGF21 acts centrally to induce sympathetic nerve activity, energy expenditure, and weight loss. *Cell Metab* 20: 670–677, 2014.

199. **Owen BM**, **Ding X**, **Morgan DA**, **Coate KC**, **Bookout AL**, **Rahmouni K**, **Kliewer SA**, **Mangelsdorf DJ**. FGF21 acts centrally to induce sympathetic nerve activity, energy expenditure, and weight loss. *Cell Metab* 20: 670–677, 2014.

200. **Owen OE**, **Kalhan SC**, **Hanson RW**. The key role of anaplerosis and cataplerosis for citric acid cycle function. *J Biol Chem* 277: 30409–30412, 2002.

201. **Patsenker E**, **Stickel F**. Role of integrins in fibrosing liver diseases. *Am J Physiol Gastrointest Liver Physiol* 301: G425–G434, 2011.

202. **Patterson RE**, **Kalavalapalli S**, **Williams CM**, **Nautiyal M**, **Mathew JT**, **Martinez J**, **Reinhard MK**, **McDougall D**, **Rocca JR**, **Yost RA**, **Cusi K**, **Garrett TJ**, **Sunny NE**. Lipotoxicity in steatohepatitis occurs despite an increase in tricarboxylic acid cycle activity. *Am J Physiol Metab* 310: E484–E494, 2016.

203. **Pearson ER**, **Boj SF**, **Steele AM**, **Barrett T**, **Stals K**, **Shield JP**, **Ellard S**, **Ferrer J**, **Hattersley AT**. Macrosomia and hyperinsulinaemic hypoglycaemia in patients with heterozygous mutations in the HNF4A gene. *PLoS Med* 4: 760–769, 2007.

204. **Pesta D**, **Gnaiger E**. High-resolution respirometry: OXPHOS protocols for human cells and permeabilized fibers from small biopsies of human muscle. In: *Mitochondrial Bioenergetics. Methods in Molecular Biology*, p. 25–58.

205. **Piper HM**, **Sezer O**, **Schleyer M**, **Schwartz P**, **Hütter JF**, **Spieckermann PG**. Development of ischemia-induced damage in defined mitochondrial subpopulations. *J Mol Cell Cardiol* 17: 885–896, 1985.

206. **Postic C**, **Magnuson MA**. DNA excision in liver by an albumin-Cre transgene occurs progressively with age. *Genesis* 26: 149–150, 2000.

207. **Potthoff MJ**, **Finck BN**. Head over hepatocytes for FGF21. *Diabetes* 63: 4013–5, 2014.

208. **Pozzi A**, **Yurchenco PD**, **Iozzo R V**. The nature and biology of basement membranes. *Matrix Biol* 57–58: 1–11, 2017.

209. **Protzer U**, **Maini MK**, **Knolle P a**. Living in the liver: hepatic infections. *Nat Rev Immunol* 12: 201–13, 2012.

210. **Puhakainen I**, **Koivisto VA**, **Yki-Järvinen H**. Lipolysis and gluconeogenesis from glycerol are increased in patients with noninsulin-dependent diabetes mellitus. *J Clin Endocrinol Metab* 75: 789–794, 1992.

211. **Pujades C**, **Forsberg E**, **Enrich C**, **Johansson S**. Changes in cell surface expression of fibronectin and fibronectin receptor during liver regeneration. *J Cell Sci* 102: 815–820, 1992.

212. **Qin J**, **Wu C**. ILK: a pseudokinase in the center stage of cell-matrix adhesion and signaling. *Curr Opin Cell Biol* 24: 607–613, 2012.

213. **Quesada I**, **Tudurí E**, **Ripoll C**, **Nadal Á**. Physiology of the pancreatic α-cell and glucagon secretion: role in glucose homeostasis and diabetes. *J Endocrinol* 199: 5–19, 2008.

214. **Rector RS**, **Thyfault JP**, **Morris RT**, **Laye MJ**, **Borengasser SJ**, **Booth FW**, **Ibdah J a**. Daily exercise increases hepatic fatty acid oxidation and prevents steatosis in Otsuka Long-Evans Tokushima Fatty rats. *Am J Physiol Gastrointest Liver Physiol* 294: G619–G626, 2008.

215. **Rector RS**, **Uptergrove GM**, **Morris EM**, **Borengasser SJ**, **Laughlin MH**, **Booth FW**, **Thyfault JP**, **Ibdah J a**. Daily exercise vs. caloric restriction for prevention of nonalcoholic fatty liver disease in the OLETF rat model. *Am J Physiol Gastrointest Liver Physiol* 300: G874–G883, 2011.

216. **Ricard-Blum S**. The Collagen Family. 2011.

217. **Ritchie ME**, **Phipson B**, **Wu D**, **Hu Y**, **Law CW**, **Shi W**, **Smyth GK**. limma powers differential expression analyses for RNA-sequencing and microarray studies. *Nucleic Acids Res* 43: e47, 2015.

218. **Robinson MD**, **Mccarthy DJ**, **Smyth GK**. edgeR: a Bioconductor package for differential expression analysis of digital gene expression data. *Bioinformatics* 26: 139–140, 2010.

219. **Rodbell M**, **Birnbaumer L**, **Pohl SL**, **Krans MJ**. The glucagon-sensitive adenyl cyclase system in plasma membranes of rat liver. *J Biol Chem* 246: 1877–1882, 1971.

220. **Rowe RG**, **Weiss SJ**. Breaching the basement membrane: who, when and how? *Trends Cell Biol* 18: 560–574, 2008.

221. **Rudel LL**, **Kelley K**, **Sawyer JK**, **Shah R**, **Wilson MD**. Dietary monounsaturated fatty acids promote aortic atherosclerosis in LDL receptor null, human ApoB100-overexpressing transgenic mice. *Arterioscler Thromb Vasc Biol* 18: 1818–1827, 1998.

222. **Rudnick D a**, **Davidson NO**. Functional Relationships between Lipid Metabolism and Liver Regeneration. *Int J Hepatol* 2012: 549241, 2012.

223. **Rui L**. Energy Metabolism in the Liver. *Compr Physiol* 4: 177–197, 2014.

224. **Ryaboshapkina M**, **Hammar M**. Human hepatic gene expression signature of non-alcoholic fatty liver disease progression, a meta-analysis. *Sci Rep* 7: 1–12, 2017.

225. **Sagot I**, **Jimenez L**, **Duvezin-Caubet S**, **Laporte D**, **Courtout F**. Mitochondrial ATP synthases cluster as discrete domains that reorganize with the cellular demand for oxidative phosphorylation. *J Cell Sci* 127: 719–726, 2013.

226. **Sakai T**, **Li S**, **Docheva D**, **Grashoff C**, **Sakai K**, **Kostka G**, **Braun A**, **Pfeifer A**, **Yurchenco PD**, **Fässler R**. Integrin-linked kinase (ILK) is required for polarizing the epiblast, cell adhesion, and controlling actin accumulation. *Genes Dev* 17: 926–940, 2003.

227. **Saks VA**, **Veksler VI**, **Kuznetsov A V.**, **Kay L**, **Sikk P**, **Tiivel T**, **Tranqui L**, **Olivares J**, **Winkler K**, **Wiedemann F**, **Kunz WS**. Permeabilized cell and skinned fiber techniques in studies of mitochondrial function in vivo. *Mol Cell Biochem* 184: 81–100, 1998.

228. **Sarruf DA**, **Thaler JP**, **Morton GJ**, **German J**, **Fischer JD**, **Ogimoto K**, **Schwartz MW**. Fibroblast growth factor 21 action in the brain increases energy expenditure and insulin sensitivity in obese rats. *Diabetes* 59: 1817–1824, 2010.

229. **Satapati S**, **Sunny NE**, **Kucejova B**, **Fu X**, **He TT**, **Méndez-Lucas A**, **Shelton JM**, **Perales JC**, **Browning JD**, **Burgess SC**. Elevated TCA cycle function in the pathology of diet-induced hepatic insulin resistance and fatty liver. *J Lipid Res* 53: 1080–92, 2012.

230. **Sauvant P**, **Cansell M**, **Atgié C**. Vitamin A and lipid metabolism: relationship between hepatic stellate cells (HSCs) and adipocytes. *J Physiol Biochem* 67: 487–96, 2011.

231. **Schaefer L**, **Reinhardt DP**. Special issue: Extracellular matrix: Therapeutic tools and targets in cancer treatment. *Adv Drug Deliv Rev* 97: 1–3, 2016.

232. **Schaffner F**, **Popper H**. Capillarization of hepatic sinusoids in man. *Gastroenterology* 44: 2019, 1963.

233. **Schliess F**, **Reissmann R**, **Reinehr R**, **vom Dahl S**, **Häussinger D**. Involvement of integrins and Src in insulin signaling toward autophagic proteolysis in rat liver. *J Biol Chem* 279: 21294–301, 2004.

234. **Schmidt C**, **Bladt F**, **Goedecke S**, **Brinkmann V**, **Zschiesche W**, **Sharpe M**, **Gherardlt E**, **Birchmeler C**. Scatter factor / hepatocyte growth factor is essential for liver development. *Lett to Nat* 373: 699–702, 1995.

235. **Sekine K**, **Chen Y-R**, **Kojima N**, **Ogata K**, **Fukamizu A**, **Miyajima A**. Foxo1 links insulin signaling to C/EBPalpha and regulates gluconeogenesis during liver development. *EMBO J* 26: 3607–3615, 2007.

236. **Septer S**, **Edwards G**, **Gunewardena S**, **Wolfe a.**, **Li H**, **Daniel J**, **Apte U**. Yes-associated protein is involved in proliferation and differentiation during postnatal liver development. *AJP Gastrointest Liver Physiol* 302: G493–G503, 2012.

237. **Shimomura I**, **Matsuda M**, **Hammer RE**, **Bashmakov Y**, **Brown MS**, **Goldstein JL**. Decreased IRS-2 and Increased SREBP-1c Lead to Mixed Insulin Resistance and Sensitivity in Livers of Lipodystrophic and ob/ob Mice. *Mol Cell* 6: 77–86, 2000.

238. **Shiojiri N**. Analysis of differentiation of hepatocytes and bile duct cells in developing mouse liver by albumin immunofluorescence. *Dev Growth Differ* 26: 555–561, 1984.

239. **Shojaee-Moradie F**, **Ma Y**, **Lou S**, **Hovorka R**, **Umpleby a M**. Prandial hypertriglyceridemia in metabolic syndrome is due to an overproduction of both chylomicron and VLDL triacylglycerol. *Diabetes* 62: 4063–9, 2013.

240. **Si-Tayeb K**, **Lemaigre FP**, **Duncan S a.** Organogenesis and Development of the Liver. *Dev Cell* 18: 175–189, 2010.

241. **Smeeton J**, **Zhang X**, **Bulus N**, **Mernaugh G**, **Lange A**, **Karner CM**, **Carroll TJ**, **Fässler R**, **Pozzi A**, **Rosenblum ND**, **Zent R**. Integrin-linked kinase regulates p38 MAPK-dependent cell cycle arrest in ureteric bud development. *Development* 137: 3233–43, 2010.

242. **Smith BJ**, **Huang K**, **Kong G**, **Chan SJ**, **Nakagawa S**, **Menting JG**, **Hu S-Q**, **Whittaker J**, **Steiiner DF**, **Katsoyannis PG**, **Ward CW**, **Weiss MA**, **Lawrence MC**. Structural resolution of a tandem hormone-binding element in the insulin receptor and its implications for design of peptide agonists. *Proc Natl Acad Sci* 107: 6771–6776, 2010.

243. **Sorrentino P**, **Terracciano L**, **D'Angelo S**, **Ferbo U**, **Bracigliano A**, **Vecchione R**. Predicting fibrosis worsening in obese patients with NASH through parenchymal fibronectin, HOMA-IR, and hypertension. *Am J Gastroenterol* 105: 336–44, 2010.

244. **Sottile J**, **Hocking DC**. Fibronectin Polymerization Regulates the Composition and Stability of Extracellular Matrix Fibrils and Cell-Matrix Adhesions. *Mol Biol Cell* 13: 3546–3559, 2002.

245. **Sumida Y**, **Yoneda M**. Current and future pharmacological therapies for NAFLD/NASH. *J Gastroenterol* 53: 362–376, 2018.

246. **Sun K**, **Tordjman J**, **Clément K**, **Scherer PE**. Fibrosis and adipose tissue dysfunction. *Cell Metab* 18: 470–477, 2013.

247. **Sutherland EW**. Studies on the mechanism of hormone action. *Science (80-)* 177: 401–408, 1972.

248. **Tamkun JW**, **DeSimone DW**, **Fonda D**, **Patel RS**, **Buck C**, **Horwitz AF**, **Hynes RO**. Structure of integrin, a glycoprotein involved in the transmembrane linkage between fibronectin and actin. *Cell* 46: 271–282, 1986.

249. **Tanoue S**, **Uto H**, **Kumamoto R**, **Arima S**, **Hashimoto S**, **Nasu Y**, **Takami Y**, **Moriuchi A**, **Sakiyama T**, **Oketani M**, **Ido A**, **Tsubouchi H**. Liver regeneration after partial hepatectomy in rat is more impaired in a steatotic liver induced by dietary fructose compared to dietary fat. *Biochem Biophys Res Commun* 407: 163–168, 2011.

250. **Targher G**, **Day CP**, **Bonora E**. Risk of cardiovascular disease in patients with nonalcoholic fatty liver disease. *N Engl J Med* 363: 1341–50, 2010.

251. **Taub R**. Liver regeneration: from myth to mechanism. *Nat Rev Mol Cell Biol* 5: 836–847, 2004.

252. **Theocharis AD**, **Skandalis SS**, **Gialeli C**, **Karamanos NK**. Extracellular matrix structure. *Adv Drug Deliv Rev* 97: 4–27, 2016.

253. **Tiedge M**, **Richter T**, **Lenzen S**. Importance of cysteine residues for the stability and catalytic activity of human pancreatic beta cell glucokinase. *Arch Biochem Biophys* 375: 251–260, 2000.

254. **Tiniakos DG**, **Kandilis A**, **Geller SA**. Tityus: A forgotten myth of liver regeneration. *J Hepatol* 53: 357–361, 2010.

255. **Trefts E**, **Gannon M**, **Wasserman DH**. The liver. *Curr Biol* 27: R1147–R1151, 2017.

256. **Trefts E**, **Hughey CC**, **Louise L**, **Lark DS**, **Boyd KL**, **Pozzi A**, **Zent R**, **Wasserman DH**. Energy metabolism couples hepatocyte integrin-linked kinase to liver glucoregulation and postabsorptive responses of mice in an age-dependent manner. *Am J Physiol - Endocrinol Metab* : 2019, 2019.

257. **Trefts E**, **Williams AS**, **Wasserman DH**. Exercise and the Regulation of Hepatic Metabolism. 1st ed. Elsevier Inc.

258. **Tremblay KD**, **Zaret KS**. Distinct populations of endoderm cells converge to generate the embryonic liver bud and ventral foregut tissues. *Dev Biol* 280: 87–99, 2005.

259. **Treyer A**, **Musch A**. Hepatocyte Polarity. *Compr Physiol* 3: 243–287, 2013.

260. **Troussard AA**, **Tan C**, **Yoganathan TN**, **Dedhar S**. Cell-extracellular matrix interactions stimulate the AP-1 transcription factor in an integrin-linked kinase- and glycogen synthase kinase 3-dependent manner. *Mol Cell Biol* 19: 7420–7427, 1999.

261. **Twig G**, **Elorza A**, **Molina AJA**, **Mohamed H**, **Wikstrom JD**, **Walzer G**, **Stiles L**, **Haigh SE**, **Katz S**, **Las G**, **Alroy J**, **Wu M**, **Py BF**, **Yuan J**, **Deeney JT**, **Corkey BE**, **Shirihai OS**. Fission and selective fusion govern mitochondrial segregation and elimination by autophagy. *EMBO J* 27: 433–446, 2008.

262. **Ueno T**, **Komatsu M**. Autophagy in the liver: Functions in health and disease. *Nat Rev Gastroenterol Hepatol* 14: 170–184, 2017.

263. **Ueno T**, **Komatsu M**. Autophagy in the liver: Functions in health and disease. *Nat Rev Gastroenterol Hepatol* 14: 170–184, 2017.

264. **Unger RH**, **Cherrington AD**. Glucagonocentric restructuring of diabetes : a pathophysiologic and therapeutic makeover. *J Cinical Investig* 122: 4–12, 2012.

265. **Varjosalo M**, **Sacco R**, **Stukalov A**, **van Drogen A**, **Planyavsky M**, **Hauri S**, **Aebersold R**, **Bennett KL**, **Colinge J**, **Gstaiger M**, **Superti-Furga G**. Interlaboratory reproducibility of large-scale human protein-complex analysis by standardized AP-MS. *Nat Methods* 10: 307–314, 2013.

266. **Wasserman DH**. Four grams of glucose. *Am J Physiol - Endocrinol Metab* 296: 11–21, 2009.

267. **Wasserman DH**, **Cherrington AD**. Hepatic fuel metabolism during exercise: role and regulation. *Am J Physiol - Endocrinol Metab* 260: E811–E824, 1991.

268. **Wasserman DH**, **Lacy DB**, **Green DR**, **Williams PE**, **Cherrington AD**. Dynamics of hepatic lactate and glucose balances during prolonged exercise and recovery in the dog. [Online]. *J Appl Physiol* 63: 2411–7, 1987. http://www.ncbi.nlm.nih.gov/pubmed/3325489.

269. **Wasserman DH**, **Spalding JA**, **Bracy D**, **Lacy DB**, **Cherrington AD**. Exercise-Induced Rise in Glucagon and Ketogenesis During Prolonged Muscular Work. *Diabetes* 38: 799–807, 1989.

270. **Wasserman DH**, **Williams PE**, **Lacy DB**, **Green DR**, **Cherrington AD**. Importance of intrahepatic mechanisms to gluconeogenesis from alanine during exercise and recovery. *Am J Physiol Metab* 254: E518–E525, 1988.

271. **Wei G**, **Bergquist A**, **Broomé U**, **Lindgren S**, **Wallerstedt S**, **Almer S**, **Sangfelt P**, **Danielsson Å**, **Sandberg-Gertzén H**, **Lööf L**, **Prytz H**, **Björnsson E**. Acute liver failure in Sweden: Etiology and outcome. *J Intern Med* 262: 393–401, 2007.

272. **Wei H**, **Liu L**, **Chen Q**. Selective removal of mitochondria via mitophagy: Distinct pathways for different mitochondrial stresses. *Biochim Biophys Acta - Mol Cell Res* 1853: 2784–2790, 2015.

273. **Weir JB de V**. New methods for calculating metabolic rate with special reference to protein metabolism [Online]. *J Physiol* 109: 1–9, 1949. https://nepp.nasa.gov/.

274. **Weisend CM**, **Kundert JA**, **Suvorova ES**, **Prigge JR**, **Schmidt EE**. Cre activity in fetal albCre Mouse hepatocytes: utility for developmental studies. *Genesis* 47: 789–792, 2010.

275. **White ES**, **Muro AF**. Fibronectin splice variants: Understanding their multiple roles in health and disease using engineered mouse models. *IUBMB Life* 63: 538–46, 2011.

276. **Wickström SA**, **Lange A**, **Montanez E**, **Fässler R**. The ILK/PINCH/parvin complex: The kinase is dead, long live the pseudokinase! *EMBO J* 29: 281–291, 2010.

277. **Wight TN**, **Potter-Perigo S**. The extracellular matrix: an active or passive player in fibrosis? *Am J Physiol Liver Physiol* 301: G950–G955, 2011.

278. **Williams AS**, **Kang L**, **Wasserman DH**. The extracellular matrix and insulin resistance. *Trends Endocrinol Metab* 26: 357–366, 2015.

279. **Williams AS**, **Kang L**, **Zheng J**, **Grueter C**, **Bracy DP**, **James FD**, **Pozzi A**, **Wasserman DH**. Integrin α1β1 Protects against Diet-induced Hepatic Insulin Resistance. *Unpublished*. .

280. **Williams AS**, **Trefts E**, **Lantier L**, **Grueter CA**, **Bracy DP**, **James FD**, **Pozzi A**, **Zent R**, **Wasserman DH**. Integrin-linked kinase is necessary for the development of diet-induced hepatic insulin resistance. *Diabetes* 66: 325–334, 2017.

281. **Williams BD**, **Wolfe RR**, **Bracy DP**, **Wasserman DH**. Gut proteolysis contributes essential amino acids during exercise. *Am J Physiol Metab* 270: E85–E90, 1996.

282. **Williamson DH**, **Lund P**, **Krebs HA**. The redox state of free nicotinamide-adenine dinucleotide in the cytoplasm and mitochondria of rat liver. [Online]. *Biochem J* 103: 514–27, 1967. http://www.pubmedcentral.nih.gov/articlerender.fcgi?artid=1270436&tool=pmcentrez&rendertype=abstract.

283. **Williamson RM**, **Price JF**, **Glancy S**, **Perry E**, **Nee LD**, **Hayes PC**, **Frier BM**, **Van Look LAF**, **Johnston GI**, **Reynolds RM**, **Strachan MWJ**. Prevalence of and risk factors for hepatic steatosis and nonalcoholic fatty liver disease in people with type 2 diabetes: The

Edinburgh type 2 diabetes study. *Diabetes Care* 34: 1139–1144, 2011.

284. **Winograd-Katz SE**, **Fässler R**, **Geiger B**, **Legate KR**. The integrin adhesome: from genes and proteins to human disease. *Nat Rev Mol Cell Biol* 15: 273–288, 2014.

285. **Wisse E**, **Braet F**, **Luo D**, **De Zanger R**, **Jans D**, **Crabbe E**, **Vermoesen A**. Structure and Function of Sinusoidal Lining Cells in the Liver. *Toxicol Pathol* 24: 100–111, 1996.

286. **Wisse E**, **De Zanger RB**, **Charels K**, **Van Der Smissen P**, **McCuskey RS**. The liver sieve: considerations concerning the structure and function of endothelial fenestrae, the sinusoidal wall and the space of Disse. [Online]. *Hepatology* 5: 683–92, 1985. http://www.ncbi.nlm.nih.gov/pubmed/3926620.

287. **Wu C**, **Woo S**, **Lu F**, **Li H**, **Dong H**, **Lange AJ**, **Guo X**, **Xu H**. Glycolysis in the control of blood glucose homeostasis. *Acta Pharm Sin B* 2: 358–367, 2012.

288. **Xu J**, **Stanislaus S**, **Chinookoswong N**, **Lau YY**, **Hager T**, **Patel J**, **Ge H**, **Weiszmann J**, **Lu S-C**, **Graham M**, **Busby J**, **Hecht R**, **Li Y-S**, **Li Y**, **Lindberg R**, **Veniant MM**. Acute glucose-lowering and insulin-sensitizing action of FGF21 in insulin-resistant mouse models--association with liver and adipose tissue effects. *AJP Endocrinol Metab* 297: E1105–E1114, 2009.

289. **Xu Z**, **Chen L**, **Leung L**, **Yen TSB**, **Lee C**, **Chan JY**. Liver-specific inactivation of the Nrf1 gene in adult mouse leads to nonalcoholic steatohepatitis and hepatic neoplasia. *Proc Natl Acad Sci* 102: 4120–4125, 2005.

290. **Yamagata K**, **Furuta H**, **Oda N**, **Kaisaki PJ**, **Menzel S**, **Cox NJ**, **Fajans SS**, **Signorini S**, **Stoffel M**, **Bell GI**. Mutations in the hepatocyte nuclear factor-4α gene in maturity-onset diabetes of the young (MODY1). *Lett to Nat* 384: 458–460, 1996.

291. **Yamasaki H**, **Sada A**, **Iwata T**, **Niwa T**, **Tomizawa M**, **Xanthopoulos KG**, **Koike T**, **Shiojiri N**. Suppression of C/EBP α expression in periportal hepatoblasts may stimulate biliary cell differentiation through increased Hnf6 and Hnf1b expression. *Development* 133: 4233–4243, 2006.

292. **Yoganathan TN**, **Costello P**, **Chen X**, **Jabali M**, **Yan J**, **Leung D**, **Zhang Z**, **Yee A**, **Dedhar S**, **Sanghera J**. Integrin-linked kinase (ILK): A “hot” therapeutic target. *Biochem Pharmacol* 60: 1115–1119, 2000.

293. **Yu H**, **Zhou D**, **Jia W**, **Guo Z-K**. Locating the source of hyperglycemia: Liver versus muscle. *J Diabetes* 4: 3831–3840, 2012.

294. **Zhang Y**, **Ikegami T**, **Honda A**, **Miyazaki T**, **Bouscarel B**, **Rojkind M**, **Hyodo I**, **Matsuzaki Y**. Involvement of integrin-linked kinase in carbon tetrachloride–induced hepatic fibrosis in rats. *Hepatology* 44: 612–622, 2006.

295. **Zong H**, **Bastie CC**, **Xu J**, **Fassler R**, **Campbell KP**, **Kurland IJ**, **Pessin JE**. Insulin resistance in striated muscle-specific integrin receptor β1-deficient mice. *J Biol Chem* 284: 4679–4688, 2009.

APPENDIX

Depicted below is the code written in the “R” language for analysis of differentially expressed genes as well as gene ontology and KEGG pathway analyses. Additionally there are several figure creation aspects included that operate through the standard R visualization methods as well as ggplot and plotly programs. With the correct files and directories this code will run start to finish and produce all data, tables, and figures present in Chapter III (Table 3.6-3.11; Figures 3.8-3.11). Also included are scripts for the production of heatmap type figures, which were not included in the dissertation. Lines with # at the start will not run in a session of R. Many of these lines are descriptive of the following code and its goals in relation to manipulating data, performing statistical analyses, or creating figures. Certain lines with # at the front are indications to install a program with R. These were excluded as they are not necessary after initial installation in R. A *de novo* R installation and attempt to use this code would require the “unmasking” of these installation code lines.

```
#edgeR gene analysis

#set the folder to work from wherever it is located. I've designated mine below
setwd("C:/Users/treftse/Dropbox (VUMC)/RNA-seq documents/HTseq count files")

#Assemble a table denoting all designating characteristics of each of your
#samples and read that into R

Pheno_data <- read.delim("181206 Pheno_data.txt", stringsAsFactors=FALSE)

#designate a novel characteristic of this table which combines all
#attributes into a single item for mine it is Genotype,Age, and Diet

group <- paste(Pheno_data$Genotype, Pheno_data$Age,
Pheno_data$Diet, sep="")

group <- factor(group)

table(group)

#Read in a table containing all samples and counts with sample names in header
#and the gene identifiers in the first column
GenewiseCounts <- read.delim("181206 HTSeqcounts-no_details.txt",
```

```
row.names="ensemblID")

colnames(GenewiseCounts) <- substring(colnames(GenewiseCounts),2)

library(edgeR)

#Create the specific item needed for edgeR differential gene expression analysis
y <- DGEList(GenewiseCounts, group=group,
        genes=GenewiseCounts[,1,drop=FALSE])

options(digits=3)
y$samples

#contingencies for altering the ensemblIDs with version identifier
library(tidyr)
library(dplyr)
library(data.table)

#Next command removes version identifier from ensembl ID rownames.
#This command is a simple text altering command and so is simply working from
#the script in the name and removing everything after and including a period
#more advanced alterations can be performed, but would have to be looked in to.

# create list of versionless ensembl IDs
ensemblIDS<-nth(tstrsplit(row.names(y), split ="\\."),n=1)

#Add column of versionless ensembl IDs to y DGE object
y$genes$ensemblIDS<-ensemblIDS

#Convert ensembl IDs to entrez IDS and add a column to the DGE object
library(org.Mm.eg.db)
y$genes$entrezid <- mapIds(org.Mm.eg.db, y$genes$ensemblIDS,
                keytype="ENSEMBL", column="ENTREZID")

#Remove any genes which did not map between ensembl and entrez IDS
y <- y[!is.na(y$genes$entrezid), ]

#Add gene symbol names as well to DGE object
y$genes$symbol <- mapIds(org.Mm.eg.db, y$genes$ensemblIDS,
                keytype="ENSEMBL", column="SYMBOL")

#remove genes without symbols
y <- y[!is.na(y$genes$symbol), ]

#determine dimensions of y (DGE object) so as to assess loss of genes
dim(y)

#want counts/library of ~10 so match counts per million (cpm) to average library size
#I have actually gone with a counts per million cutoff here, but there is no real consensus on the
appropriate cutoff
```

```
keep <- rowSums(cpm(y$counts)>=0.417) >= 5

y <- y[keep, , keep.lib.sizes=FALSE]

y <- calcNormFactors(y)

y$samples

design <- model.matrix(~0+group)

colnames(design) <- levels(group)

design

#install.packages("statmod")
#library(statmod)
y <- estimateDisp(y, design, robust=TRUE)

plotBCV(y)

fit <- glmQLFit(y, design, robust=TRUE)
head(fit$coefficients)

plotQLDisp(fit)

summary(fit$df.prior)

#MDS (similar to PCA) plot
points <- c(0,1,2,15,16,17)
colors <- rep(c("blue", "darkgreen", "red"), 2)
plotMDS(y, col=colors[group], pch=points[group])
legend("topright", legend=levels(group), pch=points, col=colors, ncol=2)

#once plot is organized to appropriate appearance output as SVG file.
svg("190315 ILK RNA seq MDS.svg",width=7,height=7)
points <- c(0,1,2,15,16,17)
colors <- rep(c("blue", "darkgreen", "red"), 2)
plotMDS(y, col=colors[group], pch=points[group])
legend("topright", legend=levels(group), pch=points, col=colors, ncol=2)
dev.off()

#Define comparison to make between gene sets

WT6chxKO6ch <- makeContrasts(KO6wkChow-WT6wkChow, levels=design)

Chow6results <- glmQLFTest(fit, contrast=WT6chxKO6ch)

#show top 10 P value DEGs and log FCs
topTags(Chow6results)

#determine differential expression test
```

```
is.de.Chow6wk <- decideTestsDGE(Chow6results,adjust.method="BH", p.value=0.05)
summary(is.de.Chow6wk)

#make results table from DGE analysis a data frame
DGE.Chow6wk <- data.frame(Chow6results$table)

#add DGE binary marker to data frame
DGE.Chow6wk$DE <- is.de.Chow6wk

#Write table
write.table(DGE.Chow6wk, file= "190315 Dissertation 6wk chow DGE.tsv", row.names=TRUE,
            col.names=NA, sep="\t")


plotMD(Chow6results, status=is.de.Chow6wk, values=c(1,-1), col=c("red","blue"),
legend="topright")


# dependencies:
#install.packages("ggplot2")
#install.packages("gridExtra")
#install.packages("plotly")
#install.packages("dplyr")
#install.packages("orca")
#install.packages("processx")
#suppressPackageStartupMessages(library("plotly"))
library(ggplot2)
library(gridExtra)
library(plotly)
library(dplyr)
library(orca)
library(processx)
Sys.setenv('MAPBOX_TOKEN'                                                                                    =
'pk.eyJ1IjoiZXRyZWZ0cyIsImEiOiJjanRhc214dDYwZWduNDltZWZ5c3JqemIyIn0.YoiKAvwoZR
BJQVptAWJ9Pg')


# path to the gene file
setwd("C:/Users/treftse/Dropbox (VUMC)/Defense/")
Chow6wkVolcano <- "C:/Users/treftse/Dropbox (VUMC)/Defense/190315 Dissertation 6wk chow
DGE.tsv"

# graph 6 wk Chow analysis
diff_df_Chow6wk <- read.delim(file = Chow6wkVolcano,header = TRUE,row.names=1,sep = '\t')
#add column of -log10p values to table
diff_df_Chow6wk$negLog10P <- (-log10(diff_df_Chow6wk$PValue))
# edit the dataframe to contain the main information used for analysis
diff_df_Chow6wk <- diff_df_Chow6wk[c("logFC", "DE", "negLog10P")]

#edit the data frame to add a column and establish criteria for significance and fold change
```

```
diff_df_Chow6wk[which(diff_df_Chow6wk['DE'] < -0.5 & abs(diff_df_Chow6wk['logFC']) > 0 ),"group"] <- "Downregulated"
diff_df_Chow6wk[which(diff_df_Chow6wk['DE'] > -0.5 & diff_df_Chow6wk['DE'] < 0.5 ),"group"] <- "Non-significant"
diff_df_Chow6wk[which(diff_df_Chow6wk['DE'] > 0.5 & abs(diff_df_Chow6wk['logFC']) > 0 ),"group"] <- "Upregulated"

#Define color scheme
palChow6wk <- c("blue", "black", "red")

palChow6wk <- setNames(palChow6wk, c("Upregulated", "Non-significant", "Downregulated"))

#plot differentially expressed gene data on a volcano plot
pChow6wk <- plot_ly(data=diff_df_Chow6wk, x=~logFC, y= ~negLog10P,  type="scatter",
mode="markers", symbol=0, color=~group, colors=pal,width=500, height=600)%>%
layout(margin= (pad=0),
title= "<b>6 Week Chow ILK <sup>lox/lox</sup> Vs. hepILK-KO RNA-seq</b>",
titlefont = list(family="Arial", size=20, color = "black"),
xaxis = list(title = '<b>log<sub>2</sub> Fold Change</b>',
autotick = FALSE, ticks = "outside", tick0 = 0,
dtick = 5, ticklen = 5, tickwidth = 2,tickcolor = toRGB("white"),
showticklabels=TRUE,tickfont=list(family="Arial", size=20, color = "black"),
titlefont = list(family="Arial", size=20, color = "black"),
zeroline = TRUE, range = c(-10, 10)), showlegend=TRUE,
legend=list(x=0.9,y=0.9,traceorder='normal',font=list(family='Arial',size=20,
color='#000'),bordercolor='#FFFFFF',borderwidth=2),
yaxis = list(title = '<b>-log<sub>10</sub> <i>p</i>-value</b>',
autotick = FALSE, ticks = "outside", tick0 = 0,
dtick = 3, ticklen = 5, tickwidth = 2,tickcolor = toRGB("white"),
showticklabels=TRUE,tickfont=list(family="Arial", size=20, color = "black"),
titlefont = list(family="Arial", size=24, color = "black"),
range = c(0,13)))
pChow6wk

#export plotly object "volcano plot" as svg
orca(pChow6wk, "190315 Chow 6wk Volcano.svg")


#save graph as html

htmlwidgets::saveWidget(p, "190315 Chow 6wk Volcano.html")


# Heat map synthesis for top 40 DE genes
#Create a CPM arrangement of the DGE object count matrix
logCPM <- cpm(y, prior.count=2, log=TRUE)
#Change the columnn names to a representation of samples with groups and numbers 1-5
colnames(logCPM) <- paste(y$samples$group, 1:5, sep="-")
#Replace rownames of CPM object with gene symbols
rownames(logCPM) <- paste(y$genes$symbol)
#Order the Pvalues based on the comparison denoted
```

```
o <- order(Chow6results$table$PValue)
#Index the logCPM object based on the highest 40 PValues from previous order function
logCPM <- logCPM[o[1:40],]

#scale each row (each gene) to have mean zero and standard deviation one
logCPM <- t(scale(t(logCPM)))

#plotting program contingency
library(gplots)

#Establish color panel to be used for heat map
col.pan <- colorpanel(100, "blue", "white", "red")

#order of columnns for heat map
cn<-c("WT6wkChow-1","WT6wkChow-2","WT6wkChow-3","WT6wkChow-4","WT6wkChow-5",
    "KO6wkChow-1","KO6wkChow-2","KO6wkChow-3","KO6wkChow-4","KO6wkChow-5")

#heat mapping function
heatmap.2(logCPM[,cn], col=col.pan,Colv=FALSE, Rowv=TRUE, scale="none",
        trace="none", dendrogram="none",cexRow=1.2, cexCol=1.2,labCol = FALSE,
        density.info="none", margin=c(2,10), lhei=c(2,8), lwid=c(2,6))

#GO and KEGG analysis
library(GO.db)

#GO analysis of res("loose") analysis
go6chow <- goana(Chow6results, geneid=y$genes$entrezid, species="Mm")
#display 15 GO terms of highest P-value
topGO(go6chow, n=15)


#write table of GO analysis
write.table(go6chow, file= "190315 Dissertation 6wk chow GO.tsv", row.names=TRUE, sep="\t")

#KEGG pathway analysis
kegg6chow <- kegga(Chow6results, geneid = y$genes$entrezid, species="Mm")
topKEGG(kegg6chow, n=15, truncate=34)

#write table of KEGG analysis
write.table(kegg6chow, file= "190315 Dissertation 6wk chow kegg.tsv",
        row.names=TRUE, sep="\t")

#enables indexing of data frame based on logical constraint
go6chowup <- go6chow[go6chow$P.Up < 0.001,]
#order in ascending order p-values
go6chowup <- go6chowup[order(go6chowup$P.Up),]
topGO(go6chowup, n=15,sort="up")
write.table(go6chowup, file= "190315 Dissertation 6wk chow GO up.tsv", row.names=TRUE,
        sep="\t")

#enables indexing of data frame based on logical constraint
```

```
go6chowdown <- go6chow[go6chow$P.Down < 0.001,]
#order in ascending order p-values
go6chowdown <- go6chowdown[order(go6chowdown$P.Down),]
topGO(go6chowdown, n=15,sort="down")
write.table(go6chowdown , file= "190315 Dissertation 6wk chow GO down.tsv",
          row.names=TRUE, sep="\t")

#enables indexing of data frame based on logical constraint
kegg6chowdown <- kegg6chow[kegg6chow$P.Down < 0.001,]
#order in ascending order p-values
kegg6chowdown <- kegg6chowdown[order(kegg6chowdown$P.Down),]
topKEGG(kegg6chowdown, n=15,sort="down")
write.table(kegg6chowdown, file= "190315 Dissertation 6wk chow KEGG down.tsv",
          row.names=TRUE, sep="\t")

kegg6chowup <- kegg6chow[kegg6chow$P.Up < 0.001,]
#order in ascending order p-values
kegg6chowup <- kegg6chowup[order(kegg6chowup$P.Up),]
topKEGG(kegg6chowup, n=15,sort="up")
write.table(kegg6chowup, file= "190315 Dissertation 6wk chow KEGG up.tsv",
          row.names=TRUE, sep="\t")



#Continuing this script will provide analysis and figures for the Chow-fed 18 week old group
################################################################################
#




#Establish new comparison for 18wk chow mice

WT18chxKO18ch <- makeContrasts(KO18wkChow-WT18wkChow, levels=design)

Chow18results <- glmQLFTest(fit, contrast=WT18chxKO18ch)

#show top 10 P value DEGs and log FCs
topTags(Chow18results)

#determine differerntial expression test
is.de.Chow18wk <- decideTestsDGE(Chow18results)
summary(is.de.Chow18wk)

#make results table from DGE analysis a data frame
DGE.Chow18wk <- data.frame(Chow18results$table)

#add DGE binary marker to data frame
DGE.Chow18wk$DE <- is.de.Chow18wk

#Write table
```

```
write.table(DGE.Chow18wk, file= "190315 Dissertation 18wk chow DGE.tsv", row.names=TRUE,
            col.names=NA, sep="\t")

plotMD(Chow18results, status=is.de.Chow18wk, values=c(1,-1), col=c("red","blue"),
legend="topright")

# dependencies:
#install.packages("ggplot2")
#install.packages("gridExtra")
#install.packages("plotly")
#install.packages("dplyr")
#install.packages("orca")
#install.packages("processx")
#suppressPackageStartupMessages(library("plotly"))
library(ggplot2)
library(gridExtra)
library(plotly)
library(dplyr)
library(orca)
library(processx)
Sys.setenv('MAPBOX_TOKEN'                                                                                    =
'pk.eyJ1IjoiZXRyZWZ0cyIsImEiOiJjanRhc214dDYwZWduNDltZWZ5c3JqemIyIn0.YoiKAvwoZR
BJQVptAWJ9Pg')


# path to the gene file
setwd("C:/Users/treftse/Dropbox (VUMC)/Defense/")
Chow18wkVolcano <- "C:/Users/treftse/Dropbox (VUMC)/Defense/190315 Dissertation 18wk
chow DGE.tsv"

# graph 18 wk Chow analysis
diff_df_Chow18wk <- read.delim(file = Chow18wkVolcano,header = TRUE,row.names=1,sep =
'\t')
#add column of -log10p values to table
diff_df_Chow18wk$negLog10P <- (-log10(diff_df_Chow18wk$PValue))
# edit the dataframe to contain the main information used for analysis
diff_df_Chow18wk <- diff_df_Chow18wk[c("logFC", "DE", "negLog10P")]

#edit the data frame to add a column and establish criteria for significance and fold change
diff_df_Chow18wk[which(diff_df_Chow18wk['DE'] < -0.5 & abs(diff_df_Chow18wk['logFC']) > 0
),"group"] <- "Downregulated"
diff_df_Chow18wk[which(diff_df_Chow18wk['DE'] > -0.5 & diff_df_Chow18wk['DE'] < 0.5
),"group"] <- "Non-significant"
diff_df_Chow18wk[which(diff_df_Chow18wk['DE'] > 0.5 & abs(diff_df_Chow18wk['logFC']) > 0
),"group"] <- "Upregulated"

#Define color scheme
palChow18wk <- c("blue", "black", "red")

palChow18wk <- setNames(palChow18wk, c("Upregulated", "Non-significant", "Downregulated"))
```

```
#plot differentially expressed gene data on a volcano plot
pChow18wk <- plot_ly(data=diff_df_Chow18wk, x=~logFC, y= ~negLog10P,  type="scatter",
mode="markers", symbol=0, color=~group, colors=pal,width=500, height=600)%>%
layout(margin= (pad=0),
title= "<b>18 Week Chow ILK <sup>lox/lox</sup> Vs. hepILK-KO RNA-seq</b>",
titlefont = list(family="Arial", size=20, color = "black"),
xaxis = list(title = '<b>log<sub>2</sub> Fold Change</b>',
autotick = FALSE, ticks = "outside", tick0 = 0,
dtick = 5, ticklen = 5, tickwidth = 2,tickcolor = toRGB("white"),
showticklabels=TRUE,tickfont=list(family="Arial", size=20, color = "black"),
titlefont = list(family="Arial", size=20, color = "black"),
zeroline = TRUE, range = c(-10, 10)), showlegend=TRUE,
legend=list(x=0.9,y=0.9,traceorder='normal',font=list(family='Arial',size=20,
color='#000'),bordercolor='#FFFFFF',borderwidth=2),
yaxis = list(title = '<b>-log<sub>10</sub> <i>p</i>-value</b>',
autotick = FALSE, ticks = "outside", tick0 = 0,
dtick = 3, ticklen = 5, tickwidth = 2,tickcolor = toRGB("white"),
showticklabels=TRUE,tickfont=list(family="Arial", size=20, color = "black"),
titlefont = list(family="Arial", size=24, color = "black"),
range = c(0,13)))
pChow18wk

#export plotly object "volcano plot" as svg
orca(p, "190315 Chow 18wk Volcano.svg")


#save graph as html

htmlwidgets::saveWidget(p, "190315 Chow 18wk Volcano.html")


# Heat map synthesis for top 40 DE genes
#Create a CPM arrangement of the DGE object count matrix
logCPM <- cpm(y, prior.count=2, log=TRUE)
#Change the columnn names to a representation of samples with groups and numbers 1-5
colnames(logCPM) <- paste(y$samples$group, 1:5, sep="-")
#Replace rownames of CPM object with gene symbols
rownames(logCPM) <- paste(y$genes$symbol)
#Order the Pvalues based on the comparison denoted
o <- order(Chow18results$table$PValue)
#Index the logCPM object based on the highest 40 PValues from previous order function
logCPM <- logCPM[o[1:40],]

#scale each row (each gene) to have mean zero and standard deviation one
logCPM <- t(scale(t(logCPM)))

#plotting program contingency
library(gplots)

#Establish color panel to be used for heat map
col.pan <- colorpanel(100, "blue", "white", "red")
```

```
#order of columnns for heat map
cn<-c("WT18wkChow-1","WT18wkChow-2","WT18wkChow-3","WT18wkChow-
4","WT18wkChow-5",
     "KO18wkChow-1","KO18wkChow-2","KO18wkChow-3","KO18wkChow-4","KO18wkChow-
5")

#heat mapping function
heatmap.2(logCPM[,cn], col=col.pan,Colv=FALSE, Rowv=TRUE, scale="none",
          trace="none", dendrogram="none",cexRow=1.2, cexCol=1.2, density.info="none",
          margin=c(10,9), lhei=c(2,8), lwid=c(2,6))

#GO and KEGG analysis
library(GO.db)

#GO analysis of res("loose") analysis
go18chow <- goana(Chow18results, geneid=y$genes$entrezid, species="Mm")
#display 15 GO terms of highest P-value
topGO(go18chow, n=15)


#write table of GO analysis
write.table(go18chow, file= "190315 Dissertation 18wk chow GO.tsv", row.names=TRUE,
sep="\t")

#KEGG pathway analysis
kegg18chow <- kegga(Chow18results, geneid = y$genes$entrezid, species="Mm")
topKEGG(kegg18chow, n=15, truncate=34)

#write table of KEGG analysis
write.table(kegg18chow, file= "190315 Dissertation 18wk chow kegg.tsv",
          row.names=TRUE, sep="\t")

#enables indexing of data frame based on logical constraint
go18chowup <- go18chow[go18chow$P.Up < 0.001,]
#order in ascending order p-values
go18chowup <- go18chowup[order(go18chowup$P.Up),]
topGO(go18chowup, n=15,sort="up")
write.table(go18chowup, file= "190315 Dissertation 18wk chow GO up.tsv", row.names=TRUE,
          sep="\t")

#enables indexing of data frame based on logical constraint
go18chowdown <- go18chow[go18chow$P.Down < 0.001,]
#order in ascending order p-values
go18chowdown <- go18chowdown[order(go18chowdown$P.Down),]
topGO(go18chowdown, n=15,sort="down")
write.table(go18chowdown , file= "190315 Dissertation 18wk chow GO down.tsv",
           row.names=TRUE, sep="\t")

#enables indexing of data frame based on logical constraint
kegg18chowdown <- kegg18chow[kegg18chow$P.Down < 0.001,]
```

```
#order in ascending order p-values
kegg18chowdown <- kegg18chowdown[order(kegg18chowdown$P.Down),]
topKEGG(kegg18chowdown, n=15,sort="down")
write.table(kegg18chowdown, file= "190315 Dissertation 18wk chow KEGG down.tsv",
        row.names=TRUE, sep="\t")

#enables indexing of data frame based on logical constraint
kegg18chowup <- kegg18chow[kegg18chow$P.Up < 0.001,]
#order in ascending order p-values
kegg18chowup <- kegg18chowup[order(kegg18chowup$P.Up),]
topKEGG(kegg18chowup, n=15,sort="up")
write.table(kegg18chowup, file= "190315 Dissertation 18wk chow KEGG up.tsv",
        row.names=TRUE, sep="\t")



#Continuing this script will provide analysis and figures for the HF-fed 18 week old group
################################################################################
#



#Establish new comparison for 18wk chow mice

WT18HFxKO18HF <- makeContrasts(KO18wkHF-WT18wkHF, levels=design)

HF18results <- glmQLFTest(fit, contrast=WT18HFxKO18HF)

#show top 10 P value DEGs and log FCs
topTags(HF18results)

#determine differerntial expression test
is.de.HF18wk <- decideTestsDGE(HF18results)
summary(is.de.HF18wk)

#make results table from DGE analysis a data frame
DGE.HF18wk <- data.frame(HF18results$table)

#add DGE binary marker to data frame
DGE.HF18wk$DE <- is.de.HF18wk

#Write table
write.table(DGE.HF18wk, file= "190315 Dissertation 18wk HF DGE.tsv", row.names=TRUE,
        col.names=NA, sep="\t")


plotMD(HF18results, status=is.de, values=c(1,-1), col=c("red","blue"), legend="topright")

# dependencies:
```

```
#install.packages("ggplot2")
#install.packages("gridExtra")
#install.packages("plotly")
#install.packages("dplyr")
#install.packages("orca")
#install.packages("processx")
#suppressPackageStartupMessages(library("plotly"))
library(ggplot2)
library(gridExtra)
library(plotly)
library(dplyr)
library(orca)
library(processx)
Sys.setenv('MAPBOX_TOKEN' =
'pk.eyJ1IjoiZXRyZWZ0cyIsImEiOiJjanRhc214dDYwZWduNDltZWZ5c3JqemIyIn0.YoiKAvwoZR
BJQVptAWJ9Pg')


# path to the gene file
setwd("C:/Users/treftse/Dropbox (VUMC)/Defense/")
HF18wkVolcano <- "C:/Users/treftse/Dropbox (VUMC)/Defense/190315 Dissertation 18wk HF
DGE.tsv"

# graph 18 wk Chow analysis
diff_df_HF18wk <- read.delim(file = HF18wkVolcano,header = TRUE,row.names=1,sep = '\t')
#add column of -log10p values to table
diff_df_HF18wk$negLog10P <- (-log10(diff_df_HF18wk$PValue))
# edit the dataframe to contain the main information used for analysis
diff_df_HF18wk <- diff_df_HF18wk[c("logFC", "DE", "negLog10P")]

#edit the data frame to add a column and establish criteria for significance and fold change
diff_df_HF18wk[which(diff_df_HF18wk['DE'] < -0.5 & abs(diff_df_HF18wk['logFC']) > 0 ),"group"]
<- "Downregulated"
diff_df_HF18wk[which(diff_df_HF18wk['DE'] > -0.5 & diff_df_HF18wk['DE'] < 0.5 ),"group"] <-
"Non-significant"
diff_df_HF18wk[which(diff_df_HF18wk['DE'] > 0.5 & abs(diff_df_HF18wk['logFC']) > 0 ),"group"]
<- "Upregulated"

#Define color scheme
palHF18wk <- c("blue", "black", "red")

palHF18wk <- setNames(pal, c("Upregulated", "Non-significant", "Downregulated"))

#plot differentially expressed gene data on a volcano plot
pHF18wk <- plot_ly(data=diff_df_HF18wk, x=~logFC, y= ~negLog10P,  type="scatter",
mode="markers", symbol=0, color=~group, colors=pal,width=500, height=600)%>%
layout(margin= (pad=0),
title= "<b>18 Week HF ILK <sup>lox/lox</sup> Vs. hepILK-KO RNA-seq</b>",
titlefont = list(family="Arial", size=20, color = "black"),
xaxis = list(title = '<b>log<sub>2</sub> Fold Change</b>',
autotick = FALSE, ticks = "outside", tick0 = 0,
```

```
dtick = 5, ticklen = 5, tickwidth = 2,tickcolor = toRGB("white"),
showticklabels=TRUE,tickfont=list(family="Arial", size=20, color = "black"),
titlefont = list(family="Arial", size=20, color = "black"),
zeroline = TRUE, range = c(-10, 10)), showlegend=TRUE,
legend=list(x=0.9,y=0.9,traceorder='normal',font=list(family='Arial',size=20,
color='#000'),bordercolor='#FFFFFF',borderwidth=2),
yaxis = list(title = '<b>-log<sub>10</sub> <i>p</i>-value</b>',
autotick = FALSE, ticks = "outside", tick0 = 0,
dtick = 3, ticklen = 5, tickwidth = 2,tickcolor = toRGB("white"),
showticklabels=TRUE,tickfont=list(family="Arial", size=20, color = "black"),
titlefont = list(family="Arial", size=24, color = "black"),
range = c(0,13)))
pHF18wk

#export plotly object "volcano plot" as svg
orca(p, "190315 HF 18wk Volcano.svg")


#save graph as html

htmlwidgets::saveWidget(p, "190315 HF 18wk Volcano.html")



# Heat map synthesis for top 40 DE genes
#Create a CPM arrangement of the DGE object count matrix
logCPM <- cpm(y, prior.count=2, log=TRUE)
#Change the columnn names to a representation of samples with groups and numbers 1-5
colnames(logCPM) <- paste(y$samples$group, 1:5, sep="-")
#Replace rownames of CPM object with gene symbols
rownames(logCPM) <- paste(y$genes$symbol)
#Order the Pvalues based on the comparison denoted
o <- order(HF18results$table$PValue)
#Index the logCPM object based on the highest 40 PValues from previous order function
logCPM <- logCPM[o[1:40],]

#scale each row (each gene) to have mean zero and standard deviation one
logCPM <- t(scale(t(logCPM)))

#plotting program contingency
library(gplots)

#Establish color panel to be used for heat map
col.pan <- colorpanel(100, "blue", "white", "red")

#order of columnns for heat map
cn<-c("WT18wkHF-1","WT18wkHF-2","WT18wkHF-3","WT18wkHF-4","WT18wkHF-5",
    "KO18wkHF-1","KO18wkHF-2","KO18wkHF-3","KO18wkHF-4","KO18wkHF-5")

#heat mapping function
heatmap.2(logCPM[,cn], col=col.pan,Colv=FALSE, Rowv=TRUE, scale="none",
```

```
        trace="none", dendrogram="none",cexRow=1.2, cexCol=1.2, density.info="none",
        margin=c(10,9), lhei=c(2,8), lwid=c(2,6))

#GO and KEGG analysis
library(GO.db)

#GO analysis of res("loose") analysis
go18HF <- goana(HF18results, geneid=y$genes$entrezid, species="Mm")
#display 15 GO terms of highest P-value
topGO(go18HF, n=15)


#write table of GO analysis
write.table(go18HF, file= "190315 Dissertation 18wk HF GO.tsv", row.names=TRUE, sep="\t")

#KEGG pathway analysis
kegg18HF <- kegga(HF18results, geneid = y$genes$entrezid, species="Mm")
topKEGG(kegg18HF, n=15, truncate=34)

#write table of KEGG analysis
write.table(kegg18HF, file= "190315 Dissertation 18wk HF kegg.tsv",
        row.names=TRUE, sep="\t")

#enables indexing of data frame based on logical constraint
go18HFup <- go18HF[go18HF$P.Up < 0.001,]
#order in ascending order p-values
go18HFup <- go18HFup[order(go18HFup$P.Up),]
topGO(go18HFup, n=15,sort="up")
write.table(go18HFup, file= "190315 Dissertation 18wk HF GO up.tsv", row.names=TRUE,
        sep="\t")

#enables indexing of data frame based on logical constraint
go18HFdown <- go18HF[go18HF$P.Down < 0.001,]
#order in ascending order p-values
go18HFdown <- go18HFdown[order(go18HFdown$P.Down),]
topGO(go18HFdown, n=15,sort="down")
write.table(go18HFdown , file= "190315 Dissertation 18wk HF GO down.tsv",
         row.names=TRUE, sep="\t")

#enables indexing of data frame based on logical constraint
kegg18HFdown <- kegg18HF[kegg18HF$P.Down < 0.001,]
#order in ascending order p-values
kegg18HFdown <- kegg18HFdown[order(kegg18HFdown$P.Down),]
topKEGG(kegg18HFdown, n=15,sort="down")
write.table(kegg18HFdown, file= "190315 Dissertation 18wk HF KEGG down.tsv",
        row.names=TRUE, sep="\t")

#enables indexing of data frame based on logical constraint
kegg18HFup <- kegg18HF[kegg18HF$P.Up < 0.001,]
#order in ascending order p-values
kegg18HFup <- kegg18HFup[order(kegg18HFup$P.Up),]
```

```
topKEGG(kegg18HFup, n=15,sort="up")
write.table(kegg18HFup, file= "190315 Dissertation 18wk HF KEGG up.tsv",
        row.names=TRUE, sep="\t")
```